OCEAN ENGINEERING GROUP

A Boundary Element Method for the Strongly Nonlinear Analysis of Ventilating Water-entry and Wave-body Interaction Problems

Vimal Vinayan

August, 2009

REPORT No.

09-02

ENVIRONMENTAL AND WATER RESOURCES ENGINEERING
DEPARTMENT OF CIVIL, ARCHITECTURAL AND ENVIRONMENTAL ENGINEERING
THE UNIVERSITY OF TEXAS AT AUSTIN
AUSTIN, TX 78712

Copyright
by
Vimal Vinayan
2009

The Dissertation Committee for Vimal Vinayan
certifies that this is the approved version of the following dissertation:

A Boundary Element Method for the Strongly Nonlinear Analysis of Ventilating Water-entry and Wave-body Interaction Problems

Committee:

Spyros A. Kinnas, Supervisor

Ben R. Hodges

Loukas F. Kallivokas

Howard M. Liljestrand

Richard Mercier

Kamy Sepehrnoori

A Boundary Element Method for the Strongly Nonlinear Analysis of Ventilating Water-entry and Wave-body Interaction Problems

by

Vimal Vinayan, B.Tech, M.S.

DISSERTATION

Presented to the Faculty of the Graduate School of

The University of Texas at Austin

in Partial Fulfillment

of the Requirements

for the Degree of

DOCTOR OF PHILOSOPHY

THE UNIVERSITY OF TEXAS AT AUSTIN

August 2009

Dedicated to my family,

to my wife Krishna,

and to the 19^{th} Batch.

Acknowledgments

The time spent at UT with the Ocean Engineering Group has been quite memorable and I sure do have a lot of people to thank for making it so. So here goes my sincere attempt at trying to express my gratitude ...

... starting with my advisor, Professor Spyros Kinnas. His encouragement and support during the course of this dissertation has been unwavering. I cannot thank him enough for his guidance and for keeping things in focus by weeding out most of my grandiose ideas, yet recognizing and giving me enough leeway to experiment on a few that have materialized into this dissertation. I sincerely appreciate the effort he has put in to recognizing my strengths and weaknesses, and for helping me grow on both an intellectual and personal level.

I would also like to express my deepest gratitude to the members of my dissertation committee Professors Ben R. Hodges, Loukas F. Kallivokas, Howard M. Liljestrand, Richard Mercier and Kamy Sepehrnoori for their advice and suggestions. I would like to thank Professor Mercier for taking the time to commute to UT from Texas A&M and for agreeing to be a member of the dissertation committee.

I wish to thank Dr. Bruce Cox for sharing with me information on his experimental observations and photographs, and Dr. Alessandro Iafrati of INSEAN (Istituto Nazionale per Studi ed Esperienze di Architettura Navale) for his valuable comments regarding the numerical aspects of the water-entry problem.

I would like to thank all my former teachers and advisors for their guidance during my high-school, undergraduate and graduate years.

It has been a real pleasure to have worked with Dr. Hanseong Lee. I have always admired his dedication and sincerity towards his work. Along with him, I would like

to thank everyone at CHL for their company and friendship. A special thanks goes to Dr. Yi-hsiang Yu for the discussions during the work on the hull dynamics.

The administrative staff at UT has been great! I sincerely thank the OTRC (Offshore Technology Research Center) staff, Paul White and Sandra Vasquez for their help during my years at UT and CHL. A special thanks goes to Kathy Rose, Rebecca Christian and Danny Quiroz for their assistance. I would like to thank the staff at the Engineering Library for maintaining an excellent library and the InterLibrary Services staff for providing all the articles not available at UT. It is a great service that has helped a lot in obtaining the literature used in this dissertation.

A big thanks goes to my friends, batch-mates from the 19th batch and the alumni from the Department of Ship Technology, Cochin University of Science and Technology for their friendship and support.

The age old Vedic adage - "**Matha** (*Mother*), **Pitha** (*Father*), **Guru** (*Teacher*), **Daivam** (*God*)" simply means - First parents, then teachers and then only God. It sums up the love I have for my parents. No words can express the thanks I owe to them and my brother for their continuous love, inspiration and PATIENCE! Lastly I wish to thank my dear wife Krishna and her family for their support. The appreciation I have for Krishna's love and encouragement is beyond words. We both wish to thank Professor Kinnas and Professor Liljestrand for helping us start a life together.

Financial support for the part of this research related to FPSO hull/wave interaction was provided by the Offshore Technology Research Center through their Cooperative Agreement with the Minerals Management Service (MMS) and its Industry Consortium. Financial support for the part of this research related to surface-piercing propellers was provided by the US Office of Naval Research in the form of research assistantship under the grant N00014-07-1-0932 (program monitor : Ms. Kelly Cooper) is gratefully acknowledged.

A Boundary Element Method for the Strongly Nonlinear Analysis of Ventilating Water-entry and Wave-body Interaction Problems

Publication No. _____

Vimal Vinayan, Ph.D.
The University of Texas at Austin, 2009

Supervisor: Spyros A. Kinnas

A two-dimensional Boundary Element Method (BEM) is developed to study the strongly nonlinear interaction between a surface-piercing body and the free-surface. The scheme is applied to problems with and without the possibility of ventilation resulting from the motion and geometric configuration of the surface-piercing body. The main emphasis of this research work is on the development of numerical methods to improve the performance prediction of surface-piercing propellers by including the whole range of free-surface nonlinearities. The scheme is applied to predict the ventilated cavity shapes resulting from the vertical and rotational motion of a blade-section with fully nonlinear free-surface boundary conditions. The current method is able to predict the ventilated cavity shapes for a wide range of angles of attack and Froude numbers, and is in good agreement with existing experimental results. Through a comparison with a linearized free-surface method, the current method highlights the shortcomings of the negative image approach used commonly in two-dimensional and three-dimensional numerical methods for surface-piercing hydrofoils or propellers. The current method with all its capabilities makes it a unique contribution to improving numerical tools for the performance prediction of surface-piercing

propellers. The scheme is also applied to predict the roll and heave dynamics of two-dimensional Floating Production Storage and Offloading (FPSO) vessel hull sections within a potential flow framework. The development of the potential flow model is aimed at validating the free-surface dynamics of an independently developed Navier Stokes Solver for predicting the roll characteristics of two-dimensional hull sections with bilge keels.

Table of Contents

Acknowledgments **v**

Abstract **vii**

List of Tables **xiii**

List of Figures **xiv**

Nomenclature **xxii**

Chapter 1. Introduction **1**

1.1 Surface-piercing Propellers 4

1.1.1 Performance Prediction 6

1.1.2 Application of the PROPCAV Model 9

1.2 Dynamics of Hull-sections 13

1.2.1 FPSO Roll Mitigation 15

1.3 Objectives 18

1.4 Organization 22

Chapter 2. Mathematical Formulation **23**

2.1 General Initial Boundary Value Problem 24

2.1.1 Boundary condition: Dirichlet Boundary $\Gamma_d(t)$ (Free-surface) . 27

2.1.2 Boundary condition: Neumann Boundary $\Gamma_n(t)$ 28

2.1.3 Initial Condition 29

2.2 The Mixed Eulerian-Lagrangian Method 29

2.3 Boundary Integral Equation 30

Chapter 3. Numerical Implementation **32**

3.1 BEM - Method of Weighted Residuals 33

3.2 Linear Boundary Element Method 34

3.3 Double Nodes 37

3.4 Treatment of jets 40
3.5 Time-stepping Scheme 42
3.5.1 Initial value problem 42
3.5.2 Free-surface updating 42
3.5.3 Stability of Time-integration 47
3.5.4 Free-surface regridding 47
3.5.5 Forces and Moments 48

Chapter 4. Validation Studies **50**
4.1 Piston Wave-maker 50
4.1.1 Formulation 50
4.1.2 Results 52
4.2 Fifth-order Gravity Waves 55
4.2.1 Formulation 55
4.2.2 Results 57
4.3 Water-entry of Wedge Sections 63
4.3.1 Initial Boundary Value Problem 64
4.3.2 Results 66
4.4 Summary 85

Chapter 5. Wave-body Interaction **88**
5.1 Forced Roll-motion of Hull Sections 88
5.1.1 Initial Boundary Value Problem 88
5.1.2 Results 91
5.2 Transient Response of Hull-sections 102
5.2.1 Results 103
5.3 Summary 108

Chapter 6. Ventilating Water-entry **109**
6.1 Physical Assumptions 111
6.2 Unique aspects of the flow 111
6.3 Vertical Entry 112
6.3.1 Previous Work - SPPAN (Linear Model) 112
6.3.2 Current work - Mathematical Formulation 114
6.3.3 Results 118

6.4 Rotating Entry 140
6.4.1 Initial Boundary Value Problem 140
6.4.2 Results 142
6.5 Summary 144

Chapter 7. Conclusions **148**
7.1 Discussions and Recommendations 150

Appendices **154**

Appendix A. 2D Influence Coefficients **155**

Appendix B. Free-surface remeshing **161**

Appendix C. Fifth-order Gravity Waves **165**
C.1 Nomenclature 165
C.2 Solution I 166
C.2.1 Wave Elevation 166
C.2.2 Wave Potential 167
C.2.3 Velocity Components 167
C.2.4 Application 168
C.3 Solution II 168
C.3.1 Wave Elevation 168
C.3.2 Wave Potential 169
C.3.3 Velocity Components 169
C.3.4 Application 170

Appendix D. FLUENT® Multiphase Model **173**
D.1 Multiphase flow 174
D.2 Dynamic Mesh 174
D.3 Mesh Characteristics 177
D.4 Boundary conditions and extents of domain 177
D.5 Solver characteristics 178
D.6 FLUENT - Input file for case generation 182
D.7 FLUENT - Input file for case execution 184
D.8 GAMBIT - Journal file for mesh generation 184

Appendix E. Axisymmetric BEM **187**

E.1 Mathematical Formulation 187

E.1.1 Properties of Elliptic Integrals : Inequalities and Limiting Behavior 189

E.1.2 Properties of Elliptic Integrals : Derivatives 189

E.1.3 Properties of Elliptic Integrals : Polynomial Approximations $0 \leq m < 1$ 189

E.2 Influence Coefficients 191

E.2.1 Self-Influence Coefficients 193

Appendix F. Multipole Expansions **195**

Bibliography **199**

Vita **211**

List of Tables

C.1 Fifth-order gravity wave coefficients [Skjelbreia and Hendrickson 1961] 171
C.2 Fifth-order gravity wave coefficients [Fenton 1985] 172

List of Figures

1.1 Ventilated cavities formed during the operation of a surface piercing propeller. View from underneath, with flow going from right to left. Taken from [Olofsson 1996]. 2

1.2 Generation of a bow-wave in the forward region of naval vessel. Taken from [Faltinsen 2005]. 3

1.3 Typical surface-propeller drive arrangement 5

1.4 Treatment of the free-surface in the 3D PROPCAV model. Only the immersed part of the blade is modeled with the free-surface assumed to be flat (its effect taken into account via the negative image method). The shaded area indicates that part of the blade that is immersed. . 8

1.5 Comparison of predicted (P) and measured (E) blade forces for J_A = 0.8. Dashed circles indicate the regions on interest - the exit and entry phases 11

1.6 Different phases in the cycle of rotation of the SP Propeller. Sketch based on figures in [Olofsson 1996] 12

1.7 Six degrees of freedom,translation-*surge*, *heave*, *sway*, rotation-*roll*, *pitch*, *yaw* 13

1.8 Typical heave and roll response of a ship.[Lewis et al. 1989] 14

1.9 A typical FPSO facility. Graphic from internet. 15

1.10 Typical hull with bilge keels 16

1.11 Wetted and ventilating entry of surface-piercing hydrofoils. P indicates the ambient pressure, P_{atm} represents the atmospheric pressure 20

1.12 Dynamics of hull-sections. P indicates the ambient pressure, P_{atm} represents the atmospheric pressure 21

2.1 General IBVP, fluid domain and corresponding boundaries for ventilating problems; $\Gamma_d(t)$: Dirichlet boundary, $\Gamma_n(t)$: Neumann boundary, $\Omega(t)$: Fluid domain; Solid lines indicate domain boundaries and dashed lines indicate the actual physical extents of the body 25

2.2 General IBVP, fluid domain and corresponding boundaries for non-ventilating problems; $\Gamma_d(t)$: Dirichlet boundary, $\Gamma_n(t)$: Neumann boundary, $\Omega(t)$: Fluid domain; Solid lines indicate domain boundaries and dashed lines indicate the actual physical extents of the body . . 26

2.3 Ventilating case: wetted and non-wetted boundaries of the body . . . 26

2.4 Free-surface schematic 27
2.5 Representation of the internal angle $\alpha_{\mathbf{p}}$ 31

3.1 Geometry and shape functions for a linear isoparametric element . . 35
3.2 Double-node approach at the body free-surface intersection 39
3.3 Details of jet truncation/cut-off model 41
3.4 Fourth-order Runge-Kutta scheme for free-surface time-stepping . . . 46
3.5 Body:Position vector and unit normal 48

4.1 Piston Wavemaker : Fluid domain and corresponding boundaries, h: wave tank depth, A: Piston stroke, L_t: Mean length of wave-tank . . 51
4.2 Piston wave-maker : Comparison of wave elevations between [Lin 1984] and BEM scheme (a) $\Delta t/T = 0.02$, (b) $\Delta t/T = 0.01$; $\bar{A} = 0.1$, $T = 4.0$, $N_{\mathbb{F}} = 200$; $\bar{\eta} = \eta/h$: wave elevation, $\bar{x} = x/h$ 53
4.3 Piston wave-maker : Wave elevations at (a) $t/T = 1.0$,(b) $t/T = 2.0$,(c) $t/T = 3.0$,(d) $t/T = 4.0$, $\Delta t/T = 0.02$, $\bar{A} = 0.1$, $N_{\mathbb{F}} = 200$; $\bar{\eta} = \eta/h$: wave elevation, $\bar{x} = x/h$ 54
4.4 Fifth-order Stokes Wave : Fluid domain and corresponding boundaries, d: water depth, L: wavelength, y : wave elevation, $s = d + y$. 56
4.5 Comparison of numerical and analytical wave elevations between $t = 4.0T$ and $t = 4.8T$ at steps of $0.2T$; $\bar{x} = x/L$, $\bar{\eta}_w = \eta_w/L$, $\bar{\eta}_n = \eta_n/L$: η_n : numerical wave elevation, η_w : analytical wave elevation; BEM characteristics : Time step $\Delta t/T = 0.025$, Number of panels on the free-surface, $N_{\mathbb{F}} = 240$ 59
4.6 Time history : Convergence of the trajectory of a fluid particle $\mathbf{P}[x(t), y(t)]$ at the upstream boundary with increase in $N_{\mathbb{F}}$, number of panels on the free-surface: (a) $N_{\mathbb{F}} = 30$, (b) $N_{\mathbb{F}} = 60$, (c) $N_{\mathbb{F}} = 120$, (d) $N_{\mathbb{F}} = 240$, (e) Analytical trajectory; Time step $\Delta t/T = 0.025$; $\bar{x} = x/L$, $\bar{y} = y/L$, $\bar{t} = t/T$ 60
4.7 Convergence of the trajectory of a fluid particle $\mathbf{P}[x(t), y(t)]$ at the upstream boundary with increase in $N_{\mathbb{F}}$, Number of panels on the free-surface : (a) $N_{\mathbb{F}} = 30$, (b) $N_{\mathbb{F}} = 60$, (c) $N_{\mathbb{F}} = 120$, (d) $N_{\mathbb{F}} = 240$, (e) Analytical trajectory; Time step $\Delta t/T = 0.025$; $\bar{x} = x/L$, $\bar{y} = y/L$, $\bar{t} = t/T$ 61
4.8 Convergence characteristics of the error between the analytical and numerical particle trajectories at time $t = 5.0T$ for (a) $\Delta t = 0.025T$, and (b) $\Delta t = 0.0125T$ $(- \circ -)$ $\epsilon_x(t)$: error in $x(t)$,(-□-) $\epsilon_y(t)$: error in $y(t)$,$\Delta\bar{x} = \frac{1}{N_{\mathbb{F}}}$ ($N_{\mathbb{F}}$ = 30,60,120,240) 61
4.9 Variation of the area under the free-surface with time; Convergence with increase in $N_{\mathbb{F}}$, number of panels on the free-surface:(a) $N_{\mathbb{F}} = 30$, (b) $N_{\mathbb{F}} = 60$, (c) $N_{\mathbb{F}} = 120$, (d) $N_{\mathbb{F}} = 240$; $\bar{\eta}_{area} = \eta_{area}/L^2$: area under the free-surface; Time step $\Delta t/T = 0.025$ 62

4.10 Water-entry of wedge sections : Fluid domain and corresponding boundaries, parameters defining the geometry of the wedge and initial conditions 67

4.11 Number of elements on the discretized boundary, $N_{\mathbb{F}}$ = total number of elements on the free-surface $S_{\mathbb{F}}(t)$ combined, $N_{\mathbb{WB}}$ = total number of elements on the combined wetted wedge surface, N_{∞} = total number of elements on the far-field boundary;c_w is the wetted characteristic length; s is the arc-length along the wetted boundary $0 \leq s \leq s_w(t)$; $s_w(t)$ is the maximum wetted length of the wedge at a particular instant of time t 72

4.12 Wedge water-entry ($\alpha_w = 18°$) : Representative case showing the effect of the time-step on the free-surface elevation predicted by the scheme. t_e =0.103075 s, (a) $\Delta t/t_e$ = 9.6e-4, (b) $\Delta t/t_e$ = 4.8e-4, (c) $\Delta t/t_e$ = 9.6e-5, (d) $\Delta t/t_e$ = 4.8e-5 73

4.13 Wedge water-entry ($\alpha_w = 18°$) : Representative case showing the effect of the time-step on the pressures predicted by the scheme on the wetted part of the body surface. t_e =0.103075 s, (a) $\Delta t/t_e$ = 9.6e-4, (b) $\Delta t/t_e$ = 4.8e-4, (c) $\Delta t/t_e$ = 9.6e-5, (d) $\Delta t/t_e$ = 4.8e-5. C_p is the pressure coefficient and s is the arc-length along the body surface. (Note : pressures shown only on one side of the wetted boundary) . . 74

4.14 Wedge water-entry ($\alpha_w = 18°$) : Representative case showing the effect of the number of panels on the pressures predicted by the scheme on the wetted part of the body surface. (a) $N_{\mathbb{WB}}$ = 2×50 panels, (b) $N_{\mathbb{WB}}$ = 2×100 panels; $N_{\mathbb{WB}}$ is the total number of panels on the wetted body surface, see Figure 4.11 75

4.15 Wedge water-entry ($\alpha_w = 18°$) : free-surface elevation at different stages of entry. Parameters of simulation : $g = 0$ (no gravity), c_w = 0.1524 m, Δt = 5e-6 s, $\Delta t/t_e$ = 4.8e-6s, $N_{\mathbb{F}}$ = 200, $N_{\mathbb{WB}}$ = 100, N_{∞} = 40 76

4.16 Wedge water-entry ($\alpha_w = 18°$) : free-surface elevation at different stages of entry expressed in terms of similarity variables ($x/(V_w t)$,$y/(V_w t)$). Parameters of simulation : $g = 0$ (no gravity), c_w = 0.1524 m, Δt = 5e-6 s, $\Delta t/t_e$ = 4.8e-6s, $N_{\mathbb{F}}$ = 250, $N_{\mathbb{WB}}$ = 100, N_{∞} = 40 77

4.17 Wedge water-entry ($\alpha_w = 60°$ and $\alpha_w = 90°$) : free-surface elevation at different stages of entry. Parameters of simulation : $g = 0$ (no gravity), c_w = 0.1524 m, Δt = 5e-6 s 78

4.18 Wedge water-entry ($\alpha_w = 18°$) : Pressure distribution along wetted boundary of the wedge at different stages of entry (pressures shown only on one side of the wetted boundary).$s_w(t)$ is the instantaneous wetted length of the wedge (see Figure 4.11). C_p is the pressure coefficient 79

4.19 Wedge water-entry ($\alpha_w = 18°$) : Comparison of pressure predicted along the wetted part of the wedge with similarity solution of [Dobrovol'skaya 1969] expressed in terms of the similarity variable $y/(V_w t)$. C_p is the pressure coefficient (Note : pressures shown only on one side of the wetted boundary) 80

4.20 Wedge water-entry ($\alpha_w = 60°$ and $\alpha_w = 90°$) : Comparison of pressure predicted along the wetted part of the wedge with similarity solution of [Dobrovol'skaya 1969] expressed in terms of the similarity variable $y/(V_w t)$. C_p is the pressure coefficient; (Note : pressures shown only on one side of the wetted boundary) 81

4.21 Wedge water-entry ($\alpha_w = 18°$) : Representative case showing the effect of the Froude number F_{nc} on the free-surface elevation. 82

4.22 Wedge water-entry ($\alpha_w = 18°$) : Representative case showing the effect of the Froude number F_{nc} on the total pressure predicted on the wetted part of the wedge surface; C_p is the pressure coefficient (Note pressure shown only on one side of the wetted boundary) . . . 83

4.23 Wedge water-entry ($\alpha_w = 18°$) : Representative case showing the effect of the Froude number F_{nc} on the total pressure predicted on the wetted part of the wedge surface; $C_{p,d}$ is the hydrodynamic part of the pressure coefficient, as given by Equation (4.24) (Note pressure shown only on one side of the wetted boundary) 84

4.24 Wedge water-entry ($\alpha_w = 18°$) : Representative case showing the effect of the Froude number F_{nc} on the total pressure predicted on the wetted part of the wedge surface; $C_{p,s}$ is the hydrostatic part of the pressure coefficient, as given by Equation (4.25) (Note pressure shown only on one side of the wetted boundary) 85

5.1 Geometry and prescribed roll configuration of a round-bilge hull-section. B : beam of hull-section; T draft (=$0.5B$), R_b : bilge radius (=$0.02B$); α_0 : amplitude of prescribed roll motion; $\alpha(t)$: instantaneous roll angle; O : origin of an inertial coordinate system 89

5.2 Hull-section roll-motion : Fluid domain and corresponding boundaries 90

5.3 Hull-section and free-surface; $\tilde{\omega} = 0.6$, $\alpha_0 = 0.4$ rad;(*Note : the horizontal and vertical scales are identical*) 93

5.4 Hull-section and free-surface with actual Lagrangian fluid particles; $\tilde{\omega} = 0.6$, $\alpha_0 = 0.4$ rad; $\bar{x} = x/B$; (*Note : the horizontal and vertical scales are identical*) 94

5.5 Comparison of linear and nonlinear free-surface elevations; (a) $\alpha_0 = 0.05$ rad, (b) $\alpha_0 = 0.40$ rad; $\tilde{\omega} = 0.6$; $N_{\mathbb{F}} = 400$, Number of panels on the starboard free-surface; (*Note : the horizontal and vertical scales are not identical*) . . 95

5.6 Scaled and un-scaled wave-elevations; $\tilde{\omega}$=0.6; $\bar{\eta} = \eta/B$: free-surface elevation; $\hat{\eta} = \bar{\eta}\frac{0.05}{\alpha_0}$ scaled wave elevation;$\bar{x} = x/B$;$N_{\mathbb{F}} = 400$, Number of panels on the starboard free-surface; (*Note : the horizontal and vertical scales are not identical*) 96

5.7 Convergence of free-surface elevations with increase in number of panels on the free-surface (a) $N_{\mathbb{F}} = 100$ (b) $N_{\mathbb{F}} = 200$ (c) $N_{\mathbb{F}} = 400$ (d) $N_{\mathbb{F}} = 500$; $N_{\mathbb{F}}$ is the number of panels on the starboard side free-surface (*Note : the horizontal and vertical scales are not identical*) 97

5.8 Comparison of the free-surface elevations between BEM and NS2D ([Yu 2008]) schemes. $\tilde{\omega}$=1.0,α_0=0.1 rad. 97

5.9 Comparison of pressure and velocity components between BEM and NS2D(IN) [Yu 2008] scheme.$\tilde{\omega}$=1.0,α_0=0.1 rad,t/T=2.75; Round bilge hull-section 98

5.10 Comparison of pressure and velocity components between BEM and NS2D(IN) [Yu 2008] scheme.$\tilde{\omega}$=1.0,α_0=0.1 rad,t/T=3.00; Round bilge hull-section 99

5.11 Comparison of pressure and velocity components between BEM and NS2D(IN) [Yu 2008] scheme.$\tilde{\omega}$=1.0,α_0=0.2 rad,t/T=2.75; Round bilge hull-section 100

5.12 Comparison of pressure and velocity components between BEM and NS2D(IN) [Yu 2008] scheme.$\tilde{\omega}$=1.0,α_0=0.2 rad,t/T=3.00; Round bilge hull-section 101

5.13 Geometry and roll/heave decay configuration of a round-bilge hull-section. B : beam of hull-section; T draft (=0.5B), R_b : bilge radius (=0.02B); y_o : initial heave displacement (=0.125 B); $y_b(t)$: instantaneous heave displacement; $\alpha(t)$: instantaneous roll angle; O : origin of an inertial coordinate system; O' : origin of a body fixed coordinate system 105

5.14 Sequential decay of the hull section in heave. Note that the dashed line represents the equilibrium draft of the hull-section about which it oscillates freely and eventually coming to a stop 106

5.15 (top) Heave decay-response of hull predicted by the BEM scheme along with the experimental/numerical results presented in [Roddier 2000]; (bottom) Logarithmic heave-decay characteristics of the hull predicted by the BEM scheme along with the experimental/numerical results presented in [Roddier 2000]. NS2D(VS) : viscous version of the NS2D solver; NS2D(IN) : inviscid version of the NS2D solver 107

6.1 Marine propeller : concept of cylindrical surface, blade element and helical line. Sketch based on figures in [Carlton 2007] 110

6.2 Brillouin-Villat Condition : The curvature of the cavity surface near the leading edge is finite. Based on the free-streamline theory of [Wu 1972]. α is the angle of attack, U_∞ is the free-stream velocity. 113

6.3 SPPAN : Surface piercing hydrofoil with coordinate system moving with the foil 114

6.4 SPPAN : Actual foil, cavity surface and corresponding images 115

6.5 Ventilating entry of a hydrofoil section : Fluid domain and corresponding boundaries 116

6.6 Ventilating entry: Graphical representation of the treatment at the leading edge 118

6.7 Ventilating entry of a surface-piercing wedge : Effect of the parameter δ_{iv} on the ventilated cavity shape. REGION C : Magnified view of the ventilated cavity shape close to the leading edge of the hydrofoil. . . 124

6.8 Ventilating entry of a surface-piercing wedge : Effect of the parameter δ_{iv} on the pressure predicted on the wetted part of the hydrofoil. C_p is the pressure coefficient, s is the arc-length along the wedge surface. 125

6.9 Ventilating entry of a surface-piercing wedge - Convergence characteristics of the ventilated cavity shape with respect to the number of panels on the cavity surface, (a) $N_{\mathbb{F},s}$=125, (b) $N_{\mathbb{F},s}$=215, (c) $N_{\mathbb{F},s}$=300.126

6.10 Ventilating entry of a surface-piercing wedge : Free-surface and ventilated cavity shapes predicted by the BEM scheme in the absence of gravity (g=0) (a) at different stages of entry (b) at time t_e=0.0419 s. Parameters of the simulation - Δt=1e-4 s, $N_{\mathbb{WB}}$=100, $N_{\mathbb{F}s}$=300, $N_{\mathbb{F}p}$=125, N_∞=40 127

6.11 Ventilating entry of a surface-piercing wedge : Pressure along the wetted part of the hydrofoil at different stages of entry in the absence of gravity $g = 0$. Parameters of the simulation - Δt=1e-4 s, $N_{\mathbb{WB}}$=100, $N_{\mathbb{F}s}$=300, $N_{\mathbb{F}p}$=125, N_∞=40. C_p is the pressure coefficient 128

6.12 Ventilating entry of a surface-piercing wedge : Free-surface and ventilated cavity shapes predicted by the BEM scheme in the presence of gravity ($g \neq 0$) (a) at different stages of entry (b) at time time t_e=0.0432 s. Parameters of the simulation - Δt=1e-4 s, $N_{\mathbb{WB}}$=100, $N_{\mathbb{F}s}$=300, $N_{\mathbb{F}p}$=125, N_∞=40 129

6.13 Ventilating entry of a surface-piercing wedge : Pressure along the wetted part of the wedge at different stages of entry in the presence of gravity ($g \neq 0$). Parameters of the simulation - Δt=1e-4 s, $N_{\mathbb{WB}}$=100, $N_{\mathbb{F}s}$=300, $N_{\mathbb{F}p}$=125, N_∞=40. C_p is the pressure coefficient 130

6.14 Ventilating entry of a surface-piercing wedge - Free-surface and ventilated cavity shape, with ($g \neq 0$) and without (g=0) the presence of gravity, at different stages of entry expressed in terms of the similarity variables. 131

6.15 Ventilated cavity shape and free-surface : Comparison between experimental and numerical (BEM) results. V_w=2.45 m/s corresponding to a 12″ fall (Photograph of experimental result from [Cox 1971] used with permission) 132

6.16 Ventilated cavity shape and free-surface : Comparison between experimental and numerical (BEM) results. V_w=2.45 m/s corresponding to a 12″ fall (Photograph of experimental result from [Cox 1971] used with permission). Effects of gravity included. 133

6.17 Ventilating entry of a surface-piercing wedge : Comparison of ventilated cavity shapes between FLUENT Multiphase (VOF with SST $k - \omega$ turbulence model), Fluent Multiphase (laminar) and BEM results. V_w=2.45 m/s corresponding to a 12″ fall. Angle of attack, α_0=10°. 134

6.18 Ventilating entry of a surface-piercing wedge : Comparison of pressure along the wetted body surface between FLUENT Multiphase (VOF with SST $k-\omega$ turbulence model) and BEM results. V_w=2.45 m/s corresponding to a 12″ fall. Angle of attack, α_0=10°. 135

6.19 Ventilating entry of a surface-piercing wedge : Comparison of ventilated cavity shapes between (a) SPPAN-linear and (b) BEM-nonlinear methods. V_w=2.45 m/s corresponding to a 12″ fall. Angle of attack, α_0=10°. 136

6.20 Ventilating entry of a surface-piercing wedge : Comparison of pressure along the wetted part of the hydrofoil SPPAN-linear and BEM-nonlinear methods. (a) BEM-Nonlinear (g=0), (b) SPPAN-linear (g=0), (c) BEM-Nonlinear ($g \neq 0$); V_w=2.45 m/s corresponding to a 12″ fall. Angle of attack, α_0=10°. 137

6.21 Ventilating entry of a surface-piercing hydrofoil : Effect of Froude number on the ventilated cavity shapes. F_{nc}=∞ corresponds to g=0. V_w=2.45 m/s for F_{nc}=2.0 and V_w=3.67 m/s for F_{nc}=3.0 138

6.22 Ventilating entry of a surface-piercing hydrofoil : Effect of angle of attack on the ventilated cavity shapes with ($g \neq 0$) and without (g=0) the presence of gravity. 139

6.23 Rotating entry of a blade section : two-dimensional sections of the ventilated cavity surfaces predicted by PROPCAV. Taken from [Young 2002] 141

6.24 Rotating entry of a blade section : Fluid domain and corresponding boundaries 142

6.25 Rotating entry of a blade section : Initial configuration of the hydrofoil 143

6.26 Surface-piercing propeller section in rotation : blade angle = 90°. Angle of attack α=0° (angle of attack defined in Figure 6.25) 145

6.27 Surface-piercing propeller section in rotation : blade angle = 180°. Angle of attack α=0° (angle of attack defined in Figure 6.25) 146

6.28 Surface-piercing propeller section in rotation : blade angle = 240°. Angle of attack α=0° (angle of attack defined in Figure 6.25) 146

6.29 Surface-piercing propeller section in rotation : blade angle $\approx$ 260°. Angle of attack α=0° (angle of attack defined in Figure 6.25) 147

6.30 Surface-piercing propeller section in rotation, collapse of ventilated cavity. Angle of attack α=-10° (angle of attack defined in Figure 6.25) 147

7.1 Constant-strength panel method, location of panel end-points and control points 151

7.2 Water-entry of a wedge with an included angle, α_w=18°. Comparison of free-surface elevations predicted by the constant-strength panel and the linear-strength BEM schemes. 152

A.1 Linear isoparametric element 155
A.2 Linear strength distribution 158
A.3 Local and global systems 159

B.1 Parametric representation of free-surface 163

C.1 Important characteristics of a nonlinear wave 165

D.1 Dynamic layering method 176
D.2 Dynamic layering method for water-entry problem 179
D.3 Details of the mesh and magnified views of specific regions 180
D.4 Extents of domain and boundary conditions 181

Nomenclature

The coordinate system, usually represented as $\mathcal{O}(x, y)$ is as follows : for a two-dimensional flow the x-axis is horizontal, generally displayed in figures as pointing to the right, with the y-axis vertical and positive upwards.

Vector symbols are printed in boldface.

Latin Symbols

b	half-breadth of hull-section, $b = 0.5B$
B	breadth of the hull-section
$\mathcal{C}_0$	Courant number
C_p	pressure coefficient, $C_p = (P - P_{atm})/(0.5\rho V_w^2)$
D	propeller diameter, $D = 2R$
$\mathcal{E}$	generic element on the domain boundary
F_{nD}	Froude number based on V_A, $F_{nD} = V_A/\sqrt{gD}$
F_{nc}	Froude number based on V_w, $F_{nc} = V_w/\sqrt{gc}$
F_r	Froude number based on n, $F_r = n^2D/g$
F_n	Froude number based on n, $F_n = nD/\sqrt{gD}$
g	gravitational acceleration
G	two-dimensional Green's function
G^{3D}	three-dimensional Green's function
G^{AX}	Axisymmetric Green's function
h	tip immersion for partially submerged propellers
J_A	advance ratio based on V_A, $J_a = V_A/nD$
J_s	advance ratio based on V_s, $J_s = V_s/nD$
K_{Fx}, K_{Fy}, K_{Fz}	dynamic blade force coefficients in ship fixed coordinates
K_{Mx}, K_{My}, K_{Mz}	dynamic blade moment coefficients in ship fixed coordinates

n	propeller rotational frequency (rev/s)
$\mathbf{p}$	field point
P	pressure
P_{atm}	atmospheric pressure
P_v	vapor pressure of water
$\mathbf{q}$	source point
$\vec{q}$	total velocity
r	radius of propeller blade section
R	propeller radius
R_b	radius of bilge
$\mathbf{s}, \mathbf{n}$	orthogonal unit vectors along the local grid directions
$S_{\mathbb{F}}$	free-surface
$S_{\mathbb{WB}}$	wetted boundary of hydrofoil
$S_{\mathbb{U}}$	wave-tank upstream boundary
$S_{\mathbb{D}}$	wave-tank downstream boundary
S	cavitating portion of wake surface
S_∞	infinite boundary surface for foil entry problem
t	time
T	hull draft or depth
	time-period of roll oscillation
$\mathbf{u}$	local fluid velocity
$\mathbf{V}$	prescribed velocity on boundary $\Gamma_n(t)$
V_A	advance speed of propeller, or
	inflow speed for 3-D hydrofoil
V_s	ship speed
W_n	Weber number, $W_n = nD/\sqrt{\sigma_k/\rho D}$
y_o	initial heave displacement in a free-decay test
x, y, z	propeller fixed coordinates
$y_b, \dot{y_b}, \ddot{y_b}$	heave displacement, velocity and acceleration
$\alpha, \dot{\alpha}, \ddot{\alpha}$	roll angle, angular velocity and acceleration
x_s, y_s, z_s	ship fixed coordinates
$\mathbf{x}$	position vector

Greek Symbols

α	angle of attack for 2-D hydrofoil
$\alpha(\mathbf{p})$	internal angle formed at the boundaries
α_w	wedge included angle
α_0	roll amplitude
β	dead-rise angle
β_i	cut-off model, threshold angle
β_R	relative angle between surfaces
δ_i	initial immersion in the case of fully wetted entry
δ_{iv}	initial immersion in the case of ventilating entry
Δt	time step size
$\Gamma(t)$	boundary of fluid domain $\Omega(t)$
$\Gamma_d(t)$	boundary with Dirichlet boundary condition
$\Gamma_n(t)$	boundary with Neumann boundary condition
η	vertical coordinate of free surface
ν	kinematic viscosity of water
ϕ	total velocity potential
(ϕ_s, ϕ_n)	tangential and normal component of fluid velocity
(ϕ_x, ϕ_y)	horizontal and vertical component of fluid velocity
ρ	fluid density
ω	rotational speed (radians/second)
$\tilde{\omega}$	Froude number in roll motion of hull-sections, $\tilde{\omega} = \omega\sqrt{b/g}$
$\Omega(t)$	fluid domain

Acronyms

2-D	Two-dimensional
3-D	Three-dimensional
BEM	Boundary Element Method
BIE	Boundary Integral Equation
BVP	Boundary Value Problem
DFSBC	Dynamic free-surface boundary condition
FSRVM	Free-surface Random Vortex Method
IBVP	Initial Boundary Value Problem
IE	Integral Equation
KFSBC	Kinematic free-surface boundary condition
MEL	Mixed-Eulerian Lagrangian
RK4	Fourth-order Runge Kutta scheme
SP	Surface-piercing (propeller)
VLM	Vortex-lattice method

Computer Program Names

FLUENT	a commercial Computational Fluid Dynamics software
GAMBIT	a commercial Mesh Generation software (part of FLUENT)
SPPAN	2-D BEM code for ventilating entry of hydrofoils
PROPCAV	cavitating propeller potential flow solver based on BEM
NS2D	a 2-D Navier-Stokes Solver
NS2D(IN)	inviscid version of Navier-Stokes Solver
NS2D(VS)	viscous version of Navier-Stokes Solver

Chapter 1

Introduction

A surface-piercing body can be defined as a marine structure or device with a part of itself above water that breaks the air-water interface or the free-surface. This definition includes the whole gamut of water-crafts, seafaring vessels, fixed/floating offshore structures, surface-piercing propellers, etc. The field of marine hydrodynamics abounds with examples where there is a strongly nonlinear interaction between a surface-piercing body and the free-surface as a result of its motion or its placement in a complex marine environment.

A marine propeller, however, might seem like an oddity in the list of surface-piercing bodies as the vast majority of propellers are designed to be fully submerged and rarely operate near the free-surface except during broaching, say in high seas or shallow waters. A flow phenomenon that is commonly encountered by submerged propellers is cavitation - noted by Sir Charles Parsons in 1894 as "vacuous cavities" that formed behind the rapidly turning propeller blades during the trials of the *Turbinia*[1] [Mackie and Hutchinson 1997]. Extreme cavitation often leads to propeller racing and undermines its ability to fully absorb the delivered power. This makes it impossible to power high-speed crafts with propulsion systems based on conventional propellers, even with the use of supercavitating sections. A way out of this quagmire was found through the use of a pre-existing concept of a *partially-submerged or surface-piercing propeller*. Hadler and Hecker [1968] describe the surface-piercing

[1]Parsons later overcame the effects of cavitation by using nine propellers, mounted three each in tandem on three shafts, to propel the *Turbinia* at a speed of 34.5 knots - a record-breaking speed during his time [Mackie and Hutchinson 1997]

propeller as a specialized overshoot of the screw propeller initially viewed as another means besides the paddle wheel for achieving shallow-draft propulsion. The report of Hadler and Hecker [1968] also provides a very interesting history of the surface-piercing propeller. Similar to a paddle wheel, a part of the partially submerged propeller pierces the water surface during a cycle of revolution. A rather interesting feature of the resulting flow is ventilation - drawing of air from the free-surface and occurrence of air-filled cavities on the propeller suction side (these cavities also get carried over into the propeller wake, see Figure 1.1). The idealized boundaries of the ventilated cavities are merely extensions of the free-surface (see Figure 1.11) and all the nonlinear effects of the propeller interacting with it get tagged along.

Figure 1.1: Ventilated cavities formed during the operation of a surface piercing propeller. View from underneath, with flow going from right to left. Taken from [Olofsson 1996].

A much more common instance of a nonlinear interaction is that between a floating body and the free-surface on which it floats. Figure 1.2 shows one such example of the generation of a steep bow-wave in the forward region of a naval vessel. In many cases it is sufficient to linearize the free-surface and body boundary conditions, and solve the linear problem. This approximation is sufficient if the amplitude of the waves generated on the free-surface and the motions of the body are small. However, the linearization fails if the amplitude of body motions is large, in which case nonlinear free-surface effects have a strong influence on the dynamics.

Figure 1.2: Generation of a bow-wave in the forward region of naval vessel. Taken from [Faltinsen 2005].

The prediction of the kinematics and dynamics of surface-piercing bodies is an area of research that has been extensively studied - mostly within the precepts of potential flow. Here we consider the ventilation characteristics of surface-piercing propellers and the dynamics of hulls or specifically FPSO (Floating, Production, Storage and Offloading) vessels. The common link between the two seemingly disparate problems is the presence of the free-surface and the resulting nonlinear interaction.

1.1 Surface-piercing Propellers

Surface-piercing propellers (hereafter referred to as SP propellers) and waterjets have emerged as the two predominant systems of propulsion for high-speed crafts (vessels that operate routinely at speeds in excess of 30 knots [Baird 1998, Faltinsen 2005]). Cavitation and its detrimental effects of loss of thrust, noise, vibration and erosion present a formidable barrier that precludes the use of subcavitating or supercavitating propeller based systems. Even though it is difficult to draw a clear demarcation between the two modes of propulsion in terms of feasibility, current trends indicate the prevalence of SP propellers for high-speed crafts with displacements below 50 t while waterjets are used for crafts with higher displacements [Blount and Bartee 1997].

The elements of the surface-piercing propulsion system are arranged in such a manner that when the vessel is under-way, only a part of the propeller is submerged during a cycle of revolution (the actual level of submergence depends on the trim of the vessel and other factors). A typical arrangement of the components of a surface-piercing drive is shown in Figure 1.3. SP propellers are also referred to as *partially-submerged propellers* because of this feature. Kamen [1990] notes some of the advantages offered by such an arrangement, which in turn translate to better propulsive efficiency and extended range of operation :

(i) The maximum feasible diameter of a fully submerged propeller is constrained by the vessel draft, engine location and shaft angle, and hull blade-tip clearance. For a given speed and thrust, this limits the maximum efficiency that can be achieved. However, a surface-piercing propeller is not constrained by these geometric/operational limitations as it can operate partially out of water allowing for a larger diameter and better efficiency.

(ii) Cavitation is a formidable barrier that limits the performance of fully submerged propellers at high speeds. Even though the performance range can be

extended with the use of supercavitating propellers, the noise, vibration and erosion resulting from cavitation outweighs the gain in efficiency. Cavitation is replaced by ventilation in the case of SP propellers with the suction side effectively being at atmospheric pressure instead of the vapour pressure of water (see Figure 1.11). This reduces most of the detrimental effects of cavitation resulting from the collapse of cavities.

(iii) Appendage drag is effectively eliminated due to the absence of shafts and struts under water.

Figure 1.3: Typical surface-propeller drive arrangement

1.1.1 Performance Prediction

Experimental Methods

In spite of being an efficient system of propulsion, the design of partially submerged propellers has often been performed on a trial and error basis with full-scale propellers or based on results from model tests. This has been so because of the lack of reliable numerical tools based on rational hydrodynamic theory. Reynolds [1874] was the first to study the air-drawing of marine propellers based on some very basic model tests. Shiba [1953] conducted one of the best known experimental studies on the air-drawing of marine propellers. During the study, Shiba [1953] performed various tests on air-drawing to establish the law of similarity for systematic tests with model propellers and put forward a method of application to actual full-scale propellers. Other notable investigations include the works of Hadler and Hecker [1968], Rose and Kruppa [1991], Rose et al. [1993]. The primary goal of these experimental studies was to determine the time averaged characteristics of the propeller. Apart from scale effects [Shen 1975, Scherer 1977] and influence of test techniques [Morgan 1966, Suhrbier and Lecoffre 1986], the biggest drawback of such tests is the lack of information on the dynamic characteristics that are important from the structural design point of view. This was remedied in the experimental work of Olofsson [1996] where the focus was on the dynamic performance characteristics. In the work of Olofsson [1996], model tests were conducted in a cavitation tunnel for a range of operating conditions. Subsequent works include that of Miller and Szantyr [1998], Dyson [2000].

Numerical Methods

The widespread use of SP propellers and the prohibitively expensive model tests, underscore the importance of developing reliable numerical tools for predicting their dynamic performance. However, the numerical modeling of the real flow associated with a SP propeller is too difficult a task to undertake without simplifying assumptions. Olofsson [1996] and Young [2002] note some of the challenges involved

(i) insufficient understanding of the physical phenomena involved at the entry and exit phases of the blade passage through the air-water interface

(ii) insufficient understanding of the dynamic loads associated with the propeller piercing the water surface at high speeds

(iii) the modeling of long ventilated cavities that extend into the wake of the propeller, which also get interrupted by the free-surface

(iv) the modeling of jets formed along the pressure side and the associated increase in the free-surface elevation at the instance of blade entry and exit

(v) the effect of blade vibrations due to cyclic loading (in water) and unloading (in air) of the propeller.

Given the challenges of dealing with the real flow, most numerical models make the following assumptions with respect to the free-surface interaction :

(i) the Froude number is assumed to be very large and thus the effects of gravity are neglected.

(ii) the free-surface jets formed as the blade enters and exits the free-surface are assumed to be negligible (i.e., the free-surface is treated as a flat surface and its effect is taken into account using the negative image method in the limit of a large Froude number[2]) (see Figure 1.1.1).

(iii) the cavities are assumed to be fully ventilated, i.e., the pressure on the cavity is constant and equal to the atmospheric pressure. Moreover, these cavities

[2]The Froude number is defined as $F_{nd} = V/\sqrt{gD}$ where V is the ship speed, g is the acceleration due to gravity and D is the propeller diameter. An alternative definition is $F_n = (nD)/\sqrt{gD}$ where n is the propeller rotational speed. In effect, the Froude number represents the relative importance of the inertial effects compared to the effects of gravity [Newman 1977]. A Large Froude number implies that the inertial effects dominate over the effects of gravity

are assumed to remain ventilated during the entire cycle of revolution. The premature collapse of these cavities results in a high-drag mixture flow that can adversely affect the performance of the propeller (see written discussion by Dr. William Vorus in [Vinayan and Kinnas 2008]).

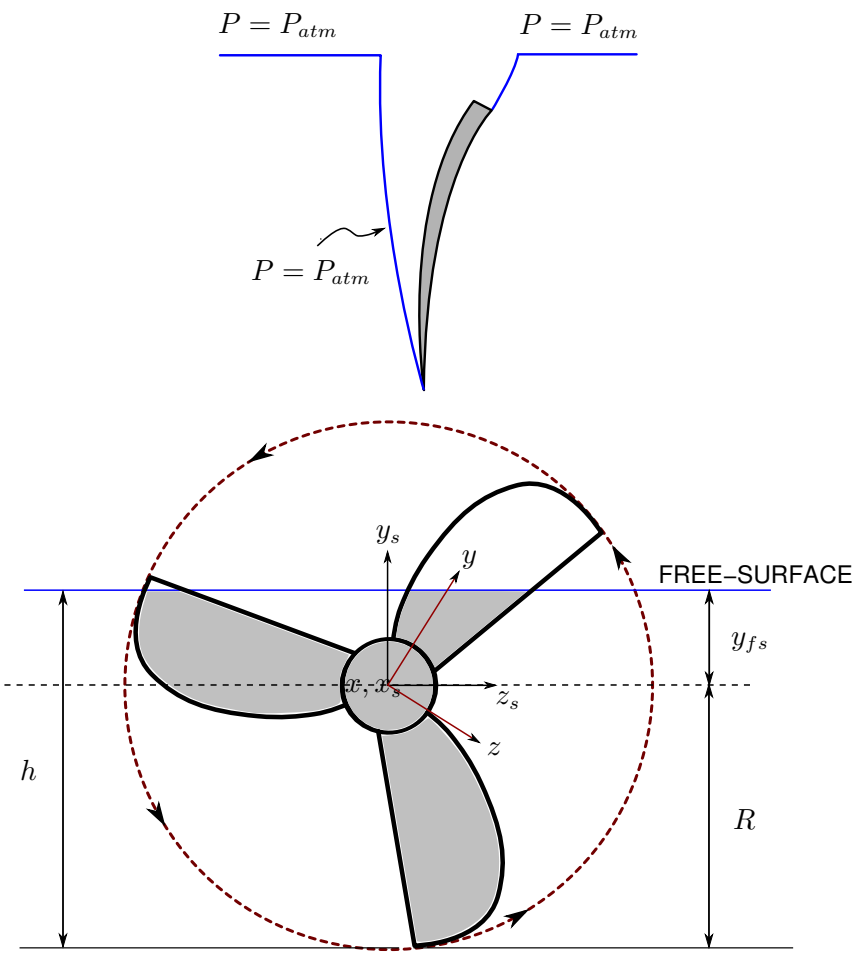

Figure 1.4: Treatment of the free-surface in the 3D PROPCAV model. Only the immersed part of the blade is modeled with the free-surface assumed to be flat (its effect taken into account via the negative image method). The shaded area indicates that part of the blade that is immersed.

In terms of numerical performance prediction of SP propellers, the first complete three-dimensional[3] model was developed by [Furuya 1985] based on a lifting-line approach with linearized boundary conditions (free-surface taken into account using the method of images). The 3-D lifting surface VLM developed by Kudo and Ukon [1994], Kudo and Kinnas [1995] for the analysis of supercavitating propellers has also been extended for the analysis of surface-piercing propellers. The extension neglects the effects of the free-surface and assumes the SP propeller (in supercavitating mode) to be fully submerged. From the fully submerged results, the mean characteristics of the SP propeller were obtained by multiplying the resultant forces with the propeller submergence ratio.

Young & Kinnas [Young 2002, Young and Kinnas 2003] developed a numerical method to predict the performance of SP propellers that also included the nonlinear analysis of unsteady sheet cavitation/ventilation with the propeller subject to a time-dependent inflow. The method was developed over an existing robust numerical tool PROPCAV (PROPeller CAVitation, [Kinnas and Fine 1992]) so named for its ability to solve the 3-D unsteady flow around cavitating propellers. PROPCAV is based on a low-order (piecewise constant dipole and source distribution) potential boundary element method (BEM) and the method of Young and Kinnas [2003] allowed it to determine the shape of the ventilated cavity surface created as a result of the passage of the blades of a SP propeller from air to water. In addition to the aforementioned simplifications regarding the free-surface, the 3-D hydrodynamic model makes the following assumptions

(i) the wake is assumed to be a helical surface with constant pitch and radius.

(ii) the influence of the shed and trailing vorticity in the wake once the blade has left the free-surface is assumed negligible.

[3]Prior to the development of 3-D methods, the performance prediction methods were primarily two-dimensional. A detailed review of the 2-D methods is presented in Chapter 6

1.1.2 Application of the PROPCAV Model

Young & Kinnas [Young 2002, Young and Kinnas 2003] applied the PROPCAV model to the `841-B` propeller tested in the experiments of Olofsson [1996]. In spite of the simplifying assumptions, the numerical model predicted ventilation patterns that agreed well with the experimental results. Figure 1.5 shows a representative comparison of the predicted and measured blade forces for an advance ratio J_A=0.8 (the different phases in the cycle of revolution of a SP propeller are shown in Figure 1.6). In comparison with the experimental results, the PROPCAV model predicts the mean forces with reasonable accuracy. However, the following discrepancies can be observed:

(i) A significant difference exists between the predicted and measured forces during the entry phase. Similar differences in the entry phase of the forces exist even for higher advance ratios.

(ii) The experimental results show "humps" in the blade forces. Olofsson [1996] attributes this to blade resonance effects as a result of the cyclic loading and unloading of the propeller. This behaviour is not captured by the PROPCAV model as it assumes the propeller to be rigid.

The difference in forces at the entry and exit phases of the propeller is mainly due to the use of the negative image method that neglects the formation of jets, rise in elevation of the free-surface and other nonlinear free-surface effects. The effect of vibration is not as significant at the entry phase because the sturdier part of the propeller enters the free-surface first.

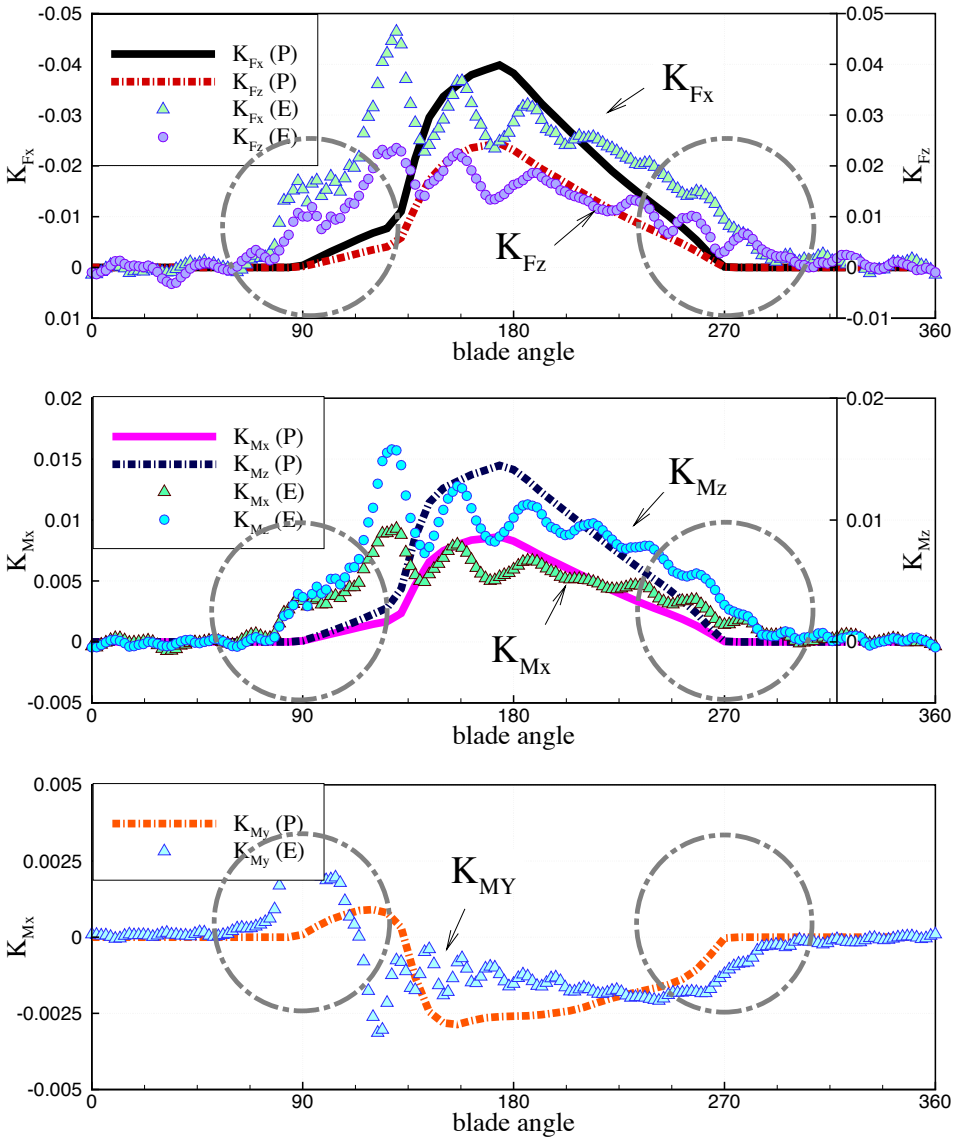

Figure 1.5: Comparison of predicted (P) and measured (E) blade forces for $J_A = 0.8$. Dashed circles indicate the regions on interest - the exit and entry phases

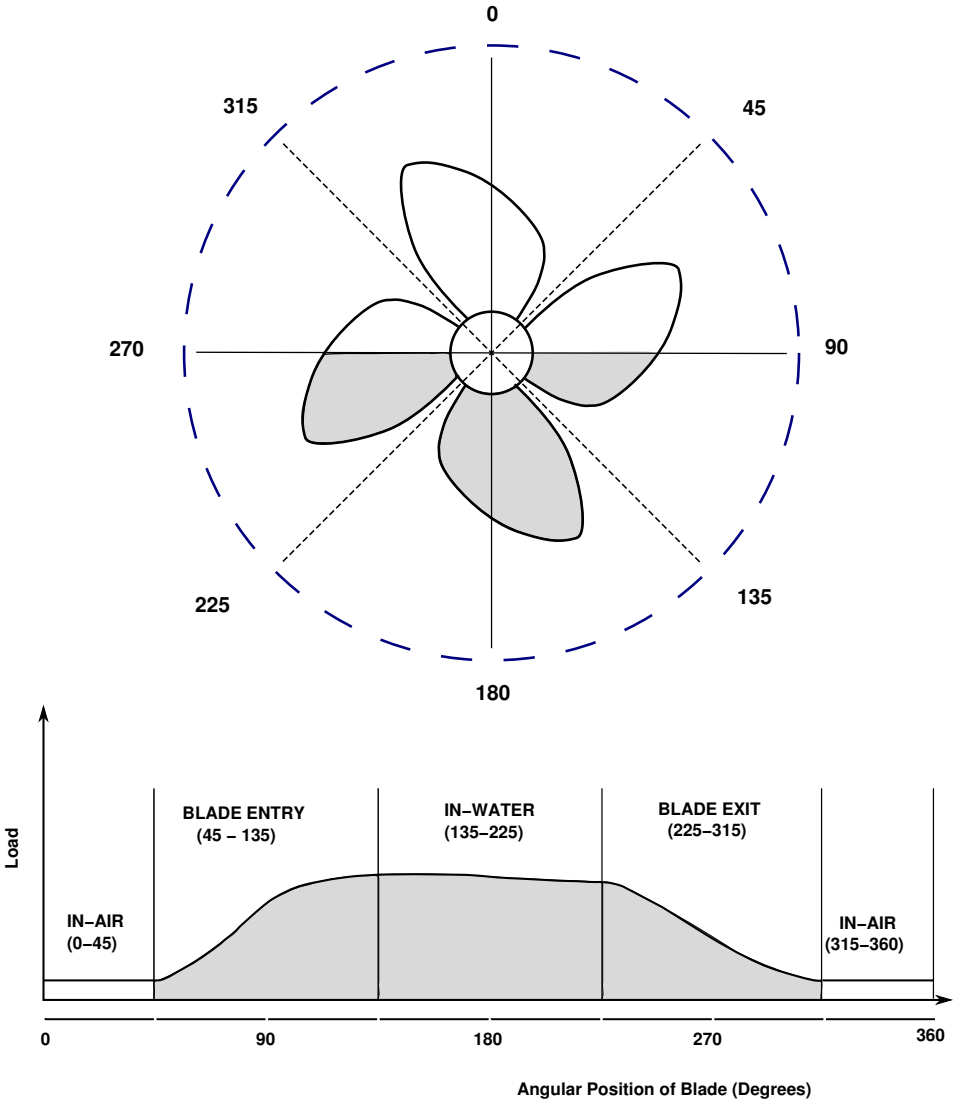

Figure 1.6: Different phases in the cycle of rotation of the SP Propeller. Sketch based on figures in [Olofsson 1996]

1.2 Dynamics of Hull-sections

A floating body in an ambient wave-field has six degrees of freedom, three translational modes - *surge*, *heave*, *sway*, and three rotational modes - *roll*, *pitch*, *yaw*. Out of these six components, the three that stand out are the motions in the vertical plane - heave, roll and pitch. Buoyancy provides a restoring force such that any excitation in these three modes tends to produce an oscillatory response or more specifically a *damped simple harmonic motion*. The motions in the horizontal plane are unrestored.

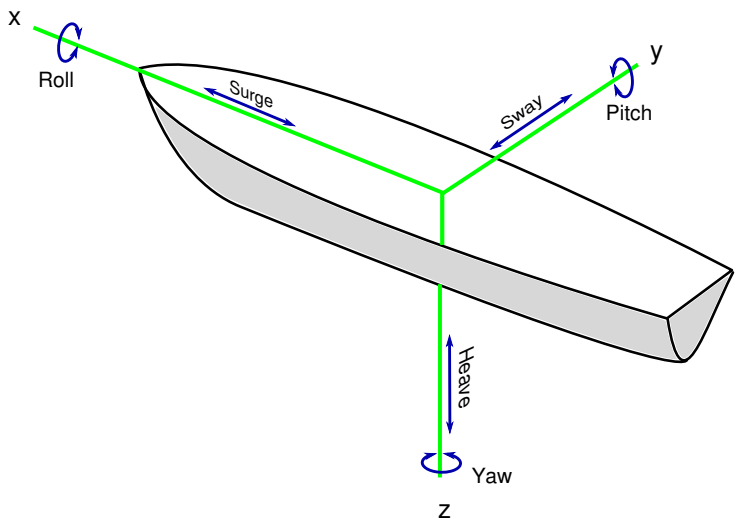

Figure 1.7: Six degrees of freedom,translation-*surge*, *heave*, *sway*, rotation-*roll*, *pitch*, *yaw*

With a simple harmonic motion (SHM) comes the issue of resonance. A SHM system will attain maximum amplitude oscillations or resonate when the excitation frequency equals the natural frequency of the system. In the case of wave-excited motion, the excitation frequency is nothing but the encounter frequency. There are primarily two sources of damping in the case of floating bodies - (i) viscous-damping

due to frictional effects, and (*ii*) wave-damping due to the energy carried away by the free-surface waves. In the case of ship-shaped bodies, wave-damping is the dominant source [Lewis et al. 1989]. This is mostly the case unless some active or passive devices are used to amplify the viscous-damping. Fortunately in heave and pitch, the wave-damping is sufficiently large to prevent resonance as the energy gets dissipated quickly. However in roll, the resultant wave-damping is almost negligible, making the system prone to resonance. These two aspects can be seen in the heave and roll response of a typical ship in Figure 1.8.

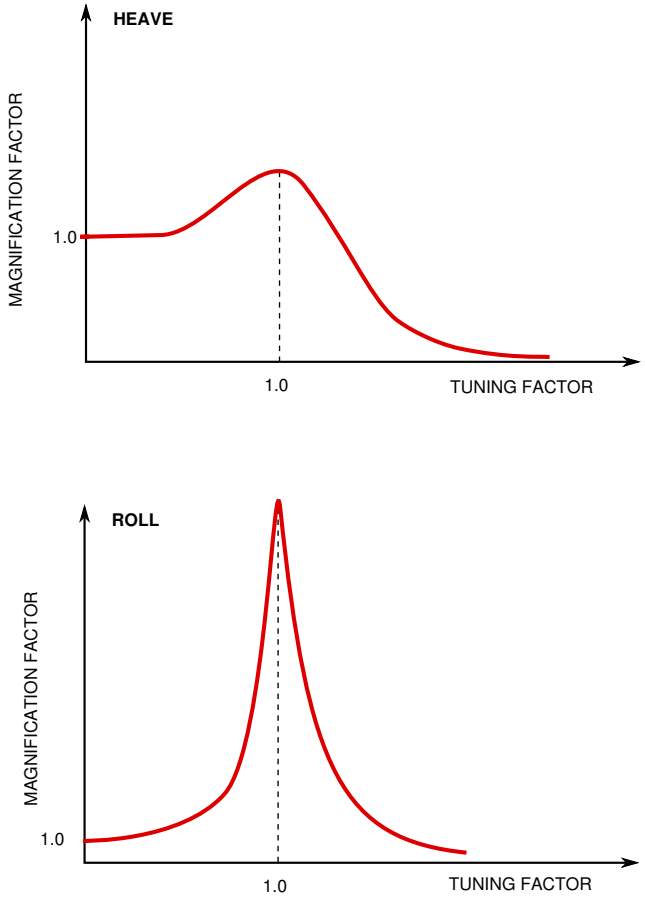

Figure 1.8: Typical heave and roll response of a ship.[Lewis et al. 1989]

1.2.1 FPSO Roll Mitigation

Floating production facilities have gained much importance in recent years with the movement of oil and gas fields into deeper waters. One of the widely used floating facilities is the Floating, Production, Storage and Offloading (FPSO) vessel, an example of which is shown in Figure 1.9.

Figure 1.9: A typical FPSO facility. Graphic from internet.

FPSOs operate in a complex ocean environment with multi-directional waves, currents, wind driven seas and swells. In such an environment, the day-to-day operations of FPSOs have often been plagued by the problem of large roll motions - a result of resonance due to negligible wave or potential damping. Such resonant motions can severely compromise the safety of the overall system and affect its efficiency. One way of mitigating these resonant roll motions is to amplify the viscous-damping component through the use of passive roll damping devices called *bilge keels*. Bilge keels are appendages fixed to each side of the hull in the "turn of bilge" that increase viscous damping by inducing flow separation. In actual construction, the bilge keels

are fabricated from small plates that are attached perpendicularly to the ship's hull (see Figure 1.10) and provide a relatively inexpensive way of increasing roll-damping compared to other active stabilizing systems like ARTs (anti-roll tanks). Predicting the effectiveness of bilge keels in reducing the resonant roll motions has been studied extensively - both numerically and experimentally.

Figure 1.10: Typical hull with bilge keels

Developing a 3-D numerical model to solve the roll dynamics of FPSOs, with the whole range of viscous and nonlinear free-surface effects, has its challenges - mostly in terms of computational resources needed to accurately model the viscous effects. To circumvent some of the challenges, the prediction of roll dynamics has often been done in the context of strip-theory, originally introduced by Korvin-Kroukovsky (see [Korvin-Kroukovsky and Jacobs 1957]). In the strip-theory approach, the ship is divided into two-dimensional sections, with each section being considered to be

part of an infinitely long prismatic cylinder. The individual sections are treated as separate two-dimensional problems, the results of which are integrated in a suitable manner to obtain a three-dimensional solution. An important restriction in the above simplification is that the geometry of the ship must be slender, i.e., the beam and draft must be small compared with the length. Also, the shape and dimensions of the two-dimensional sections must vary slowly along the length (for the other restrictions imposed by a strip-theory approach, see Ogilvie and Tuck [1969]). The hull-form of the FPSO is such that both these condition are met, making it amenable to a two-dimensional analysis.

The majority of the numerical schemes developed to predict ship motions have been within the framework of inviscid or potential flow theory. This is because viscous effects do not significantly affect the free-surface or the hull dynamics (with the exception of special scenarios like roll prediction where the effects of viscosity are important). This aspect has been proven over and again in the notable numerical schemes based on potential flow of Faltinsen [1977], Vinje and Brevig [1981], Lin et al. [1984] and Dommermuth and Yue [1987][4], and the experimental investigations of Vugts [1968] and Roddier [2000] . Even though potential flow methods are limited in predicting the viscous effects due to bilge keels, they provide a quick and reliable way to gauge the nonlinear free-surface aspects of the roll-dynamics problem.

The development of a viscous flow solver to predict the effectiveness of bilge keels has been an area of focus within the Ocean Engineering Group at the University of Texas at Austin - included in the works of Kakar [2002], Kacham [2004] and Yu [2008]. During the development of these viscous solvers, several simplifications were made regarding the treatment of the free-surface and the movement of the hull-

[4]This is not an exhaustive list of numerical schemes developed to predict the dynamics of hull-sections within the framework of potential flow theory. A detailed review of the application of potential flow methods to the prediction of nonlinear free-surface dynamics is provided in Yeung [1982] and Tsai and Yue [1996]

section. Kakar [2002] and Kacham [2004] made the following simplifications

(i) free-surface boundary conditions are based on linear-wave theory.

(ii) motions of the hull are assumed to be small and hence a non-moving grid is used to represent the domain (this is equivalent to the boundary conditions being applied on the mean body surface subject to roll or heave).

These approximations were found to be sufficient for small angles of roll (amplitude of roll upto 5°), but failed for resonant motions with roll angles in the range of 15°-20°. It was concluded that both fully nonlinear free-surface boundary conditions and a moving-grid formulation are required to model the resonant roll motion. Yu [2008] developed a Navier Stokes solver (NS2D) that improved on the linear approximations of Kakar [2002] and Kacham [2004] by including a moving grid formulation to take into account the extreme motions of the hull-section. The solver also included a nonlinear free-surface tracking scheme.

1.3 Objectives

The objectives of this research are the following:

Two-dimensional analysis of surface-piercing hydrofoils

The three-dimensional PROPCAV based hydrodynamic model for the performance prediction of SP propellers lacks a nonlinear free-surface model and its absence is seen to cause discrepancies in the overall dynamic behaviour of the forces. It was also mentioned that including the whole range of nonlinear free-surface effects in the 3-D model is fraught with challenges. We feel that it is prudent to first focus on the development of a two-dimensional numerical method with fully nonlinear free-surface boundary conditions that considers the effects of gravity explicitly and that can be applied to the ventilating entry of arbitrarily shaped blade sections. The

insight gained through the 2-D study can be used as a basis for improving the 3-D model. The objectives of the 2-D study are :

(1) *Quantify the effects of the Froude number* : The Froude number, defined as $F_n = nD/\sqrt{gD}$ with D being the diameter of the propeller and n the rate of revolution, essentially measures the influence of gravity, g. The effect of gravity is negligible in the fully ventilated regime (at low advance ratios) when $F_n > 3$ [Olofsson 1996, Shiba 1953]. However, in the partially ventilated regime (at high advance ratios), the Froude number can have an effect on the overall ventilation characteristics. Moreover, each section of the propeller operates at a different "local" Froude number. The 2-D model can be used to identify sections that could either partially or fully ventilate.

(2) *Quantify the added hydrodynamic forces* due to nonlinearity of the free-surface and the ventilated cavity surface.

The specific problems to be studied are shown in Figure 1.11.

- **Wetted-Entry** : The velocity, the geometry of the blade-section and the other characteristics of the entry problem are such that there is no ventilation. Both the suction side and the pressure side of the section are wetted.

- **Ventilating-Entry** : The velocity, the geometry of the blade-section and the other characteristics of the entry problem are such that there is ventilation. In this case, the suction side is assumed to be fully ventilated, which is an ideal scenario for a SP propeller.

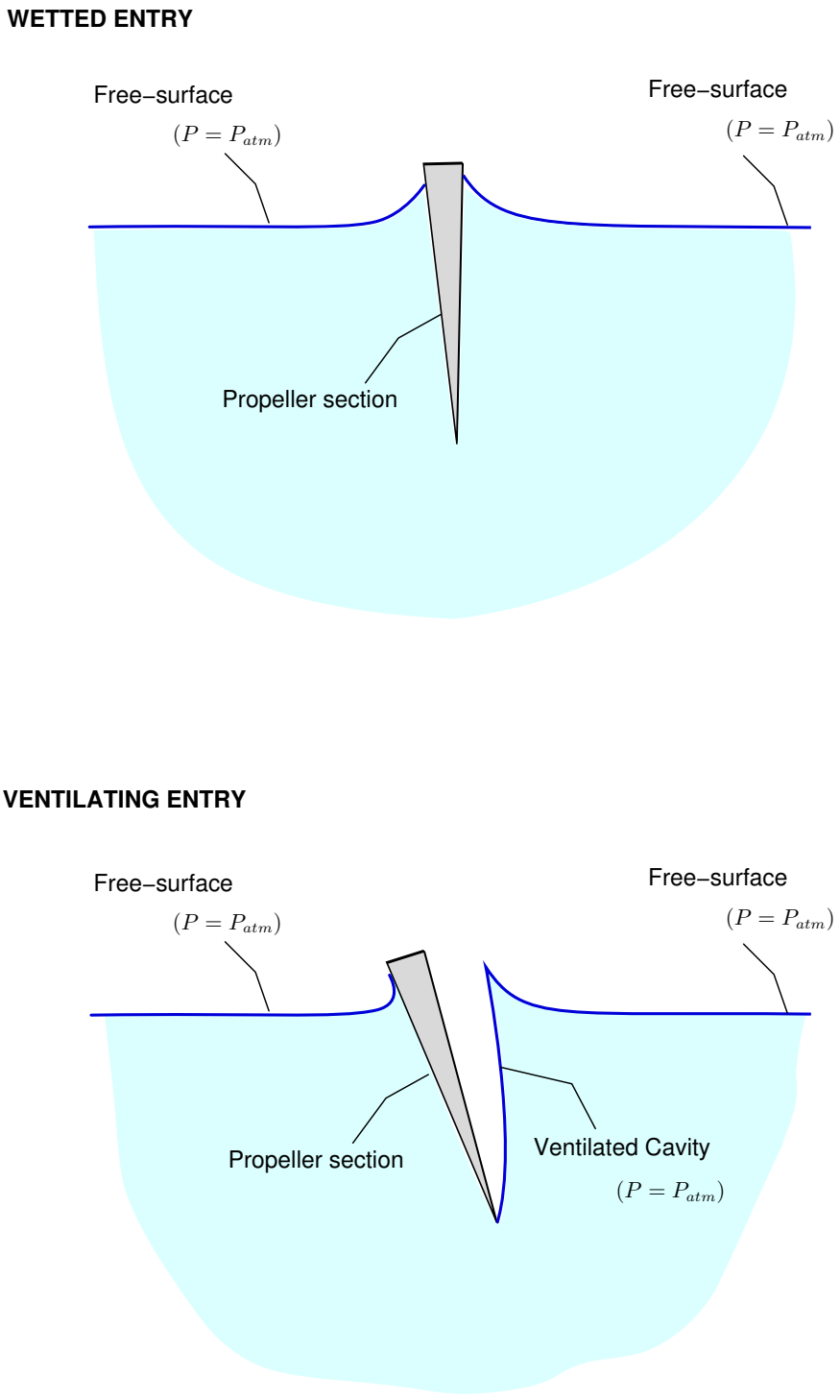

Figure 1.11: Wetted and ventilating entry of surface-piercing hydrofoils. P indicates the ambient pressure, P_{atm} represents the atmospheric pressure

Analysis of two-dimensional hull-sections

The principle behind the use of bilge keels is to amplify the viscous damping effects in roll to mitigate the resonant motions. During the development of the NS2D viscous flow solver [Yu 2008], a need was felt to develop an alternate numerical scheme that mainly dealt with the nonlinear aspects of the free-surface. The objectives here are:

(1) Develop a potential flow solver to model the kinematics and dynamics of two-dimensional hull section within the context of strip theory.

(2) Provide a framework to gauge the nonlinear effects of the free-surface and validate an inviscid version of the NS2D solver [Yu 2008].

Only hull-sections with a round bilge geometry are considered here as the potential flow solver is incapable of taking into account the effects of viscosity and flow separation due to bilge keels.

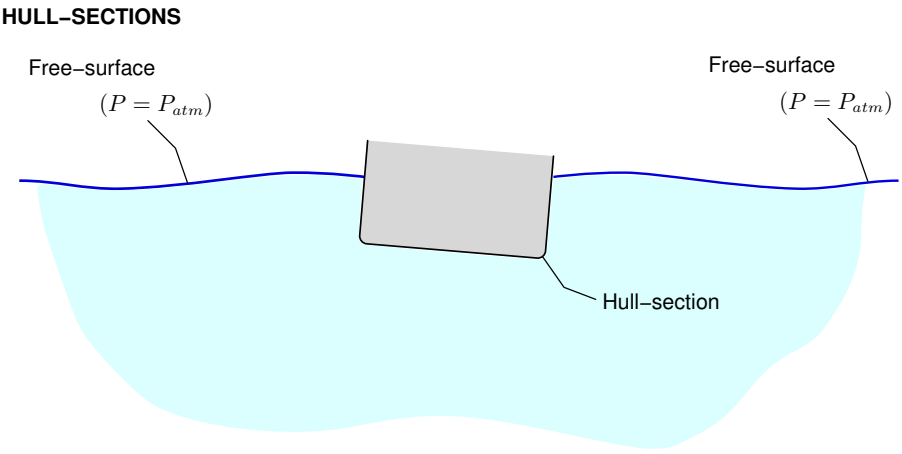

Figure 1.12: Dynamics of hull-sections. P indicates the ambient pressure, P_{atm} represents the atmospheric pressure

1.4 Organization

The dissertation is organized into six chapters:

Chapter 2 : Introduces the mathematical formulation of a generalized boundary value problem for a nonlinear free-surface body interaction.

Chapter 3 : Deals with numerical implementation of the free-surface problem and provides details of the key aspects of the numerical algorithm.

Chapter 4 : Provides details of the different studies performed to validate the numerical algorithm before being applied to the problems of interest.

Chapter 5 : The study of the dynamics of two-dimensional hull sections is presented here.

Chapter 6 : Deals with the study of the ventilating entry of a two-dimensional hydrofoil, in both vertical and rotational motion.

Chapter 7 : Conclusions and recommendations for future work are presented here.

Some of the relevant details of the numerical algorithm are presented in the Appendices.

Chapter 2

Mathematical Formulation

In this chapter, an outline of the basic equations, boundary conditions and the underlying assumptions pertaining to the solution of a class of two-dimensional free-surface problems is presented.

The basic assumption is that of *potential flow*, which makes the problem more tractable through the application of integral-equation (IE) methods. The IE methods have the advantage of reducing the spatial dimensions by one (see [Yeung 1982]). This is so because, unlike the space discretization methods like finite-difference, finite-volume and finite-element, the quantities of interest are solved only on the boundaries of the domain in IE methods. Values in the interior of the domain can be derived exclusively from those specified or solved for at its boundaries.

In essence, the free-surface problem is formulated as an *Initial Boundary Value Problem* (IBVP) for a velocity potential that satisfies the Laplace equation. The IBVP is solved by combining the *Mixed-Eulerian-Lagrangian* (MEL) method of [Longuet-Higgins and Cokelet 1976; 1978] for tracking the free-surface with the solution of a *Boundary Integral Equation* (BIE). The first part of the chapter focuses on the formulation of the general initial boundary value problem for fully nonlinear free-surface flows. Subsequent parts of the chapter present the formulation of the BIE that reduces the solution of the Laplace equation (for the velocity potential) over the entire domain to that over its boundary surfaces.

2.1 General Initial Boundary Value Problem

An *ideal* fluid is considered and assuming that the flow starting from rest is subject to *conservative forces*, the motion of the fluid at all subsequent times is deemed *irrotational* when observed from a *non-rotating frame of reference* by Kelvin's Circulation Theorem [Batchelor 2000, Kundu and Cohen 2004]. A *fixed* (non-rotating inertial frame of reference) Cartesian coordinate system $O(x, y)$ consistent with Kelvin's theorem is chosen to represent the flow with its origin at the undisturbed water level. Based on these assumptions, the flow can be represented in terms of a harmonic function $\phi(\mathbf{x}, t)$ commonly referred to as the *velocity potential*. Here, $\mathbf{x} = (x, y)$ represents the spatial location with respect to the fixed coordinate system, with x being the horizontal measure and y the vertical measure positive upward.

The *governing equation* for the flow is the Laplace equation

$$\nabla^2\phi(\mathbf{x}, t) = 0, \quad \mathbf{x} \in \Omega(t) \tag{2.1}$$

where $\Omega(t) \subset \mathcal{R}^2$ represents a simply connected fluid domain[1] with its boundary defined as $\Gamma(t)$. $\Gamma(t)$ and $\Omega(t)$ are assumed to be functions of time to account for deforming free-surfaces and moving bodies forming a part of the boundary. Also, the local fluid velocity is given as

$$\mathbf{u} = \nabla\phi = (\phi_x, \phi_y) \tag{2.2}$$

The formulation of the boundary value problem is not complete without the boundary conditions specified on the domain boundary $\Gamma(t)$. The boundary conditions are important since $\phi(\mathbf{x}, t)$ is a harmonic function and its value throughout the domain can be determined solely on the basis of conditions specified on the

[1] A domain is an open region, i.e., a connected set containing none of its boundary points. A domain $\mathcal{D}$ is said to be simply connected if every closed curve in $\mathcal{D}$ can be shrunk, by a continuous deformation, to any point in $\mathcal{D}$ [Greenberg 1998].

boundaries. Most commonly, Dirichlet or Neumann type boundary conditions are applied on specific parts of the boundary with $\Gamma_d(t) \subset \Gamma(t)$ denoting the part with Dirichlet conditions and $\Gamma_n(t) \subset \Gamma(t)$ the part with Neumann conditions. Figure 2.1 illustrates the fluid domain and its boundaries for a ventilating free-surface problem, while Figure 2.2 shows the same for a non-ventilating case. The major distinction between the two problems is that, for the ventilating case a part of the body is no longer in contact with surrounding *fluid* or in other words is no longer *wetted*. For the ventilating case, the Neumann boundary $\Gamma_n(t)$ consists only of the wetted part (see Figure 2.3). Note that in Figures 2.1 and 2.2, the solid lines indicate the domain boundaries $\Gamma(t)$ while the dashed lines indicate the actual geometry of the body. Also $\mathbf{n}$ is the normal vector on the domain boundary $\Gamma(t)$, defined to be positive when pointing out of the fluid domain.

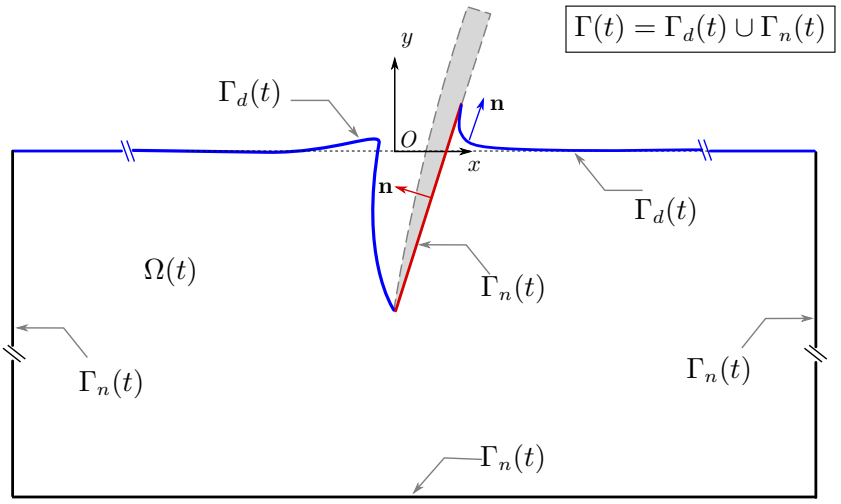

Figure 2.1: General IBVP, fluid domain and corresponding boundaries for ventilating problems; $\Gamma_d(t)$: Dirichlet boundary, $\Gamma_n(t)$: Neumann boundary, $\Omega(t)$: Fluid domain; Solid lines indicate domain boundaries and dashed lines indicate the actual physical extents of the body

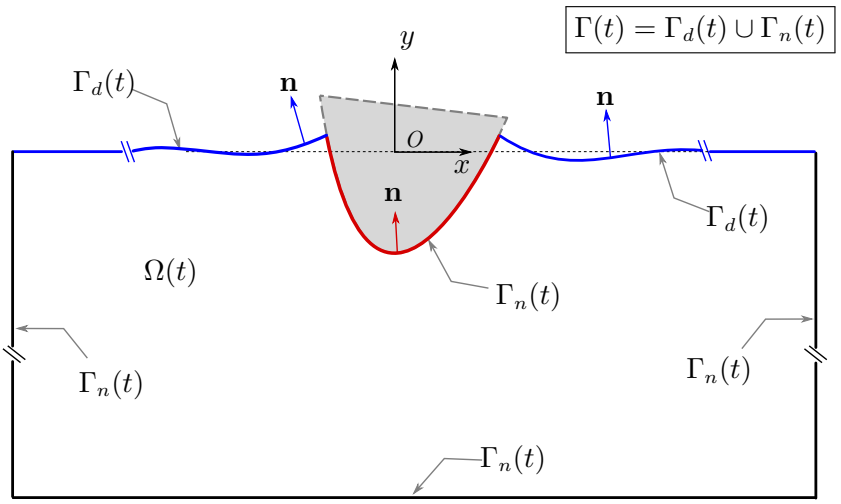

Figure 2.2: General IBVP, fluid domain and corresponding boundaries for non-ventilating problems; $\Gamma_d(t)$: Dirichlet boundary, $\Gamma_n(t)$: Neumann boundary, $\Omega(t)$: Fluid domain; Solid lines indicate domain boundaries and dashed lines indicate the actual physical extents of the body

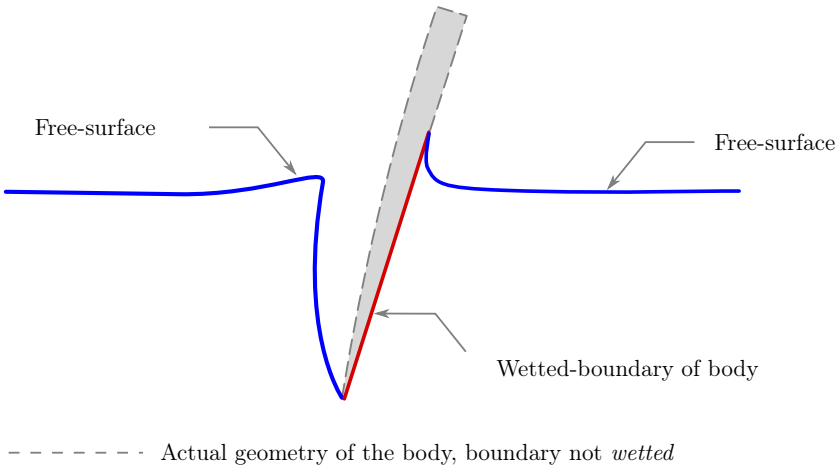

Figure 2.3: Ventilating case: wetted and non-wetted boundaries of the body

2.1.1 Boundary condition: Dirichlet Boundary $\Gamma_d(t)$ (Free-surface)

A common element in all the problems studied here is the free-surface. Two kinds of conditions are imposed on the free-surface $\Gamma_d(t) \equiv S_{\mathbb{F}}(t)$, namely the kinematic boundary condition (KFSBC) and the dynamic boundary condition (DFSBC).

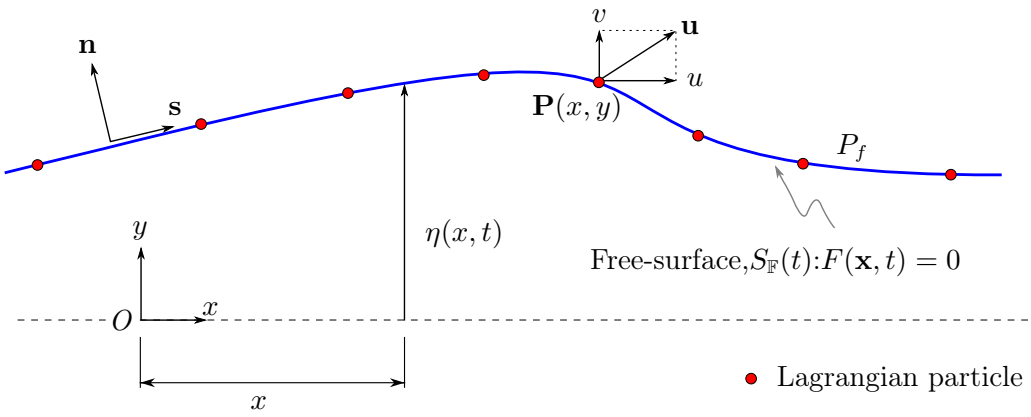

Figure 2.4: Free-surface schematic

The KFSBC is obtained by assuming $S_{\mathbb{F}}(t)$ to be a bounding surface, i.e., no material passes across the free-surface [Dussan V 1976]. Based on the schematic shown in Figure 2.4, let the free-surface be represented as $F(\mathbf{x}, t) = y - \eta(x, t) = 0$. The KFSBC on the free-surface can then be written as [Wehausen and Laitone 1960, Dussan V 1976]

$$\frac{D}{Dt}F(\mathbf{x}, t) = 0 \tag{2.3}$$

where $\dfrac{D}{Dt} = \dfrac{\partial}{\partial t} + \nabla\phi \cdot \nabla$ is the material derivative [Batchelor 2000] denoting a Lagrangian representation. $\mathbf{u} = \nabla\phi = (\phi_x, \phi_y)$ is the fluid velocity on the free-surface and $y = \eta(x, t)$ is the free-surface elevation. Also in Figure 2.4, $\mathbf{n}$ and $\mathbf{s}$ represent the normal and tangent vectors to the free-surface respectively.

From a Lagrangian representation of the free-surface, for a particle $\mathbf{P}(x, y)$ on the free-surface, the KFSBC can also be written as [Longuet-Higgins and Cokelet 1976]

$$\frac{D\mathbf{x}}{Dt} = \mathbf{u} = \nabla\phi \quad \text{or} \quad \left\{ \begin{array}{l} \dfrac{Dx}{Dt} = u = \phi_x \\ \\ \dfrac{Dy}{Dt} = v = \phi_y \end{array} \right\} \quad \mathbf{x} \in S_{\mathbb{F}}(t) \tag{2.4}$$

The dynamic boundary condition (DFSBC) is obtained from the Bernoulli's equation and assuming the pressure to be continuous across the free-surface. It is assumed that the wavelength of the free-surface elevation is long enough to neglect the effects of surface tension. Thus the pressure underneath the free-surface must equal the atmospheric pressure above giving the most general form of the free-surface DFSBC

$$\frac{\partial\phi}{\partial t} + \frac{1}{2}|\nabla\phi|^2 + gy + \frac{P_f}{\rho} = 0, \quad \mathbf{x} \in S_{\mathbb{F}}(t) \tag{2.5}$$

where g is the acceleration due to gravity. The common form of the DFSBC is obtained by expressing the pressure as gage pressure, in which case the pressure on the free-surface $P_f = 0$. For a Lagrangian particle $\mathbf{P}(x, y)$, the DFSBC can be rewritten as

$$\frac{D\phi}{Dt} = \frac{1}{2}|\nabla\phi|^2 - gy, \quad \mathbf{x} \in S_{\mathbb{F}}(t) \tag{2.6}$$

2.1.2 Boundary condition: Neumann Boundary $\Gamma_n(t)$

On a prescribed impervious boundary $\Gamma_n(t)$, the normal velocity of the flow equals that of the boundary

$$\frac{\partial\phi}{\partial n} \equiv \phi_n = \mathbf{V}(\mathbf{x}, t) \cdot \mathbf{n}, \quad \mathbf{x} \in \Gamma_n(t) \tag{2.7}$$

where $\mathbf{n}$ is the unit normal of $\Gamma_n(t)$ (positive pointing out of the fluid domain) and $\mathbf{V}(\mathbf{x}, t)$ is the prescribed velocity of $\Gamma_n(t)$.

2.1.3 Initial Condition

The IBVP is not complete without specifying the initial conditions. Since the initial condition to be specified is unique to the particular type of free-surface problem being solved, its form is presented along with formulation of the specific problem in later chapters.

2.2 The Mixed Eulerian-Lagrangian Method

The mixed Eulerian-Lagrangian (MEL) method was introduced in the seminal work of [Longuet-Higgins and Cokelet 1976; 1978] to simulate the deformation of two-dimensional steep surface waves within the context of potential flow, which is a good approximation up to the point of breaking. Since then, the method has become the workhorse for simulating highly nonlinear waves and wave-body problems in both two and three dimensions. A detailed review of the application of the MEL to different free-surface problems can be found in [Yeung 1982, Tsai and Yue 1996, Mei et al. 2005].

The relative success of the MEL-approach in simulating nonlinear free-surface problems stems from its ability to decouple the time variation imposed by the free-surface boundary conditions from the solution of the boundary value-problem. For a typical free-surface problem starting with specified initial conditions, the MEL approach consists of two steps that get repeated during the simulation [Mei et al. 2005]

Eulerian Step : Given $\Gamma_n(t)$ and $\phi_n(\mathbf{x} \in \Gamma_n)$, $\Gamma_d(t)$ and $\phi(\mathbf{x} \in \Gamma_d)$, solve the boundary value problem (BVP) for $\phi_n(\mathbf{x} \in \Gamma_d)$. Note that $\Gamma_d(t)$ refers to the free-surface since it is a Dirichlet boundary. The BVP is solved using

a boundary-integral equation (BIE) formulation with respect to the *Eulerian* variables. One advantage of the BIE formulation is that only values at the domain boundaries need to be solved for. Since ϕ is known on the free-surface, the tangential velocity ϕ_s is also known (say through numerical differentiation). In essence, this step involves the calculation of the velocity on the free-surface $\mathbf{u} = \nabla\phi = (\phi_x, \phi_y) = f(\phi_s, \phi_n, \mathbf{s}, \mathbf{n})$.

Lagrangian Step : Obtain the new free-surface location $\Gamma_d(t + \Delta t)$ and velocity potential $\phi(\mathbf{x}, t + \Delta t)$ for $\mathbf{x} \in \Gamma_d(t + \Delta t)$ by integrating the *Lagrangian* form of the KFSBC (Equation (2.4)) and DFSBC (Equation (2.6)) in time. Note that the time integration is explicit in nature.

These two steps get repeated during the course of the simulation. Most of the computational effort is expended in the Eulerian step, which involves the solution of the BIE.

2.3 Boundary Integral Equation

A Boundary Integral Equation (BIE) forms a crucial part of the Eulerian step in the MEL approach, which involves the solution of the boundary-value problem (BVP). The BVP for the velocity potential is formulated as a BIE by introducing the two-dimensional Green's function $G(\mathbf{p}, \mathbf{q}) = -\dfrac{1}{2\pi} \ln r_{\mathbf{pq}}$ (satisfies the Laplace equation). Here $r_{\mathbf{pq}} = |\mathbf{p} - \mathbf{q}|$ is the Euclidean distance between the field point $\mathbf{p} \equiv \mathbf{p}(\mathbf{x})$ and the source point $\mathbf{q} \equiv \mathbf{q}(\mathbf{x})$. The BIE obtained by applying Green's third identity to $\phi(\mathbf{x}, t)$ and $G(\mathbf{p}, \mathbf{q})$ can be written as

$$\frac{\alpha(\mathbf{p})}{2\pi}\, \phi(\mathbf{p}) + \int\limits_{\Gamma(t)} \phi(\mathbf{q}) G_n(\mathbf{p}, \mathbf{q})\, dS_{\mathbf{q}} = \int\limits_{\Gamma(t)} G(\mathbf{p}, \mathbf{q}) \phi_n(\mathbf{q})\, dS_{\mathbf{q}} \tag{2.8}$$

where $\alpha(\mathbf{p})$ is the internal angle formed at the boundaries, which is introduced as a result of the exclusion of the singular nature of the Green's function (see Figure

2.5). Consider a fluid domain Ω with its boundary Γ, which is smooth everywhere except at the corner point $\mathbf{C}$. The internal angle $\alpha(\mathbf{p}) = \alpha_c$ when $\mathbf{p} = \mathbf{C}$. Also, $\alpha(\mathbf{p}) = \alpha_s = \pi$ when $\mathbf{p} = \mathbf{S}$, a generic point on the smooth part of the boundary (see [Pozrikidis 2002]).

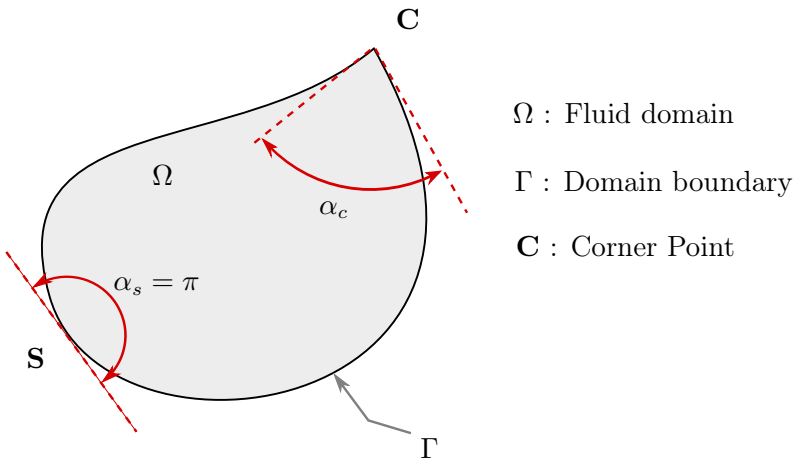

Figure 2.5: Representation of the internal angle $\alpha_{\mathbf{p}}$

In Equation (2.8), $G_n(\mathbf{p},\mathbf{q}) = \nabla G(\mathbf{p},\mathbf{q}) \cdot \mathbf{n_q}$ and $\phi_n(\mathbf{p},\mathbf{q}) = \nabla\phi(\mathbf{p},\mathbf{q}) \cdot \mathbf{n_q}$. $\mathbf{n_q}$ is the normal vector at $\mathbf{q}$ positive out of the fluid. For the general boundary value problem formulated in Section 2.1, the BIE (Equation (2.8)) can be rearranged to account for surfaces with Dirichlet and Neumann type boundary conditions. For $\Gamma_n(t)$ the value of ϕ_n is specified and $\Gamma_d(t)$ the value of ϕ is known. The BIE in its rearranged form can be written as

$$\frac{\alpha(\mathbf{p})}{2\pi}\,\phi(\mathbf{p}) + \int\limits_{\Gamma_n(t)} \phi(\mathbf{q}) G_n(\mathbf{p},\mathbf{q})\, dS_{\mathbf{q}} - \int\limits_{\Gamma_d(t)} G(\mathbf{p},\mathbf{q})\phi_n(\mathbf{q})\, dS_{\mathbf{q}} = \int\limits_{\Gamma_n(t)} G(\mathbf{p},\mathbf{q})\phi_n(\mathbf{q})\, dS_{\mathbf{q}} - \int\limits_{\Gamma_d(t)} \phi(\mathbf{q}) G_n(\mathbf{p},\mathbf{q})\, dS_{\mathbf{q}} \tag{2.9}$$

Equation (2.9) in turn can be solved for the boundary values ϕ on $\Gamma_n(t)$ and ϕ_n on $\Gamma_d(t)$.

Chapter 3

Numerical Implementation

The previous chapter introduced the mixed Eulerian-Lagrangian (MEL) approach of solving a general free-surface IBVP. In summary, the MEL approach consists of two steps used repetitively - starting from initial conditions (i) solve a well-defined BVP, formulated as a BIE, for a given set of Dirichlet and Neumann conditions on the domain boundaries, (ii) update the geometry of the free-surface and the velocity potential on it by integrating the KFSBC and DFSBC in time, based on the velocities obtained from the previous step. The proper treatment of these two MEL steps dominate the numerical implementation of the free-surface problems.

This chapter presents details of the numerical implementation of the two MEL steps. A Boundary Element Method (BEM)[1] with linear isoparametric elements is used to solve the BVP in the first MEL step. Two very important aspects of the BEM implementation (a) treatment of corners with double nodes (b) treatment of the free-surface jets formed during high-speed water-entry of bodies, are addressed in detail. With regard to the time-stepping of the free-surface boundary conditions in the second step of the MEL approach, the implementation of a fourth-order Runge-Kutta scheme is presented in detail.

The goal of the chapter is to present an overview of the numerical aspects associated with the solution of the general initial boundary value problem. Only aspects that are common to the different classes of free-surface problems are covered here and

[1]The Boundary Element Method (BEM) is a numerical method of solution of boundary integral equations, based on a discretization procedure [Wrobel 2002]

details that are specific to a type of problem are presented along with its formulation in later chapters.

3.1 BEM - Method of Weighted Residuals

Consider a generic integral equation of the form

$$\mathcal{L}u - b = 0 \tag{3.1}$$

which is defined in an arbitrary domain Ω with a boundary Γ. $\mathcal{L}$ is an arbitrary linear operator with constant coefficients. u is the field variable and b is an arbitrary source distribution in Ω [Gaul et al. 2003].

Let the exact solution u be approximated such that

$$u \approx \bar{u} = \sum_{j=1}^{n} a_j N_j(\mathbf{x}) \tag{3.2}$$

where $N_j(\mathbf{x})$ are a set of linearly independent basis functions and a_j are unknown arbitrary coefficients. We can define a residual R for the approximation based on Equation (3.2), written as

$$R = \mathcal{L}\bar{u} - b \tag{3.3}$$

The notion of the method of weighted residuals is to minimize the residual, in some average sense, over the domain. This can be written as

$$\int_{\Gamma} RW_j dS = 0, \qquad j = 1, 2.., n \tag{3.4}$$

where the number of *weight functions* W_j is equal to the number of unknown coefficients a_j. Equation 3.4 results in n equations for the unknown coeffcients a_j.

The Boundary Element Method is based on (i) point collocation method - class of weighted residual methods with $W_j(\mathbf{x}) = \delta(\mathbf{x} - \mathbf{x}_j)$, and (ii) local piecewise approximation for the interpolation functions $N_j(\mathbf{x})$, i.e., $N_j(\mathbf{x})$ are piecewise smooth on subregions of Γ.

3.2 Linear Boundary Element Method

Linear isoparametric elements form the basis for the numerical solution of the BIE (Equation (2.8)). Following the notation given in [Wrobel 2002] and [Brebbia et al. 1984], the variation of ϕ (velocity potential or dipole strength) and ϕ_n (normal velocity or source strength), over a generic element $\mathcal{E}_j$, is written as

$$\left.\begin{aligned} \phi(\xi) &= \phi_j^{(1)} N_{(1)}(\xi) + \phi_j^{(2)} N_{(2)}(\xi) \\ \phi_n(\xi) &= \phi_{n,j}^{(1)} N_{(1)}(\xi) + \phi_{n,j}^{(2)} N_{(2)}(\xi) \end{aligned}\right\} -1 \le \xi \le +1 \tag{3.5}$$

The geometry of the element can also be represented in a similar manner with

$$\left.\begin{aligned} x(\xi) &= x_j N_{(1)}(\xi) + x_{j+1} N_{(2)}(\xi) \\ y(\xi) &= y_j N_{(1)}(\xi) + y_{j+1} N_{(2)}(\xi) \end{aligned}\right\} -1 \le \xi \le +1 \tag{3.6}$$

In the above representation $(\phi_j^{(1)}, \phi_{n,j}^{(1)})$ and $(\phi_j^{(2)}, \phi_{n,j}^{(2)})$ are the values of the potential and the flux at the two nodal points of the element. ξ is an intrinsic element coordinate. To ensure compatibility of the potential (ϕ) and the flux (ϕ_n) between the elements, the two nodal points, (x_j, y_j) and (x_{j+1}, y_{j+1}), are chosen to be the end-points of the element (see Figure 3.1). Note that (1) and (2) represent the local numbering, while j and $j+1$ correspond to the global numbering of the nodes of the element $\mathcal{E}_j$. With the nodal points at the end-points of the element, the interpolation or *shape functions* $N_{(1)}(\xi)$ and $N_{(2)}(\xi)$ can be written as

$$\left.\begin{aligned} N_{(1)}(\xi) &= \frac{1}{2}(1-\xi) \\ N_{(2)}(\xi) &= \frac{1}{2}(1+\xi) \end{aligned}\right\} -1 \le \xi \le +1 \tag{3.7}$$

The integral equation, Equation (2.8), is solved numerically by discretizing the boundary $\Gamma = \Gamma_d \cup \Gamma_n$ based on the above representation. The boundaries Γ_d and Γ_n are subdivided into piecewise linear elements such that [Mei et al. 2005]

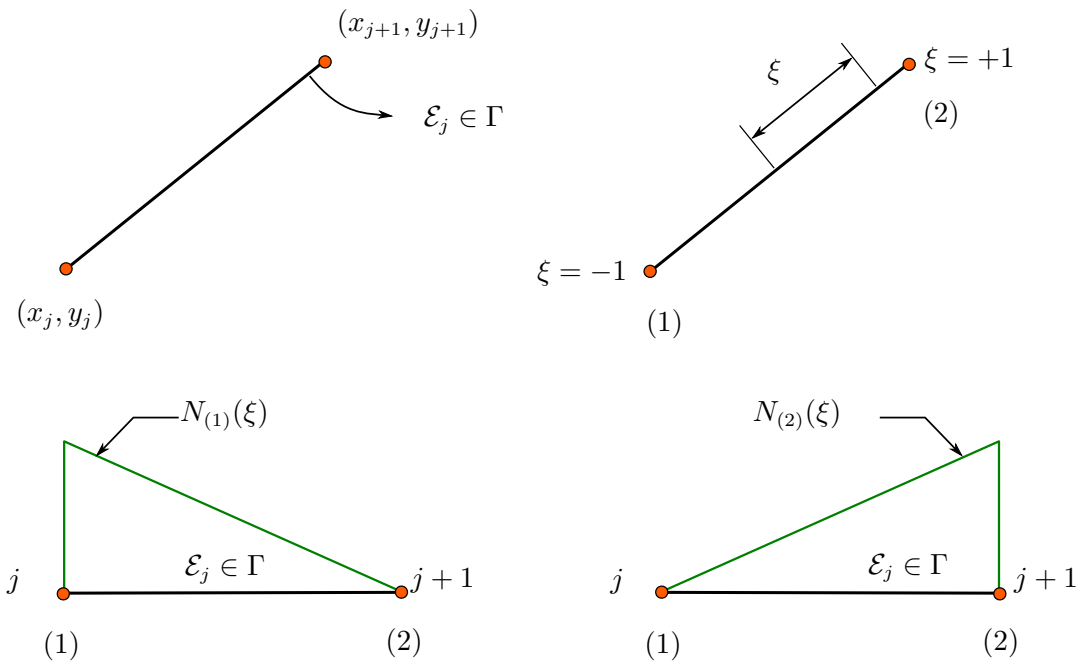

Figure 3.1: Geometry and shape functions for a linear isoparametric element

$$\begin{aligned} \Gamma_d(t) &= \bigcup_{j=1}^{N_d} \mathcal{E}_j \\ \Gamma_n(t) &= \bigcup_{j=1}^{N_n} \mathcal{E}_j \end{aligned} \tag{3.8}$$

where N_n and N_d are the number of elements on $\Gamma_n(t)$ and $\Gamma_d(t)$ respectively. The discretized form of Equation (2.8) can then be written as [Mei et al. 2005]

$$\begin{aligned} \sum_{j=1}^{N_n} I_D(\mathbf{p}) - \sum_{j=1}^{N_d} I_S(\mathbf{p}) = &- \alpha'(\mathbf{p})\phi(\mathbf{p}) \\ &- \sum_{j=1}^{N_d} I_D(\mathbf{p}) + \sum_{j=1}^{N_s} I_S(\mathbf{p}); \quad \mathbf{p} \in \Gamma_d \end{aligned} \tag{3.9}$$

and

$$\alpha'(\mathbf{p})\phi(\mathbf{p}) + \sum_{j=1}^{N_n} I_D(\mathbf{p}) - \sum_{j=1}^{N_d} I_S(\mathbf{p}) = \sum_{j=1}^{N_n} I_S(\mathbf{p}) - \sum_{j=1}^{N_d} I_D(\mathbf{p}); \quad \mathbf{p} \in \Gamma_n \tag{3.10}$$

where

$$\alpha'(\mathbf{p}) = \frac{\alpha(\mathbf{p})}{2\pi}$$

$$I_S(\mathbf{p}) = \int_{\mathcal{E}_j} \phi_n(\mathbf{q}) G(\mathbf{p},\mathbf{q}) dS_{\mathbf{q}} = \phi_{n,j}^{(1)} I_{s,j}^{(1)} + \phi_{n,j}^{(2)} I_{s,j}^{(2)} \tag{3.11}$$

$$I_D(\mathbf{p}) = \int_{\mathcal{E}_j} \phi(\mathbf{q}) G_n(\mathbf{p},\mathbf{q}) dS_{\mathbf{q}} = \phi_j^{(1)} I_{d,j}^{(1)} + \phi_j^{(2)} I_{d,j}^{(2)}$$

and,

$$\left.\begin{aligned} I_{s,j}^{(k)} &= \int_{\mathcal{E}_j} N_{(k)}(\xi) G(\mathbf{p},\mathbf{q}) dS_{\mathbf{q}} \\ I_{d,j}^{(k)} &= \int_{\mathcal{E}_j} N_{(k)}(\xi) G_n(\mathbf{p},\mathbf{q}) dS_{\mathbf{q}} \end{aligned}\right\} k = 1,2 \tag{3.12}$$

The elemental integrals $I_{s,j}^{(k)}$ and $I_{d,j}^{(k)}$ are commonly referred to as the influence coefficients. For linear isoparametric elements, these integrals can be evaluated analytically (see Appendix A for closed-form expressions for these integrals). The subscript $_{(s)}$ denotes source influence coefficients while $_{(d)}$ the dipole coefficients.

For a purely Dirichlet or Neumann problem, the discretized BIE can be written in a matrix form as [Wrobel 2002]

$$[\mathbf{H}]\{\phi\} = [\mathbf{G}]\{\phi_n\} \tag{3.13}$$

where $[\mathbf{H}]$ and $[\mathbf{G}]$ are the influence coefficient matrices, $\{\phi\}$ and $\{\phi_n\}$ are the vectors containing the nodal values of the potential and its normal derivatives respectively. The elements of the influence coefficient matrices have the form

$$\left.\begin{aligned} G_{ij} &= I^{(2)}_{s,(i,j)} + I^{(1)}_{s,(i,j+1)} \\ \hat{H}_{ij} &= I^{(2)}_{d,(i,j)} + I^{(1)}_{d,(i,j+1)} \end{aligned}\right\} \mathbf{p} = \mathbf{x}_i \in \Gamma \tag{3.14}$$

where $I^{(2)}_{s,(i,j)}$ and $I^{(2)}_{d,(i,j)}$ represent the contribution from $\mathcal{E}_j$, while $I^{(2)}_{s,(i,j+1)}$ and $I^{(2)}_{d,(i,j+1)}$ represent the contribution from the adjacent element $\mathcal{E}_{j+1}$. Note that $\hat{H}_{ij}$ is that part of $[\mathbf{H}]$ that does not include the self influence coefficient ($\mathbf{p} \in \mathcal{E}_j$ denoting the singular part of the influence integrals). This is calculated by virtue of the property

$$H_{ii} = -\sum_{\substack{j \\ j \neq i}} \hat{H}_{ij} \tag{3.15}$$

The linear system of equations can be re-ordered based on either Neumann or Dirichlet type boundary conditions specified on the domain boundaries and can be written as

$$[\mathbf{A}]\{\mathbf{X}\} = \{\mathbf{F}\} \tag{3.16}$$

where $\{\mathbf{X}\}$ is the vector of unknowns and $\{\mathbf{F}\}$ is the so called "*load*" vector [Wrobel 2002]. A direct LU-solver ([Press et al. 1992]) is used to solve the re-ordered system of equations to obtain the unknown values of ϕ on Γ_n and ϕ_n on Γ_d.

3.3 Double Nodes

A domain to be discretized using boundary elements can have corners at the intersection of individual surfaces comprising its boundary. These corners, apart from being points of discontinuous slopes, can have a confluence of boundary conditions of the same or differing types. A common method of dealing with such corners is through a double-node approach. In the case of a linear isoparametric BEM scheme, the use of a double-node increases the number of degrees of freedom at a corner to three. However, out of these three degrees of freedom, only one is solved for in the BEM scheme. [Gaul et al. 2003, Brebbia and Dominguez 1992] list the different

possibilities occurring at a double node in terms of the primary variable (velocity potential) and the secondary variable (normal velocity or flux) :

(a) Known values: fluxes *before* and *after* the corner.
Unknown value: potential.

(b) Known values: potential and flux *before* the corner.
Unknown value: flux *after* the corner.

(c) Known values: potential and flux *after* the corner.
Unknown value: flux *before* the corner.

(d) Known values: potential.
Unknown values: flux *before* and *after* the corner.

A corner of importance is the one at the intersection of the free-surface ($S_{\mathbb{F}}$) with the body ($S_{\mathbb{B}}$). At this corner there is a confluence of boundary conditions - a Dirichlet condition from the free-surface side and a Neumann condition from the body side. The different aspects of the double-node approach at the $S_{\mathbb{F}} \cap S_{\mathbb{B}}$ intersection point are shown in Figure 3.2.

In Figure 3.2, $j-1$, j, $j+1$, etc., represent the global numbering of the boundary element nodes (nodes are the end-points of a panel/element). For a generic element, represented as $\mathcal{E}$, (1) and (2) represent the local numbering of nodes belonging to the element. Element $\mathcal{E}_j$ belongs to the body-surface $S_{\mathbb{B}}$ with a Neumann boundary condition, while element $\mathcal{E}_{j+1}$ belongs to the free-surface $S_{\mathbb{F}}$ with a Dirichlet boundary condition. The double-node approach at node $j+1$ is based on the following steps:

(i) For the element $\mathcal{E}_{j+1} \in S_{\mathbb{F}}$, both $\phi_{j+1}^{(1)}$ and $\phi_{j+1}^{(2)}$ are known as a result of the Dirichlet boundary condition (velocity potential specified as an initial condition is known at all times as it gets updated via the dynamic and kinematic free-surface boundary conditions). A jump in the velocity potential is not allowed

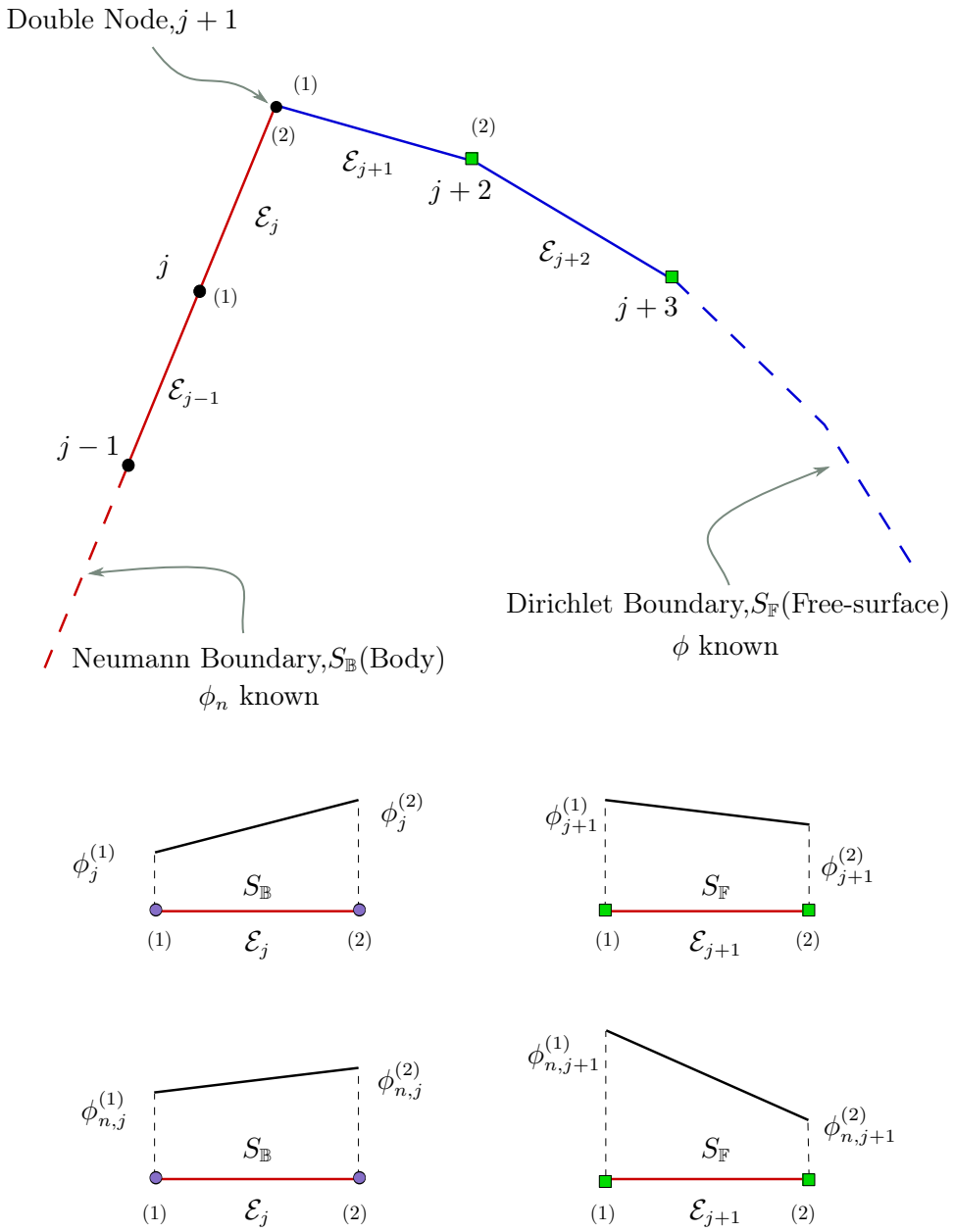

Figure 3.2: Double-node approach at the body free-surface intersection

at the intersection point and this leads to the condition $\phi_j^{(2)} = \phi_{j+1}^{(1)}$ with $\phi_j^{(2)}$ being a part of $\mathcal{E}_j \in S_{\mathbb{B}}$.

(ii) Node (2) of $\mathcal{E}_j \in S_{\mathbb{B}}$ and Node (1) of $\mathcal{E}_{j+1} \in S_{\mathbb{F}}$ are treated separately (hence

the name "*double-node*"). The discontinuity in the slope is considered explicitly by having different surface normals on either boundary. This corresponds to a discontinuous flux and leads to the condition $\phi^{(2)}_{n,j} \neq \phi^{(1)}_{n,j+1}$. Note that $\phi^{(2)}_{n,j}$ is known since $\mathcal{E}_j \in S_{\mathbb{B}}$ with a Neumann boundary condition (velocity on the body is known).

From (i) and (ii), it can be inferred that the free-surface body intersection is a double-node of type (b). Out of the three variables at the intersection, $\phi^{(1)}_{j+1}$, $\phi^{(2)}_{n,j}$ and $\phi^{(1)}_{n,j+1}$, the only unknown solved for is $\phi^{(1)}_{n,j+1}$ which is the flux on the free-surface. This is in essence explains the double-node approach at the free-surface body intersection. Corners of types (a) and (c) also occur in the domain, and are treated in a similar manner.

The angle $\alpha(\mathbf{p})$ in the BIE (Equation (2.8)) is not calculated explicitly at a corner point. It is determined instead using Equation (3.15).

3.4 Treatment of jets

In the case of high speed water-entry of hydrofoils and wedges, thin jets of high-velocity with primarily one-dimensional flow, develop along the wetted part. These jets are difficult to handle numerically as extremely small panels are required to capture the shape and this results in a corresponding reduction in the time-step. The most common approach to alleviate the numerical issues is to let the jet evolve for a certain duration and then truncate it when a specified criteria is met.

In the current nonlinear BEM scheme, the relative angle (β_R) between the free-surface and the wetted part of the body is used as the truncation criteria. Figure 3.3 illustrates the truncation process of the jet region. Once the angle β_R reaches the threshold limit β_i, which is specified a priori, the first free-surface panel adjacent to the body is cut off. A new free-surface panel is created joining the two surfaces such

that the relative angle is greater than the threshold angle. The value of the velocity potential at the intersection of the new free-surface panel with the body surface is obtained via cubic interpolation of the potentials on the body-surface. The range of the threshold limit for the relative angle is based on the self-similar solution of [Dobrovol'skaya 1966; 1969] and is chosen to be in the range $\pi/15 \leq \beta_i \leq \pi/9$. This model is in concept similar to that used by [Zhao and Faltinsen 1993] where the last panel is aligned perpendicular to the body surface.

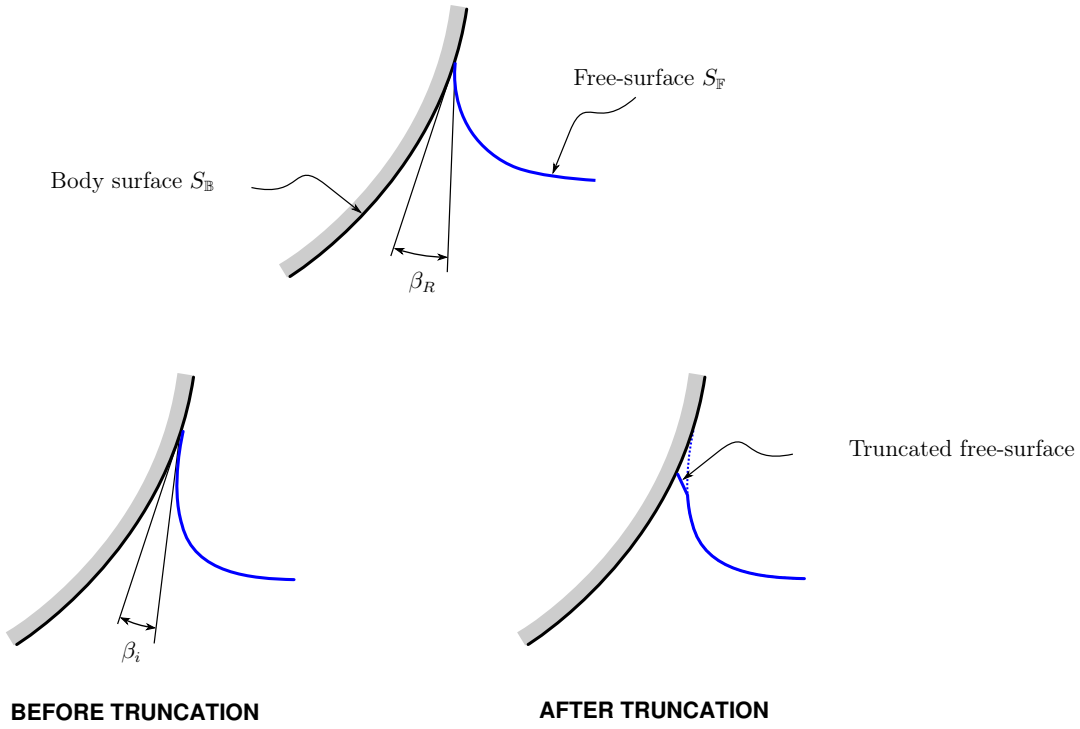

β_R : relative angle between surfaces

β_i : threshold angle

Figure 3.3: Details of jet truncation/cut-off model

3.5 Time-stepping Scheme

The time-stepping scheme forms an integral part of the numerical scheme. A fourth-order Runge-Kutta (RK4) scheme is used to integrate the time-dependent kinematic (KFSBC) and dynamic (DFSBC) free-surface boundary conditions. The free-surface boundary conditions expressed in the Lagrangian form are

$$\left.\begin{aligned} \text{KFSBC}: \quad & \frac{D\mathbf{x}}{Dt} = \nabla\phi = \mathbf{u} \\ \text{DFSBC}: \quad & \frac{D\phi}{Dt} = \frac{1}{2}|\nabla\phi|^2 - gy \end{aligned}\right\} \mathbf{x} \in S_{\mathbb{F}}(t) \tag{3.17}$$

3.5.1 Initial value problem

Let an initial value problem be specified as [Hildebrand 1974]

$$\dot{y} = f(t, y), y(t_0) = y_0 \tag{3.18}$$

The fourth-order Runge-Kutta method leads to the following equations:

$$\begin{aligned} y^{(m+1)} &= y^{(m)} + \frac{h}{6}(k_0 + 2k_1 + 2k_2 + k_3) + \mathcal{O}(h^5) \\ \text{with,} \quad k_0 &= hf\big(t^{(m)}, y^{(m)}\big) \\ k_1 &= hf\big(t^{(m)} + 0.5h, y^{(m)} + 0.5k_0\big) \\ k_2 &= hf\big(t^{(m)} + 0.5h, y^{(m)} + 0.5k_1\big) \\ k_3 &= hf\big(t^{(m)} + h, y^{(m)} + k_2\big) \end{aligned} \tag{3.19}$$

In eqn. (3.19), $h = \Delta t$ is the spacing or size of the time-step such that $t^{(m+1)} = t^{(m)} + h$; superscripts $^{(m)}$ and $^{(m+1)}$ represent the values of the function at $t = t^{(m)}$ and $t = t^{(m+1)}$ respectively; k_0, k_1, k_2 and k_3 are the slopes or derivatives evaluated at each intermediate level of the RK4 scheme.

3.5.2 Free-surface updating

Updating the free-surface location and the velocity potential on it requires the application of the RK4 scheme to both the KFSBC and DFSBC. At a given instant

of time $t = t^{(m)}$, $S_{\mathbf{F}}^{(m)} \equiv S_{\mathbf{F}}\big(t^{(m)}\big)$ represents the free-surface and, $\phi^{(m)} \equiv \phi\big(\mathbf{x}^{(m)}, t\big)$, with $\mathbf{x}^{(m)} = \big(x^{(m)}, y^{(m)}\big) \in S_{\mathbf{F}}^{(m)}$, represents the corresponding velocity potential. The following steps explain in detail the procedure required to obtain the free-surface characteristics at time $t = t^{(m+1)} = t^{(m)} + h$.

STEP (1) : time $t = t^{(m)}$

(i) Solve the BVP to obtain the normal velocity $\phi_n^{(m)}$ on the free-surface. Based on $\phi_n^{(m)}$ and $\phi_s^{(m)}$, obtain the horizontal and vertical components of the velocity $\mathbf{u}^{(m)} = \big(\phi_x^{(m)}, \phi_y^{(m)}\big)$ using the coordinate transformation

$$\begin{aligned} \phi_x^{(m)} &= \quad \phi_s^{(m)} n_y^{(m)} + \phi_n^{(m)} n_x^{(m)} \\ \phi_y^{(m)} &= -\phi_s^{(m)} n_x^{(m)} + \phi_n^{(m)} n_y^{(m)} \end{aligned} \tag{3.20}$$

$\phi_s^{(m)}$ is the tangential component of the velocity on the free-surface and is obtained through a second-order finite difference scheme based on the arc-length. $\mathbf{n}^{(m)} = (n_x^{(m)}, n_y^{(m)})$ is the normal vector on $S_{\mathbf{F}}^{(m)}$.

(ii) Evaluate the derivatives k_{0x}, k_{0y} and k_{0p}, where

$$\begin{aligned} k_{0x} &= \Delta t \phi_x^{(m)} \\ k_{0y} &= \Delta t \phi_y^{(m)} \\ k_{0p} &= \Delta t \left(\frac{1}{2} \big| \mathbf{u}^{(m)} \big|^2 - g y^{(m)} \right) \end{aligned} \tag{3.21}$$

(iii) Obtain the characteristics of the free-surface at time $t^{(i)} = t^{(m)} + 0.5\Delta t$ using the derivatives from sub-step (ii)

$$\begin{aligned} x^{(i)} &= x^{(m)} + 0.5 k_{0x} \\ y^{(i)} &= y^{(m)} + 0.5 k_{0y} \\ \phi^{(i)} &= \phi^{(m)} + 0.5 k_{0p} \end{aligned} \tag{3.22}$$

where superscript $^{(i)}$ denotes the values at the first intermediate step of the RK4 scheme.

STEP (2) : time $t^{(i)} = t^{(m)} + 0.5\Delta t$

(i) Repeat sub-step (i) of **STEP (1)** for the free-surface $S_{\mathbf{F}}^{(i)} \equiv S_{\mathbf{F}}\big(t^{(i)}\big)$ with velocity potential $\phi^{(i)}$.

(ii) Evaluate the derivatives k_{1x}, k_{1y} and k_{1p}, where

$$\begin{aligned} k_{1x} &= \Delta t \phi_x^{(i)} \\ k_{1y} &= \Delta t \phi_y^{(i)} \\ k_{1p} &= \Delta t \left(\frac{1}{2} \big| \mathbf{u}^{(i)} \big|^2 - g y^{(i)} \right) \end{aligned} \tag{3.23}$$

(iii) Obtain the characteristics of the free-surface at time $t^{(ii)} = t^{(m)} + 0.5\Delta t$ using the derivatives from sub-step (ii)

$$\begin{aligned} x^{(ii)} &= x^{(m)} + 0.5 k_{1x} \\ y^{(ii)} &= y^{(m)} + 0.5 k_{1y} \\ \phi^{(ii)} &= \phi^{(m)} + 0.5 k_{1p} \end{aligned} \tag{3.24}$$

where superscript $^{(ii)}$ denotes the values at the second intermediate step of the RK4 scheme.

STEP (3) : time $t^{(ii)} = t^{(m)} + 0.5\Delta t$

(i) Repeat sub-step (i) of **STEP (1)** for the free-surface $S_{\mathbf{F}}^{(ii)} \equiv S_{\mathbf{F}}\big(t^{(ii)}\big)$ with velocity potential $\phi^{(ii)}$.

(ii) Evaluate the derivatives k_{2x}, k_{2y} and k_{2p}, where

$$\begin{aligned} k_{2x} &= \Delta t \phi_x^{(ii)} \\ k_{2y} &= \Delta t \phi_y^{(ii)} \\ k_{2p} &= \Delta t \left(\frac{1}{2} \big| \mathbf{u}^{(ii)} \big|^2 - g y^{(ii)} \right) \end{aligned} \tag{3.25}$$

(iii) Obtain the characteristics of the free-surface at time $t^{(iii)} = t^{(m)} + \Delta t$

using the derivatives from sub-step (ii)

$$\begin{aligned} x^{(iii)} &= x^{(m)} + k_{2x} \\ y^{(iii)} &= y^{(m)} + k_{2y} \\ \phi^{(ii)} &= \phi^{(m)} + k_{2p} \end{aligned} \tag{3.26}$$

where superscript $^{(iii)}$ denotes the values at the third intermediate step of the RK4 scheme.

STEP (4) : time $t^{(iii)} = t^{(m)} + \Delta t$

(i) Repeat sub-step (i) of **STEP (1)** for the free-surface $S_{\mathbf{F}}^{(iii)} \equiv S_{\mathbf{F}}\big(t^{(iii)}\big)$ with velocity potential $\phi^{(iii)}$.

(ii) Evaluate the derivatives k_{3x}, k_{3y} and k_{3p}, where

$$\begin{aligned} k_{3x} &= \Delta t \phi_x^{(iii)} \\ k_{3y} &= \Delta t \phi_y^{(iii)} \\ k_{3p} &= \Delta t \left(\frac{1}{2} \left| \mathbf{u}^{(iii)} \right|^2 - g y^{(iii)} \right) \end{aligned} \tag{3.27}$$

(iii) Obtain the characteristics of the free-surface at time $t^{(m+1)} = t^{(m)} + \Delta t$

$$\begin{aligned} x^{(m+1)} &= x^{(m)} + \frac{1}{6}\big(k_{0x} + 2k_{1x} + 2k_{2x} + k_{3x}\big) \\ y^{(m+1)} &= y^{(m)} + \frac{1}{6}\big(k_{0y} + 2k_{1y} + 2k_{2y} + k_{3y}\big) \\ \phi^{(m+1)} &= \phi^{(m)} + \frac{1}{6}\big(k_{0p} + 2k_{1p} + 2k_{2p} + k_{3p}\big) \end{aligned} \tag{3.28}$$

This represents the final step of the RK4 scheme and all the free-surface characteristics are obtained at the end of the interval.

The solution is carried over in time by repeating **STEPS (1)** through **(4)** for each time interval. It is important to note that the BVP/BEM is solved at each of the four steps of the RK4 scheme.

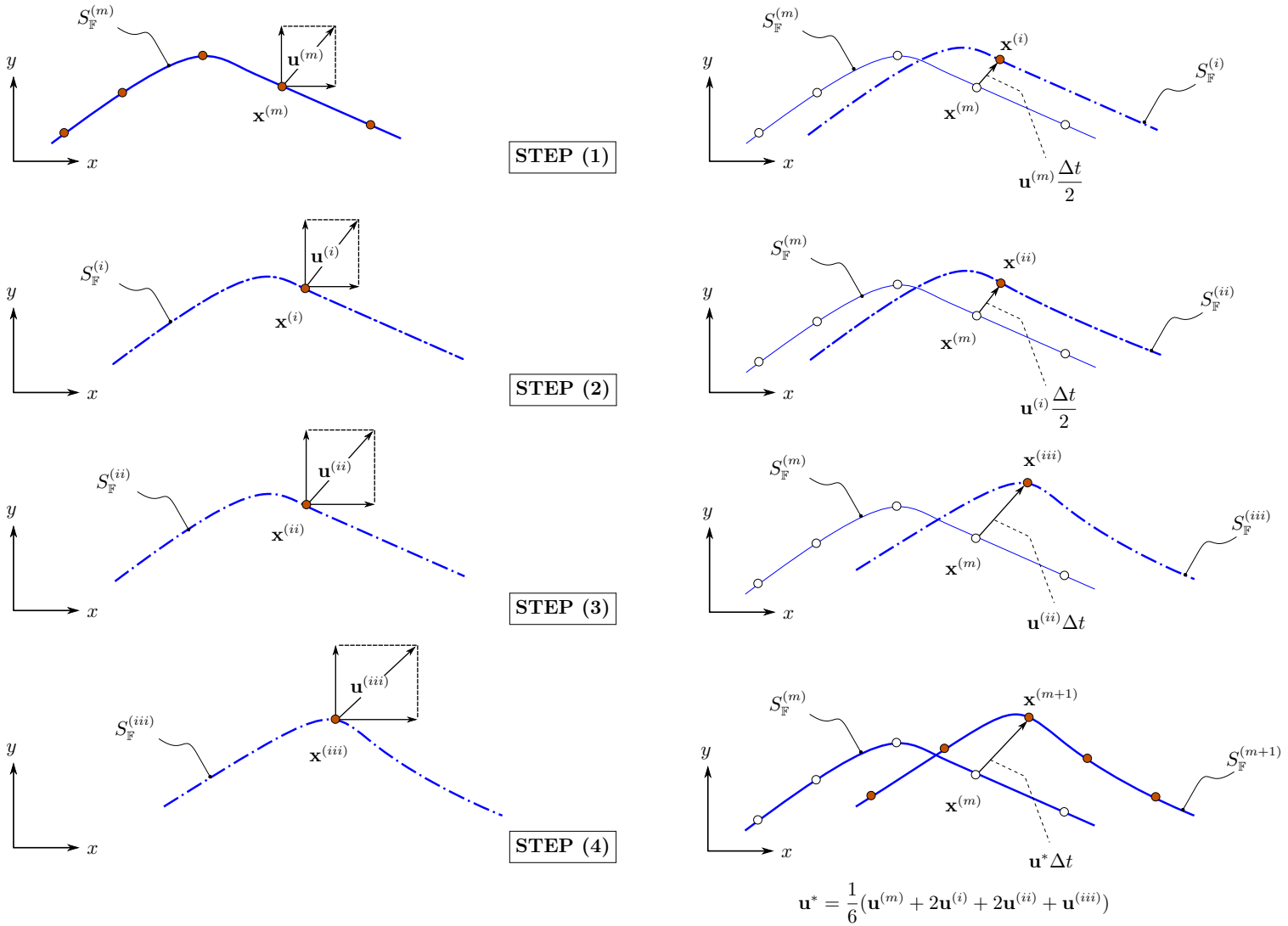

Figure 3.4: Fourth-order Runge-Kutta scheme for free-surface time-stepping

3.5.3 Stability of Time-integration

It is a formidable task to attempt a stability analysis of the fourth-order Runge-Kutta scheme applied to a fully nonlinear free-surface problem and is also beyond the scope of the current work. The current nonlinear scheme monitors the ratio

$$\max\left(\frac{|\nabla\phi|}{\Delta s}\right)\Delta t = \mathcal{C}_0 \tag{3.29}$$

during the course of the simulation for a fixed value of the time-step size Δt.

In Equation (3.29), $\nabla\phi$ and Δs are the velocity and panel length on the free-surface respectively. $\mathcal{C}_0$ is the Courant number typically < 1. It was found that a value of $\mathcal{C}_0$=0.25 was needed to obtain a stable solution.

3.5.4 Free-surface regridding

In the Mixed-Eulerian-Lagrangian method, the free-surface consists of a set of present Langrangian markers or particles. The motion of these markers is tracked as a part of the evolution of the free-surface based on the kinematic and dynamic free-surface boundary conditions. For nonlinear free-surface simulations, these particles have a tendency to accumulate in regions of high velocity gradient and this can lead to instabilities. One way to avoid the clustering of the particles is to redistribute them along the free-surface, based on a specified criteria of equal/graded arc-length or curvature, at regular intervals of time during the simulation. The redistribution or remeshing of the Lagrangian markers involves cubic-splines and is based on a parametric representation of the free-surface. The key to a good remeshing scheme is the choice of a proper parameter to represent the free-surface. The details of the remeshing scheme are presented in Appendix B.

3.5.5 Forces and Moments

The forces and moments are calculated by integrating the pressure over the body surface. For a body $S_{\mathbb{B}}$

$$\mathbf{F} = \int_{S_{\mathbb{B}}} P\mathbf{n}ds \tag{3.30}$$

$$\mathbf{M} = \int_{S_{\mathbb{B}}} P(\mathbf{r} \times \mathbf{n})ds \tag{3.31}$$

where $\mathbf{F}$ and $\mathbf{M}$ are vector quantities representing the forces and moments with respect to an inertial coordinate system $O(x, y, z)$ as shown in Figure 3.5.5. P is the pressure, $\mathbf{n} = (n_x, n_y, n_z)$ is the normal vector (positive into the body surface), $\mathbf{r} = (x, y, z)$ is the position vector representing a point on the body surface.

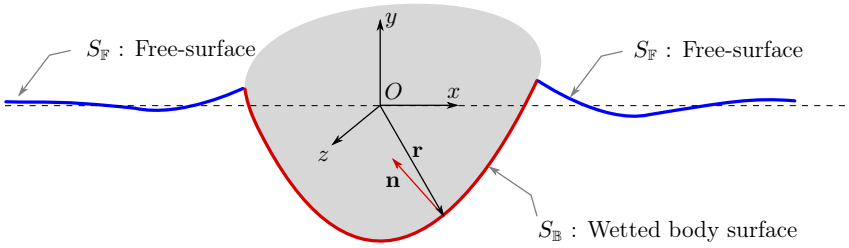

Figure 3.5: Body:Position vector and unit normal

For a 2D body, the forces and moments reduce to the following components

$$\begin{aligned}
&\text{Component of force } \mathbf{F} \text{ in the } x\text{-direction}, && F_x &&= \int_{S_{\mathbb{B}}} Pn_x ds \\
&\text{Component of force } \mathbf{F} \text{ in the } y\text{-direction}, && F_y &&= \int_{S_{\mathbb{B}}} Pn_y ds \\
&\text{Component of moment } \mathbf{M} \text{ about the } z\text{-axis}, && M_z &&= \int_{S_{\mathbb{B}}} P(xn_y - yn_x) ds
\end{aligned} \tag{3.32}$$

The pressure on the body surface is obtained from the Bernoulli's equation

$$\frac{P}{\rho} = -\frac{\partial \phi}{\partial t} - \frac{1}{2}|\nabla \phi|^2 - gy \tag{3.33}$$

The critical part of expression for the pressure is the estimation of the time derivative $\frac{\partial \phi}{\partial t}$. While calculating the pressure on the body it is also important to note that the body surface changes with time and also due to re-gridding. Taking these factors into consideration, we have

$$\frac{\delta \phi}{\delta t} = \frac{\partial \phi}{\partial t} + \mathbf{V}_g \cdot \nabla \phi \tag{3.34}$$

$\mathbf{V}_g$ is the local grid velocity of the body surface and represented as

$$\mathbf{V}_g = \left(\frac{\delta x}{\delta t}, \frac{\delta y}{\delta t} \right) \tag{3.35}$$

From (3.33) and (3.34), we have

$$\frac{P}{\rho} = -\frac{\delta \phi}{\delta t} + \mathbf{V}_g \cdot \nabla \phi - \frac{1}{2}|\nabla \phi|^2 - gy \tag{3.36}$$

The derivatives $\frac{\delta \phi}{\delta t}$, $\frac{\delta x}{\delta t}$ and $\frac{\delta y}{\delta t}$ are calculated as a part of the fourth-order Runge-Kutta scheme (see [Kim and Hong 2000])

$$\begin{aligned} \frac{\delta f(t_0 + \Delta t)}{\delta t} &= \frac{1}{4\Delta t}\left[-2f(t_0) - 4f^{(1)}\left(t_0 + \frac{\Delta t}{2} \right) \right. \\ &\quad \left. -4f^{(2)}\left(t_0 + \frac{\Delta t}{2} \right) + 10 f(t_0 + \Delta t) \right] - \frac{1}{2}\frac{\delta f(t_0)}{\delta t} \end{aligned} \tag{3.37}$$

where f can be either ϕ, x or y. The scheme utilizes the mid-step values of the fourth-order Runge-Kutta scheme with superscripts $^{(1)}$ and $^{(2)}$ indicating the first and second mid-steps respectively.

Chapter 4

Validation Studies

Up to this point, the basic mathematical and numerical concepts needed to solve a general free-surface IBVP have been presented. This chapter presents the application of these concepts to a set of problems specifically chosen to validate the numerical building blocks of the scheme.

4.1 Piston Wave-maker

This problem simulates the transient free-surface waves generated in a numerical wave-tank. A piston-type wave-maker, at one end of the wave-tank, is subject to a sinusoidal motion to generate waves starting from a state of rest.

4.1.1 Formulation

The fluid domain $\Omega(t)$ corresponding to a numerical wave tank with a piston wave-maker is as shown in Figure 4.1. $S_{\mathbb{W}}(t)$ represents the instantaneous position of the wave-maker and has a sinusoidal horizontal translation of the form

$$x_p(t) = -\frac{A}{2}\cos(\omega t) \tag{4.1}$$

where A is the amplitude or stroke of the piston wave-maker and ω is the circular frequency of the sinusoidal motion. $S_{\mathbb{F}}(t)$ is the instantaneous free-surface, $S_{\mathbb{B}}(t)$ is the impervious bottom surface and $S_{\mathbb{D}}$ is the downstream wall of the wave tank.

• **Governing Equation**

$$\nabla^2\phi(\mathbf{x},t) = 0, \quad \mathbf{x} \in \Omega(t) \tag{4.2}$$

with $\Gamma_d(t) = S_{\mathbb{F}}(t)$ and $\Gamma_n(t) = S_{\mathbb{W}}(t) \cup S_{\mathbb{B}}(t) \cup S_{\mathbb{D}}$.

• **Boundary Condition on Wave-maker** $S_{\mathbb{W}}(t)$

Along the piston surface, a kinematic boundary condition of the form

$$\nabla\phi \cdot \mathbf{n} = u_p(t), \quad \mathbf{x} \in S_{\mathbb{W}}(t) \tag{4.3}$$

is applied, where $\mathbf{n}$ is the unit surface normal pointing out of the fluid domain. From the sinusoidal motion of the piston as specified by Equation (4.3), we have

$$u_p(t) = \dot{x}_p(t) = \frac{A}{2}\,\omega \sin(\omega t) \tag{4.4}$$

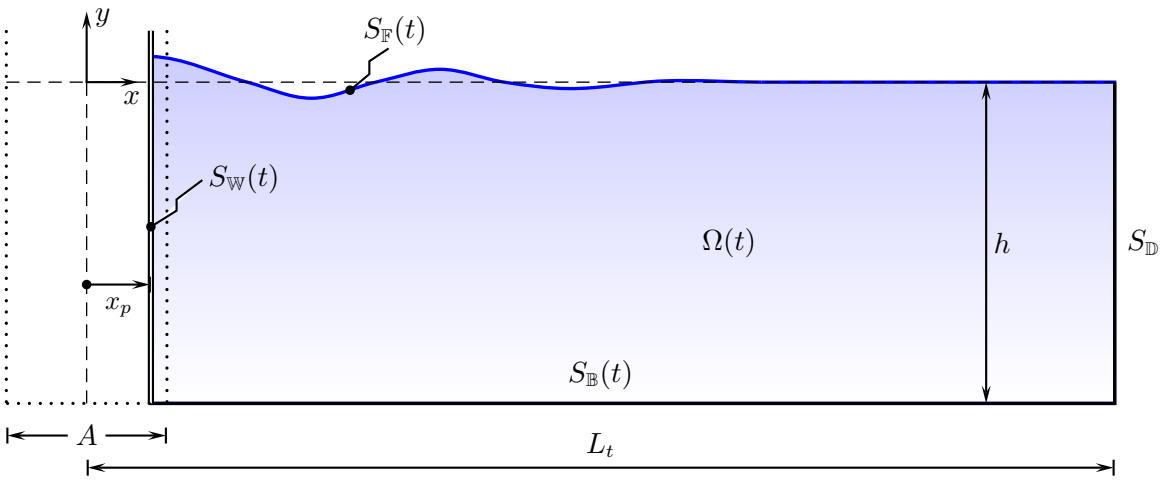

Figure 4.1: Piston Wavemaker : Fluid domain and corresponding boundaries, h: wave tank depth, A: Piston stroke, L_t: Mean length of wave-tank

• **Boundary Condition on** $S_{\mathbb{B}}(t), S_{\mathbb{D}}$

Both the bottom and downstream surfaces are assumed to be no-flux surfaces and the following kinematic boundary condition is applied

$$\nabla\phi \cdot \mathbf{n} = 0, \quad \mathbf{x} \in S_{\mathbb{B}}(t), S_{\mathbb{D}} \tag{4.5}$$

• **Initial Conditions**

At time $t = 0$, the relevant initial conditions are

$$\left.\begin{array}{rcl} \phi(\mathbf{x}, 0) & = & 0 \\ \eta(x, 0) & = & 0 \end{array}\right\} \mathbf{x} \in S_{\mathbb{F}}(t) \tag{4.6}$$

It can be observed from the sinusoidal motion, as specified by Equation (4.1), that the wave-maker is at a position of extreme displacement of $x_p(0) = -\frac{A}{2}$ at time $t = 0$. This arrangement is introduced to prevent an impulsive start to the simulation with non-zero velocities at the wave-maker.

4.1.2 Results

[Lin 1984] developed a numerical scheme based on the Cauchy-integral formulation, along with an MEL approach, to simulate this problem. The results from Lin's scheme were found to agree well with the experimental observations - see [Greenhow and Lin 1983] comparing the numerical and experimental free-surfaces generated as a result of an impulsive start of the wave-maker. The numerical results presented in [Lin 1984] are used as a basis for validating the current algorithm.

For the simulation, a wave tank of depth $h = 1.0$ is chosen with a mean length of $L_t = 10h$. The piston wave-maker placed at the left end of the tank has a stroke $A = 0.1h$ and oscillates with a period of $T = 4.0$ ($\omega = 0.5\pi$). These quantities, in non-dimensional form, are consistent with the parameters specified in [Lin 1984].

Figure 4.2 compares the transient wave elevations between [Lin 1984] and the BEM scheme at $t = 2T$ and $t = 4T$ (the intermediate steps are not presented for clarity, but shown separately in Figure 4.3). The simulations are performed with number of panels on the free-surface $N_{\mathbb{F}} = 200$ and time steps $\Delta t = 0.02T$ and $\Delta t = 0.01T$. The overall comparison between the two methods is good and a detailed analysis of the wave-maker is not undertaken as its sole purpose is to verify the accuracy of the BEM scheme.

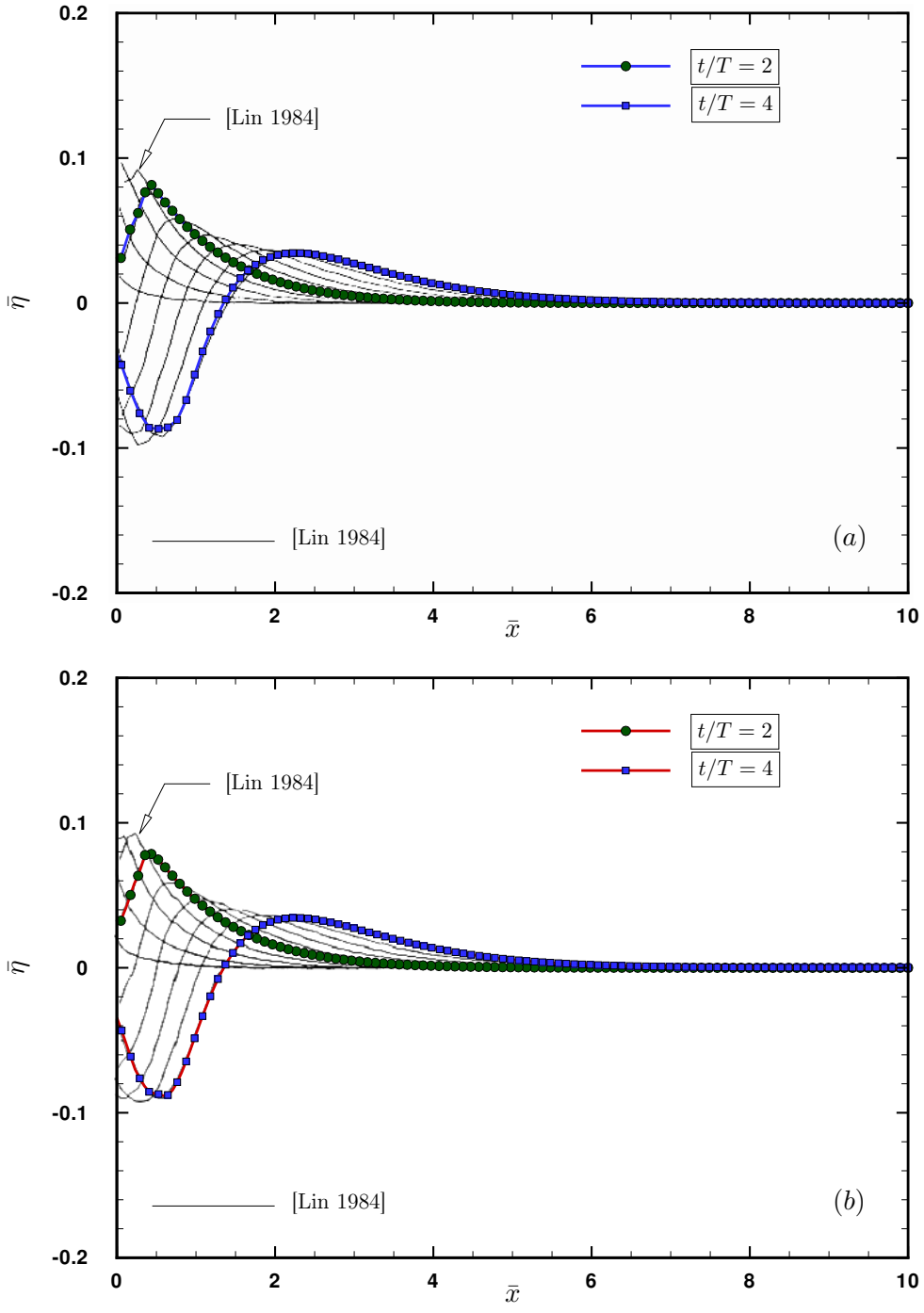

Figure 4.2: Piston wave-maker : Comparison of wave elevations between [Lin 1984] and BEM scheme (a) $\Delta t/T = 0.02$, (b) $\Delta t/T = 0.01$; $\bar{A} = 0.1$, $T = 4.0$, $N_{\mathbb{F}} = 200$; $\bar{\eta} = \eta/h$: wave elevation, $\bar{x} = x/h$

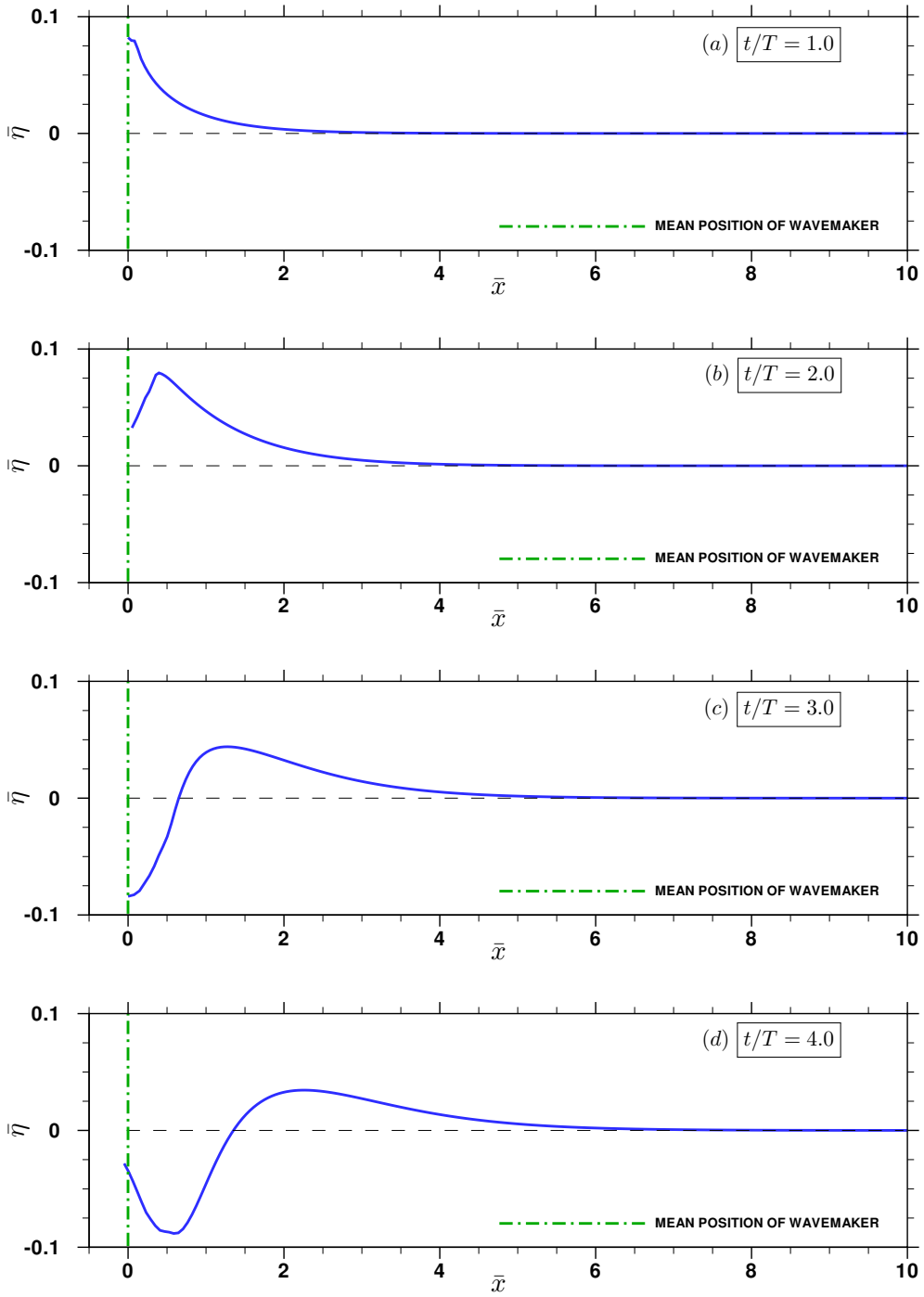

Figure 4.3: Piston wave-maker : Wave elevations at (a) $t/T = 1.0$,(b) $t/T = 2.0$,(c) $t/T = 3.0$,(d) $t/T = 4.0$, $\Delta t/T = 0.02$, $\bar{A} = 0.1$, $N_{\mathbb{F}} = 200$; $\bar{\eta} = \eta/h$: wave elevation, $\bar{x} = x/h$

4.2 Fifth-order Gravity Waves

The accuracy with which a scheme preserves the shape of a nonlinear wave of permanent form, propagating through a periodic domain, has often been used as a benchmark to validate a numerical algorithm (see [Grilli et al. 1989]).

The domain is initialized with a periodic nonlinear wave obtained from the fifth-order gravity wave theory of [Fenton 1985]. Appendix C provides a detailed derivation of the analytical expressions for the wave elevation and velocity potential over the entire physical domain. The numerical scheme is allowed to propagate the initial wave with inflow and outflow boundary conditions specified at the extents of the numerical domain. These boundary conditions are readily available from the analytical expressions for the velocity potential. At the end of a given period of simulation, a numerical scheme should essentially conserve all the properties of the nonlinear wave and preserve its shape. This can easily be verified with the analytical wave-form at the same instant of time.

4.2.1 Formulation

The fluid domain $\Omega(t)$ and its corresponding boundaries are as shown in Figure 4.4. $S_{\mathbb{F}}(t)$ represents the instantaneous position of the free-surface, $S_{\mathbb{U}}(t)$ and $S_{\mathbb{D}}(t)$ are the upstream and downstream periodic boundaries of the domain, and $S_{\mathbb{B}}(t)$ represents an impervious bottom surface.

• **Governing Equation**

$$\nabla^2\phi(\mathbf{x},t) = 0, \quad \mathbf{x} \in \Omega(t) \tag{4.7}$$

with $\Gamma_d(t) = S_{\mathbb{F}}(t)$ and $\Gamma_n(t) = S_{\mathbb{U}}(t) \cup S_{\mathbb{B}}(t) \cup S_{\mathbb{D}}(t)$.

• **Boundary Condition on $S_{\mathbb{U}}(t)$, $S_{\mathbb{D}}(t)$**

$S_{\mathbb{U}}(t)$ and $S_{\mathbb{D}}(t)$ represent the periodic inflow and outflow wave boundaries respec-

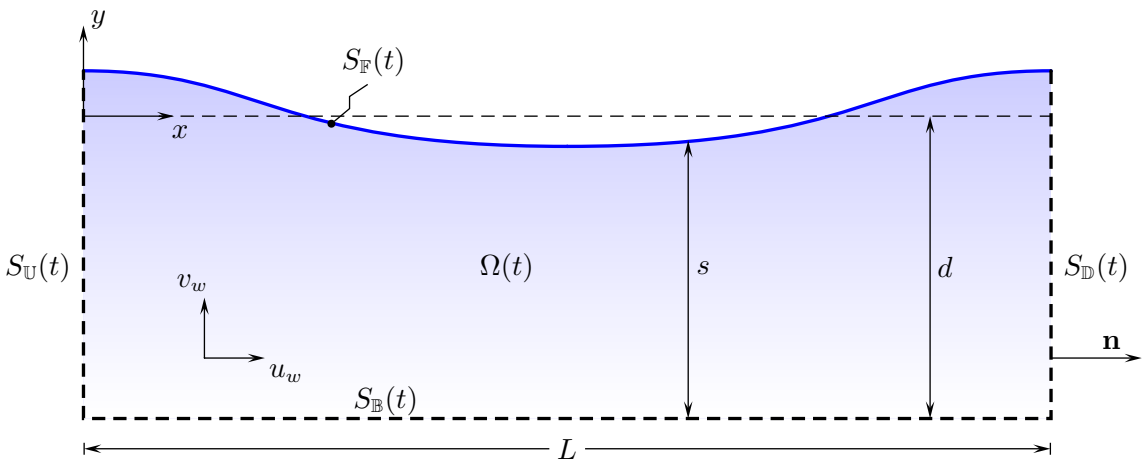

Figure 4.4: Fifth-order Stokes Wave : Fluid domain and corresponding boundaries, d: water depth, L: wavelength, y : wave elevation, $s = d + y$

tively. In the modeling of the propagation of the Stokes waves, kinematic boundary conditions of the form

$$\begin{aligned} S_{\mathbb{U}}(t): \quad \nabla\phi \cdot \mathbf{n} = \quad -u_w \\ S_{\mathbb{D}}(t): \quad \nabla\phi \cdot \mathbf{n} = \quad +u_w \end{aligned} \tag{4.8}$$

are imposed on these surfaces. Here $\mathbf{n}$ is the unit surface normal positive outward. u_w is the horizontal velocity component corresponding to a fifth-order Stokes wave and has the form

$$u_w = u_w^* \sum_{m=1}^{5} \epsilon^m \, m \, a_m \cosh(mks) \cos(m\theta) \tag{4.9}$$

where $s = d + y$ and $\theta = 2\pi\left(\dfrac{x}{L} - \dfrac{t}{T}\right)$ with T being the wave period and L the wavelength; $\epsilon = \dfrac{kH}{2}$ is the dimensionless expansion parameter with H being the wave height and $k = \dfrac{2\pi}{L}$ the wave-number; $a_1, a_2 \cdots a_m$ are coefficients that are functions of ϵ and $\dfrac{d}{L}$; u_w^* is the dimensional scaling velocity. This form is consistent with the fifth-order gravity wave theory of [Fenton 1985]. For brevity only the functional form

is presented here and a more detailed explanation of the terms in Equation (4.9) is presented in Appendix C.

• **Boundary Condition on $S_{\mathbb{B}}(t)$**

The bottom surface is assumed to be immovable and impervious and the corresponding boundary condition is

$$\nabla\phi \cdot \mathbf{n} = 0, \quad \mathbf{x} \in S_{\mathbb{B}}(t) \tag{4.10}$$

• **Initial Conditions**

At time $t = 0$, i.e., at the beginning of the simulation, the following conditions are applied on the free-surface

$$\left.\begin{array}{rcl} \phi(\mathbf{x}, 0) & = & \phi_w(\mathbf{x}, 0) \\ \eta(x, 0) & = & \eta_w(x, 0) \end{array}\right\} \mathbf{x} \in S_{\mathbb{F}}(t) \tag{4.11}$$

where ϕ_w and η_w are the velocity potential and wave elevation corresponding to a fifth-order Stokes wave. The functional forms of ϕ_w and η_w are described in detail in Appendix C.

4.2.2 Results

A wave with wave length $L = 65\ m$, wave height $H = 5.0\ m$, wave period $T = 6.38\ s$ and water depth $d = 20\ m$ $\left(\frac{d}{gT^2} = 0.05,\ \frac{H}{gT^2} = 0.0125,\ \frac{H}{L} = 0.0769\right)$ is chosen to simulate the propagation of periodic gravity waves. At the beginning of the simulation, the characteristics of the wave as obtained from analytical expressions of [Fenton 1985] are specified as initial conditions on the free-surface. The BEM scheme is then allowed to propagate the wave based on the boundary conditions specified on the upstream and downstream surfaces, $S_{\mathbb{U}}(t)$ and $S_{\mathbb{D}}(t)$ respectively.

A comparison between the analytical (η_w, [Fenton 1985]) and numerical (η_n) wave profiles is shown in Figure 4.5. The simulation is carried out for $N_{\mathbb{F}} = 240$ and $N_{\mathbb{T}} = 500$ linear BEM panels with a time step $\Delta t = 0.025T$. Here, $N_{\mathbb{F}}$ is the total

number of panels on the free-surface $S_{\mathbb{F}}(t)$, and $N_{\mathbb{T}}$ is the total number of panels over the entire BEM domain $S_{\mathbb{T}} \equiv S_{\mathbb{F}} \cup S_{\mathbb{D}} \cup S_{\mathbb{B}} \cup S_{\mathbb{U}}$. The scheme is allowed to propagate the waves for a total simulation time of $5.0T$, and Figure 4.5 compares the analytical and numerical wave profiles between $t = 4.0T$ and $t = 4.8T$ at steps of $0.2T$. It can be observed that the BEM scheme is able to preserve the form and characteristics of the initial wave profile over long periods of time.

Convergence Study

The spatial and temporal convergence characteristics of the scheme are studied by comparing the analytical and numerical drifts of a Lagrangian fluid particle $\mathbf{P}[x(t), y(t)]$, placed at the intersection of the free-surface $S_{\mathbb{F}}$ and the upstream boundary $S_{\mathbb{U}}$. To determine the analytical drift (particle trajectory), the system of equations

$$\frac{Dx}{Dt} = u_w(x, y, t) \; ; \; \frac{Dy}{Dt} = v_w(x, y, t) \tag{4.12}$$

is numerically integrated using a fourth-order Runge-Kutta scheme. Here, u_w and v_w respectively are the horizontal and vertical components of the wave velocity (based on analytical expressions, [Fenton 1985]).

The trajectory and time-history of the fluid particle $\mathbf{P}$ and its convergence towards the analytical values are shown in Figure 4.7 and Figure 4.6 respectively. These figures summarize the results of simulations performed over a duration of $5.0T$ for $N_{\mathbb{F}} = 30, 60, 120, 240$ ($N_{\mathbb{T}}$ = 75,150,300,500) and $\Delta t = 0.0125T$, $0.025T$. To quantify the convergence characteristics of the BEM scheme, the error between the analytical and numerical particle trajectories is compared at the end of the simulation, $t = 5.0T$, for different levels of discretization and time-steps. It is observed that (see Figure 4.8) for $\Delta t = 0.0125T$ and $\Delta t = 0.025T$, $|\epsilon_x(t)| \approx \mathcal{O}(\Delta\bar{x}^{1.1})$ and $|\epsilon_y(t)| \approx \mathcal{O}(\Delta\bar{x}^{1.25})$. Here, $\epsilon_x(t)$ and $\epsilon_y(t)$ are the errors between the analytical and numerical $\bar{x}(t) \equiv x(t)/L$ and $\bar{y}(t) \equiv y(t)/L$ respectively, $\Delta\bar{x} = \dfrac{1}{N_{\mathbb{F}}}$ is a measure of the panel length.

Conservation of Mass

It is important that the BEM scheme conserve mass and for free-surface simulations this property can be quantified by monitoring the area under the free-surface η_{area} (ideally $\eta_{area} = 0$). Figure 4.9 illustrates the time-history of $\bar{\eta}_{area} = \eta_{area}/L^2$ for different levels of discretization. The maximum error in $\bar{\eta}_{area}$ is observed to be $3 \times 10^{-2}\%$ and $6.5 \times 10^{-4}\%$ for $N_{\mathbb{F}} = 30$ and $N_{\mathbb{F}} = 240$ respectively.

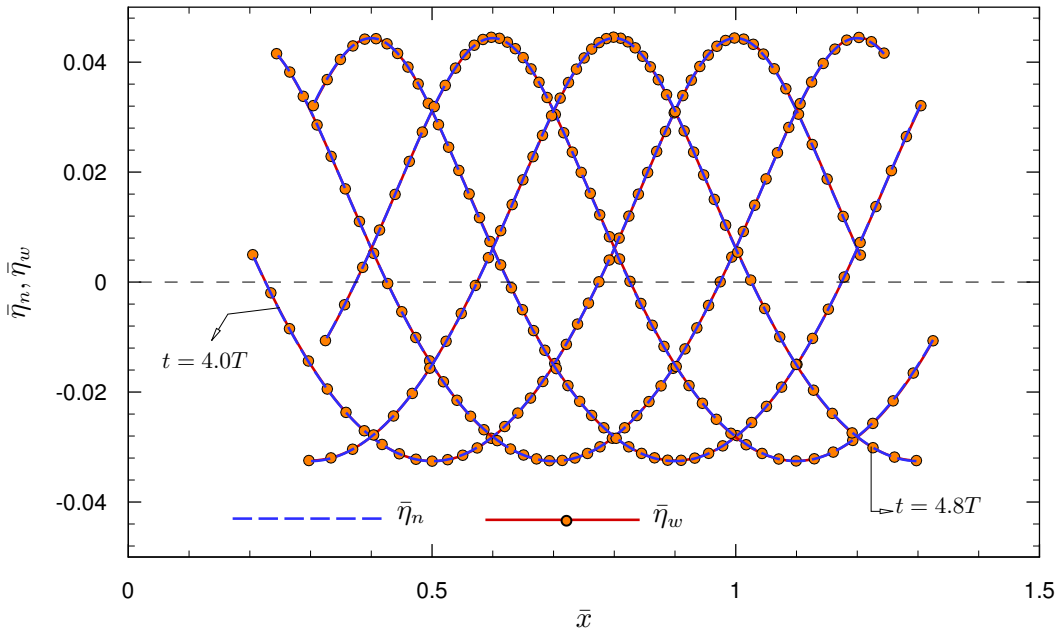

Figure 4.5: Comparison of numerical and analytical wave elevations between $t = 4.0T$ and $t = 4.8T$ at steps of $0.2T$; $\bar{x} = x/L$, $\bar{\eta}_w = \eta_w/L$, $\bar{\eta}_n = \eta_n/L$: η_n : numerical wave elevation, η_w : analytical wave elevation; BEM characteristics : Time step $\Delta t/T = 0.025$, Number of panels on the free-surface, $N_{\mathbb{F}} = 240$

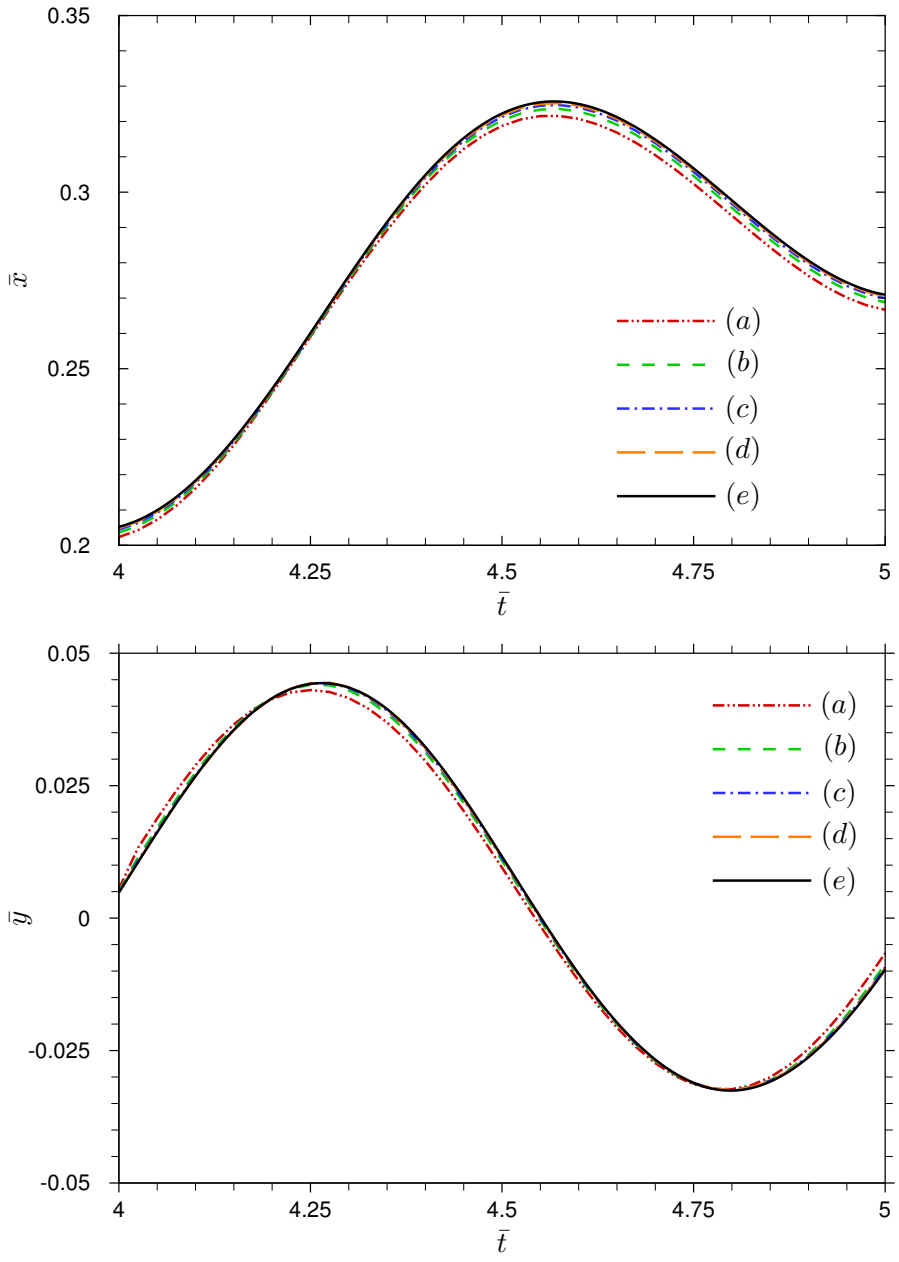

Figure 4.6: Time history : Convergence of the trajectory of a fluid particle $\mathbf{P}[x(t), y(t)]$ at the upstream boundary with increase in $N_{\mathbb{F}}$, number of panels on the free-surface: (a) $N_{\mathbb{F}} = 30$, (b) $N_{\mathbb{F}} = 60$, (c) $N_{\mathbb{F}} = 120$, (d) $N_{\mathbb{F}} = 240$, (e) Analytical trajectory; Time step $\Delta t/T = 0.025$; $\bar{x} = x/L$, $\bar{y} = y/L$, $\bar{t} = t/T$

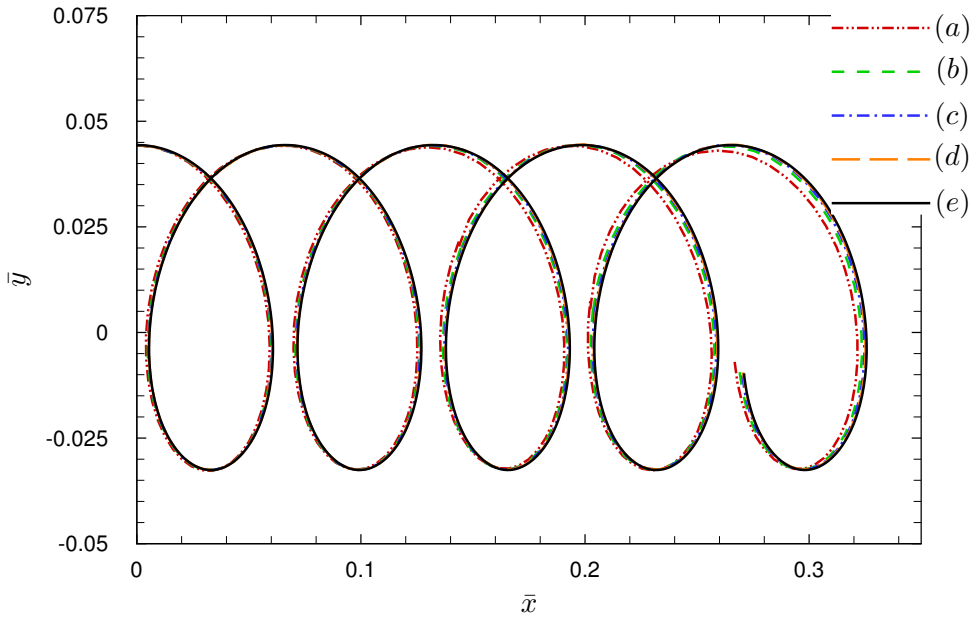

Figure 4.7: Convergence of the trajectory of a fluid particle $\mathbf{P}[x(t), y(t)]$ at the upstream boundary with increase in $N_{\mathbb{F}}$, Number of panels on the free-surface : (a) $N_{\mathbb{F}} = 30$, (b) $N_{\mathbb{F}} = 60$, (c) $N_{\mathbb{F}} = 120$, (d) $N_{\mathbb{F}} = 240$, (e) Analytical trajectory; Time step $\Delta t/T = 0.025$; $\bar{x} = x/L$, $\bar{y} = y/L$, $\bar{t} = t/T$

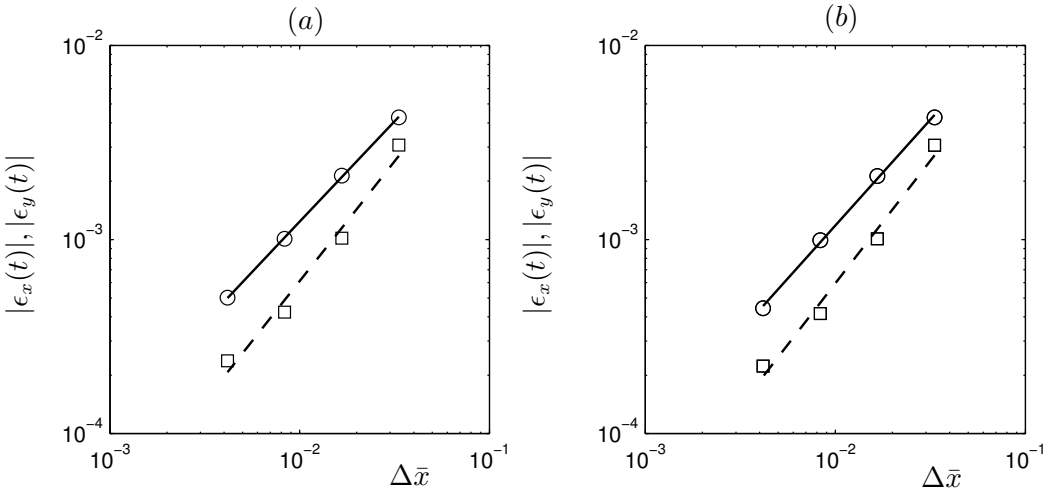

Figure 4.8: Convergence characteristics of the error between the analytical and numerical particle trajectories at time $t = 5.0T$ for (a) $\Delta t = 0.025T$, and (b) $\Delta t = 0.0125T$ $(- \circ -)$ $\epsilon_x(t)$: error in $x(t)$,(-□-) $\epsilon_y(t)$: error in $y(t)$,$\Delta\bar{x} = \frac{1}{N_{\mathbb{F}}}$ ($N_{\mathbb{F}}$ = 30,60,120,240)

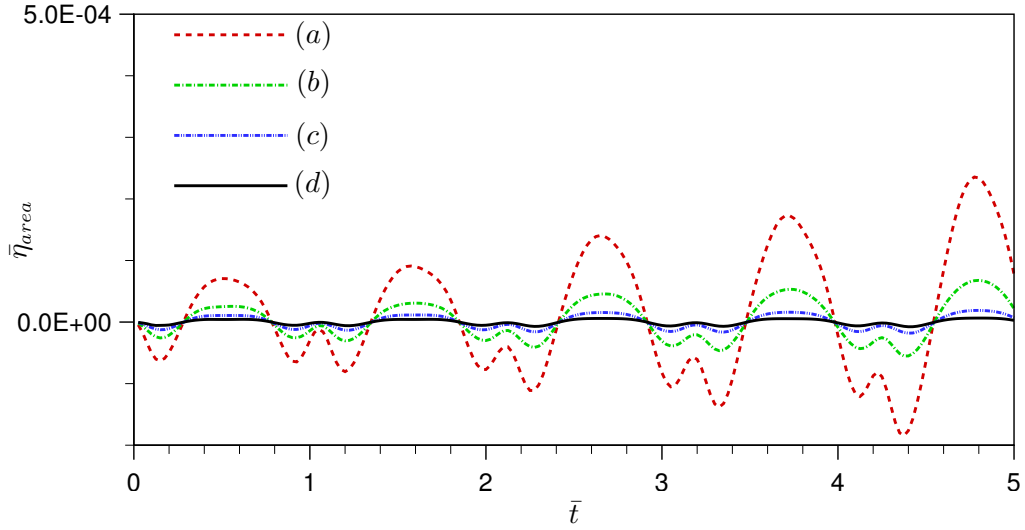

Figure 4.9: Variation of the area under the free-surface with time; Convergence with increase in $N_{\mathbb{F}}$, number of panels on the free-surface:(a) $N_{\mathbb{F}} = 30$, (b) $N_{\mathbb{F}} = 60$, (c) $N_{\mathbb{F}} = 120$, (d) $N_{\mathbb{F}} = 240$; $\bar{\eta}_{area} = \eta_{area}/L^2$: area under the free-surface; Time step $\Delta t/T = 0.025$

4.3 Water-entry of Wedge Sections

The water-entry of two-dimensional rigid bodies was pioneered by [Von Karman 1929] and [Wagner 1932], who introduced it in the context of the impact on seaplanes during landing. Since then the topic has been widely studied leading to several elegant mathematical solutions along with numerical and experimental investigations. A review of the research work on water-entry problems is given in [Korobkin and Pukhnachov 1988].

Most of the development in this field has been based on potential theory as the effects of viscosity are often negligible at the usual high speeds of entry. An assumption that has long dominated the mathematical development and numerical implementation is that of flow self-similarity. This assumption is valid as long as the water entry speed is constant and high enough to neglect the effects of gravity, and the body is of infinite extent. An explicit solution was given by [Mackie 1962] for the linearized water-entry problem. Later, [Dobrovol'skaya 1969] and [Hughes 1972; 1973] derived similarity solutions with fully nonlinear and exact boundary conditions. Unlike [Mackie 1962], the solutions of [Dobrovol'skaya 1969] were not expressed explicitly and had to be solved numerically. [Dobrovol'skaya 1966] presented a numerical method to solve the nonlinear singular integral equations based on which results were presented in [Dobrovol'skaya 1969] for deadrise angles larger than 30°. [Zhao and Faltinsen 1993] later obtained numerical results based on the solution of [Dobrovol'skaya 1969] for deadrise angles in the extended range of 4° - 81°.

The similarity solutions of [Dobrovol'skaya 1969, Zhao and Faltinsen 1993] express the whole range of nonlinearities of the free-surface interaction - the most critical of them being the analytical description of the thin jet flow. A common observation in any impact scenario is the formation of a very thin jet than runs up along the body surface. In a real fluid the thin jet eventually disappears as spray un-

der the influence of surface tension [Greenhow and Lin 1983, Imas 1998]. Since the formation of spray cannot be accounted for in a mathematical setting, the similarity solutions retain the entire extent of the jet, and solve for the contact angle between the jet and the wedge surface. The contact angle varies from 12.88° (deadrise angle 81°) to 0.04° (deadrise angle 4°). An aspect of the jet-flow revealed by the similarity solution is that the pressure in the jet is nearly atmospheric and its influence on the overall flow characteristics is negligible. The analytical contact angle and the negligible gage pressure inside the jet has been exploited by many numerical methods to develop a "*cut-off*" model.

The thin jet flow and the small contact angle often leads to numerical errors at the body free-surface intersection. [Zhao and Faltinsen 1993] in their nonlinear BEM scheme truncated the jet at the spray root, once a critical contact angle is reached, to obviate the numerical issues. In their scheme, a new panel is introduced at the spray root perpendicular to the body surface to close the BEM domain (this new panel or contact surface was explicitly taken into account in the BIE formulation). Subsequently many variations of the cut-off model have been introduced, see [Kihara 2004], [Battistin and Iafrati 2004] and [Sun and Faltinsen 2007] for water-entry of wedges. A similar approach was employed by [Tsai and Yue 1993] to truncate the jet formed along a horizontally moving surface-piercing plate.

The aim of this part of the thesis are the following:

(i) Apply the BEM scheme to the water-entry of symmetric wedges for different deadrise angles.

(ii) Compare the free-surface elevation and the pressure predicted on the wetted part of the wedge with the self-similar solutions of [Dobrovol'skaya 1969, Zhao and Faltinsen 1993]. This is done to validate the numerical aspects of the scheme, specifically the jet cut-off scheme described in Section 3.4 and the calculation of pressure on the wetted boundary (see section 3.5.5).

4.3.1 Initial Boundary Value Problem

The fluid domain $\Omega(t)$ along with its boundaries representing the water-entry of a wedge is shown in Figure 4.10. Also shown in Figure 4.10 are the parameters defining the geometry of the wedge section, where α_w is the included wedge angle and β is the deadrise angle. β and α_w are related by the relation $\beta = (\pi - \alpha_w)/2$.

$S_{\mathbb{WB}}(t)$ represents the instantaneous *wetted* boundary of the wedge, moving vertically downward with a velocity V_w. S_∞ is the far-field boundary or more appropriately a truncated numerical boundary placed far enough so as not to reflect any free-surface disturbances reaching it.

• **Governing Equation**

$$\nabla^2\phi(\mathbf{x}, t) = 0, \quad \mathbf{x} \in \Omega(t) \tag{4.13}$$

with $\Gamma_d(t) = S_{\mathbb{F}}(t)$ and $\Gamma_n(t) = S_{\mathbb{WB}}(t) \cup S_\infty(t)$.

• **Boundary Condition on** $S_{\mathbb{WB}}(t)$

Along the wetted boundary of the wedge, a kinematic boundary condition of the form

$$\nabla\phi \cdot \mathbf{n} = \mathbf{V} \cdot \mathbf{n}, \quad \mathbf{x}, \mathbf{n} \in S_{\mathbb{WB}}(t) \tag{4.14}$$

is applied, where $\mathbf{n}$ is the unit surface normal pointing out of the fluid domain. For the vertical entry case $\mathbf{V} = (0, -V_w)$

• **Boundary Condition on** S_∞

The truncated boundary is treated as a wall leading to the kinematic boundary condition

$$\nabla\phi \cdot \mathbf{n} = 0, \quad \mathbf{x}, \mathbf{n} \in S_\infty \tag{4.15}$$

• Initial Conditions

In the previous two problems that did not involve a surface-piercing body, initial conditions were only needed for the free-surface. For this case, in addition to the initial conditions on the free-surface, the initial geometry of the body is also needed.

For the body surface, a fraction of the wedge is assumed to be immersed initially, as shown in Figure 4.10. The apex of the wedge **A** is at a distance δ_i below the undisturbed free-surface level. Note that since the velocity of entry (V_w) is known a priori, the initial immersion δ_i can also be expressed in terms of a time parameter, $t_0 = \delta_i / V_w$.

For the free-surface, its position and the corresponding velocity potential are assumed to be known at $t = 0$. Two types of initial conditions can be specified (see Figure 4.10)

$$\text{(i)} \quad \phi = 0, \eta(x, 0) = 0 \tag{4.16}$$

$$\text{(ii)} \quad \phi = \phi_0(x, \eta_0), \eta(x, 0) = \eta_0 \tag{4.17}$$

where ϕ_0 and η_0 are obtained from the linearized water-entry theory of [Mackie 1962; 1969] for small included angles. An initial free-surface shape obtained from the modified Wagner-theory of [Mei et al. 1999] is used as an initial shape for large included angles.

4.3.2 Results

All the results presented in this section pertain to the symmetric water-entry of wedge sections. The main parameters that are used in the numerical simulation are shown in Figures 4.10 and 4.11. Note that even though a symmetric case is considered, no assumptions of symmetry are made in the numerical or mathematical formulation. The scheme can easily be applied to an asymmetric case.

As shown in Figure 4.11, $N_{\mathbb{F}}$ represents the total number of elements on the free-surface $S_{\mathbb{F}}(t)$ (including both sides of the free-surface), $N_{\mathbb{WB}}$ the total number

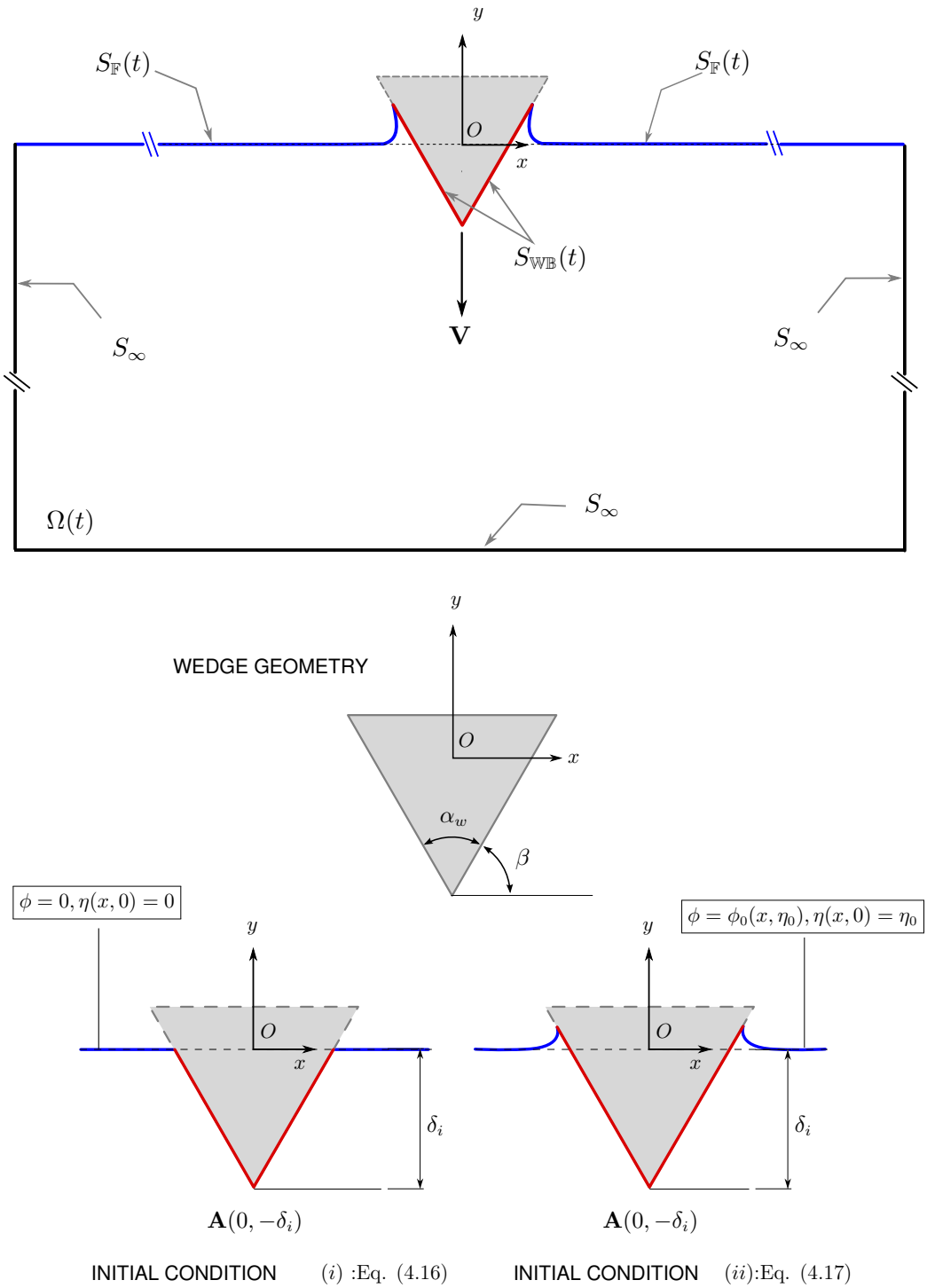

Figure 4.10: Water-entry of wedge sections : Fluid domain and corresponding boundaries, parameters defining the geometry of the wedge and initial conditions

of elements on the combined wetted wedge surface, and N_∞ the total number of elements on the far-field boundary. In a theoretical framework, a self-similar flow (in the absence of gravity) has no physical length scale. However, to terminate the numerical solution, an arbitrary characteristic length (c_w) is chosen representing the wetted length along the wedge. c_w is chosen to be $6''$=0.1524 m. t_e is the time at which the wetted length of the wedge equals c_w. s represents the arc-length along the wetted boundary of the wedge with s=0 at the apex and s=$s_w(t)$ at the body free-surface intersection. At time t=t_e, $s_w(t)$=c_w.

Effect of time-step and number of panels

A representative case showing the effect of the time-step Δt on the free-surface elevation is shown in Figure 4.12, for a wedge with an inclined angle α_w=18°. The free-surface elevation converges quite well with a change in size of the time-step and no discernible difference is seen between Δt=1e-5 s and Δt=5e-6 s (as seen in the close-up of jet region - Region AA). The largest value of Δt=1e-4 s is chosen to keep the Courant number $\mathcal{C}_0$ below 0.25. Figure 4.13 and 4.14 respectively show the effect of the time-step and the number of panels $N_{\mathbb{WB}}$ on the pressure predicted by the scheme on the wetted part of the boundary. In both the cases the results converge well. For all these $N_{\mathbb{F}}$ is chosen to 125, a value found to be sufficient through a convergence study.

Similarity Solution

Figure 4.15 shows the free-surface elevation predicted by the scheme at different stages of entry in the absence of gravity (g=0). The initial condition with a part of the wedge immersed initially corresponds to the time t=0.0 s. As we have neglected gravity, the numerical solution should conserve the important aspect of self-similarity of the flow. Figure 4.16 illustrates this aspect, expressing the free-surface elevations in terms of the similarity variables $x/(V_w t)$ and $y/(V_w t)$. The scheme is able to

attain a state of self-similarity very quickly and sustain it over the entire course of the simulation (the free-surface elevations beyond t=0.02s all overlap). Figure 4.17 shows the free-surface elevation at different stages of entry for α_w=60° and α_w=90°. For both the cases, the scheme is able to accurately track the fast moving jet formed along the wetted part of the wedge.

Figure 4.18 shows the pressure distribution along the wetted boundary of the wedge at different stages of entry (pressures are shown only on one side of the wetted boundary). The pressure coefficient C_p is defined as

$$C_p = \frac{P - P_{atm}}{0.5\rho V_w^2} \tag{4.18}$$

where P is the pressure on the body surface, P_{atm} the atmospheric pressure and ρ the density.

A comparison with the self-similar solution of [Dobrovol'skaya 1969] is shown in Figure 4.19 and 4.20. Note that the pressure on the wetted side is expressed as a function of the similarity variable $y/(V_w t)$. In all the cases, the agreement between the self-similar solution of [Dobrovol'skaya 1969] and the predicted pressures is excellent. The scheme also predicts equally well the fact that the pressure inside the jet region is almost atmospheric or $C_p = 0$.

Effect of Froude Number

The results presented upto this point neglect the effects of gravity, which is consistent with a self-similar assumption. One of the aims of this research work is to address the effects of the Froude number on the free-surface characteristics. To this end, a Froude number is defined as

$$F_{nc} = \frac{V_w}{\sqrt{gc}} \tag{4.19}$$

where V_w is the velocity of entry, g is the acceleration due to gravity and c is the chord-length of the wedge.

Note

The dynamic free-surface boundary condition is written as

$$\phi_t + \frac{1}{2}|\nabla\phi|^2 + gy = 0 \tag{4.20}$$

or in the non-dimensionalized form

$$\phi_t^* + \frac{1}{2}|\nabla^*\phi^*|^2 + \frac{y*}{F_{nc}^2} = 0 \tag{4.21}$$

based on a velocity scale V_w and length scale c. The superscript * indicates the non-dimensional values. As F_{nc} increasess, the effect of the hydrostatic component becomes negligible.

From Equation 4.19, it can easily be seen that g=0 would correspond to an infinite Froude number (F_{nc}=∞). Figure 4.21 shows the effect of the Froude number on the free-surface elevation predicted by the scheme. The free-surface elevation is seen to converge towards the self-similar solution with an increase in the Froude number. It can be observed from the results that the F_{nc}=3.0 case is practically equivalent to the self-similar solution. This is consistent with the results presented in [Yim 1971] in the case of a symmetric entry of a wedge with linearized boundary conditions.

A similar conclusion can be drawn from Figures 4.22 through 4.24, which show the effect of the Froude numbers on the predicted pressures. The pressure on the wedge surface is written as

$$\frac{P - P_{atm}}{\rho} = -\phi_t - \frac{1}{2}|\nabla\phi|^2 - gy \tag{4.22}$$

or in terms of the pressure coefficient as

$$C_p = \frac{P - P_{atm}}{\frac{1}{2}\rho V_w^2} = C_{p,d} + C_{p,s} \tag{4.23}$$

where,

$$C_{p,d} = \frac{\left(-\phi_t - \frac{1}{2}|\nabla\phi|^2\right)}{\frac{1}{2}V_w^2} \tag{4.24}$$

and

$$C_{p,s} = \frac{-gy}{\frac{1}{2}V_w^2} \tag{4.25}$$

$C_{p,s}$ and $C_{p,d}$ denote the hydrostatic and hydrodynamic components respectively.

Note

The hydrostatic component of the pressure is expressed as

$$C_{p,s} = \frac{-gy}{\frac{1}{2}V_w^2} \tag{4.26}$$

With the Froude number defined as $V_w/\sqrt{gc}$, we have

$$C_{p,s} = \frac{-y}{\frac{1}{2}cF_{nc}^2} \tag{4.27}$$

as $F_{nc} \to \infty$ $C_{p,s} \to 0$

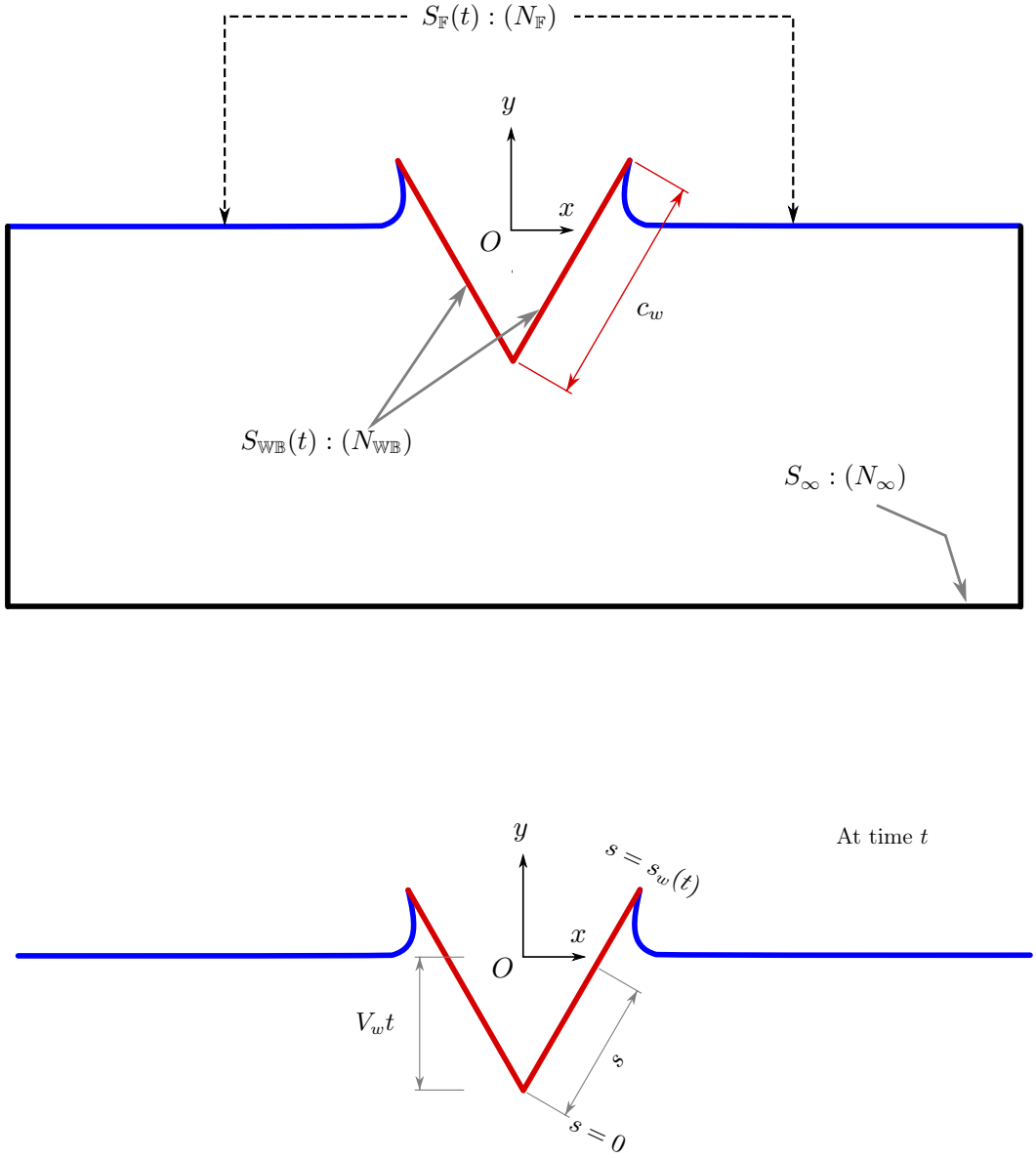

Figure 4.11: Number of elements on the discretized boundary, $N_{\mathbb{F}}$ = total number of elements on the free-surface $S_{\mathbb{F}}(t)$ combined, $N_{\mathbb{WB}}$ = total number of elements on the combined wetted wedge surface, N_∞ = total number of elements on the far-field boundary;c_w is the wetted characteristic length; s is the arc-length along the wetted boundary $0 \leq s \leq s_w(t)$; $s_w(t)$ is the maximum wetted length of the wedge at a particular instant of time t

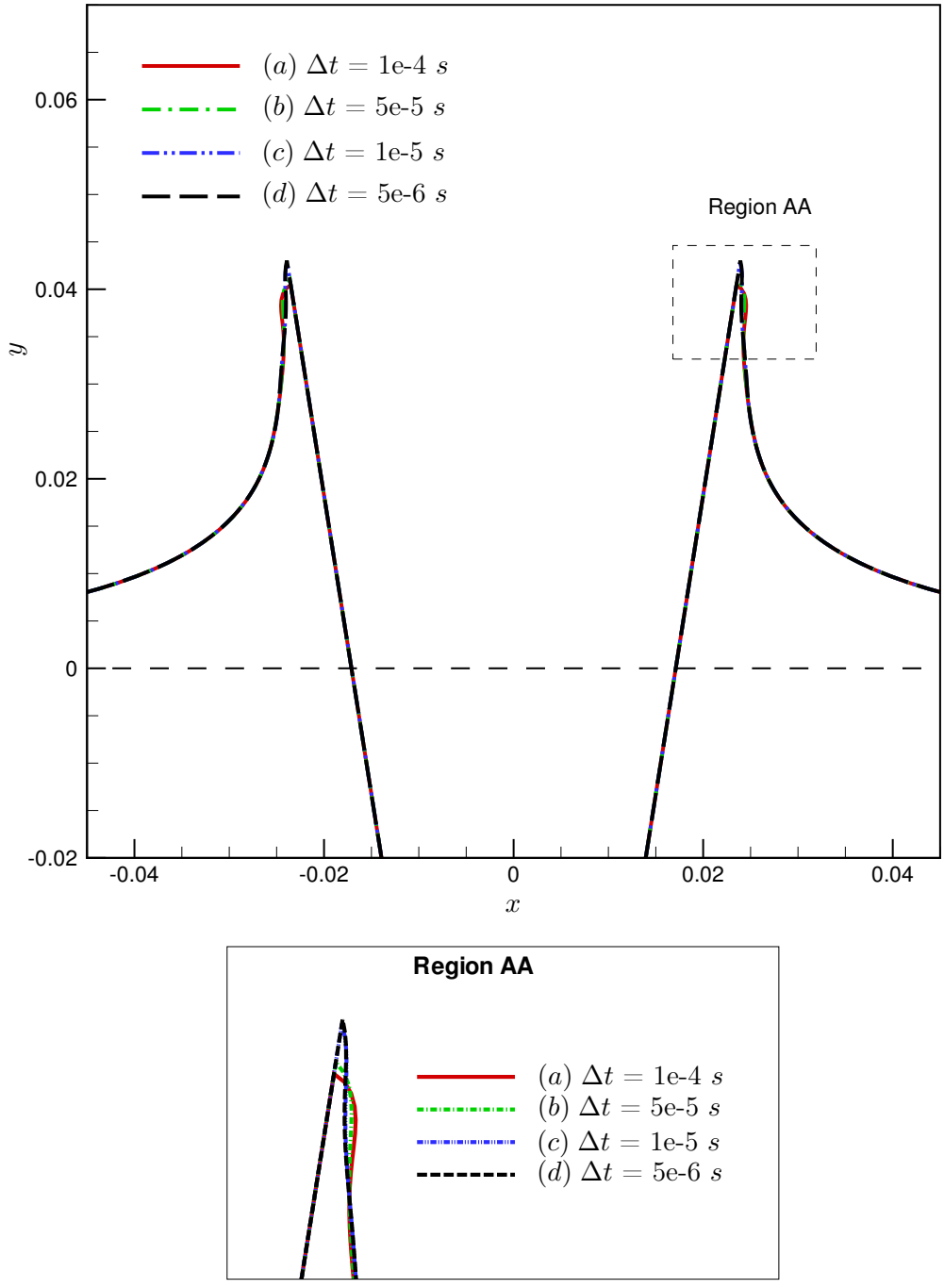

Figure 4.12: Wedge water-entry ($\alpha_w = 18°$) : Representative case showing the effect of the time-step on the free-surface elevation predicted by the scheme. t_e =0.103075 s, (a) $\Delta t/t_e$ = 9.6e-4, (b) $\Delta t/t_e$ = 4.8e-4, (c) $\Delta t/t_e$ = 9.6e-5, (d) $\Delta t/t_e$ = 4.8e-5

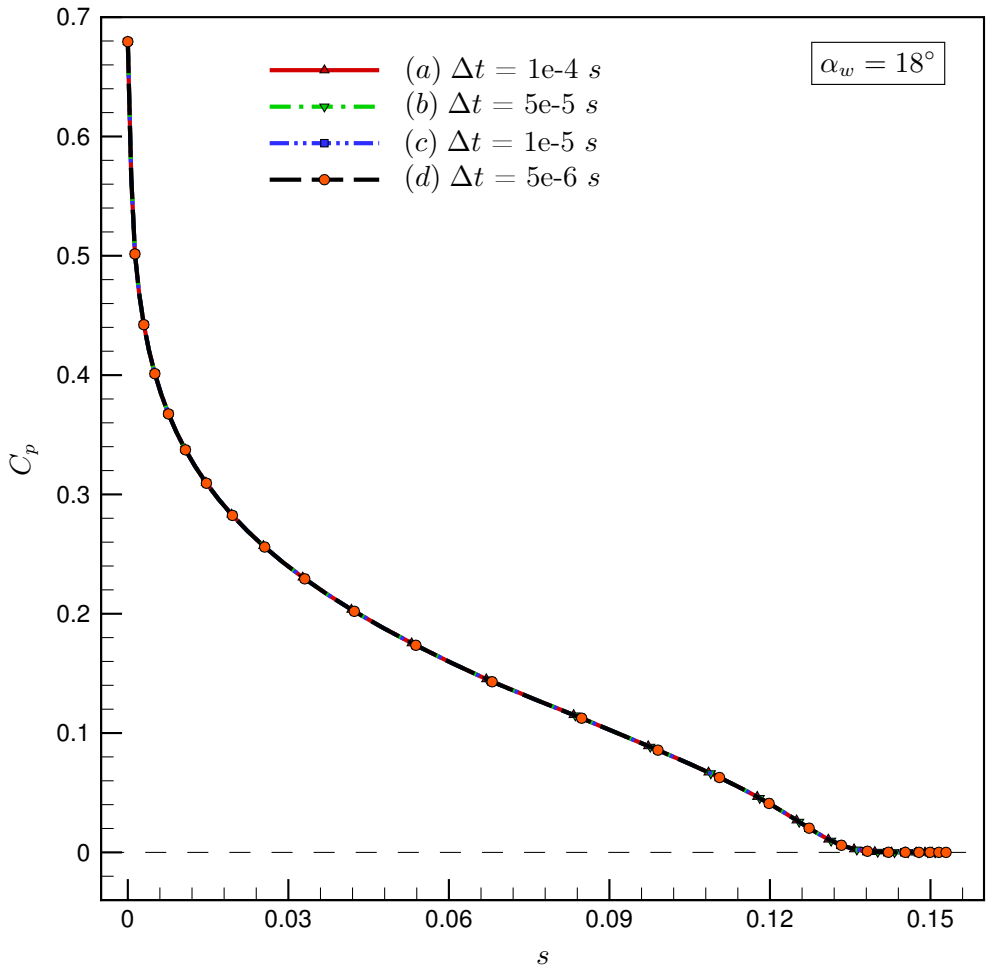

Figure 4.13: Wedge water-entry ($\alpha_w = 18°$) : Representative case showing the effect of the time-step on the pressures predicted by the scheme on the wetted part of the body surface. t_e =0.103075 s, (a) $\Delta t/t_e$ = 9.6e-4, (b) $\Delta t/t_e$ = 4.8e-4, (c) $\Delta t/t_e$ = 9.6e-5, (d) $\Delta t/t_e$ = 4.8e-5. C_p is the pressure coefficient and s is the arc-length along the body surface. (Note : pressures shown only on one side of the wetted boundary)

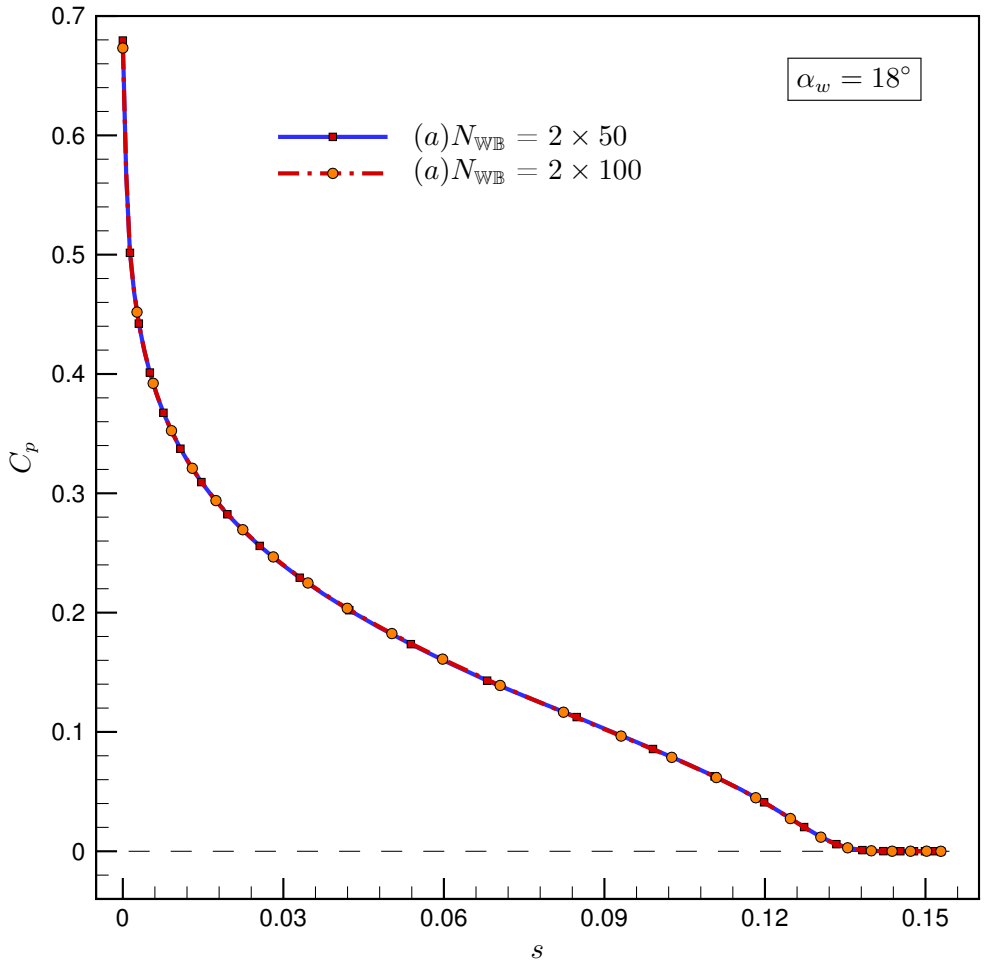

Figure 4.14: Wedge water-entry ($\alpha_w = 18°$) : Representative case showing the effect of the number of panels on the pressures predicted by the scheme on the wetted part of the body surface. (a) $N_{\mathbb{WB}} = 2{\times}50$ panels, (b) $N_{\mathbb{WB}} = 2{\times}100$ panels; $N_{\mathbb{WB}}$ is the total number of panels on the wetted body surface, see Figure 4.11

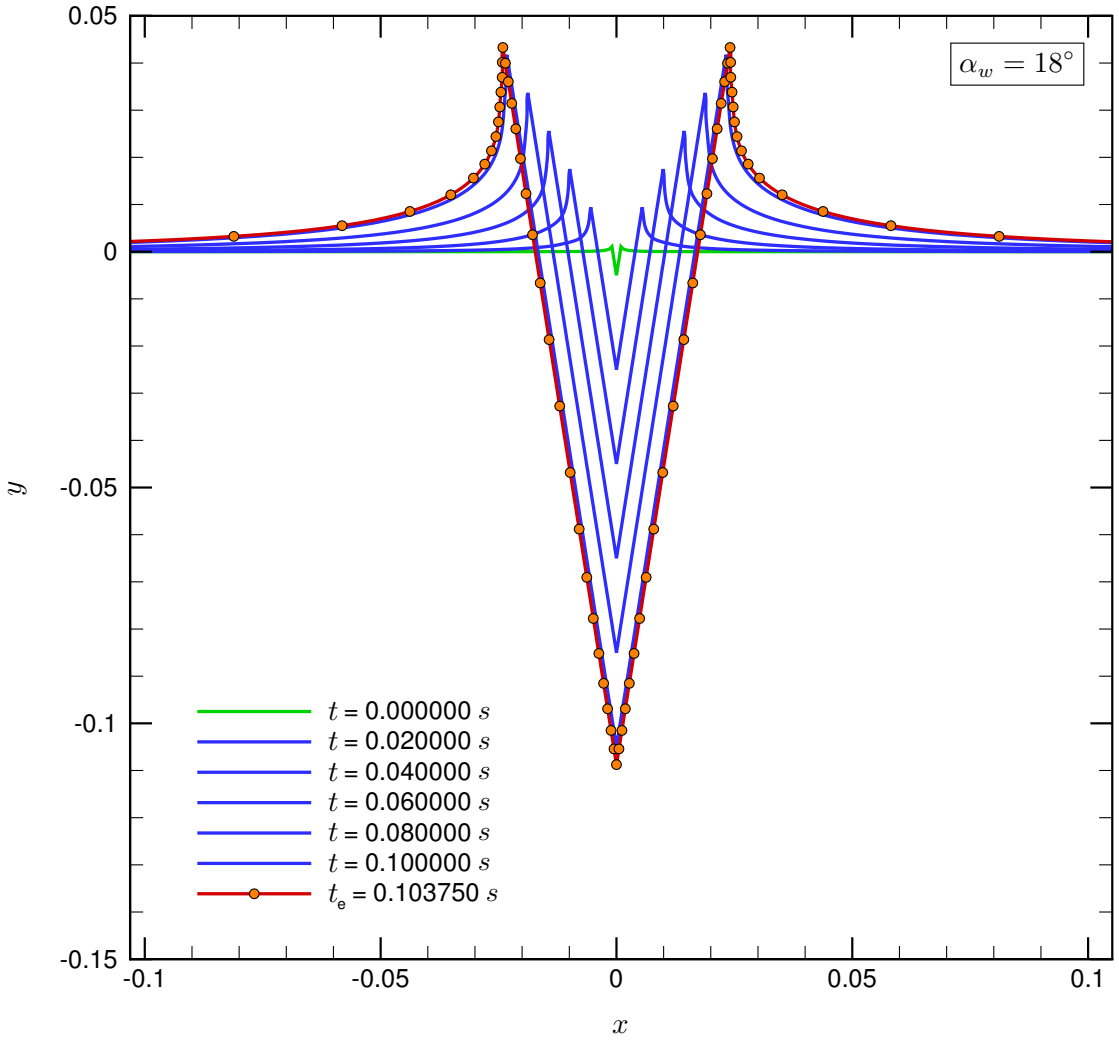

Figure 4.15: Wedge water-entry ($\alpha_w = 18°$) : free-surface elevation at different stages of entry. Parameters of simulation : $g = 0$ (no gravity), $c_w = 0.1524$ m, Δt = 5e-6 s, $\Delta t/t_e$ = 4.8e-6s, $N_{\mathbb{F}} = 200$, $N_{\mathbb{WB}} = 100$, $N_\infty = 40$

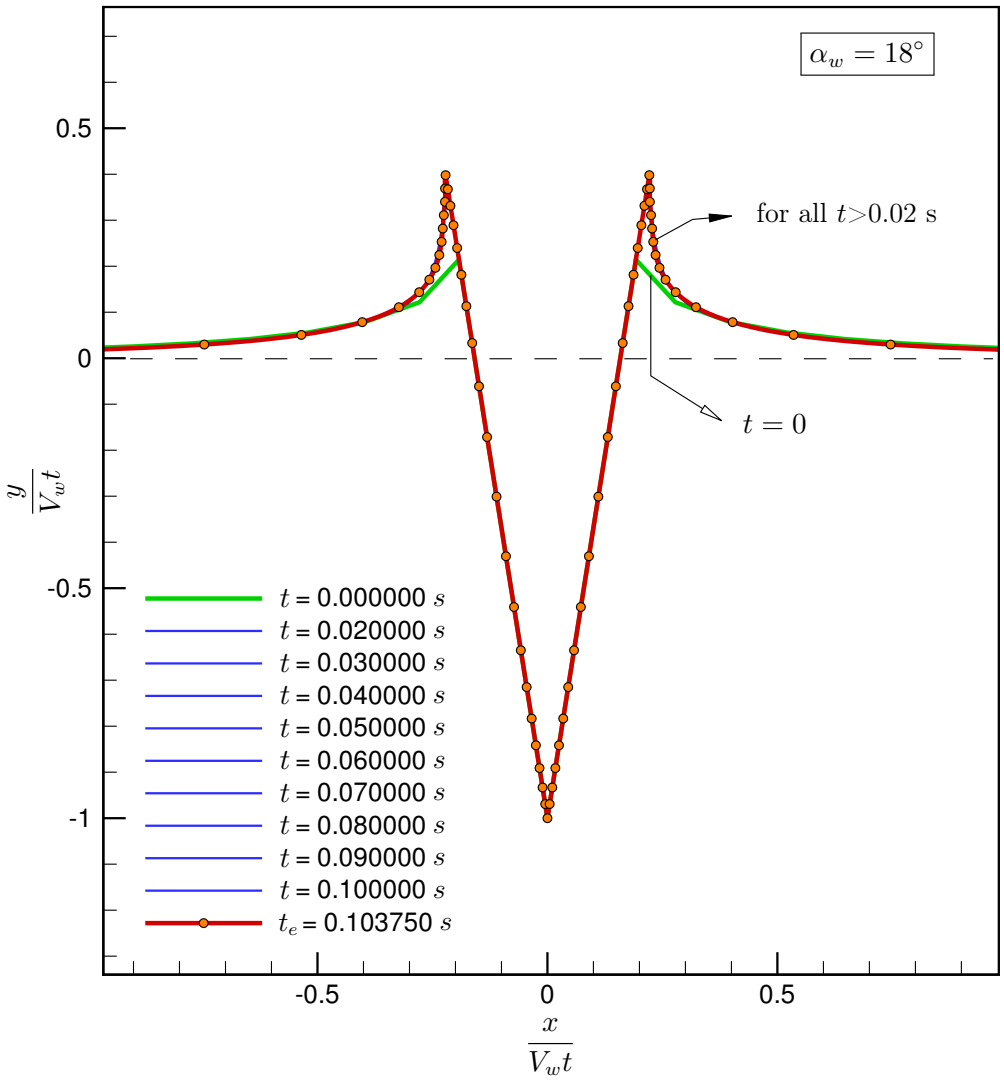

Figure 4.16: Wedge water-entry ($\alpha_w = 18°$) : free-surface elevation at different stages of entry expressed in terms of similarity variables ($x/(V_w t)$,$y/(V_w t)$). Parameters of simulation : $g = 0$ (no gravity), $c_w = 0.1524$ m, Δt = 5e-6 s, $\Delta t/t_e$ = 4.8e-6s, $N_{\mathbb{F}} = 250$, $N_{\mathbb{WB}} = 100$, $N_\infty = 40$

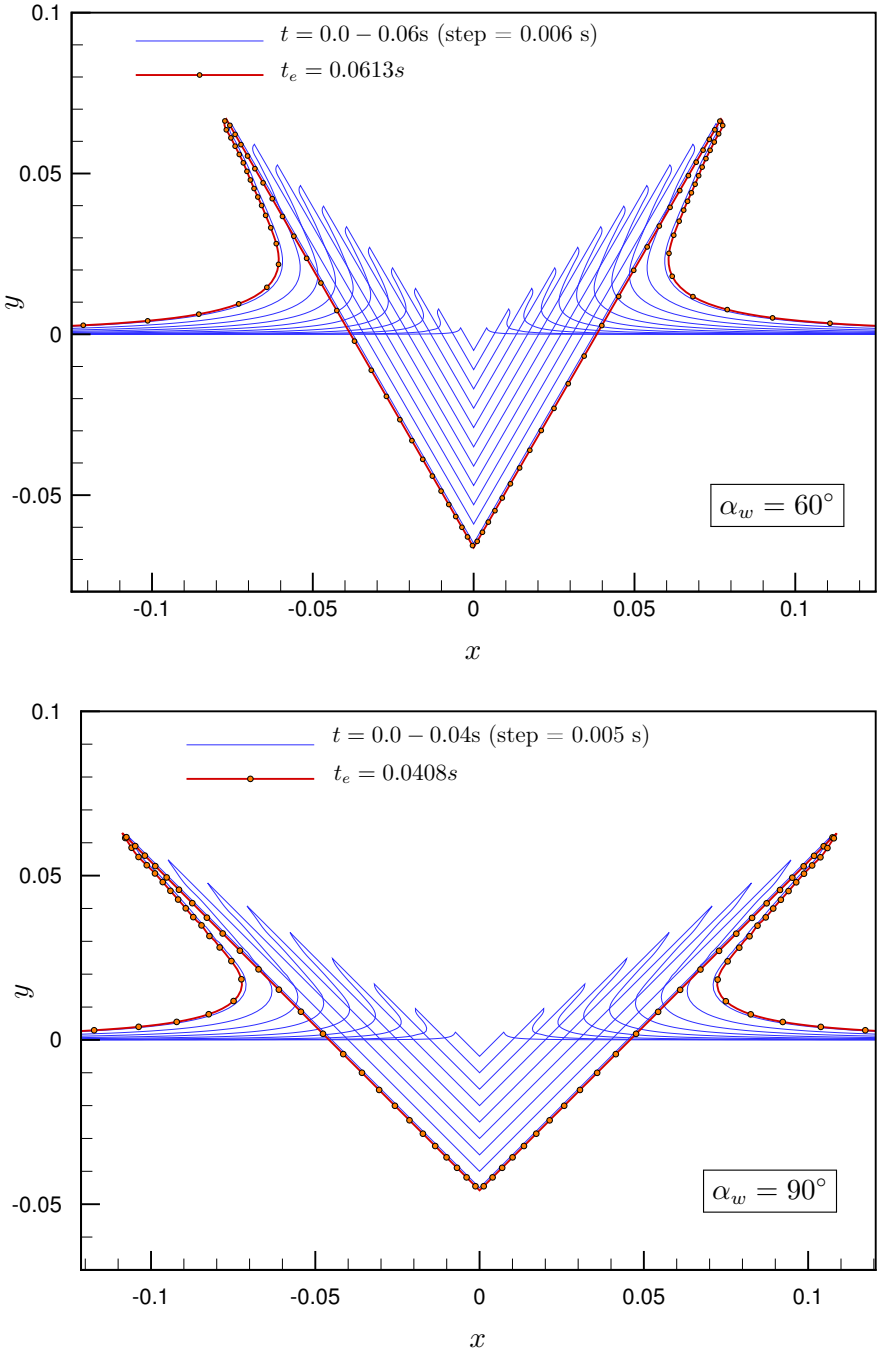

Figure 4.17: Wedge water-entry ($\alpha_w = 60°$ and $\alpha_w = 90°$) : free-surface elevation at different stages of entry. Parameters of simulation : $g = 0$ (no gravity), $c_w = 0.1524$ m, $\Delta t =$ 5e-6 s

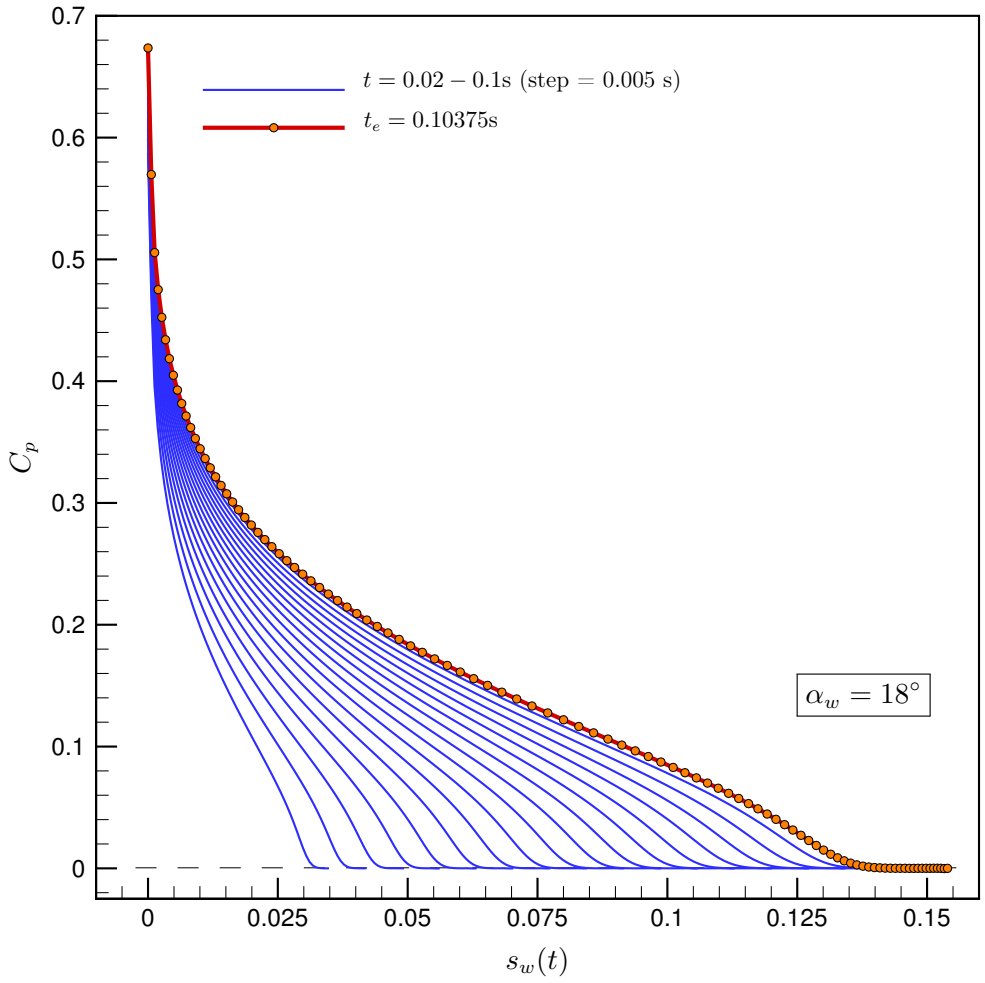

Figure 4.18: Wedge water-entry ($\alpha_w = 18°$) : Pressure distribution along wetted boundary of the wedge at different stages of entry (pressures shown only on one side of the wetted boundary).$s_w(t)$ is the instantaneous wetted length of the wedge (see Figure 4.11). C_p is the pressure coefficient

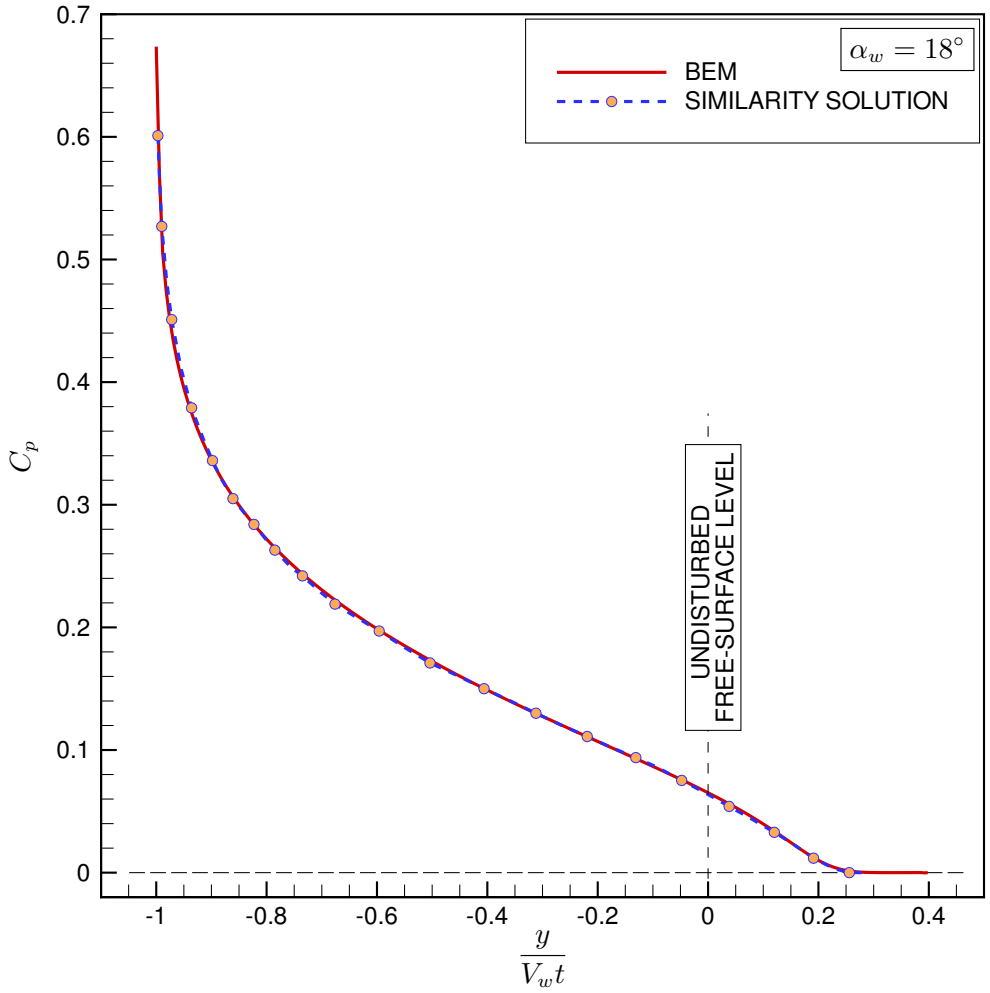

Figure 4.19: Wedge water-entry ($\alpha_w = 18°$) : Comparison of pressure predicted along the wetted part of the wedge with similarity solution of [Dobrovol'skaya 1969] expressed in terms of the similarity variable $y/(V_w t)$. C_p is the pressure coefficient (Note : pressures shown only on one side of the wetted boundary)

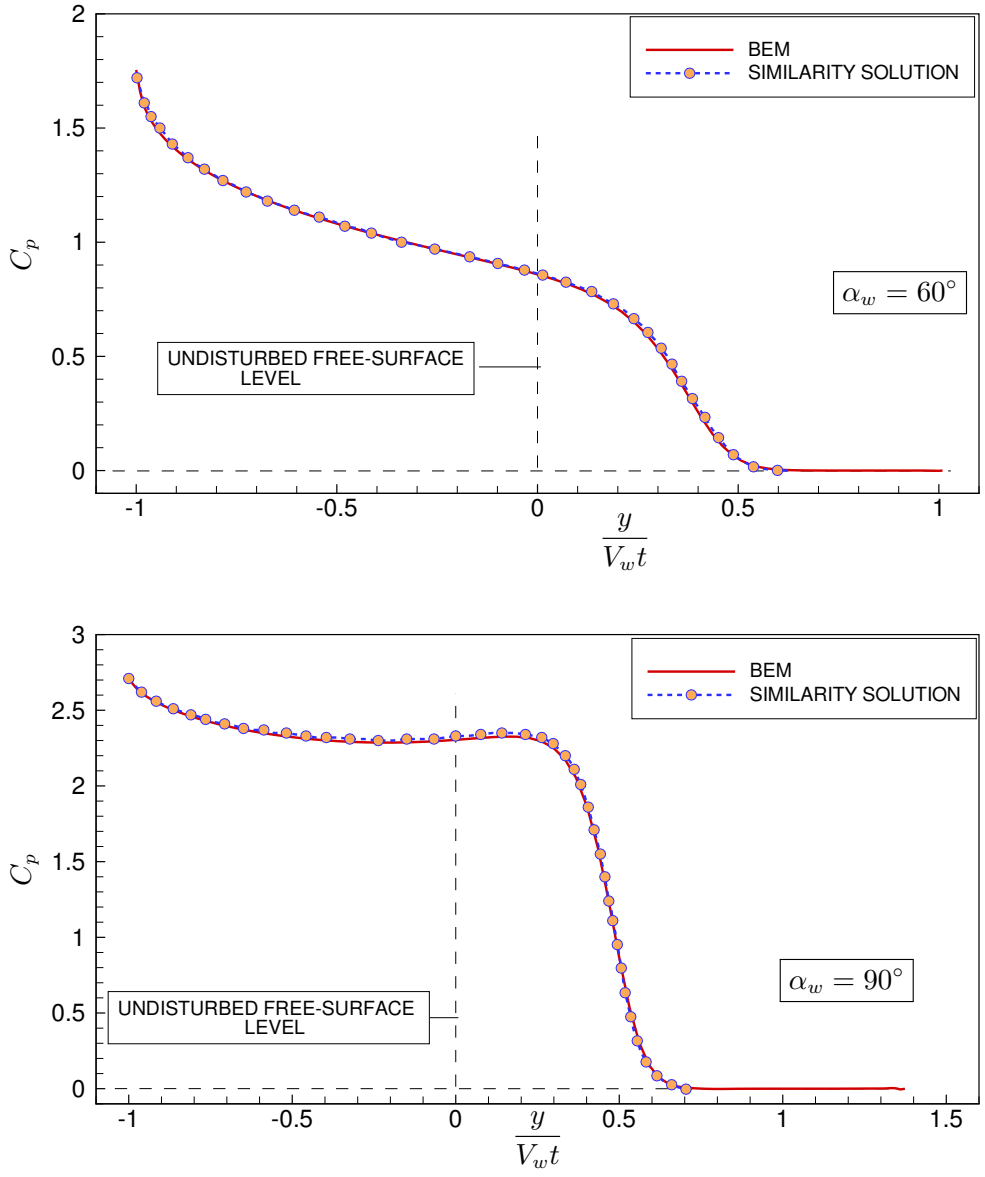

Figure 4.20: Wedge water-entry ($\alpha_w = 60°$ and $\alpha_w = 90°$) : Comparison of pressure predicted along the wetted part of the wedge with similarity solution of [Dobrovol'skaya 1969] expressed in terms of the similarity variable $y/(V_w t)$. C_p is the pressure coefficient; (Note : pressures shown only on one side of the wetted boundary)

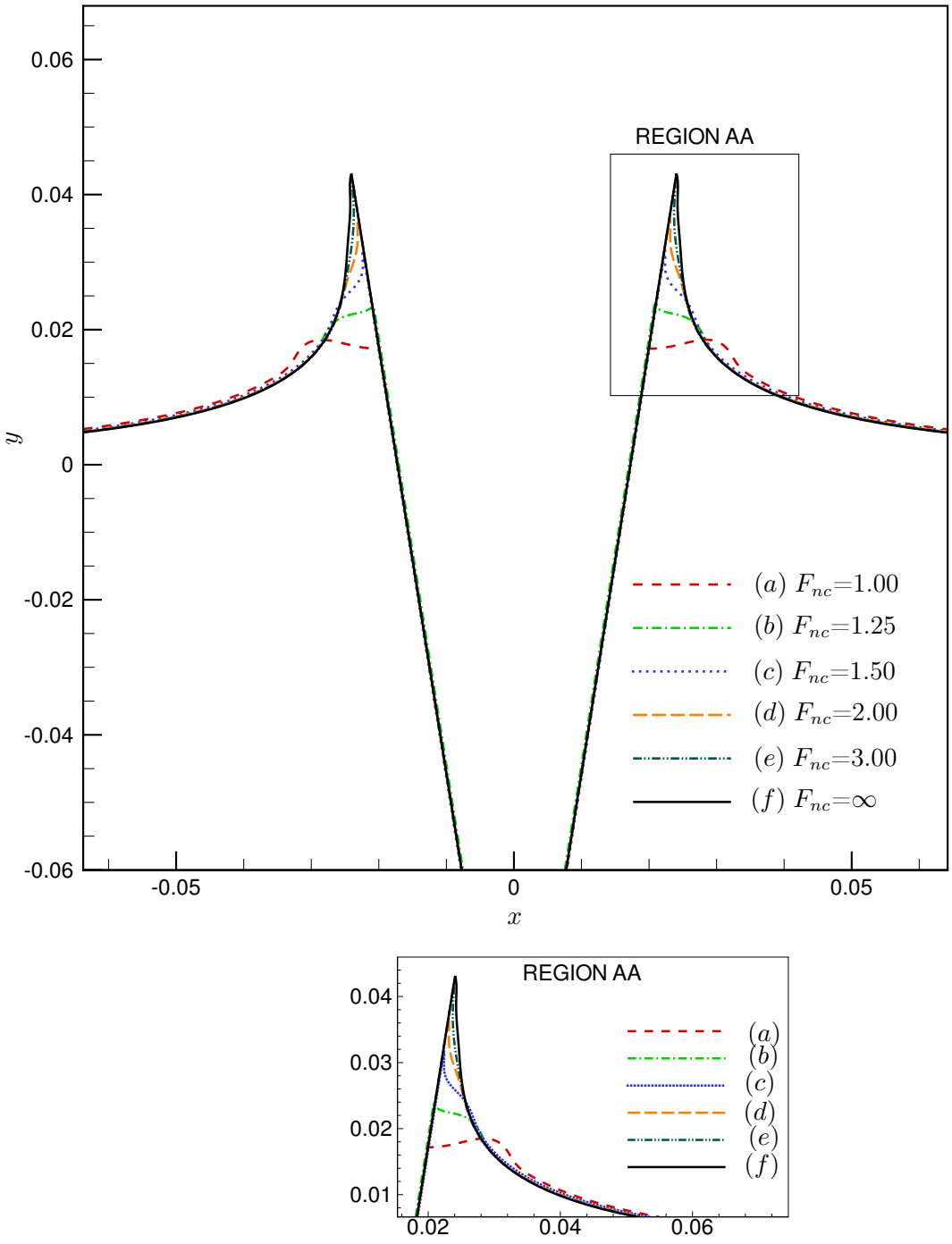

Figure 4.21: Wedge water-entry ($\alpha_w = 18°$) : Representative case showing the effect of the Froude number F_{nc} on the free-surface elevation.

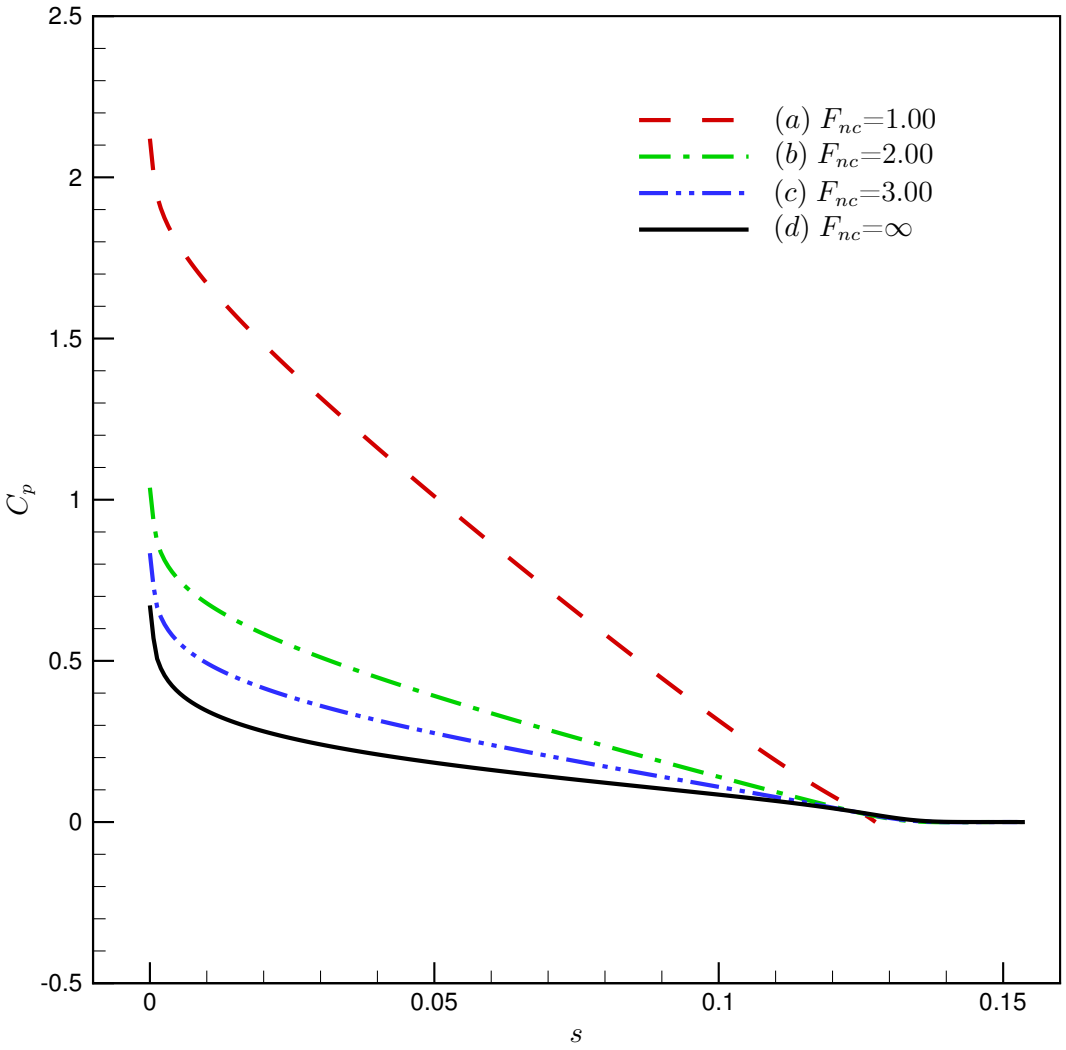

Figure 4.22: Wedge water-entry ($\alpha_w = 18°$) : Representative case showing the effect of the Froude number F_{nc} on the total pressure predicted on the wetted part of the wedge surface; C_p is the pressure coefficient (Note pressure shown only on one side of the wetted boundary)

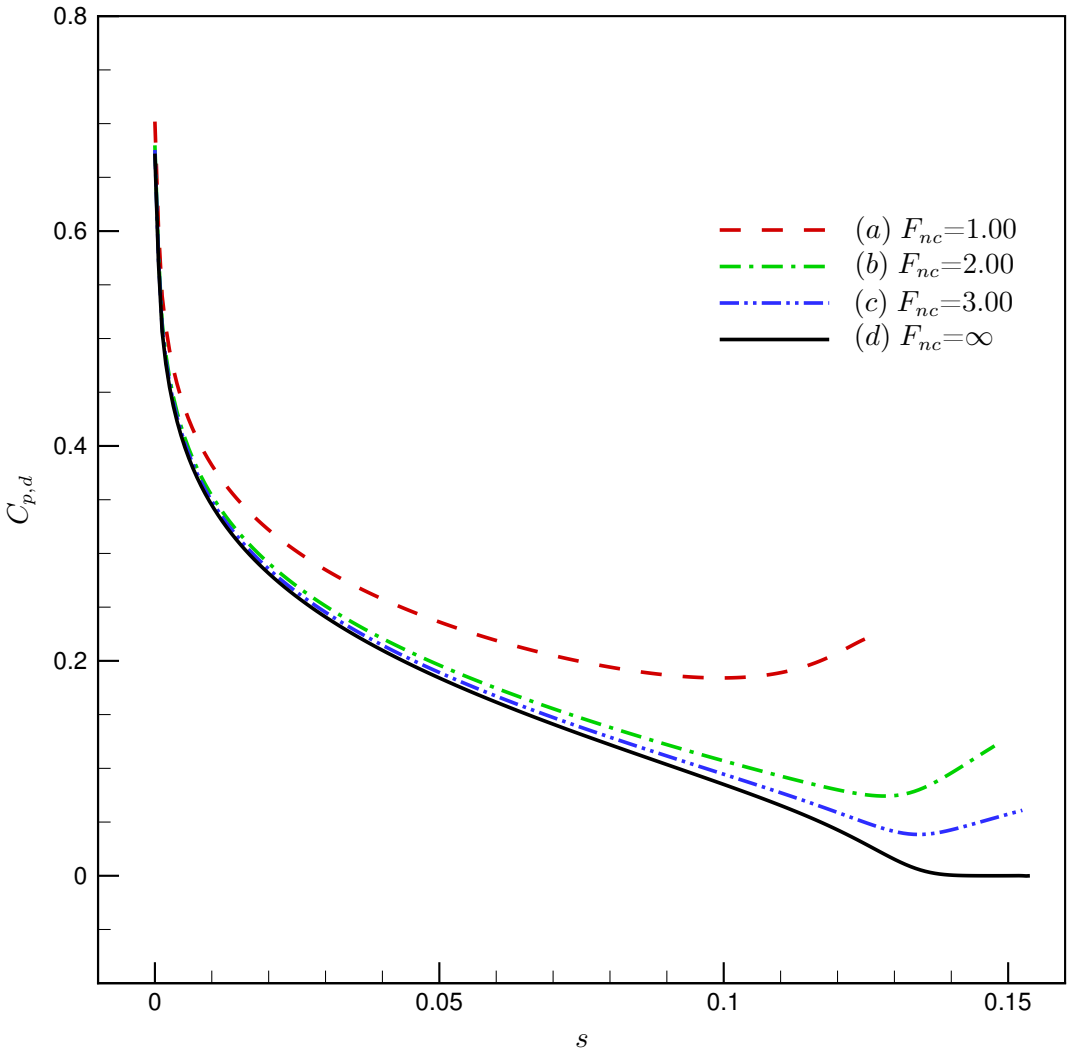

Figure 4.23: Wedge water-entry ($\alpha_w = 18°$) : Representative case showing the effect of the Froude number F_{nc} on the total pressure predicted on the wetted part of the wedge surface; $C_{p,d}$ is the hydrodynamic part of the pressure coefficient, as given by Equation (4.24) (Note pressure shown only on one side of the wetted boundary)

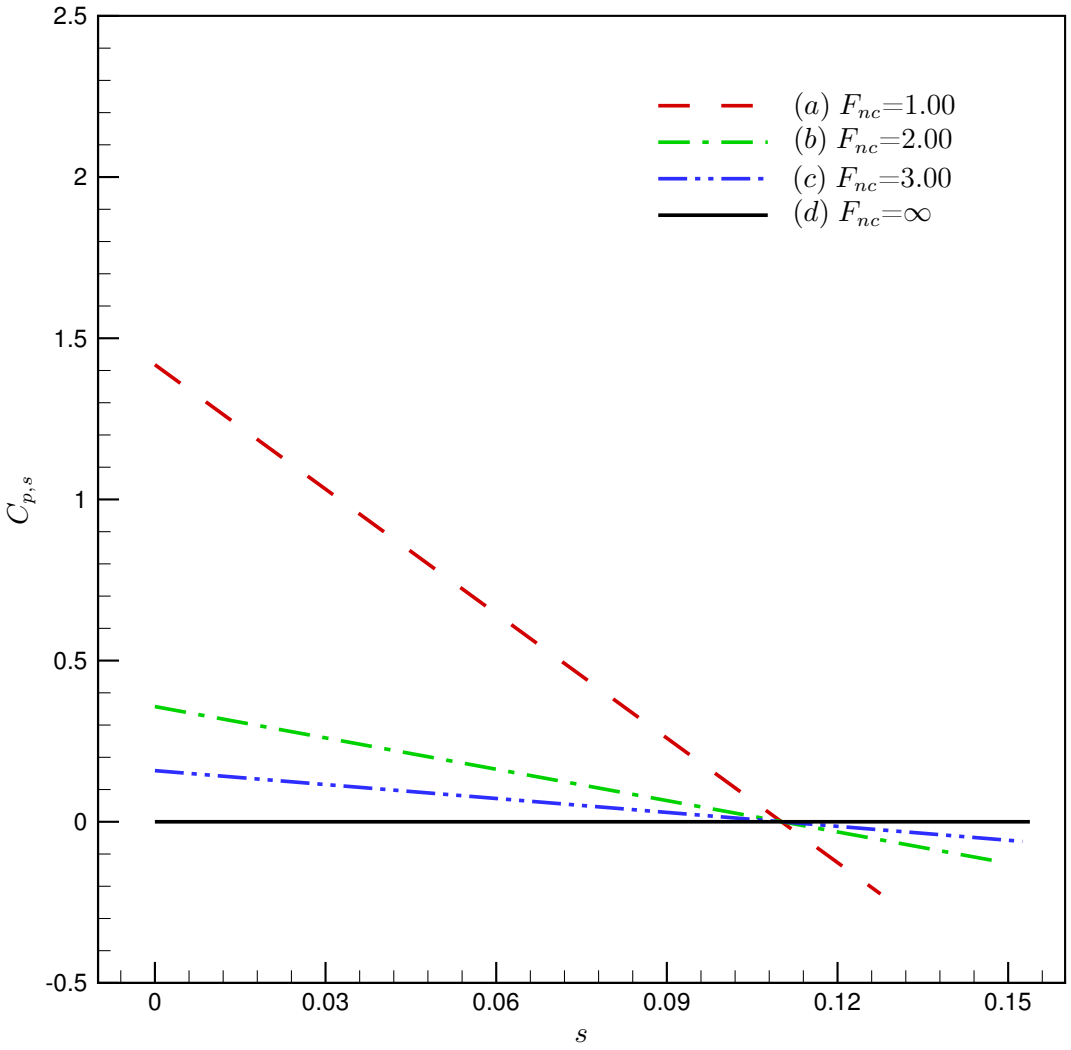

Figure 4.24: Wedge water-entry ($\alpha_w = 18°$) : Representative case showing the effect of the Froude number F_{nc} on the total pressure predicted on the wetted part of the wedge surface; $C_{p,s}$ is the hydrostatic part of the pressure coefficient, as given by Equation (4.25) (Note pressure shown only on one side of the wetted boundary)

4.4 Summary

The intent of this chapter was to validate the numerical building blocks, which put together are required to solve a general free-surface IBVP in a robust manner.

This has been achieved by applying a boundary element method based on linear isoparametric elements, along with an MEL approach, to simulate three specific problems (*i*) transient waves generated by a piston type wave-maker, (*ii*) propagation of nonlinear gravity waves of fixed form, and (*iii*) high speed water-entry of a wedge section. In each of these cases, the results from the present method were compared with available numerical or analytical solutions. In addition, the dependence of the results from the present method on numerical parameters such as number of panels, time step size, etc., were studied in detail.

Piston-type wave-maker

The BEM scheme was applied to numerically simulate a wave-tank with a piston type wave-maker at one end. Starting from rest, transient free-surface waves were generated through the sinusoidal motion of the piston wave-maker. The results obtained from the current BEM scheme were found to be in good agreement with the numerical results of Lin et al. [1984].

The body free-surface intersection point is often a source of error if not treated in a proper way. The current scheme, with double nodes at the intersection point, is able to simulate the generation of free-surface waves without errors (as seen in the comparisons with Lin's results).

Even though an elaborate study was not conducted, the results obtained here prove the potential of the current scheme in simulating a full-fledged numerical wave-tank. The scheme can, with ease, be extended to include a fixed or floating two-dimensional body to simulate its interaction with an ambient wave field.

Propagation of gravity waves of fixed form

This part of the validation involved the application of the BEM scheme to the propagation of gravity waves of permanent form. The scheme is allowed to propagate

a wave over a certain period of time and the numerical results were compared with an analytical solution. The present method is able to preserve the shape of the wave during the entire course of the simulation. This in essence proves the ability of the method to conserve mass and validates the implementation of the fourth-order Runge-Kutta scheme used in the time-stepping of the kinematic and dynamic free-surface boundary conditions.

In addition to validating the present method, the analytical forms of the non-linear wave can be used to simulate a numerical wave tank. This can be done by replacing the piston-type wave-maker with inflow boundary conditions obtained from the analytical expression of the horizontal velocity due to a wave.

Water-entry of wedge

The symmetric entry of a wedge is one of the most difficult problems in marine hydrodynamics because of the strong nonlinear free-surface interaction. The present scheme is able to simulate the water-entry and capture all the nonlinearities accurately as shown in the comparison with the self-similar solutions of [Dobrovol'skaya 1969]. The key aspect is the accurate treatment of the thin jet that runs up along the wedge surface. Along with the cut-off model, the scheme is able to capture the jet with sufficient accuracy and also conserve the important property that the pressure inside the region is almost atmospheric or the pressure coefficient C_p=0.

The Froude number is an important parameter in free-surface flows as it measures the relative importance of gravitational effects over inertial effects. In the case of water entry, the higher the speed of entry the lesser the importance of gravity. This effect has been shown to be true through a systematic study based on the Froude number as a parameter.

Chapter 5

Wave-body Interaction

This chapter describes the application of the BEM scheme to study the dynamics of two-dimensional hull-sections floating on the free-surface of the ocean. Two types of simulations are presented (i) the prescribed or forced roll-motion of a hull-section and (ii) transient or free-decay motion of a hull-section.

5.1 Forced Roll-motion of Hull Sections

A typical hull-section used in the two-dimensional analysis is shown in Figure 5.1. The bilge radius R_b is usually expressed in terms of the breadth B with a typical value being $0.02B$ (the experimental hull-sections of both [Vugts 1968] and [Roddier 2000] have the same bilge radius). The hull-section is assumed to float at a draft T=$0.5B$. The center-of-gravity is assumed to be at O, which is the origin of a fixed coordinate system with the x-axis along the undisturbed free-surface level.

5.1.1 Initial Boundary Value Problem

For the roll-motion of a 2-D hull-section (see Figure 5.2), $S_{\mathbb{F}}(t)$ and $S_{\mathbb{H}}(t)$ represent the instantaneous positions of the free-surface and the hull surface respectively. S_∞ represents the far-field boundary used to truncate the infinite domain into a finite one and placed far enough from the hull to avoid reflection of the radiated waves. $\mathbf{n}$ is the unit normal to a surface, positive out of the fluid.

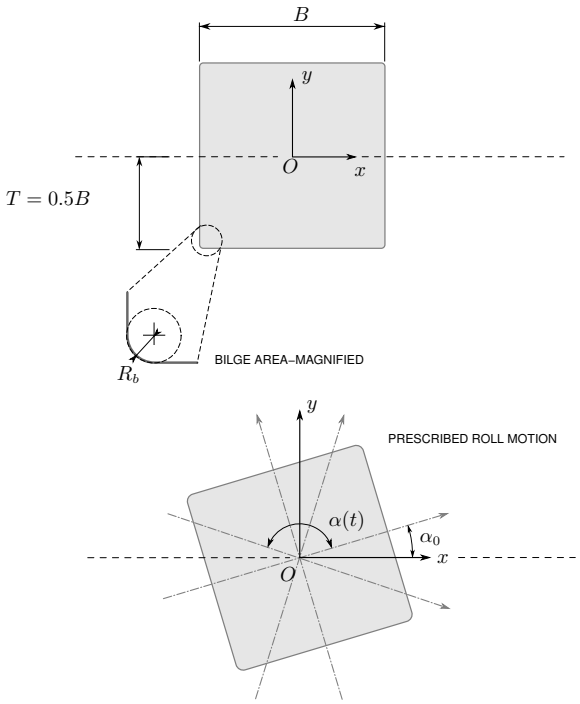

Figure 5.1: Geometry and prescribed roll configuration of a round-bilge hull-section. B : beam of hull-section; T draft (=$0.5B$), R_b : bilge radius (=$0.02B$); α_0 : amplitude of prescribed roll motion; $\alpha(t)$: instantaneous roll angle; O : origin of an inertial coordinate system

• **Governing Equation**

$$\nabla^2\phi(\mathbf{x},t) = 0, \quad \mathbf{x} \in \Omega(t) \tag{5.1}$$

with $\Gamma_d(t) = S_{\mathbb{F}}(t)$ and $\Gamma_n(t) = S_{\mathbb{H}}(t) \cup S_\infty$.

• **Boundary Condition on Hull** $S_{\mathbb{H}}(t)$

On the hull surface $S_{\mathbb{H}}(t)$,

$$\nabla\phi \cdot \mathbf{n} = \mathbf{V}(\mathbf{x},t) \cdot \mathbf{n}, \quad \mathbf{x} \in S_{\mathbb{H}}(t) \tag{5.2}$$

where $\mathbf{V}(\mathbf{x},t)$ is the prescribed motion of the hull. In the case of roll, the hull is subject to a forced sinusoidal angular motion of the form

$$\alpha(t) = \alpha_0 \sin(\omega t) \tag{5.3}$$

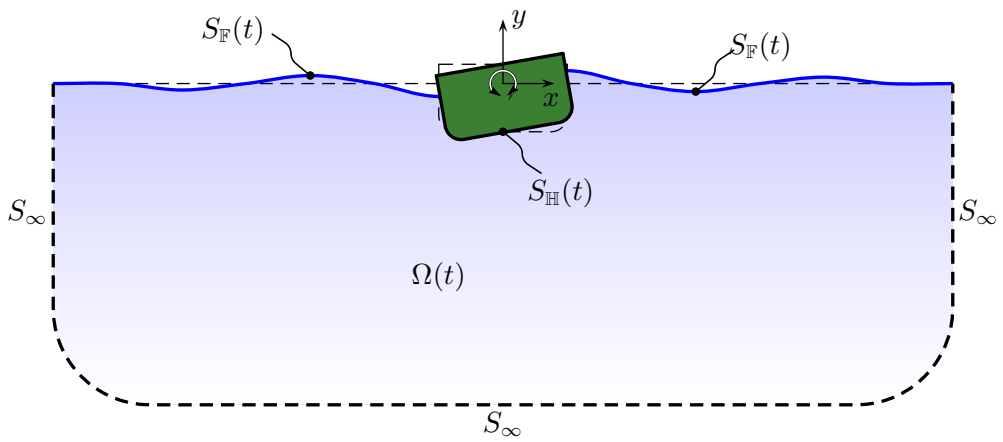

Figure 5.2: Hull-section roll-motion : Fluid domain and corresponding boundaries

α_0 is the amplitude of roll motion and ω is the corresponding circular frequency. In terms of Cartesian components, the prescribed roll motion is

$$\mathbf{V}(\mathbf{x}, t) = (-y\dot{\alpha}, x\dot{\alpha}) \tag{5.4}$$

• **Boundary Condition on Far Field Boundary S_∞**

The far-field boundary S_∞ is assumed to be a no-flux surface and the corresponding boundary condition is

$$\nabla\phi \cdot \mathbf{n} = 0, \quad \mathbf{x} \in S_\infty \tag{5.5}$$

Special attention is paid to place the boundary far away from the body to avoid reflection of the waves generated by the hull motion. The simulation is terminated before these waves reach the far-field boundary.

• **Initial Conditions**

At time $t = 0$, the relevant initial conditions are

$$\left.\begin{array}{rcl} \phi(\mathbf{x}, 0) & = & 0 \\ \eta(x, 0) & = & 0 \end{array}\right\} \mathbf{x} \in S_{\mathbb{F}}(t) \tag{5.6}$$

5.1.2 Results

The BEM scheme, which has been validated through studies presented in the previous chapter, is now applied to the roll-motion of a 2-D hull section. Two important parameters that govern the roll-motion of a hull-section are (i) the amplitude of roll, α_0 and (ii) the Froude number

$$\tilde{\omega} = \omega\sqrt{\frac{B}{2g}} \tag{5.7}$$

where ω is the frequency of roll-motion and B the breadth of the hull-section. $\tilde{w}$ also represents the non-dimensional frequency of roll.

The primary aim of the scheme is to ascertain the extent to which linear free-surface boundary conditions are applicable and the results presented here focus on this aspect. For a representative Froude number, $\tilde{w} = 0.6$, the effects of nonlinearity are analyzed for different amplitudes of roll-motion. Figure 5.3 and 5.4 illustrate the position of the hull and the free-surface elevation for a fully nonlinear simulation with $\alpha_0 = 0.40$ rad.($\approx 23^\circ$) over a duration of $8T$, where $T = \dfrac{2\pi}{\omega}$ is the period of oscillation. Figure 5.4 also shows a few Lagrangian fluid particles that are tracked to model the free-surface. For both the port and starboard side free-surfaces, 400 panels are used over an approximate length of $100B$. The panels have a distribution that is dense in a region close to the hull and coarse further away to increase the computational efficiency. A time-step of $\Delta t = 0.01T$ is used for the fourth-order Runge-Kutta scheme.

A comparison of the free-surface elevations obtained from the linear and nonlinear versions of the BEM scheme is shown in Figure 5.5. For $\alpha_0 = 0.05$ rad ($\approx 3^\circ$), there is no discernible difference between the linear and nonlinear free-surface elevations. However, this is not true in the case of $\alpha_0 = 0.40$ rad ($\approx 23^\circ$), where the effect of the nonlinear free-surface boundary conditions is clearly evident with the presence of secondary waves of smaller wavelength. A similar observation is made

in Figure 5.6(a), where the effect of the nonlinear free-surface boundary conditions is shown to increase with the amplitude of roll. An alternate way to represent the effects of nonlinearity is to scale the wave elevations with the amplitude of roll α_0, see Figure 5.6(b). Ideally for a linear phenomenon, the scaled free-surface elevations should be identical. It can be observed that up to an amplitude of roll of $\alpha_0 = 0.1$ rad ($\approx 6^\circ$), the effects of nonlinearity are small.

A convergence test is also carried out to ascertain the grid-independence of the nonlinear secondary waves seen in Figure 5.6 by varying the number of elements on the free-surface. For $N_{\mathbb{F}} = 400$ and $N_{\mathbb{F}} = 500$, the free-surface elevations are identical in the vicinity of the hull and the presence of the secondary waves is still observed (see Figure 5.7). Note that the port and starboard free-surfaces each have $N_{\mathbf{F}}$ panels.

Correlation with NS2D Solver

One of the objectives of the current work was the development of an independent potential flow model to validate the free-surface tracking algorithm of the NS2D solver [Yu 2008]. A comparison of the free-surface elevations predicted by the two schemes, BEM and NS2D, is shown in Figure 5.8. The overall agreement between the predicted elevations is good. Apart from validating the free-surface algorithm, the BEM solver can also be used to validate an inviscid version of the NS2D solver in terms of the pressure and fluid velocities on the hull boundary. The inviscid version is only applied to the case of round bilge hull sections. Figure 5.9 and 5.10 show a comparison of the pressures and velocities at t/T=2.75 and t/T=3.0 for an α_0=0.1 radians and $\tilde{\omega}$=1.0. Figures 5.11 and 5.12 show a similar comparison for α_0=0.2 radians. (Note that at t/T=2.75, the angular velocity of roll, $\dot{\alpha}$=0, while at t/T=3.0, $\dot{\alpha}$ is a maximum.). In all the cases the agreement between the two schemes is excellent.

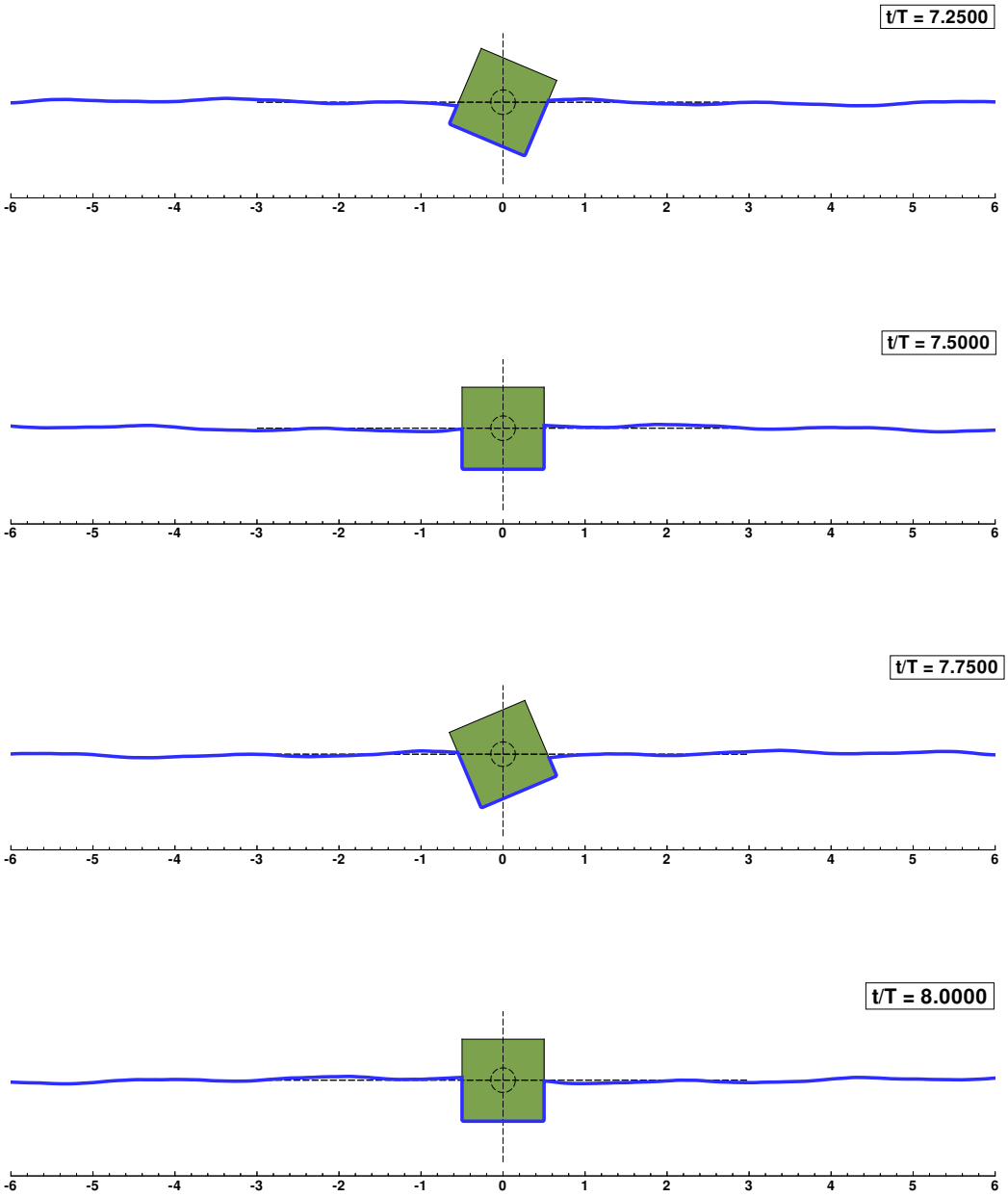

Figure 5.3: Hull-section and free-surface; $\tilde{\omega} = 0.6$, $\alpha_0 = 0.4$ rad;(*Note : the horizontal and vertical scales are identical*)

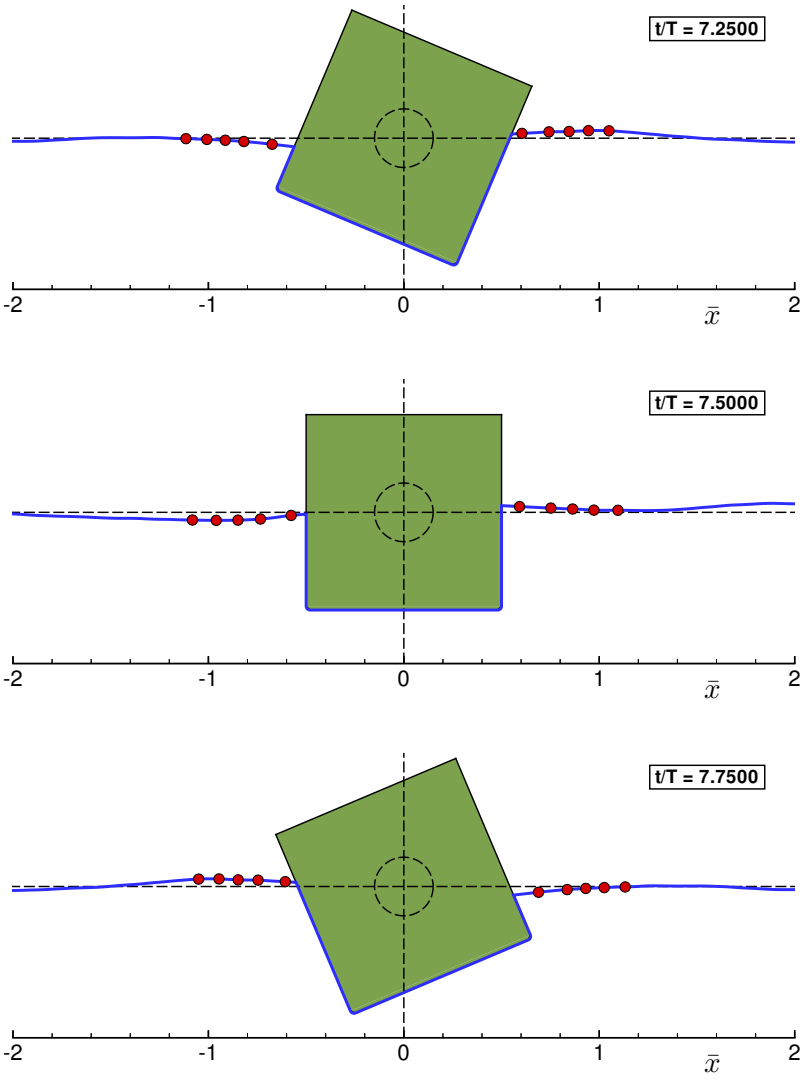

Figure 5.4: Hull-section and free-surface with actual Lagrangian fluid particles; $\tilde{\omega} = 0.6$, $\alpha_0 = 0.4$ rad; $\bar{x} = x/B$; (*Note : the horizontal and vertical scales are identical*)

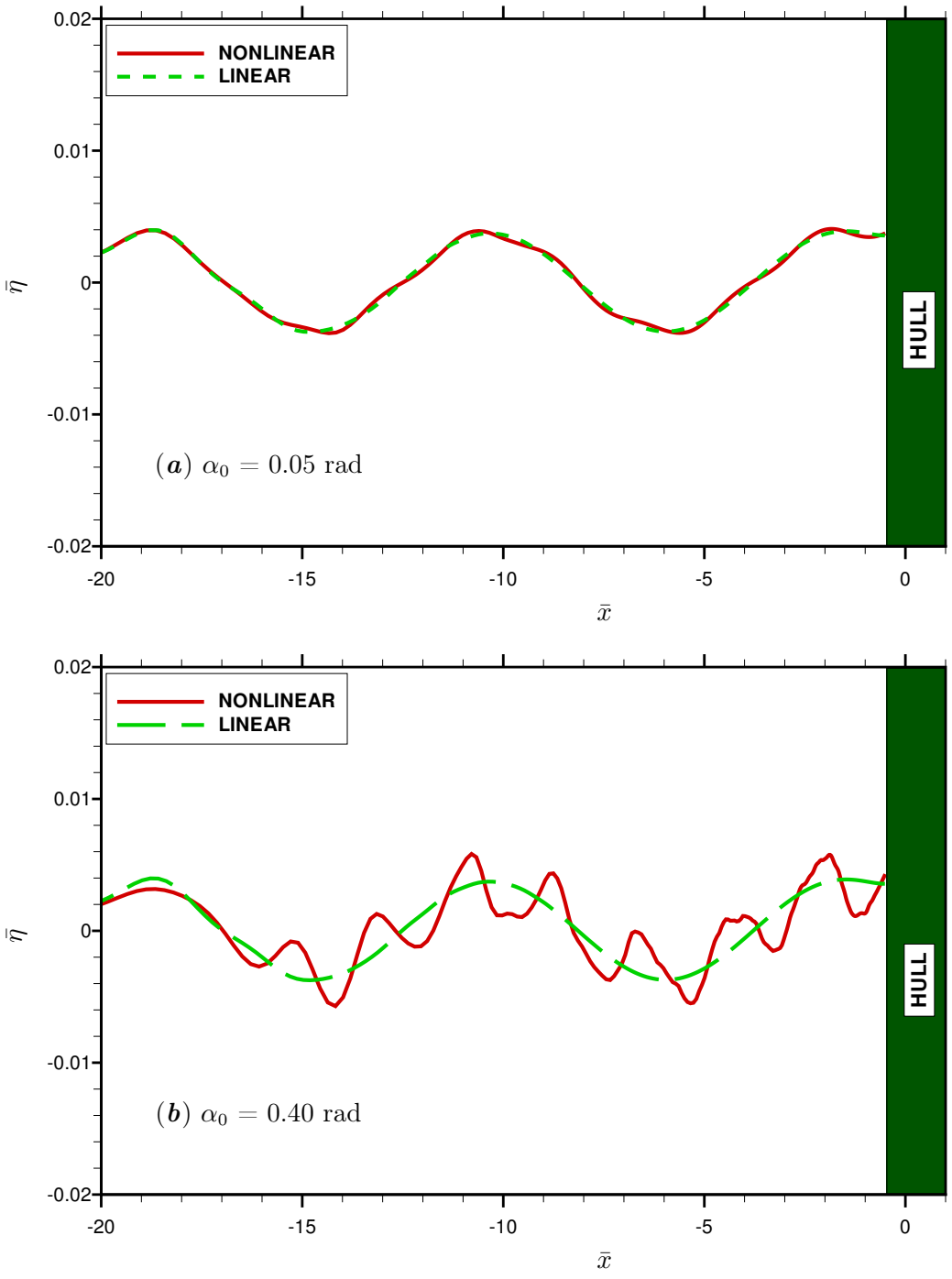

Figure 5.5: Comparison of linear and nonlinear free-surface elevations; (a) $\alpha_0 = 0.05$ rad, (b) $\alpha_0 = 0.40$ rad; $\tilde{\omega} = 0.6$; $N_{\mathbb{F}} = 400$, Number of panels on the starboard free-surface; (*Note : the horizontal and vertical scales are not identical*)

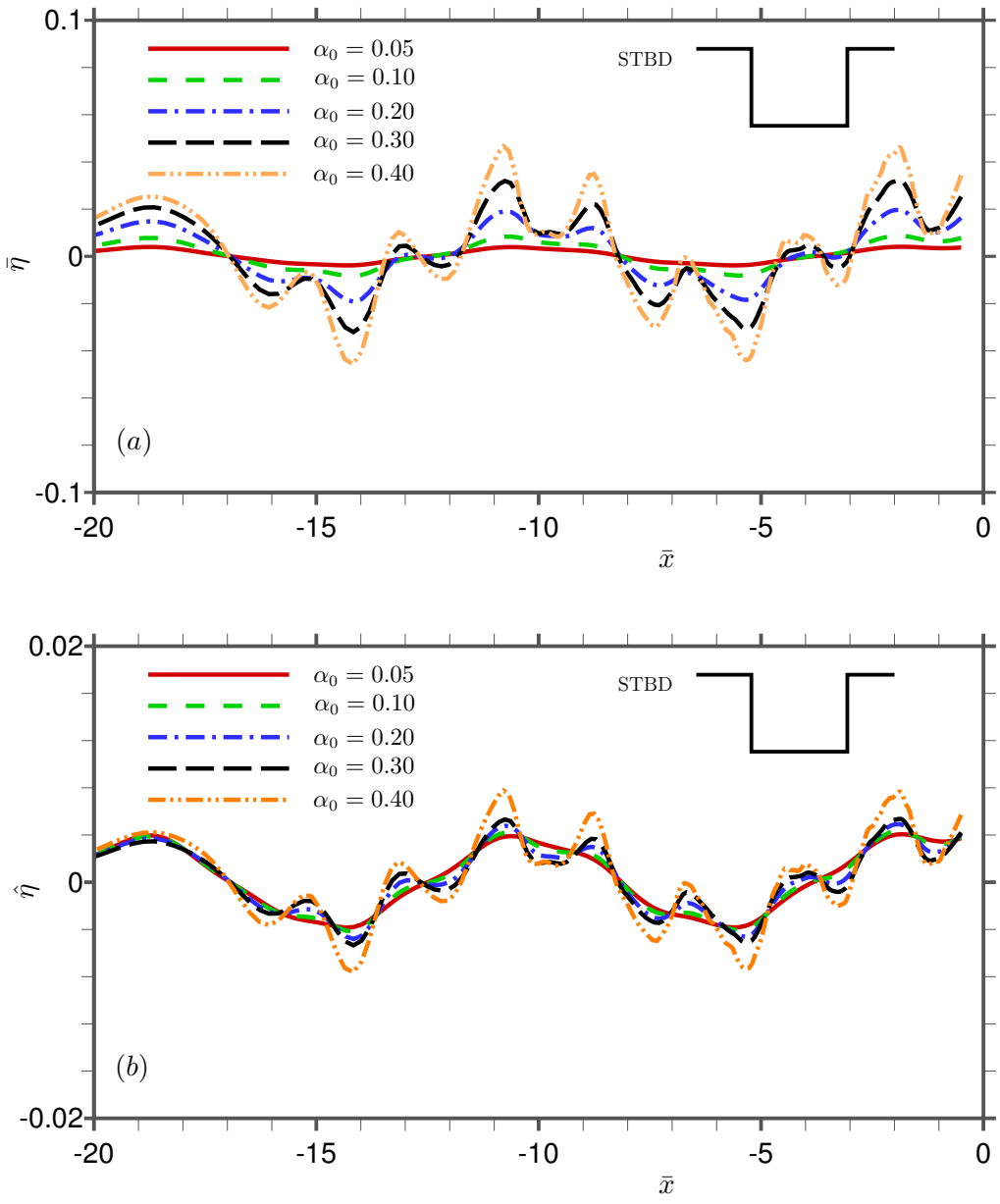

Figure 5.6: Scaled and un-scaled wave-elevations; $\tilde{\omega}$=0.6; $\bar{\eta} = \eta/B$: free-surface elevation; $\hat{\eta} = \bar{\eta}\frac{0.05}{\alpha_0}$ scaled wave elevation;$\bar{x} = x/B$;$N_{\mathbb{F}} = 400$, Number of panels on the starboard free-surface; (*Note : the horizontal and vertical scales are not identical*)

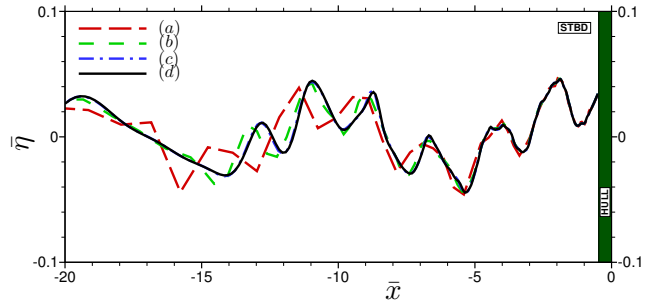

Figure 5.7: Convergence of free-surface elevations with increase in number of panels on the free-surface (a) $N_{\mathbb{F}} = 100$ (b) $N_{\mathbb{F}} = 200$ (c) $N_{\mathbb{F}} = 400$ (d) $N_{\mathbb{F}} = 500$; $N_{\mathbb{F}}$ is the number of panels on the starboard side free-surface (*Note : the horizontal and vertical scales are not identical*)

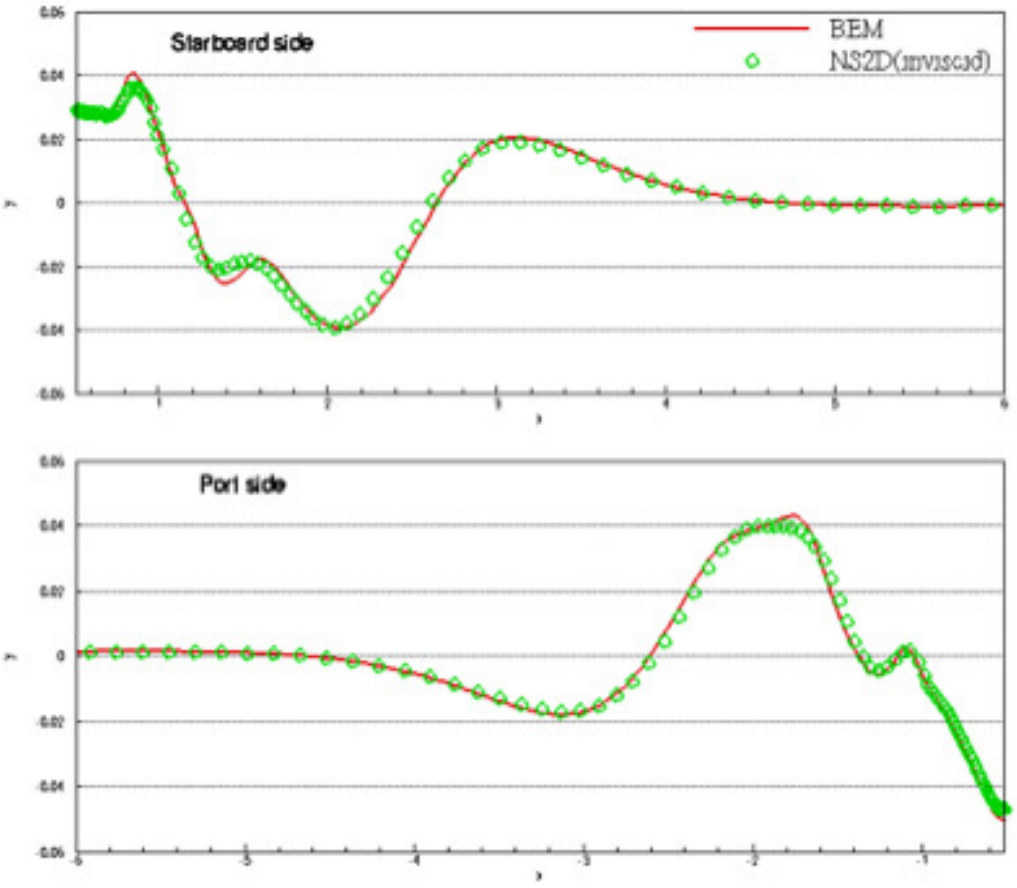

Figure 5.8: Comparison of the free-surface elevations between BEM and NS2D ([Yu 2008]) schemes. $\tilde{\omega}$=1.0,α_0=0.1 rad.

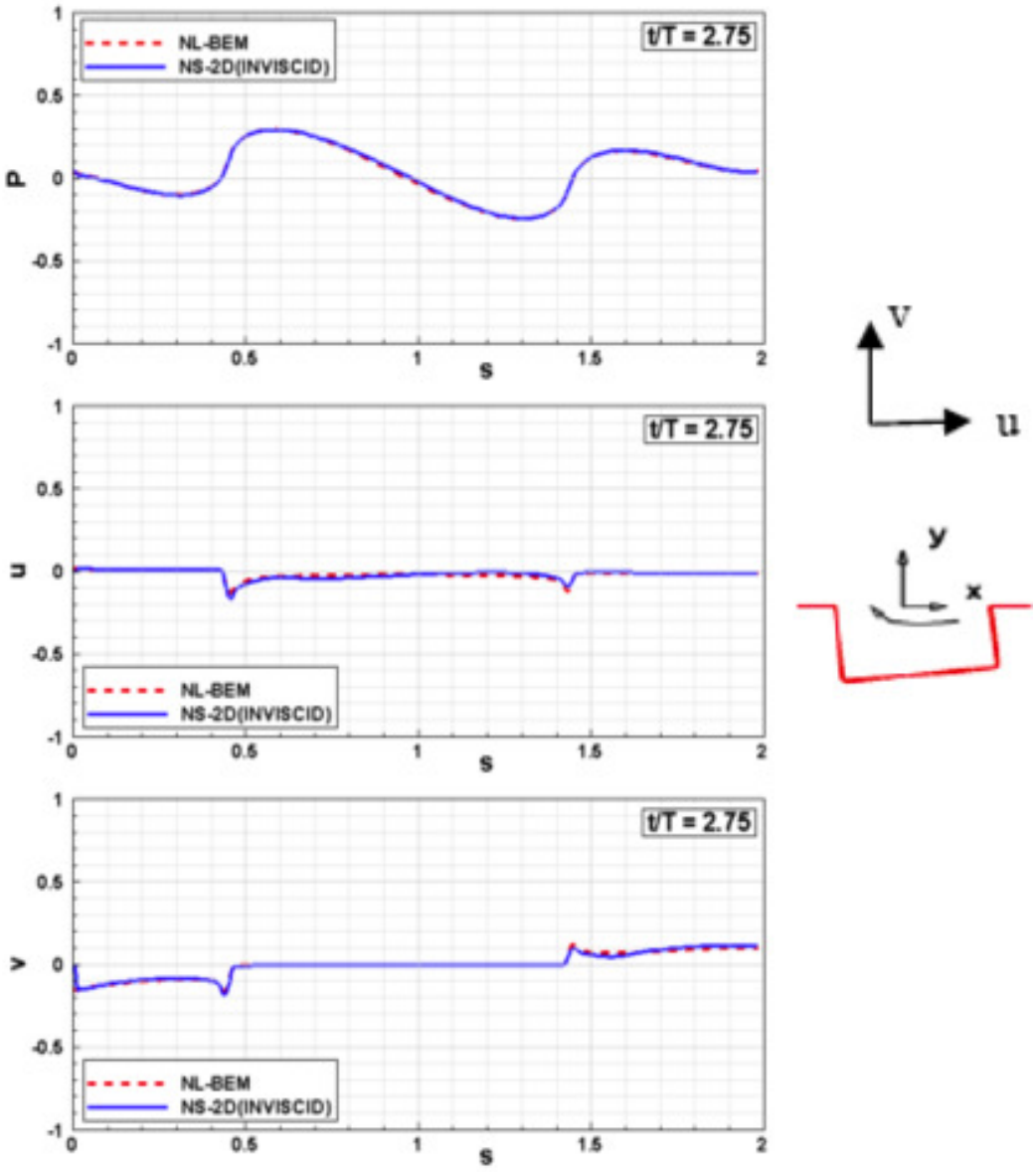

Figure 5.9: Comparison of pressure and velocity components between BEM and NS2D(IN) [Yu 2008] scheme.$\tilde{\omega}$=1.0,α_0=0.1 rad,t/T=2.75; Round bilge hull-section

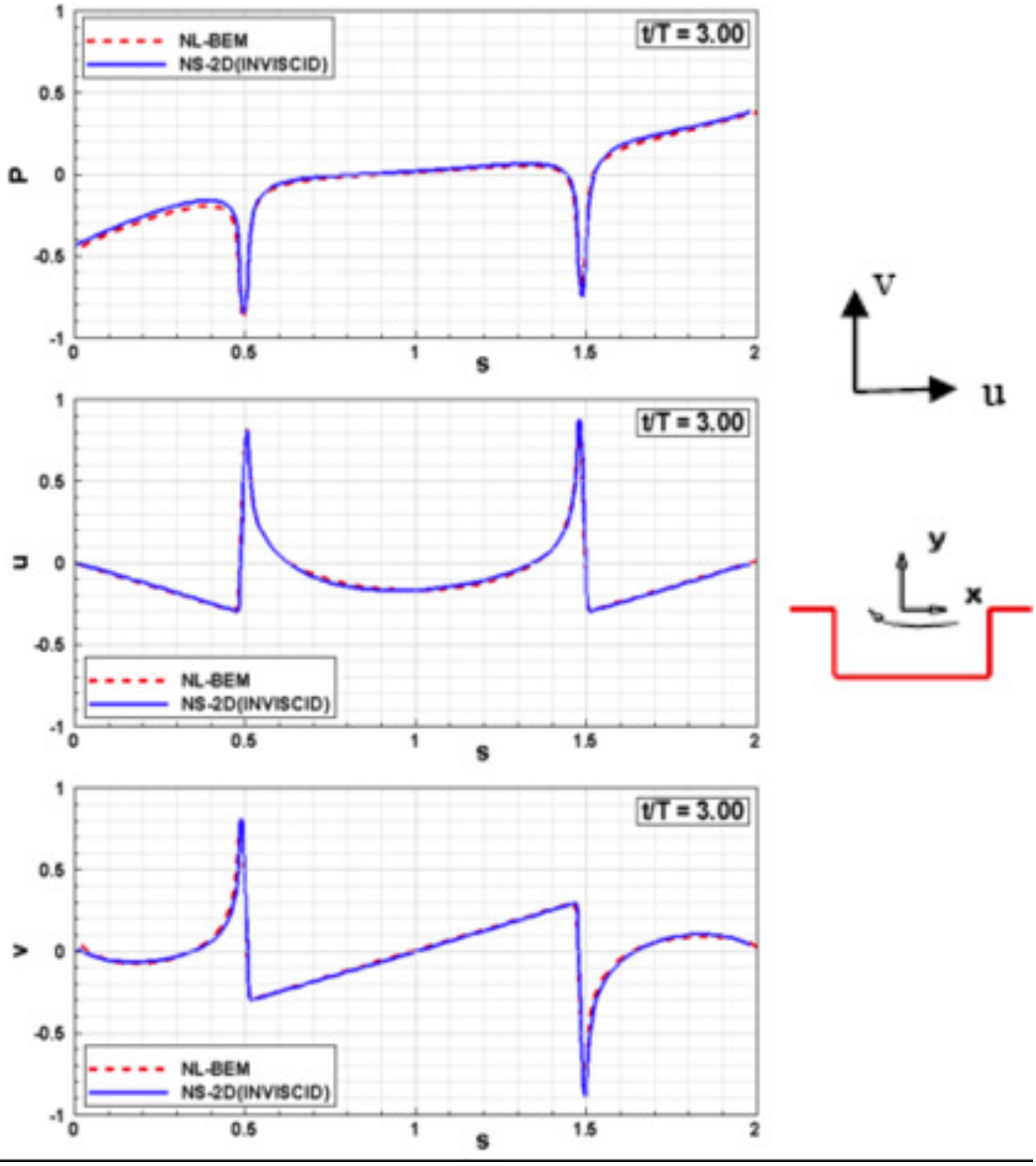

Figure 5.10: Comparison of pressure and velocity components between BEM and NS2D(IN) [Yu 2008] scheme.$\tilde{\omega}$=1.0,α_0=0.1 rad,t/T=3.00; Round bilge hull-section

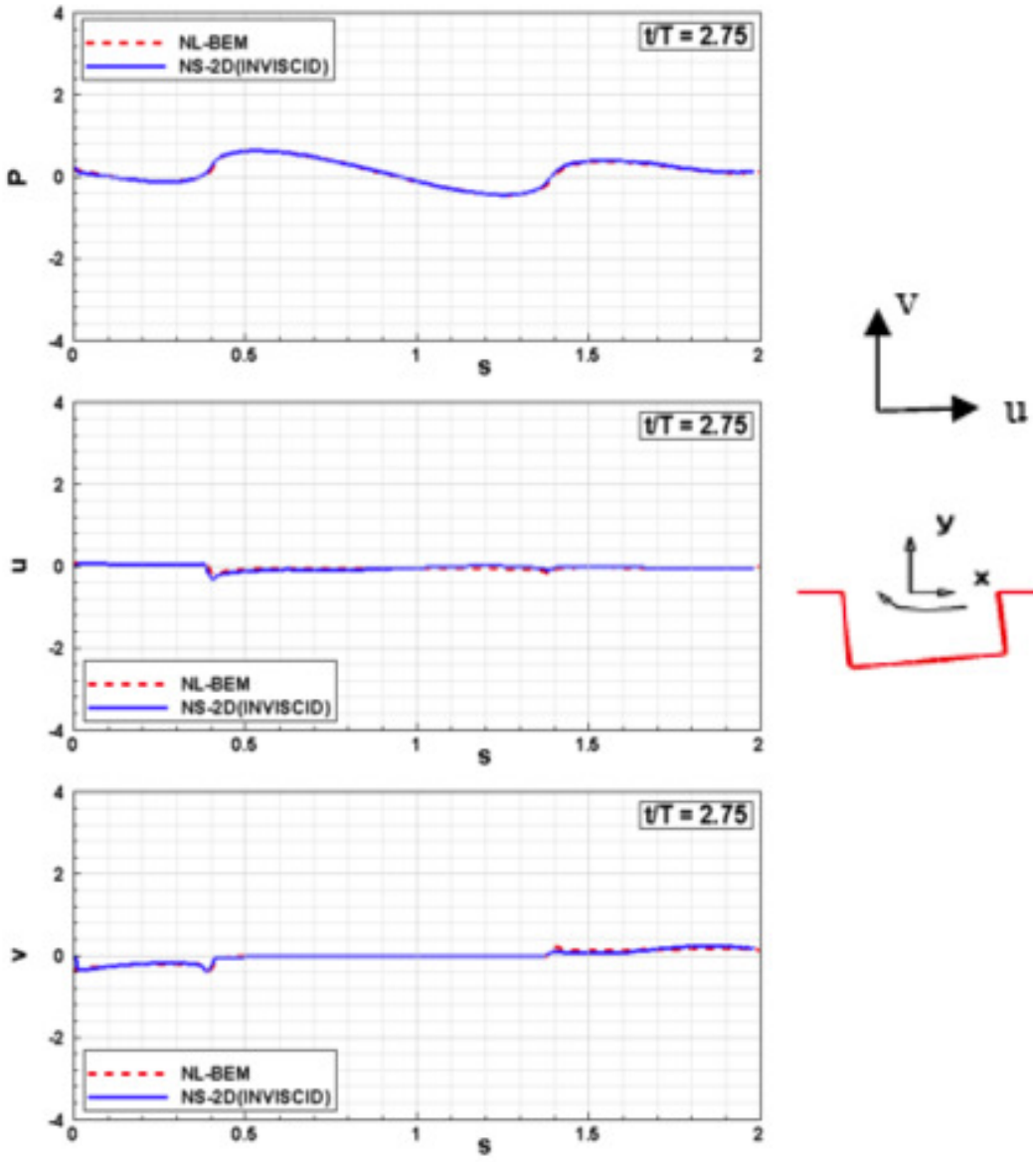

Figure 5.11: Comparison of pressure and velocity components between BEM and NS2D(IN) [Yu 2008] scheme.$\tilde{\omega}$=1.0,α_0=0.2 rad,t/T=2.75; Round bilge hull-section

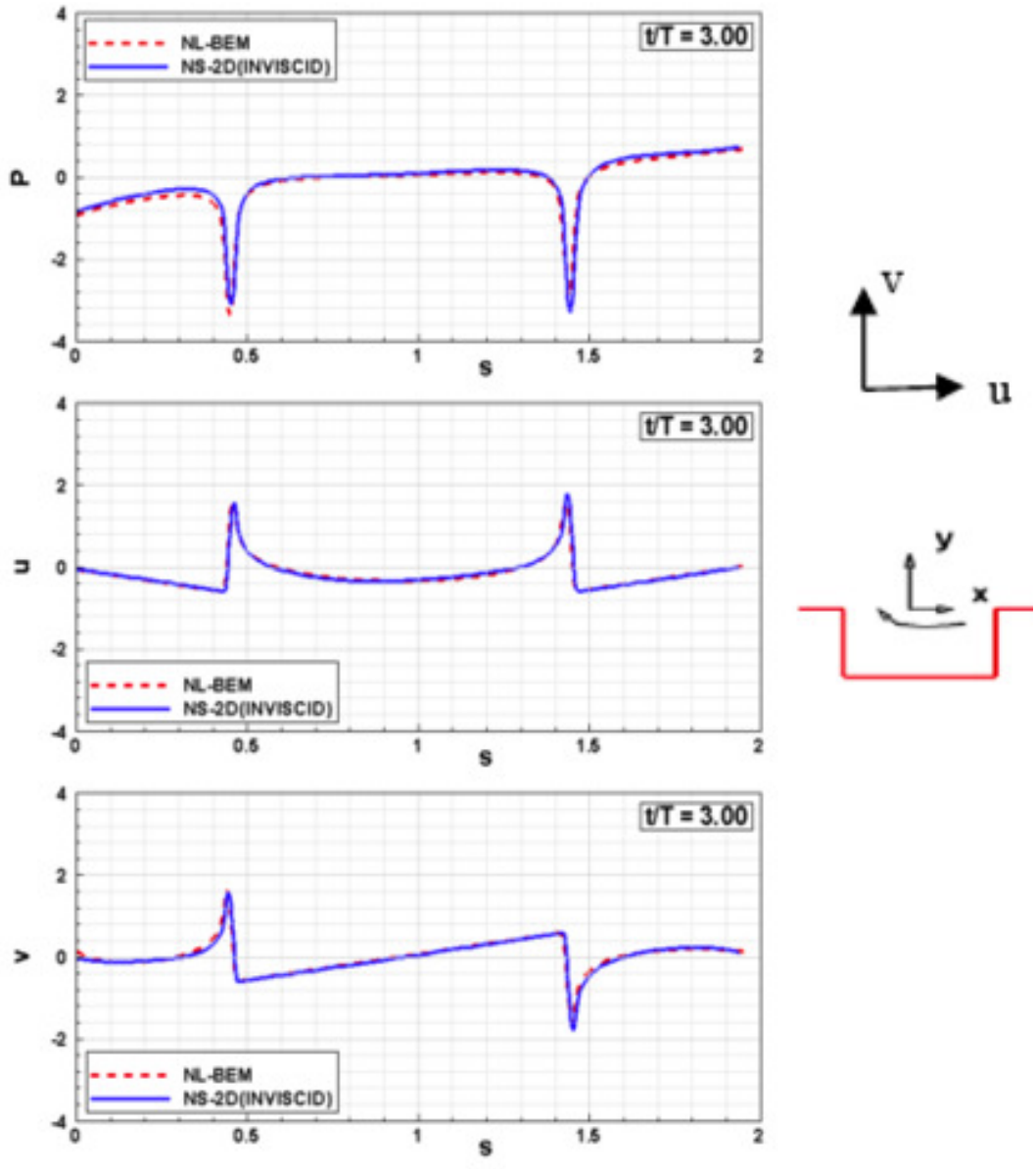

Figure 5.12: Comparison of pressure and velocity components between BEM and NS2D(IN) [Yu 2008] scheme.$\tilde{\omega}$=1.0,α_0=0.2 rad,t/T=3.00; Round bilge hull-section

5.2 Transient Response of Hull-sections

This section provides a brief overview of the application of the BEM scheme to the prediction of the transient response of hull sections in calm water. An important difference from the forced motion case is that the acceleration of the body, hence the velocity field and displacement of the body, is obtained as a part of the solution instead of being specified. This involves the solution of the rigid body equations of motion in conjunction with the external fluid forces and moments.

For a two-dimensional hull section, the relevant modes of motion are sway (translation about the x-axis), heave (translation about the y-axis) and roll (rotation about the z-axis). The sway component is not important due to the absence of a restoring force trying to bring the hull-section back to its equilibrium position. In the case of roll and heave, buoyancy provides the restoring force and along with damping effects (damping provided by viscous effects and generation of surface waves) produces an oscillatory response. Figure 5.13 shows parameters that define the geometry of the hull-section along with the heave/roll decay configuration. The hull-section has a round bilge with a radius of $0.02B$, where B is the breadth of the hull-section (this geometry is identical to one used in the experimental work of [Roddier 2000]).

The rigid body equations of motion in heave can be expressed as

$$M_b \ddot{y}_b = F_y - M_b g \tag{5.8}$$

and in roll as

$$I_o \ddot{\alpha} = M_z - M_b g \bar{x}_g \tag{5.9}$$

where M_b is the mass of the body, I_o is the mass-moment of inertia about the origin O. F_y is the y-component of the fluid force and M_z is the roll-component of the fluid force. $\ddot{y}_b$ is the heave acceleration while $\ddot{\alpha}$ is the roll angular acceleration. The above equations are simplified forms of the generalized rigid body equations of motion (see [Abkowitz 1969, Roddier 2000] for the complete set of equations).

The external fluid forces (in the case of heave, F_y) and moments (for roll, M_z) on the body can be obtained by integrating the pressure over the body surface. In terms of the pressure

$$P = -\rho\left(\frac{\partial\phi}{\partial t} + \frac{1}{2}|\nabla\phi|^2 + gy\right) \tag{5.10}$$

F_y and M_z can be expressed as

$$F_y = \int_{S_{\mathbb{B}}} P n_y dS \tag{5.11}$$

$$M_z = \int_{S_{\mathbb{B}}} P(x n_y - y n_x) dS \tag{5.12}$$

where $S_{\mathbb{B}}$ is the wetted body surface, $\mathbf{n} = (n_x, n_y)$ and $\mathbf{x} = (x, y)$ respectively are the normal vector and position vector on the body surface (the coordinate system is identical to that shown in Figure 5.13).

It can be observed from the equations of motion that its solution is directly related to the solution of $\dfrac{\partial\phi}{\partial t} \equiv \phi_t$. The mode decomposition method (see [Vinje and Brevig 1981]) is used to decompose the total acceleration field into its components. For heave, the decomposed acceleration field is expressed as

$$\phi_t = \ddot{y}_b\varphi_1 + \varphi_4 \tag{5.13}$$

and, for roll

$$\phi_t = \ddot{\alpha}\varphi_2 + \varphi_4 \tag{5.14}$$

where φ_1 and φ_2 are related to the unit body accelerations in heave and roll respectively, and φ_4 is related to the velocity field and generation of surface waves. The solution of the different modes is obtained by solving a BIE for each mode of the acceleration based on the method presented in [Tanizawa 1995].

5.2.1 Results

The scheme is applied to predict the transient response of a hull-section and to measure its natural frequency. In the case of heave, the hull is displaced vertically

by an amount $y_o/B = 0.125$ and the resulting heave motion is predicted by solving Equation (5.8). The value of $y_o/B = 0.125$ is chosen to make a comparison with experimental results of [Roddier 2000].

Figure 5.14 shows the instantaneous position of the hull-section in heave, where $t = 0.0$ represents the initially displaced position. The dashed line represents the equilibrium draft (T=0.5B) about which the hull-section oscillates. A comparison of the heave response predicted by the BEM scheme with the experimental and inviscid/viscous FSRVM results of [Roddier 2000] is shown in Figure 5.15. On the whole, the response predicted by the current scheme agrees well with the experimental/numerical results. The heave response of the hull-section has characteristics of a lightly damped spring-mass system as shown in Figure 5.15. The logarithmic decay of the heave maxima predicted by the BEM scheme agrees well with the experimental results even though the predicted natural period is slightly higher compared to the experimental value. The primary reason for a good correlation between the inviscid BEM and experimental results is that for heave decay the damping effect of viscosity is negligible compared to the damping effect provided by the radiated free-surface waves. Along with the logarithmic decay characteristics predicted by the BEM scheme, Figure 5.15 shows those obtained from the NS2D(IN) and NS2D(VS) solvers. The results obtained from all the three solvers are identical.

Initial tests for predicting the roll decay motion showed that the wave damping was negligible and the scheme sustained the roll motion for a long period of time, i.e., predicted a much lower natural frequency compared to the experimental results. The application of the current inviscid BEM scheme to the prediction of the roll response was not pursued further as viscous effects cannot be taken into account.

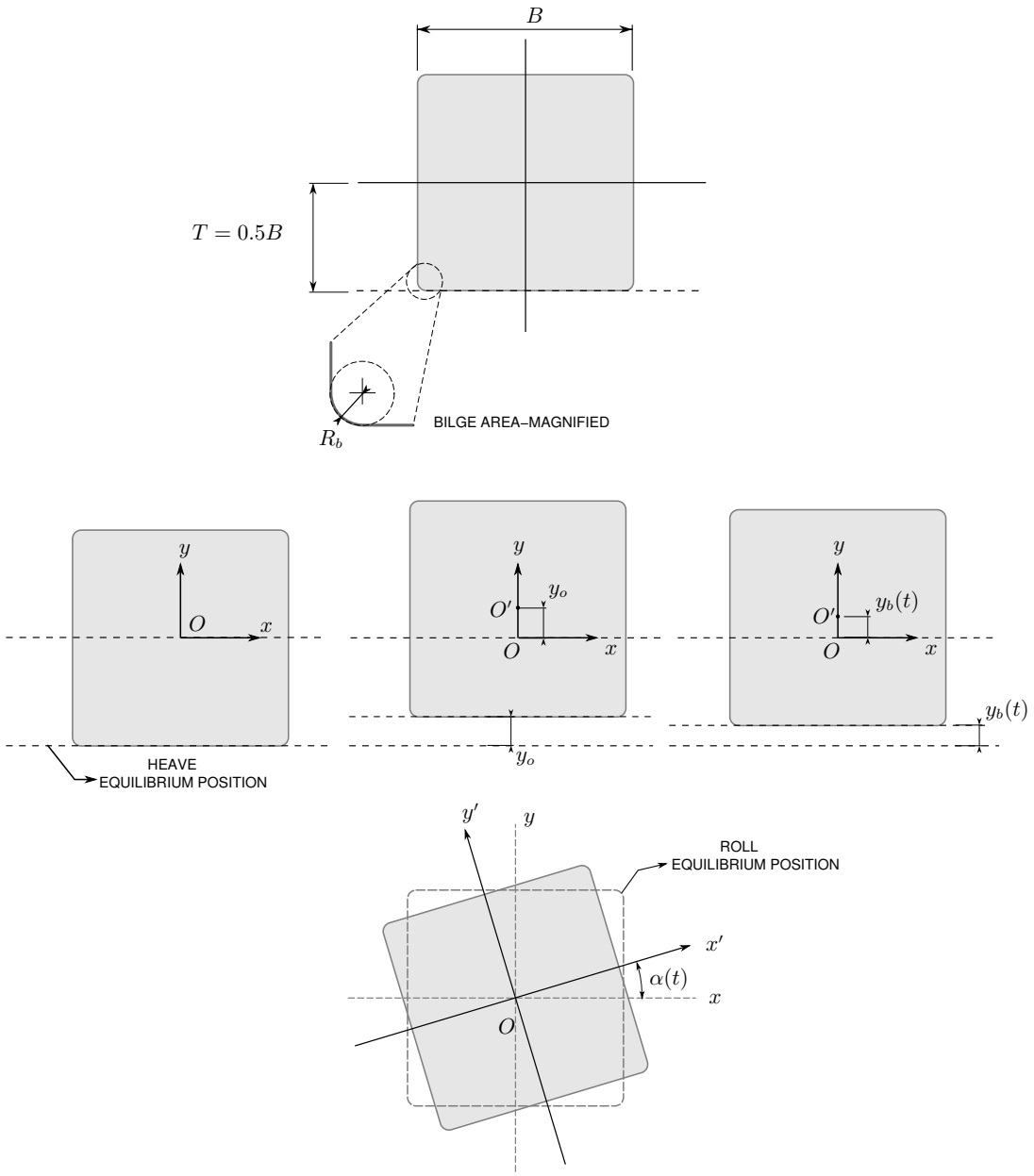

Figure 5.13: Geometry and roll/heave decay configuration of a round-bilge hull-section. B : beam of hull-section; T draft (=0.5B), R_b : bilge radius (=0.02B); y_o : initial heave displacement (=0.125 B); $y_b(t)$: instantaneous heave displacement; $\alpha(t)$: instantaneous roll angle; O : origin of an inertial coordinate system; O' : origin of a body fixed coordinate system

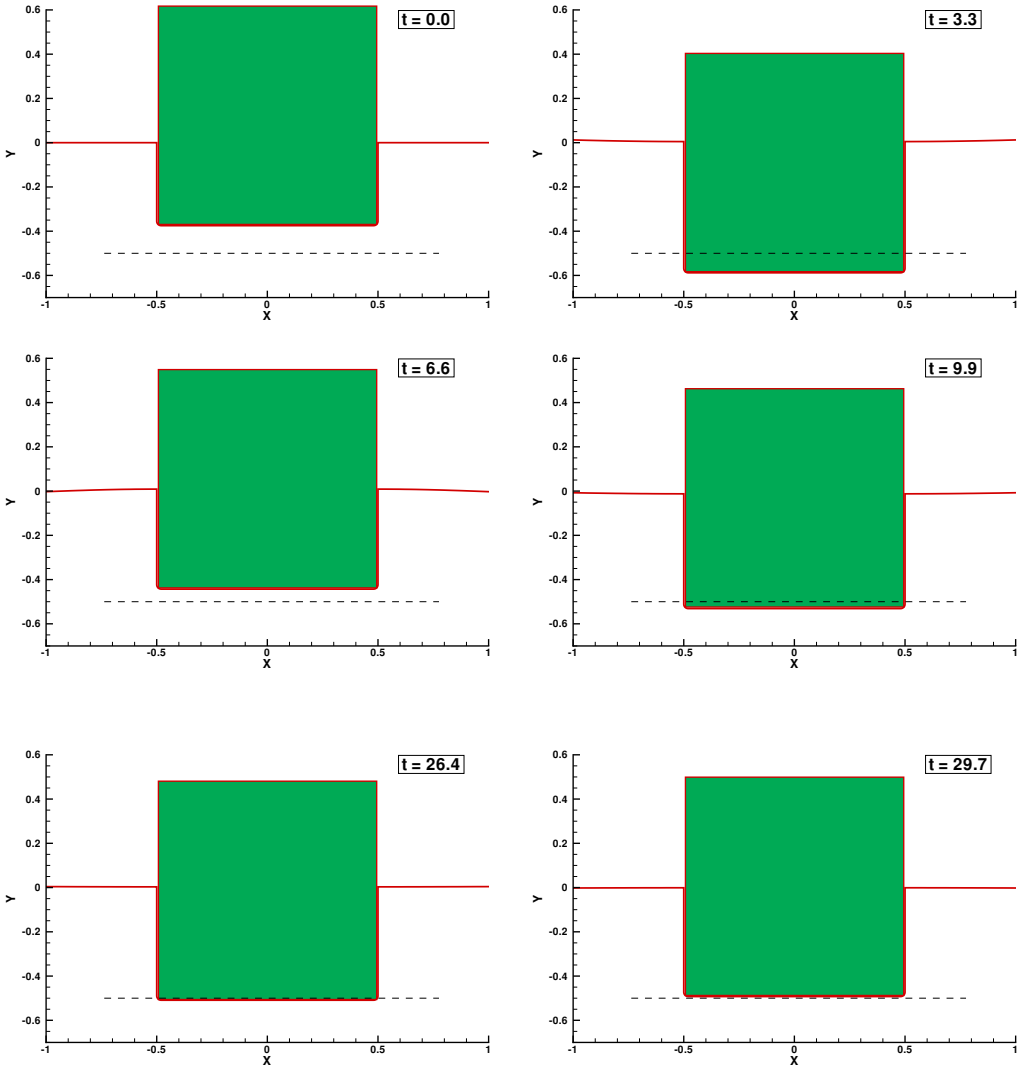

Figure 5.14: Sequential decay of the hull section in heave. Note that the dashed line represents the equilibrium draft of the hull-section about which it oscillates freely and eventually coming to a stop

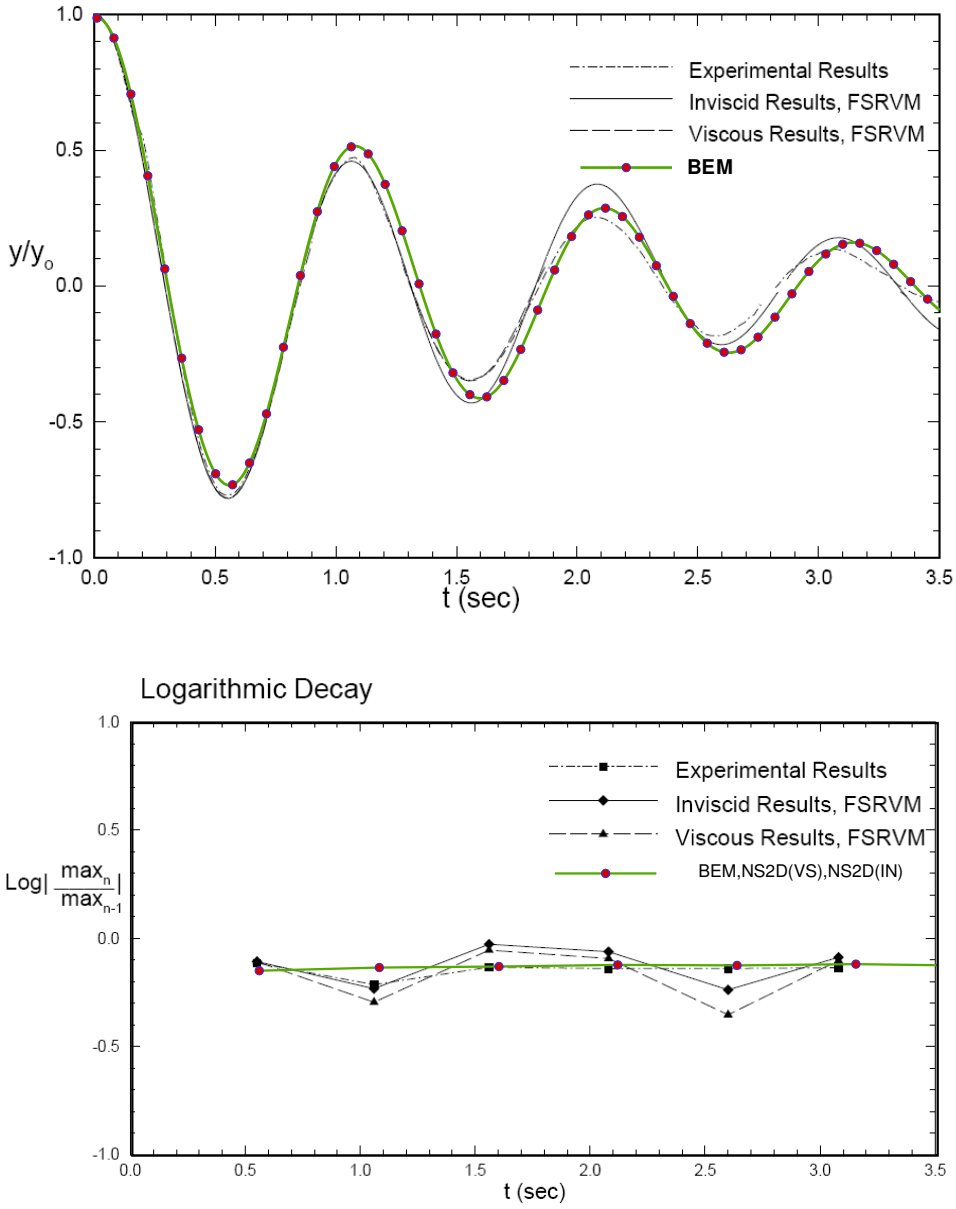

Figure 5.15: (top) Heave decay-response of hull predicted by the BEM scheme along with the experimental/numerical results presented in [Roddier 2000]; (bottom) Logarithmic heave-decay characteristics of the hull predicted by the BEM scheme along with the experimental/numerical results presented in [Roddier 2000]. NS2D(VS) : viscous version of the NS2D solver; NS2D(IN) : inviscid version of the NS2D solver

5.3 Summary

One of the objectives of the development of a potential flow solver presented in this chapter was the validation of the inviscid (IN) version of the NS2D solver. This has been met by extending the current scheme to study the dynamics of two-dimensional hull-sections (round-bilge) in both forced/prescribed and free-decay motions.

In the case of hull-sections subject to forced roll, the free-surface elevations predicted by the NS2D(IN) solver are found to be in good agreement with those from the present method. In addition, the pressure and velocities predicted on the hull surface are also in agreement.

It is known from experimental results that the effect of viscosity is not very significant in the case of heave. This observation gives credence to the extension of the present potential-flow method to study the free-decay of a hull-section in heave. Here too, the results obtained from the two solvers are found to be in good agreement. Moreover, no differences are observed in the viscous and inviscid free-decay responses. This is in accord with the observation that the effects of viscosity are negligible in the case of heave.

Most of the contents in this part of the thesis have been published in the papers [Vinayan et al. 2005], [Kinnas et al. 2007] and [Vinayan and Kinnas 2007].

Chapter 6

Ventilating Water-entry

The development of theoretical and numerical methods for the performance prediction of surface-piercing propellers is inherently complicated due to the presence of a free-surface. Some of the challenges involved are even more accentuated in the case of a three-dimensional analysis. To simplify the problem to a certain extent, a two-dimensional analysis is often used similar to a blade-element approach in air-screw theory [Milne-Thomson 1973, Furuya 1985].

Yim [Yim 1969; 1971; 1974] pioneered the development of theoretical methods to predict the performance characteristics of surface-piercing propellers by assuming a two-dimensional flow field, which is obtained by unfolding the cylindrical surface containing the blade element at a certain radius (see Figure 6.1). The two-dimensional flow field, in essence, consists of a horizontal layer of water - thickness of which is equivalent to the distance traveled by the leading edge of the blade element along the helical line during one revolution. The blade element enters the layer at the top and exits through the bottom part. This approach was applied by Yim [Yim 1969; 1971; 1974] to develop a linear theory for the entry-and-exit of a thin foil and a base-vented symmetric wedge. Cox [1971] studied the linear water-entry problem both theoretically and experimentally. Wang [Wang 1977; 1979] applied the same approach as Yim to blade profiles with full ventilation and also extended the scheme for an oblique entry-and-exit. Another notable work based on linear theory is that of Terent'ev [1979].

Common to all the above theoretical methods is the linearization of the blade

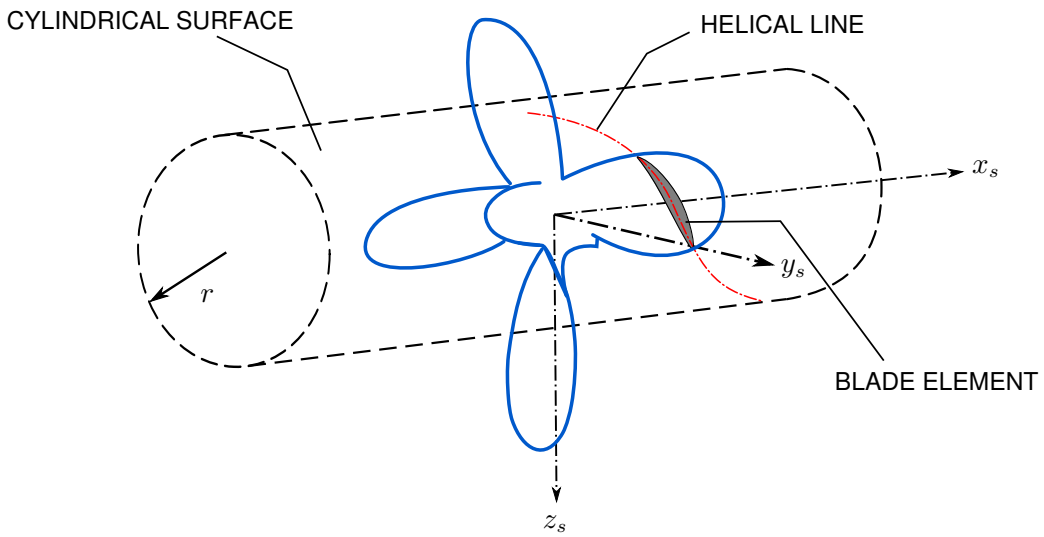

Figure 6.1: Marine propeller : concept of cylindrical surface, blade element and helical line. Sketch based on figures in [Carlton 2007]

and ventilated cavity surfaces assuming that both are thin. [Yim 1969; 1971; 1974], [Wang 1977; 1979] and [Terent'ev 1979] based their methods on an infinite Froude number (no gravity) approximation for the free-surface assuming that the duration of the entry-and-exit event is short and the velocity of entry is high. An exception to this is the method of [Cox 1971] that considered an arbitrary entry speed and included the effects of gravity.

Very few theoretical methods exist that take into account the full nonlinearity of the ventilating problem. Two notable works include that of Chekin [1989] and Faltinsen and Semenov [2008]. Both the methods solved the ventilating entry of a semi-infinite flat plate within the precepts of self-similarity. The application of the above linear and nonlinear theories is limited to simple geometries, and the effect of gravity cannot be considered explicitly. These two shortcomings provide the motivation for this work - *The development of a numerical method with fully nonlinear free-surface boundary conditions that considers the effects of gravity explicitly and*

that can be applied to the ventilating entry of arbitrarily shaped blade sections.

6.1 Physical Assumptions

The physical assumptions made in the modeling of the ventilating problem are as follows:

(i) The flow is considered to be inviscid and irrotational. The speed of entry is high enough to limit the effects of viscosity to a thin boundary layer along the body.

(ii) The dynamics of the surrounding air is neglected except for maintaining the ventilated cavity interface/free-surface at a constant pressure - in the case of ventilation, the cavity is maintained at atmospheric pressure.

(iii) The fluid is incompressible assuming that the speed of entry is less than the speed of sound. This assumption maybe violated locally at the instant of impact of the leading edge with the water surface due to the large accelerations.

(iv) The effects of surface tension are ignored - it primarily affects spray formation in the splash region.

(v) The propeller blade section is assumed to be rigid. This neglects any possible interaction between the fluid and the blade section due to vibration (the propeller blade vibrates as a consequence of the cyclic loading and unloading as it enters and exits the water surface).

6.2 Unique aspects of the flow

Inception of ventilation : The inception of ventilation is too complicated a process to be modeled accurately within the framework of potential theory. All

of the linear and nonlinear theoretical models assume the foil to be ventilating from the very beginning, with ventilation starting at the leading edge.

Detachment locations : The ventilated surface is nothing but a cavity that vents into the atmosphere and is maintained at atmospheric pressure. An important aspect of cavity flows is the problem of specifying the detachment location - the point at which the cavity separates from the body surface [Birkhoff and Zarantonello 1957, Gilbarg 1960]. Fixed detachment is appropriate for cases where the point of detachment of the cavity is known *a priori*, for example, bodies with sharp leading edges. For smooth foils, say with round leading edges, the cavity detachment location is not known beforehand and has to be determined as a part of the solution. Since typical surface-piercing propeller sections have sharp leading edges, the ventilated cavity is assumed to start right at the leading edge.

Brillouin-Villat Condition : The Brillouin-Villat (B-V) condition implies that *the curvature of a free streamline at detachment is either finite or equal to that of the fixed boundary at the separation point.* The B-V condition can be better understood through the example of a supercavitating flat plate in an unbounded flow domain (based on the cavity free-streamline theory of [Wu 1972]). The curvature of the cavity surface or the free-streamline is same as that of the flat-plate near the leading edge, as seen in Figure 6.2.

6.3 Vertical Entry

6.3.1 Previous Work - SPPAN (Linear Model)

[Savineau and Kinnas 1995, Savineau 1996] solved the flow field around a fully ventilated two-dimensional surface-piercing hydrofoil using a time-marching lower-order boundary element method. The method solved for the shape of the ventilated

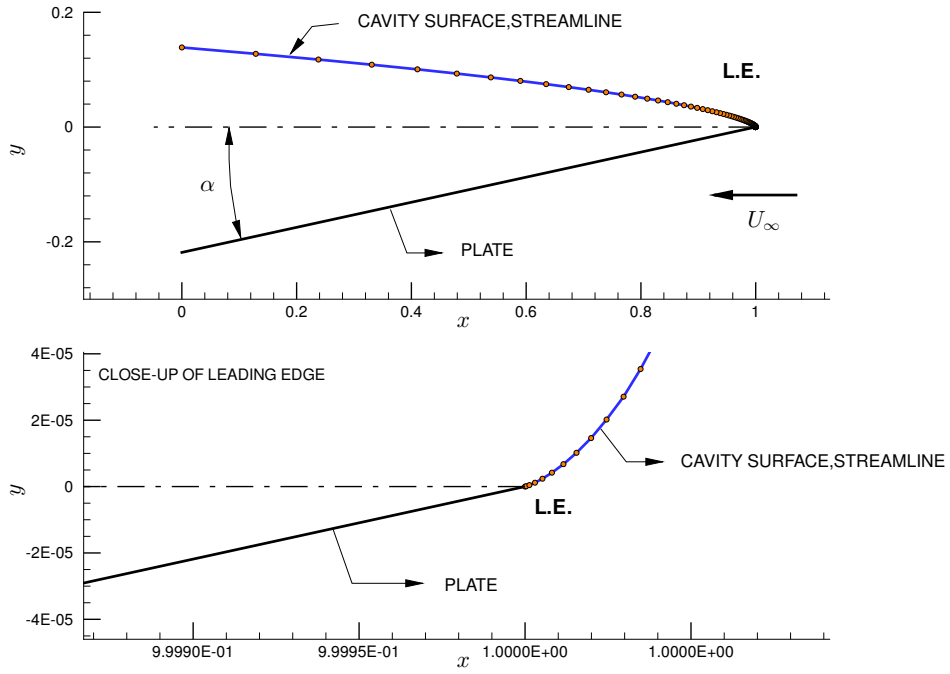

Figure 6.2: Brillouin-Villat Condition : The curvature of the cavity surface near the leading edge is finite. Based on the free-streamline theory of [Wu 1972]. α is the angle of attack, U_∞ is the free-stream velocity.

cavity and the pressure on the surface of the hydrofoil in the entry-phase. The important characteristics of the method are as follows:

(i) The flow is solved with respect to a coordinate system that moves along with the foil, as shown in Figure 6.3. In Figure 6.3, U_∞ is the vertical velocity of entry of the hydrofoil, u,v are the horizontal and vertical components of the perturbation velocity, $\vec{q}$ is the total velocity with $|\vec{q}| = \sqrt{(U_\infty + v)^2 + u^2}$, α is the angle of attack, c is the chord length and y_{fs} is the instantaneous location of the free-surface at time t.

(ii) The vertical velocity of entry (U_∞) is assumed to be sufficiently high for ventilation to start at the sharp leading edge of the foil and form a cavity along the suction side.

(iii) An infinite Froude number (F_n) is assumed with

$$F_n = \frac{U_\infty}{\sqrt{gc}} \tag{6.1}$$

where g is the acceleration due to gravity. With this assumption, the free-surface boundary conditions are linearized and the effects of gravity are neglected.

(iv) The total potential, hence the velocity field, is decomposed into inflow and perturbation components. A boundary-value problem is solved to obtain the perturbation potential at each time-step of the time-marching scheme.

(v) The linearized free-surface boundary conditions are enforced using a "*negative*" image method as shown in Figure 6.4.

(vi) The ventilated cavity shape is found iteratively by aligning the panels with the flow and at convergence the cavity surface is tangent to the flow.

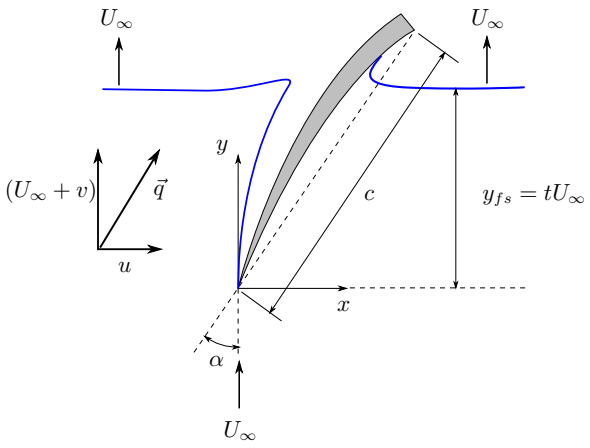

Figure 6.3: SPPAN : Surface piercing hydrofoil with coordinate system moving with the foil

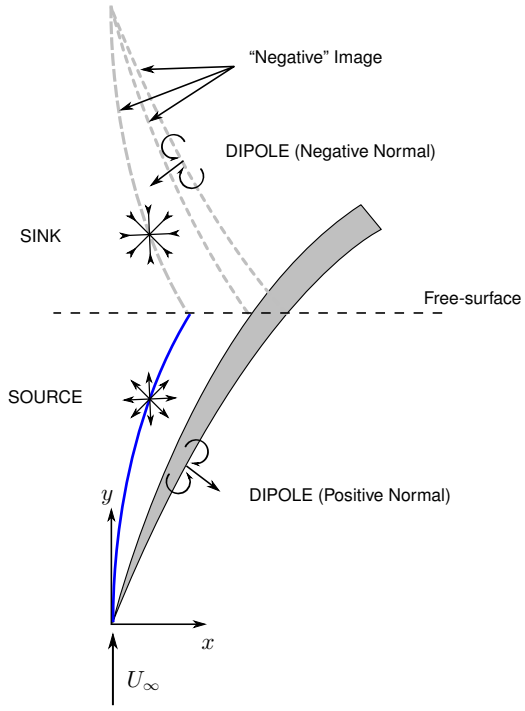

Figure 6.4: SPPAN : Actual foil, cavity surface and corresponding images

6.3.2 Current work - Mathematical Formulation

Consider a rigid, 2-D hydrofoil entering an initially calm domain with a constant velocity $\mathbf{V}(t)$ and an angle of attack α, as shown in Fig. 6.5. An ideal fluid is considered and the flow is assumed to irrotational. A *fixed* (non-rotating) Cartesian coordinate system is chosen to represent the flow with its origin at the undisturbed water level. The flow is represented in terms of a harmonic function $\phi(\mathbf{x}, t)$ commonly referred to as the *velocity potential*. Also, the local fluid velocity is given as $\mathbf{u} = \nabla\phi = (\phi_x, \phi_y) = (u, v)$. Here, $\mathbf{x} = (x, y)$ represents the spatial location with respect to the fixed coordinate system, with x being the horizontal measure and y the vertical measure positive upward. The fluid domain and the corresponding boundary surfaces are shown in Figure 6.5. $S_{\mathbb{WB}}(t)$ represents the "*wetted*" part of the hydrofoil surface, $S_{\mathbb{F}}(t)$ is the free-surface that also includes a part of the ventilated surface on the

suction side of the hydrofoil and S_∞ is the far-field boundary placed *far* enough to minimize interference.

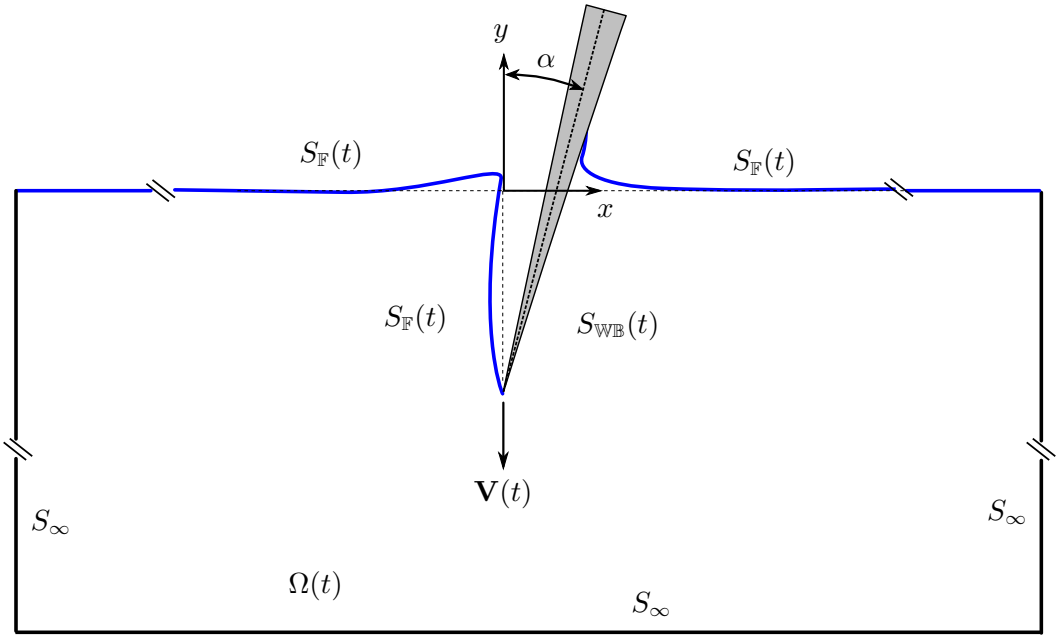

Figure 6.5: Ventilating entry of a hydrofoil section : Fluid domain and corresponding boundaries

• **Boundary Condition on Hydrofoil $S_{\mathbb{WB}}(t)$**

On the "wetted" part of the hydrofoil surface $S_{\mathbb{WB}}(t)$,

$$\nabla\phi \cdot \mathbf{n} = \mathbf{V}(t) \cdot \mathbf{n}, \quad \mathbf{x} \in S_{\mathbb{WB}}(t) \tag{6.2}$$

where $\mathbf{V}(t)$ is the prescribed velocity of the hydrofoil.

• **Boundary Condition on Far Field Boundary S_∞**

The far-field boundary S_∞ is assumed to be a no-flux surface with

$$\nabla\phi \cdot \mathbf{n} = 0; \quad \mathbf{x} \in S_\infty \tag{6.3}$$

and special attention is paid to place the boundary far away from the body to avoid reflection.

• **Initial Conditions**

The initial conditions for this problem depend on the angle of attack α and the existence of a ventilated cavity on the suction side of the hydrofoil. The treatment of the fully ventilating case requires special attention. For a hydrofoil with a sharp leading edge, ventilation is triggered right at the leading edge. However, during the process of the development of the method it was found extremely difficult to numerically *trigger* ventilation at the leading edge. According to [Wang 1977] the flow field surrounding a ventilating foil is identical to that of supercavitating flat plate (in an unbounded fluid domain) with zero cavitation number. This aspect of the flow forms the basis for getting the initial conditions for the ventilating flow. The proposed model consists of the following steps : (i) Assume an initial shape of the ventilated cavity - the initial shape is derived from the analytical expressions for the supercavity produced by a flat plate in an infinite flow domain. These expressions are obtained from the free-streamline theory of [Wu 1955]. The initial cavity length is assumed to be a fraction of the chord-length of the hydrofoil. (ii) Instead of being treated as a free-surface, the initial shape of the ventilated cavity is assumed to be rigid or wetted. With this assumption, the free-surface problem is solved as an asymmetric water entry. (iii) After the hydrofoil has traveled a certain extent, a part of the initial cavity assumed to be wetted is appended to the adjoining free-surface. (iv) The actual solution of the ventilating problem starts from this point onwards. The intersection of the initial ventilated cavity (modeled as wetted) and the free-surface is treated as a fixed separation point. The solution is allowed to progress with the free-surface on the suction side continuously detaching from the intersection point. A graphical representation of the treatment at the leading edge is shown in Figure 6.6.

• **Treatment at a fixed separation point**

At the fixed separation point, the normal velocity of the free-surface is assumed

to be the same as that of the hydrofoil. This assumption assures continuity of slope between the wetted body and the ventilated surface. This is consistent with the analytical solution for the local flow presented in [Faltinsen 2005] and [Zhao et al. 1996]. The potential is inherently continuous by virtue of the use of linear isoparametric elements. The boundary integral equation is not solved at the separation point as both the primary variable (ϕ) and the secondary variable (ϕ_n) are known.

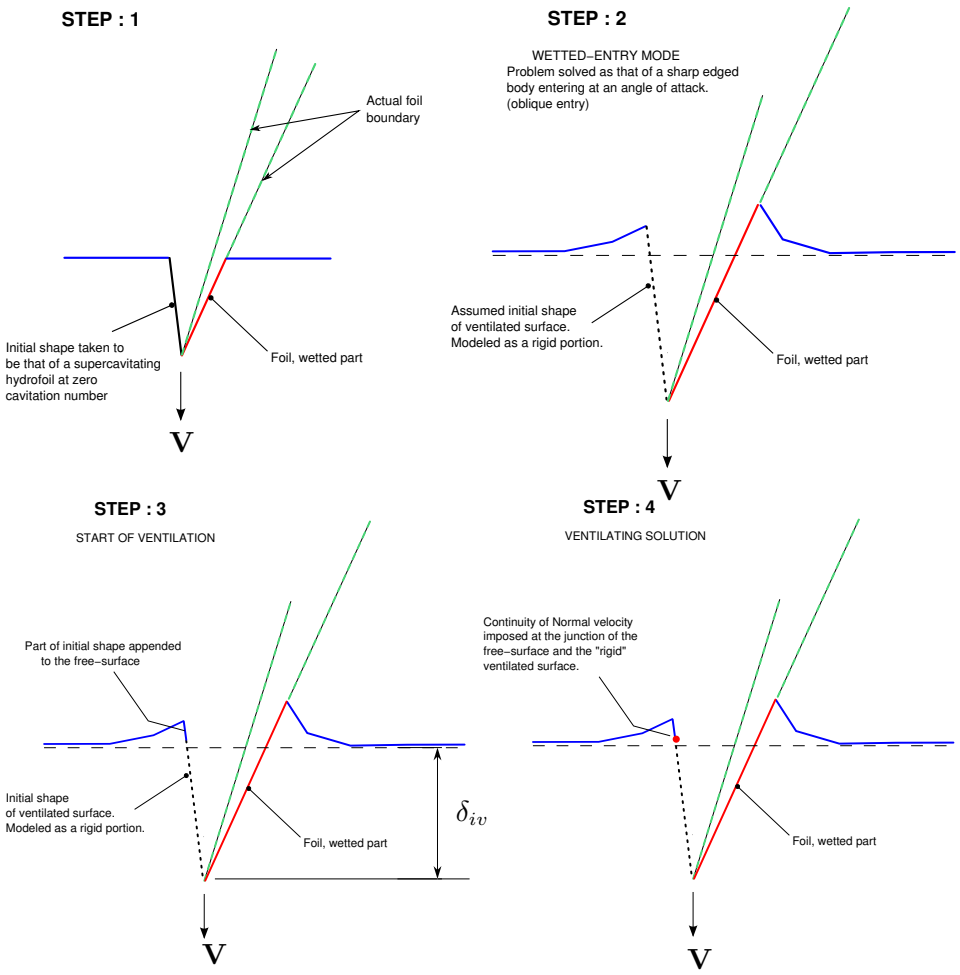

Figure 6.6: Ventilating entry: Graphical representation of the treatment at the leading edge

6.3.3 Results

[Cox 1971] conducted a series of experiments with a symmetric wedge of dimensions 0.5" (12.7 mm) by 6" (152.4 mm) with a chord length of 6". In the experiments, the wedge was dropped from different heights (equivalent to changing the velocity of entry V_w) and at different angles of attack, α. For each instance, the ventilated cavity shape was photographed after the wedge had approximately traveled its length through the water surface. These photographs provide an excellent source of validation for the BEM model. As a representative case, a velocity of entry of 2.45 m/s (corresponding to a drop of 12") is chosen for validation. All the subsequent BEM results correspond to this geometry and velocity.

Effect of initial condition

It was mentioned in the numerical formulation that an initial guess for the ventilated cavity shape is obtained from the corresponding solution of a supercavitating flat plate. The length of the initial guess is expressed as a percentage of the total chord c of the hydrofoil and is represented by the parameter δ_{iv}. Figure 6.7 shows the effect of the parameter δ_{iv} on the final ventilated cavity shape (the simulation is stopped once the free-surface on the wetted side reaches the base of the wedge). In terms of a chord length $c = 152.4$ mm, the minimum δ_{iv} of $2\%c$ would be about 3mm, while the maximum would be about 7mm. On the whole, the parameter δ_{iv} does not effect the final shape of the ventilated cavity and the free-surface elevation on the wetted-side. Differences are observed in the region where the vertical part of the ventilated cavity meets the horizontal free-surface. The similarity solution of [Chekin 1989] and [Faltinsen and Semenov 2008] predict a cusp at the point where the two convex free-surfaces meet. This aspect of the flow is not considered in the numerical scheme and leads to the observed differences. Figure 6.8 shows the effect of δ_{iv} on the wetted-side pressure and no discernible differences are observed. (All the subsequent calculations are with $\delta_{iv} = 2\%c$.)

The convergence characteristics of the ventilated cavity shape with respect to a change in the number of panels on the cavity surface is shown in Figure 6.9, where $N_{\mathbb{F},s}$ represents the number of panels on the entire free-surface, including the ventilated cavity, on the suction side of the hydrofoil.

Effect of gravity

Figures 6.10 and 6.12 respectively show the ventilated cavity surfaces for different levels of submergence, with ($g \neq 0$) and without ($g = 0$) the effects of gravity. Defining a Froude number in terms of the chord length c as $F_{nc} = V_w/\sqrt{gc}$, $g = 0$ would correspond to $F_{nc} = \infty$ and $g \neq 0$ to F_{nc}=2. (Note that in the figures, only the wetted boundary of the hydrofoil is shown. Although the thickness form is not shown, the ventilated cavity does not intersect the suction side of the hydrofoil). The effect of gravity becomes apparent when the free-surface elevations are expressed in terms of the similarity variables as shown in Figures 6.14. In the absence of gravity all the free-surface profiles, starting with the first instance when similarity is observed to the end of the simulation, are seen to overlap. The scheme is able to preserve the self-similarity of the flow. The lack of self-similarity, as expected, can be observed in Figure 6.14 when the effect of gravity is included. Figure 6.11 and 6.13 show the corresponding pressure distributions on the wetted part of the wedge.

Comparison with experiments

In Figure 6.15, a comparison between the predicted cavity surface and that observed from the experiments of Cox [Cox 1971] is shown for an angle of attack of 10°. The free-surface elevation and the ventilated surface are compared for the same level of submergence. There appears to be two lines representing the ventilated cavity surface in the photograph. Cox [Cox 1971] attributes this to the presence of glass walls that form the boundaries of the experimental tank set-up. The outline farthest away from the wedge that is generally convex to the fluid is presumably the

location of the boundary layer attachment on the glass. This layer is formed due to the large retarding forces experienced by the fluid particles close to the glass surface. Cox [Cox 1971] mentions that the inner line represents the actual cavity shape over most of the chord. Based on these observations, it can be seen that the overall agreement between the predicted and the experimental ventilated cavity surfaces is good.

A similar comparison between the experimental and predicted results is shown in Figure 6.16 for smaller angles of attack of 0°, 2° and 4° respectively. In each of these cases, the experimental photographs indicate that there is no ventilation on the suction side of the wedge. In line with these observations the numerical predictions are performed with both sides of the wedge wetted, i.e., the pressure and suction sides of the wedge are assumed to be fully wetted (unlike the ventilating case where the suction side is not wetted). The fully-wetted formulation presented along with the validation studies is used here with the wedge entering the water surface at the specified angle of attack. For all the three angles of attack considered here, the comparison between the predicted and experimental results is satisfactory.

Comparison with multiphase model

The BEM model is based within a framework of potential flow, which neglects the real fluid effects of viscosity and surface tension. A FLUENT based multiphase model, the details of which are presented in Appendix D, is used to gauge the deficiencies if any in neglecting these effects. Figure 6.17 shows a comparison of the ventilated surface on the suction side along with the free-surface elevation on the pressure side of the wedge predicted by the multiphase and BEM models. One of the differences observed is the peeling away of the free-surface jet from the surface of the wedge in the case of the multiphase model. During the initial stages of entry, the BEM model predicts a region of negative pressure close to the intersection point of the free-surface and the pressure side of the wedge. As the wedge penetrates further, this

region of negative pressure tends to disappear. The occurrence of negative pressure is due to the assumption in the BEM model that the fluid particles initially in contact with wedge surface will always stay in contact as no gaps are allowed in the physical domain. In the multiphase model, no such assumption is necessary. Once a region of negative pressure is encountered, the fluid particles no longer stay in contact with the wedge surface and behave approximately as free projectiles moving under the influence of gravity [Greenhow 1987]. A comparison of the pressure distributions, as seen in Figure 6.18, shows that the pressures predicted by the two methods are not affected by this aspect.

The second difference is the occurrence of instabilities at the air-water interface in the multiphase model. One possibility is that these are Rayleigh-Taylor instabilities occurring as a result of the dynamic interaction between the air and water mediums. The BEM model cannot predict these instabilities as it neglects viscosity and the dynamic effects of the surrounding air. In spite of these differences, the overall agreement between the BEM and multiphase models is satisfactory.

In terms of CPU time, the total simulation time upto the point of comparison for the BEM scheme is about 1 hr, while for the FLUENT simulation is 50 hrs (wall-time for a parallel run with 8 nodes. Single node - 1.6 GHz AMD Opteron Dual-core processor with 4GB RAM). The above mentioned simulation times are for Δt=1e-5 s with 500 panels in the BEM scheme and approximately 460000 cells in the multiphase model. The BEM scheme has a definite advantage in predicting the ventilated cavity shapes in terms of the CPU time.

Comparison with SPPAN (linear free-surface model)

A comparison of the pressure distribution along the wetted face, between SPPAN (linear) and the current nonlinear method is shown in Figure 6.20. The linear method is clearly deficient in terms of capturing the excess pressure due to the nonlinear free-surface effects. The excess pressure corresponds to the region $y > 0$ where $y = 0$

corresponds to the undisturbed free-surface level. This difference was shown to exist even in the very early stages of entry in [Vinayan and Kinnas 2008]. Figures 6.19 and 6.20 highlight the shortcomings of the negative-image method and the importance of including the nonlinear free-surface effects in the 3-D PROPCAV model.

Effect of Froude number and angle of attack

Olofsson [1996] mentions that in the fully ventilated regime, the effect of the Froude number is negligible when $F_n > 3$. This is because the ventilated cavities have asymptotically attained their final shapes and a subsequent increase in the Froude number makes no difference. A similar observation can be made from the 2-D solutions as shown in Figure 6.21. The ventilated cavity shapes are seen to converge rapidly towards the $F_{nc} = \infty$ ($g = 0$) shape.

Figure 6.22 shows the effect of the angle of attack on the ventilated cavity shapes ($g \neq 0$ corresponds to $F_{nc} = 2$). The cavity volume is seen to increase with a corresponding increase in the angle of attack. From the experimental results of [Cox 1971], no ventilation is seen for angles less than 6°. For the smaller angles of attack, the fully-wetted mode can be used instead to calculate the pressure on the wedge (see Figure 6.16).

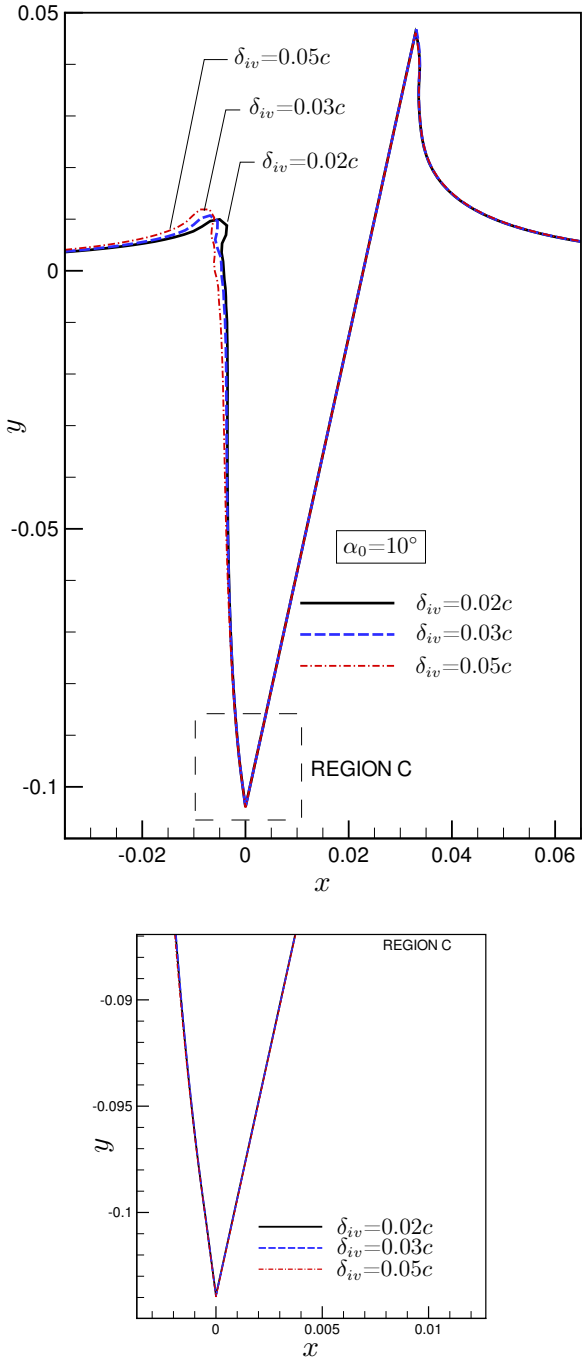

Figure 6.7: Ventilating entry of a surface-piercing wedge : Effect of the parameter δ_{iv} on the ventilated cavity shape. REGION C : Magnified view of the ventilated cavity shape close to the leading edge of the hydrofoil.

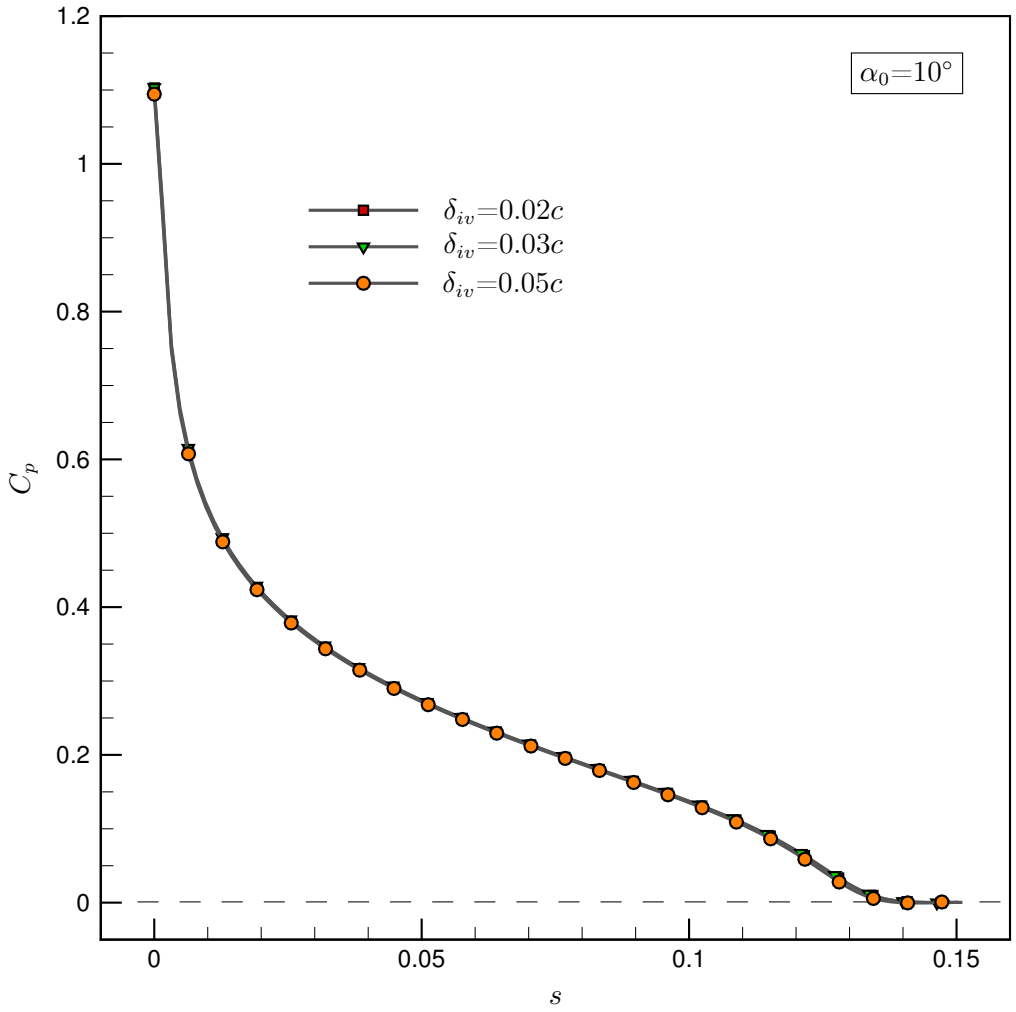

Figure 6.8: Ventilating entry of a surface-piercing wedge : Effect of the parameter δ_{iv} on the pressure predicted on the wetted part of the hydrofoil. C_p is the pressure coefficient, s is the arc-length along the wedge surface.

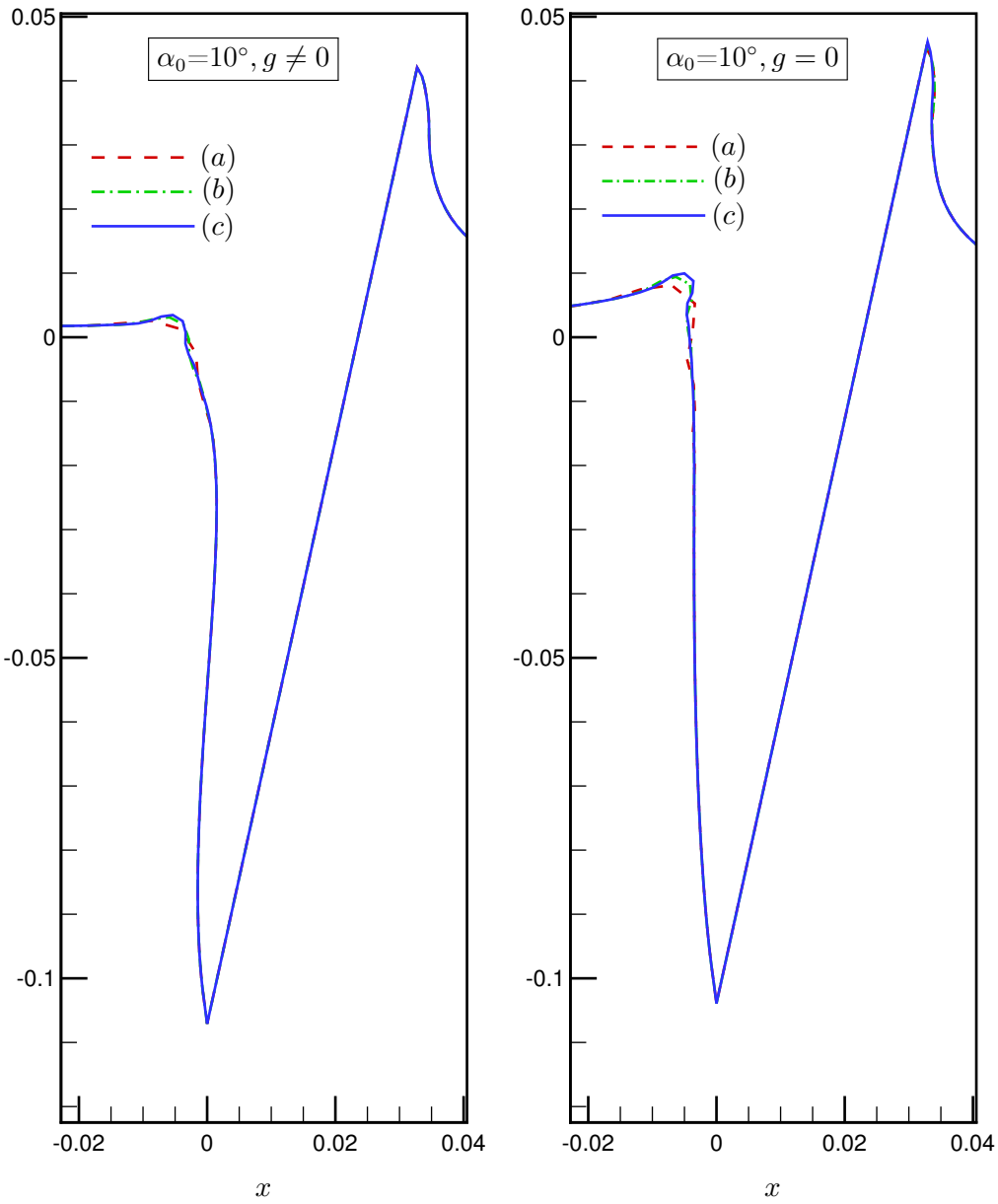

Figure 6.9: Ventilating entry of a surface-piercing wedge - Convergence characteristics of the ventilated cavity shape with respect to the number of panels on the cavity surface, (a) $N_{\mathbb{F},s}$=125, (b) $N_{\mathbb{F},s}$=215, (c) $N_{\mathbb{F},s}$=300.

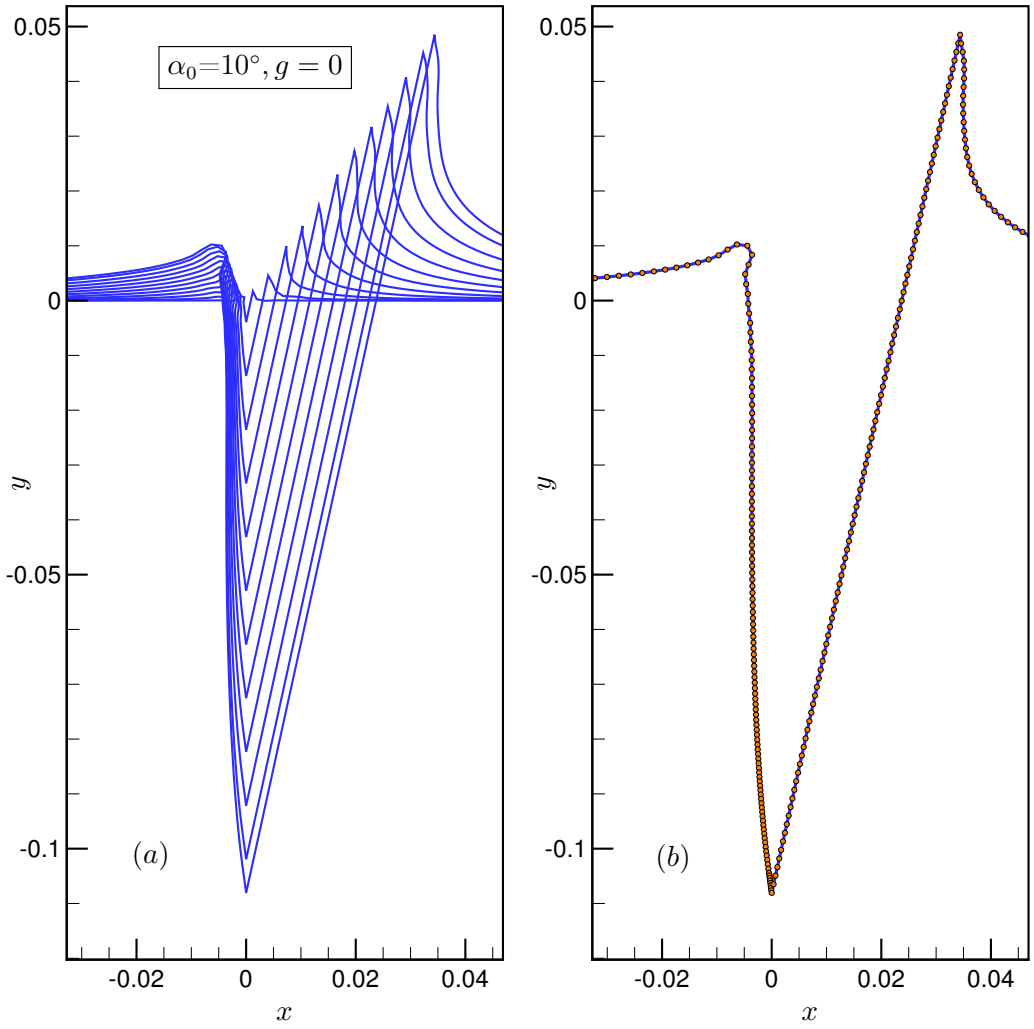

Figure 6.10: Ventilating entry of a surface-piercing wedge : Free-surface and ventilated cavity shapes predicted by the BEM scheme in the absence of gravity (g=0) (a) at different stages of entry (b) at time t_e=0.0419 s. Parameters of the simulation - Δt=1e-4 s, $N_{\mathbb{WB}}$=100, $N_{\mathbb{F}s}$=300, $N_{\mathbb{F}p}$=125, N_∞=40

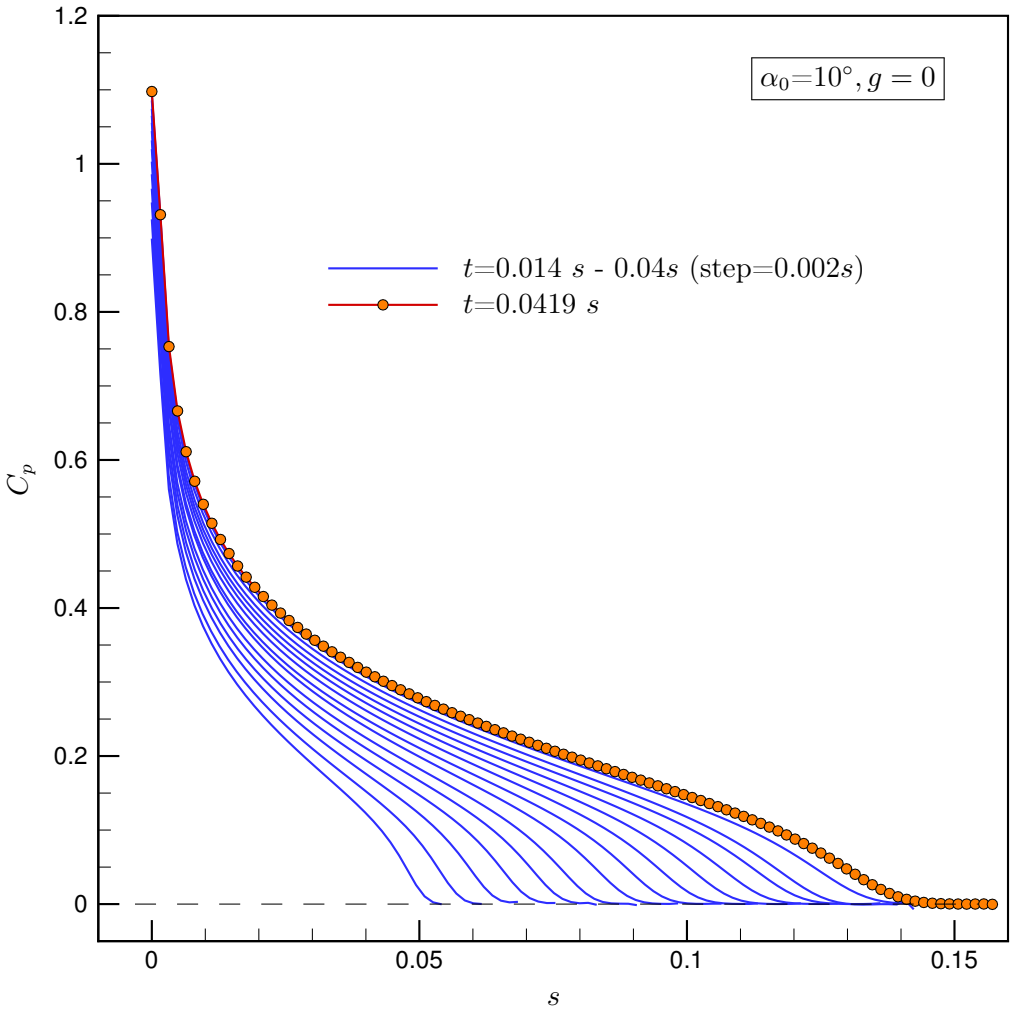

Figure 6.11: Ventilating entry of a surface-piercing wedge : Pressure along the wetted part of the hydrofoil at different stages of entry in the absence of gravity $g = 0$. Parameters of the simulation - Δt=1e-4 s, $N_{\mathbb{WB}}$=100, $N_{\mathbb{F}s}$=300, $N_{\mathbb{F}p}$=125, N_∞=40. C_p is the pressure coefficient

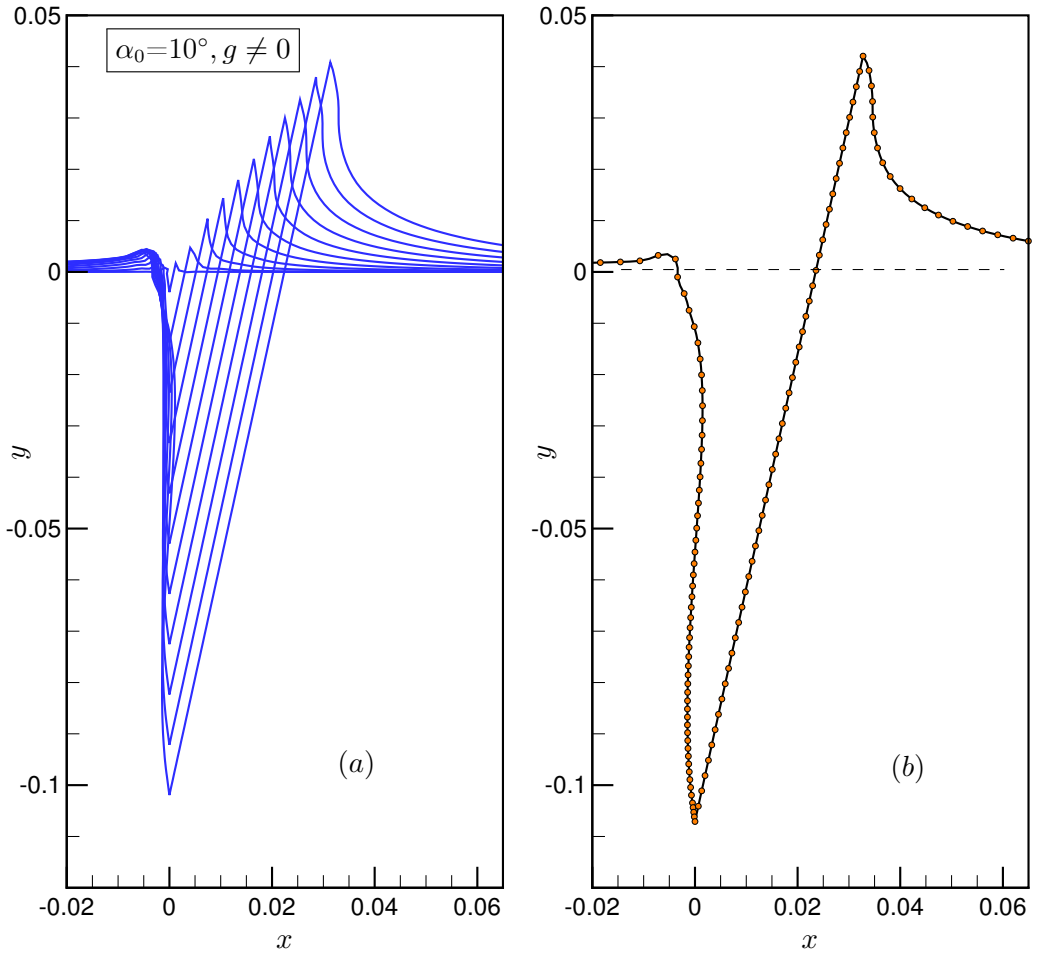

Figure 6.12: Ventilating entry of a surface-piercing wedge : Free-surface and ventilated cavity shapes predicted by the BEM scheme in the presence of gravity ($g \neq 0$) (a) at different stages of entry (b) at time time t_e=0.0432 s. Parameters of the simulation - Δt=1e-4 s, $N_{\mathbb{WB}}$=100, $N_{\mathbb{F}s}$=300, $N_{\mathbb{F}p}$=125, N_{∞}=40

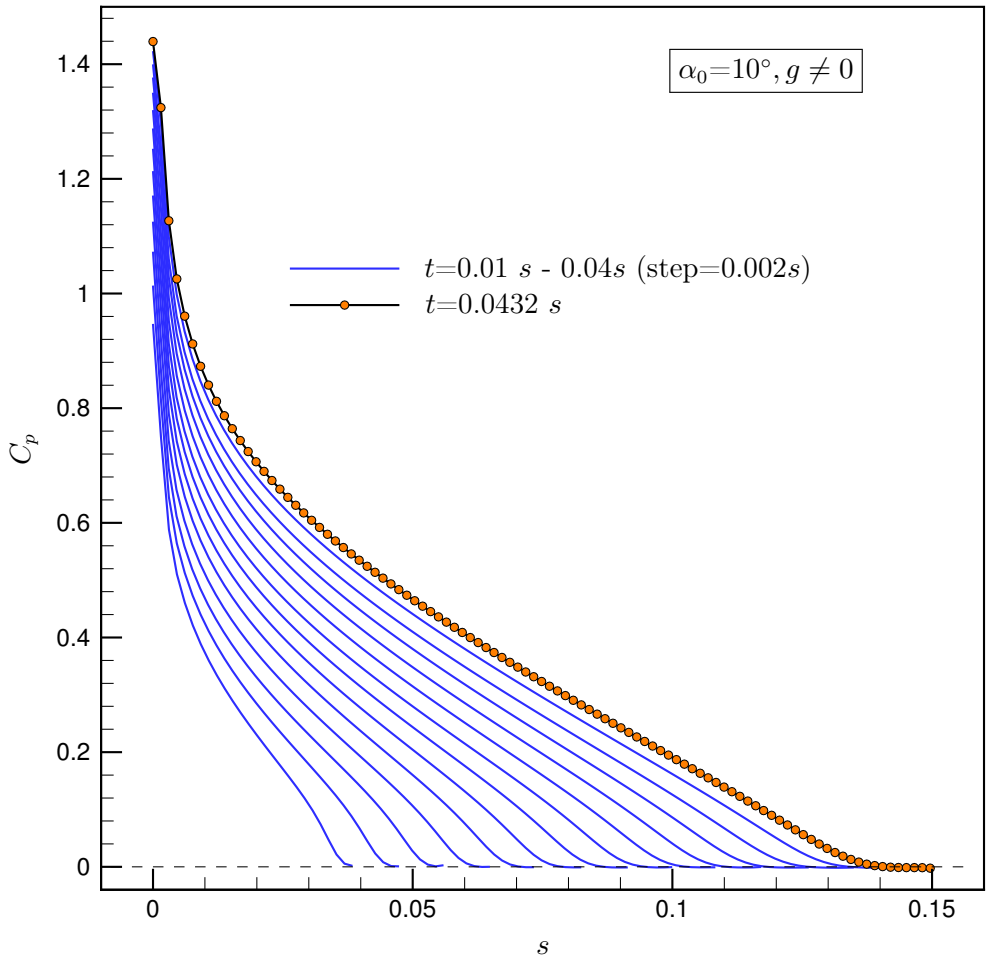

Figure 6.13: Ventilating entry of a surface-piercing wedge : Pressure along the wetted part of the wedge at different stages of entry in the presence of gravity ($g \neq 0$). Parameters of the simulation - Δt=1e-4 s, $N_{\mathbb{WB}}$=100, $N_{\mathbb{F}s}$=300, $N_{\mathbb{F}p}$=125, N_{∞}=40. C_p is the pressure coefficient

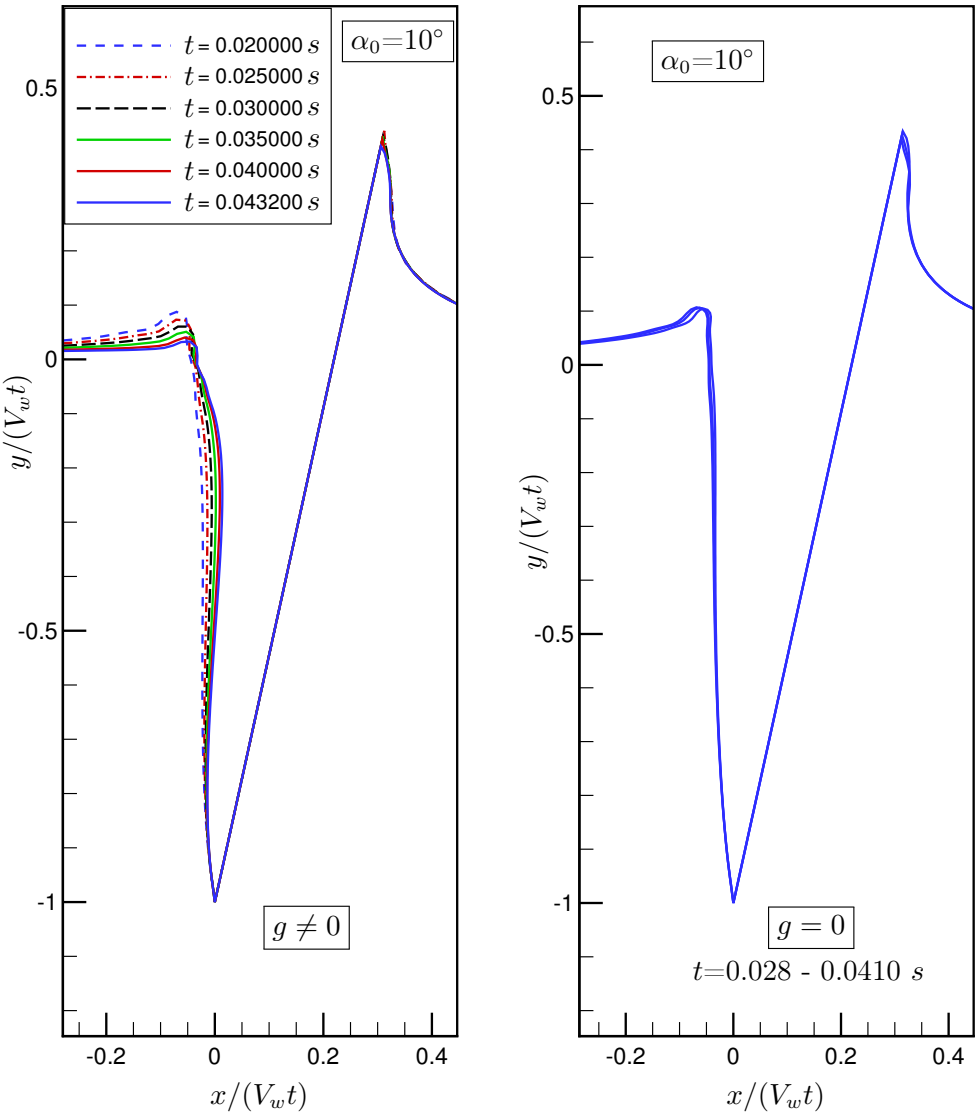

Figure 6.14: Ventilating entry of a surface-piercing wedge - Free-surface and ventilated cavity shape, with ($g \neq 0$) and without (g=0) the presence of gravity, at different stages of entry expressed in terms of the similarity variables.

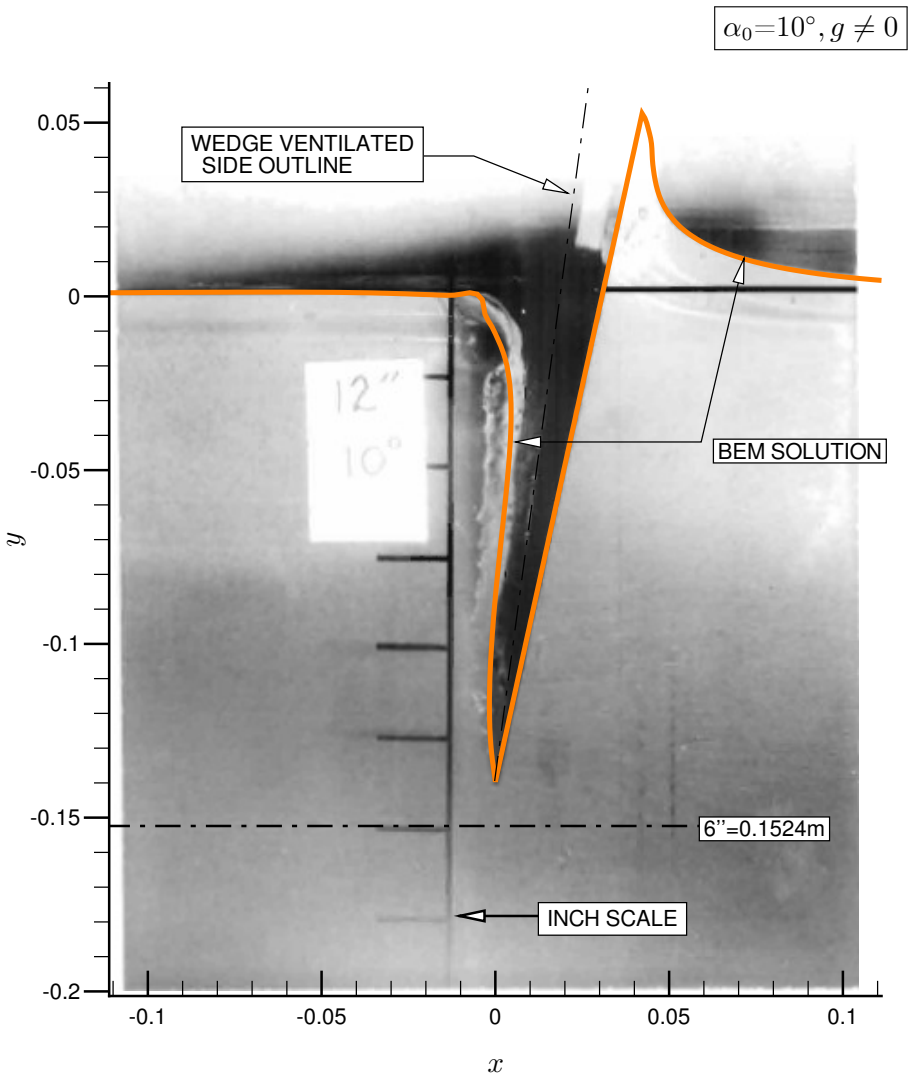

Figure 6.15: Ventilated cavity shape and free-surface : Comparison between experimental and numerical (BEM) results. V_w=2.45 m/s corresponding to a 12″ fall (Photograph of experimental result from [Cox 1971] used with permission)

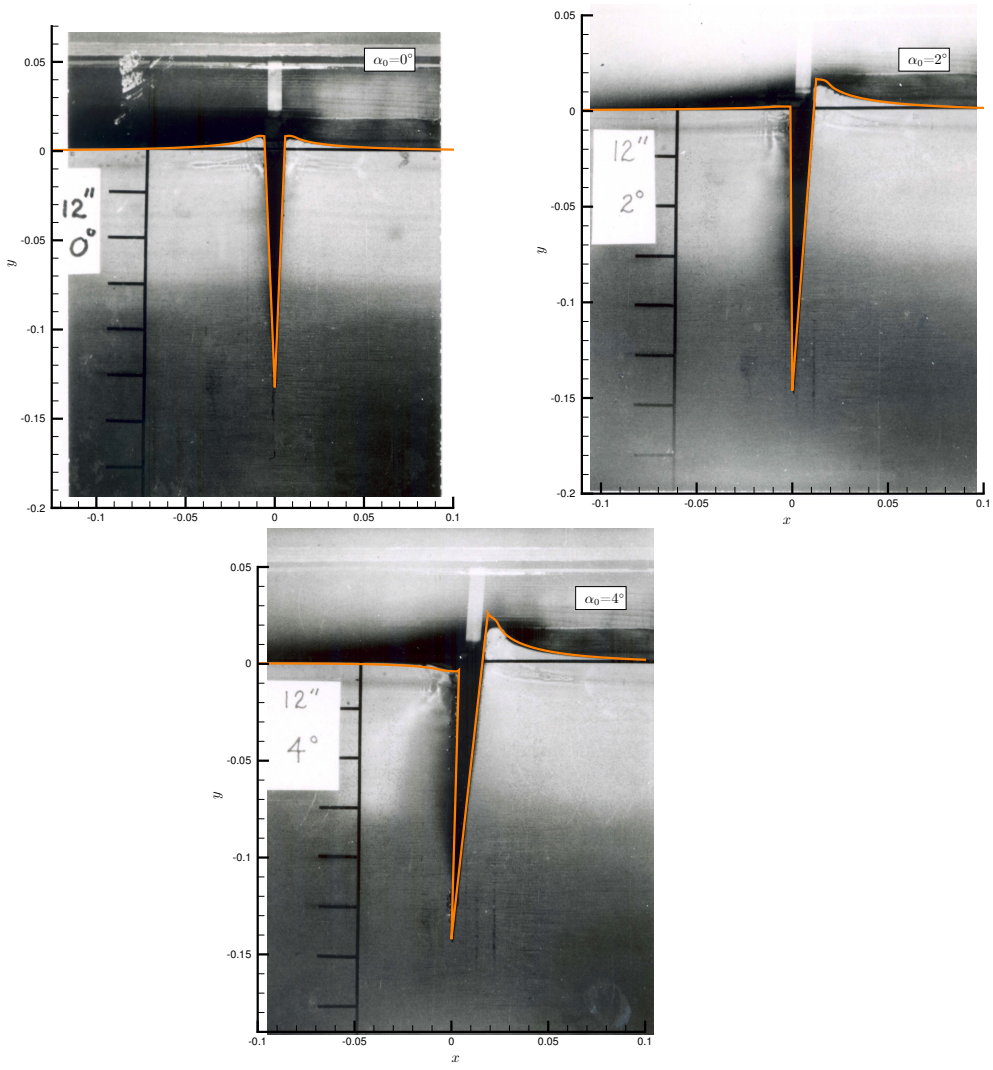

Figure 6.16: Ventilated cavity shape and free-surface : Comparison between experimental and numerical (BEM) results. V_w=2.45 m/s corresponding to a 12″ fall (Photograph of experimental result from [Cox 1971] used with permission). Effects of gravity included.

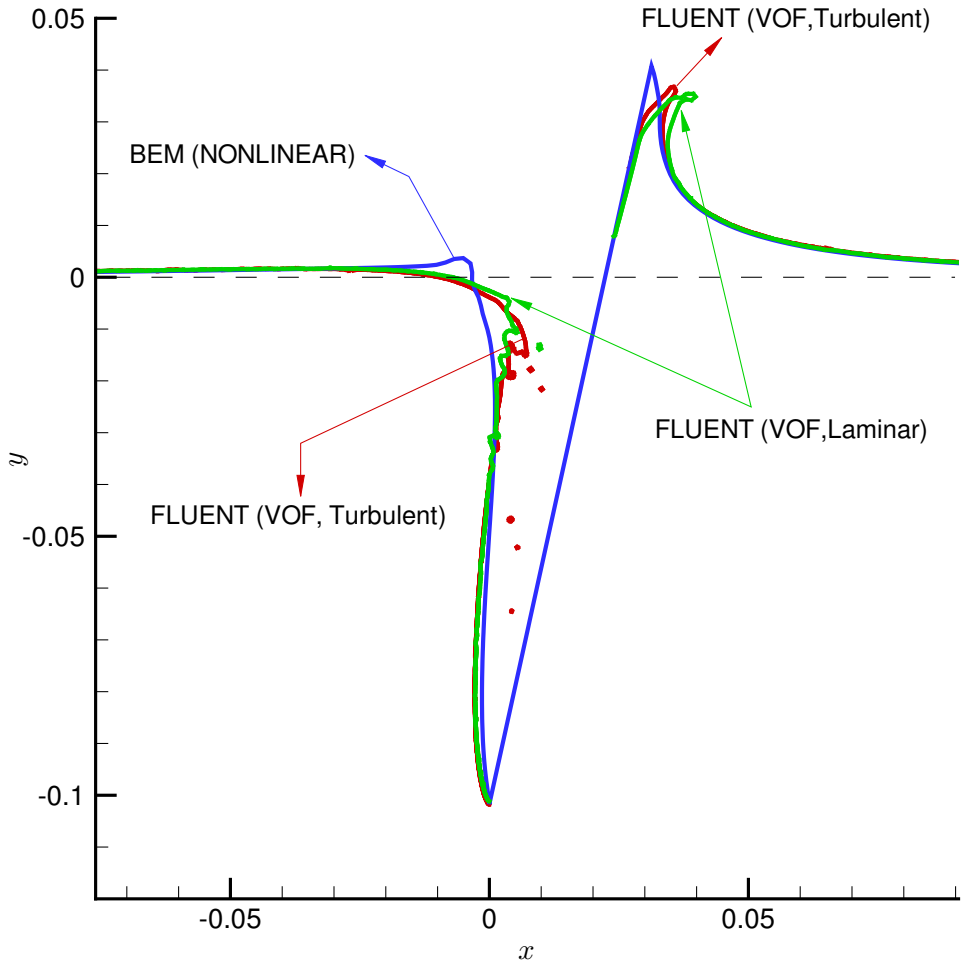

Figure 6.17: Ventilating entry of a surface-piercing wedge : Comparison of ventilated cavity shapes between FLUENT Multiphase (VOF with SST $k-\omega$ turbulence model), Fluent Multiphase (laminar) and BEM results. V_w=2.45 m/s corresponding to a 12″ fall. Angle of attack, α_0=10°.

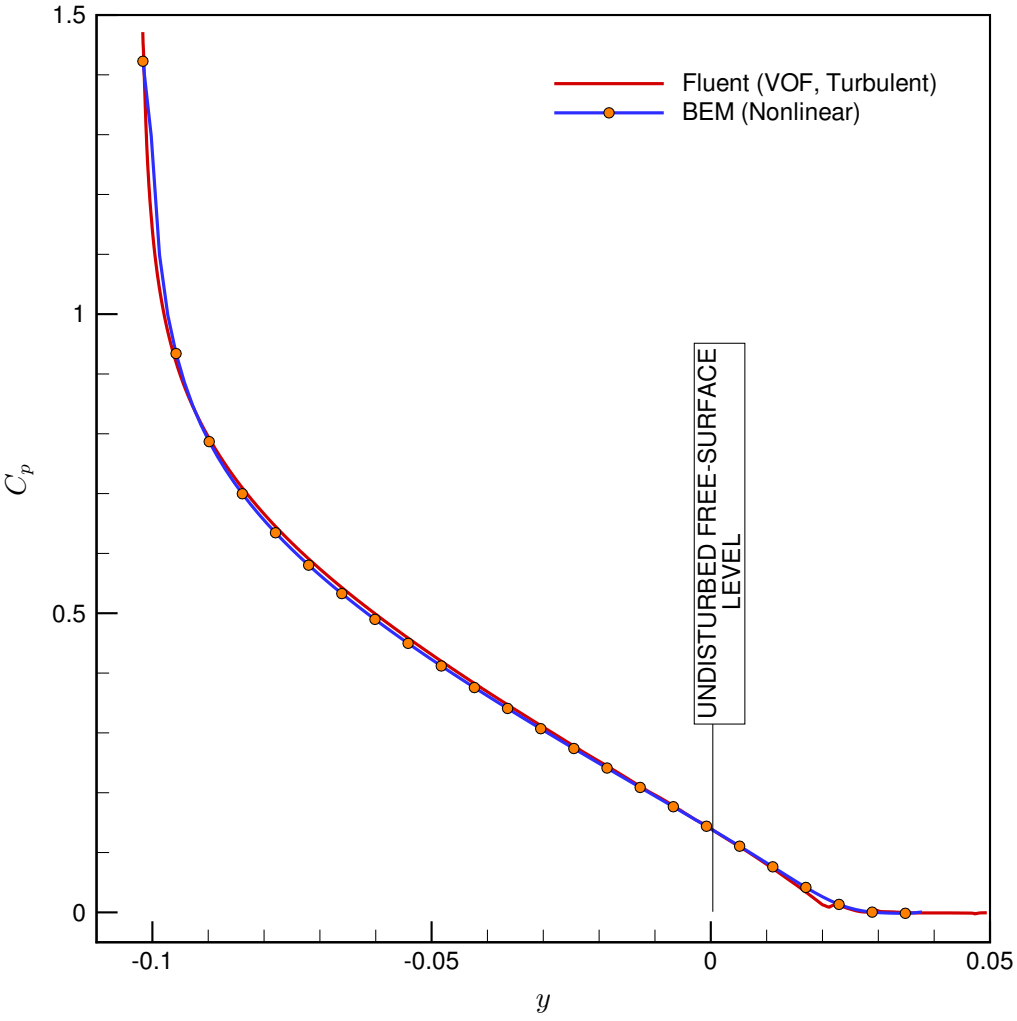

Figure 6.18: Ventilating entry of a surface-piercing wedge : Comparison of pressure along the wetted body surface between FLUENT Multiphase (VOF with SST $k-\omega$ turbulence model) and BEM results. V_w=2.45 m/s corresponding to a 12″ fall. Angle of attack, α_0=10°.

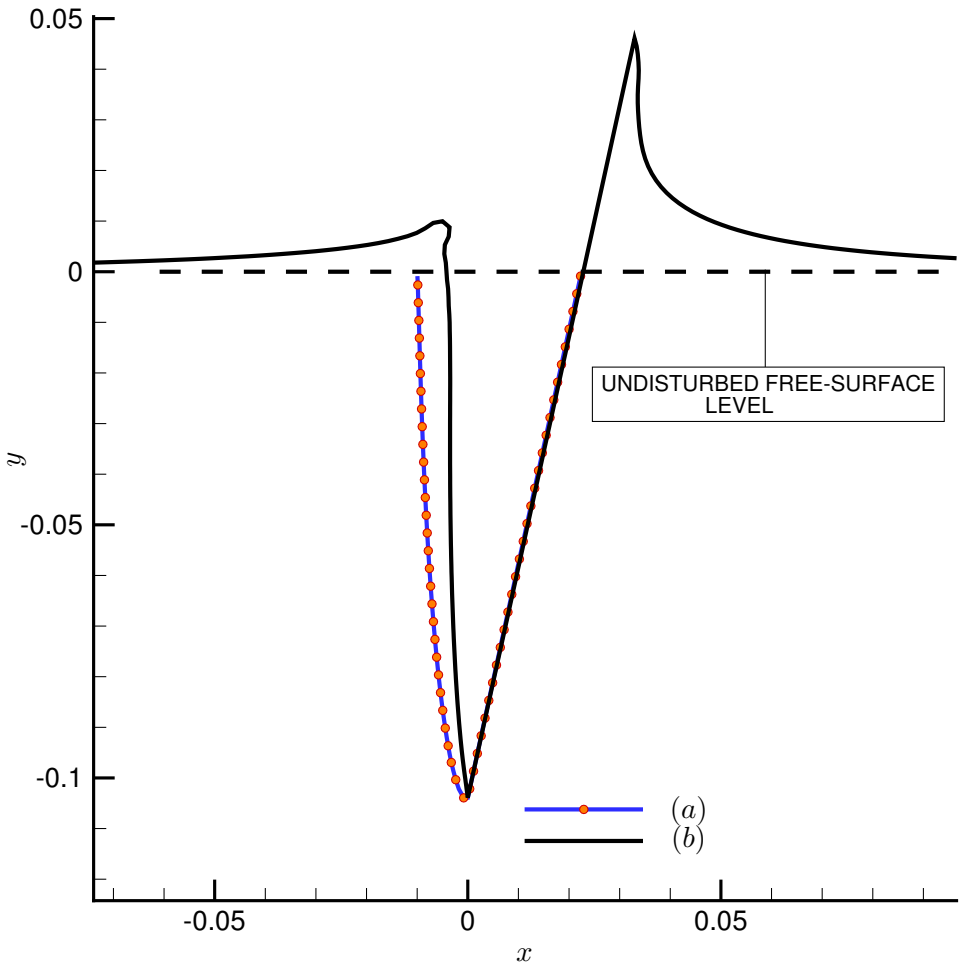

Figure 6.19: Ventilating entry of a surface-piercing wedge : Comparison of ventilated cavity shapes between (a) SPPAN-linear and (b) BEM-nonlinear methods. V_w=2.45 m/s corresponding to a 12″ fall. Angle of attack, α_0=10°.

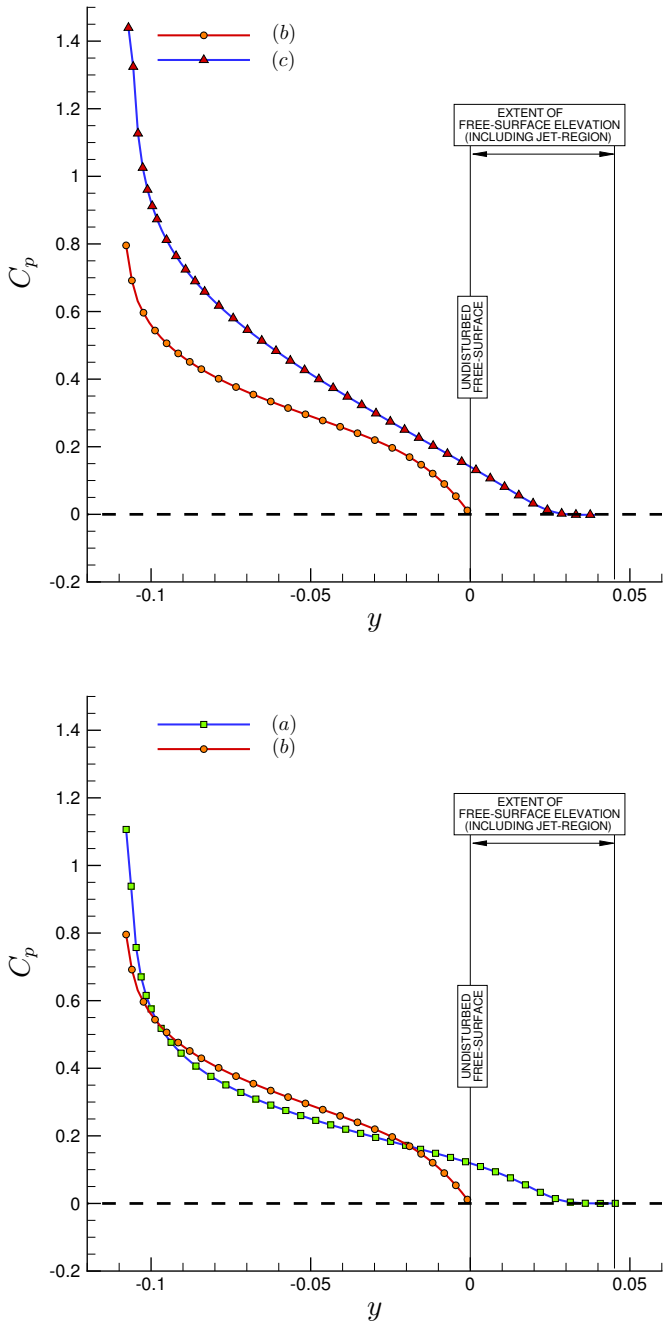

Figure 6.20: Ventilating entry of a surface-piercing wedge : Comparison of pressure along the wetted part of the hydrofoil SPPAN-linear and BEM-nonlinear methods. (a) BEM-Nonlinear (g=0), (b) SPPAN-linear (g=0), (c) BEM-Nonlinear ($g \neq 0$); V_w=2.45 m/s corresponding to a 12″ fall. Angle of attack, α_0=10°.

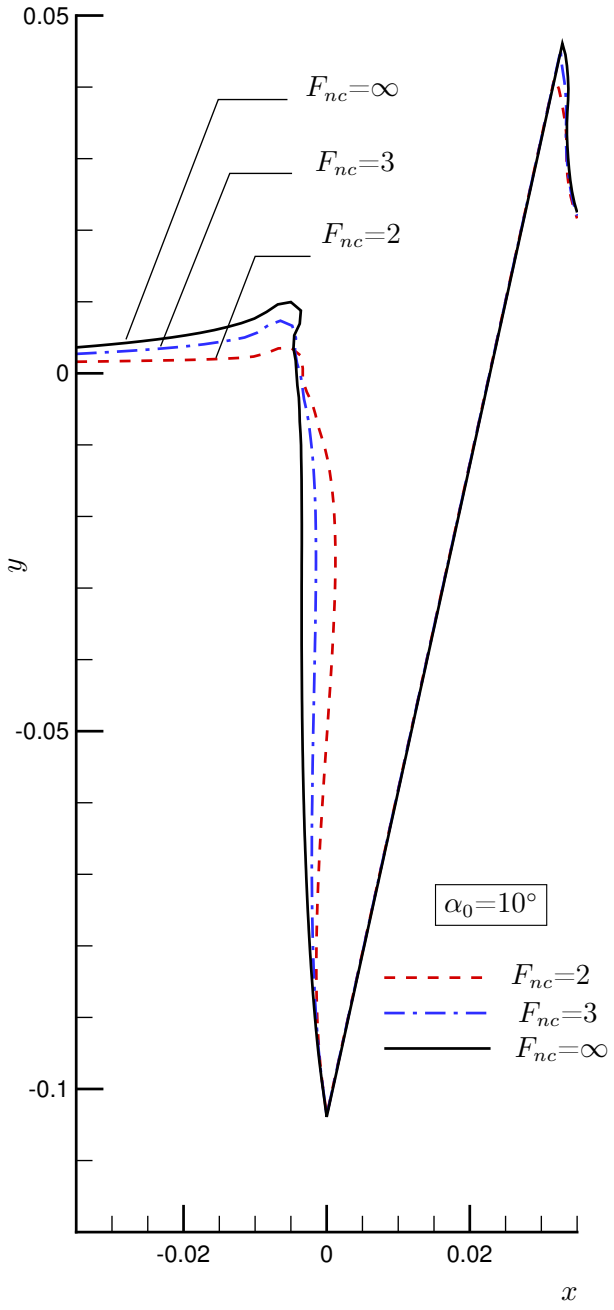

Figure 6.21: Ventilating entry of a surface-piercing hydrofoil : Effect of Froude number on the ventilated cavity shapes. F_{nc}=∞ corresponds to g=0. V_w=2.45 m/s for F_{nc}=2.0 and V_w=3.67 m/s for F_{nc}=3.0

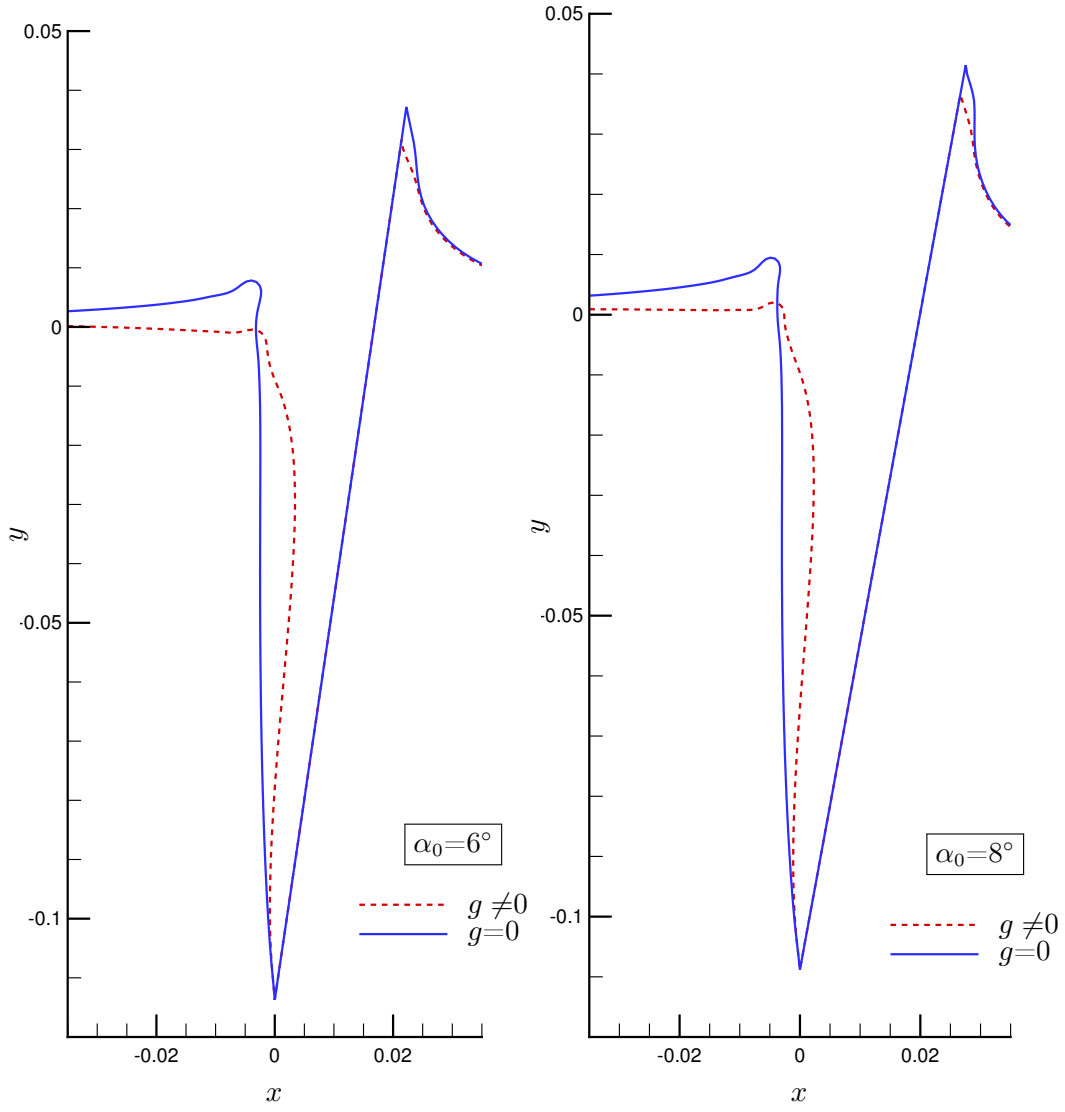

Figure 6.22: Ventilating entry of a surface-piercing hydrofoil : Effect of angle of attack on the ventilated cavity shapes with ($g \neq 0$) and without (g=0) the presence of gravity.

6.4 Rotating Entry

The two-dimensional approach of Yim [Yim 1969; 1971; 1974] is based on the concept of having the blade element pass through a horizontal layer of water sandwiched between semi-infinite expanses of air. This makes the problem of ventilating entry more amenable to mathematical modeling but difficult to realize in a numerical setting. As shown in Figure 6.1, the blade element of a marine propeller follows a helical path on a cylindrical surface and the two-dimensional approach was based on expanding this surface into a horizontal layer of water. An alternative approach that closely mimics the actual setting is to model the flow as seen in the plane of the propeller (the $y_s - z_s$ plane or as seen in the ship-fixed coordinate system).

The concept can be better understood from the two-dimensional sections of the ventilated cavity surface predicted on the propeller blade sections, as shown in Figure 6.23. The top part of Figure 6.23 shows the ventilated cavity surface in the x-z plane, along with the propeller section at mid-radius, at different angular positions. The actual rotational path of the propeller section, along with the ventilated cavity surface, is shown in the bottom part of Figure 6.23.

6.4.1 Initial Boundary Value Problem

The equivalent two-dimensional problem is that of a blade-section rotating with the propeller rotational speed ω at a radius r (the radius at which the propeller section is located) as shown in Figure 6.24. The fluid domain and its corresponding boundaries are as shown in Figure 6.24.

• **Boundary Condition on Hydrofoil $S_{\mathbb{WB}}(t)$**

On the "wetted" part of the hydrofoil surface $S_{\mathbb{WB}}(t)$,

$$\nabla\phi \cdot \mathbf{n} = \mathbf{V}(t) \cdot \mathbf{n}, \quad \mathbf{x} \in S_{\mathbb{WB}}(t) \tag{6.4}$$

where $\mathbf{V}(t)$ is the prescribed velocity of the hydrofoil.

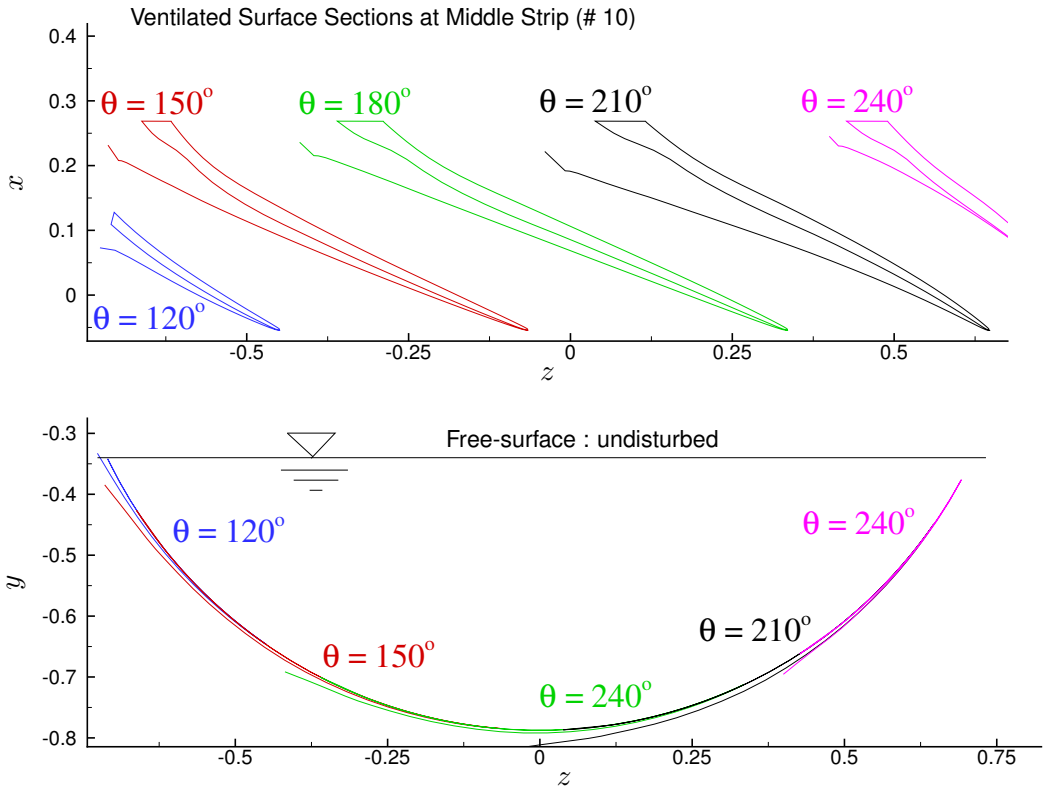

Figure 6.23: Rotating entry of a blade section : two-dimensional sections of the ventilated cavity surfaces predicted by PROPCAV. Taken from [Young 2002]

• **Boundary Condition on Far Field Boundary S_∞**

The far-field boundary S_∞ is assumed to be a no-flux surface with

$$\nabla\phi \cdot \mathbf{n} = 0; \quad \mathbf{x} \in S_\infty \tag{6.5}$$

and special attention is paid to place the boundary far away from the body to avoid reflection of the free-surface disturbance generated by its motion.

The solution of the problem is similar to the vertical entry case upto the point the hydrofoil/blade-section is fully immersed. Once the hydrofoil is immersed completely, the flow is assumed to leave tangentially from the trailing edge with it being treated as a fixed separation point.

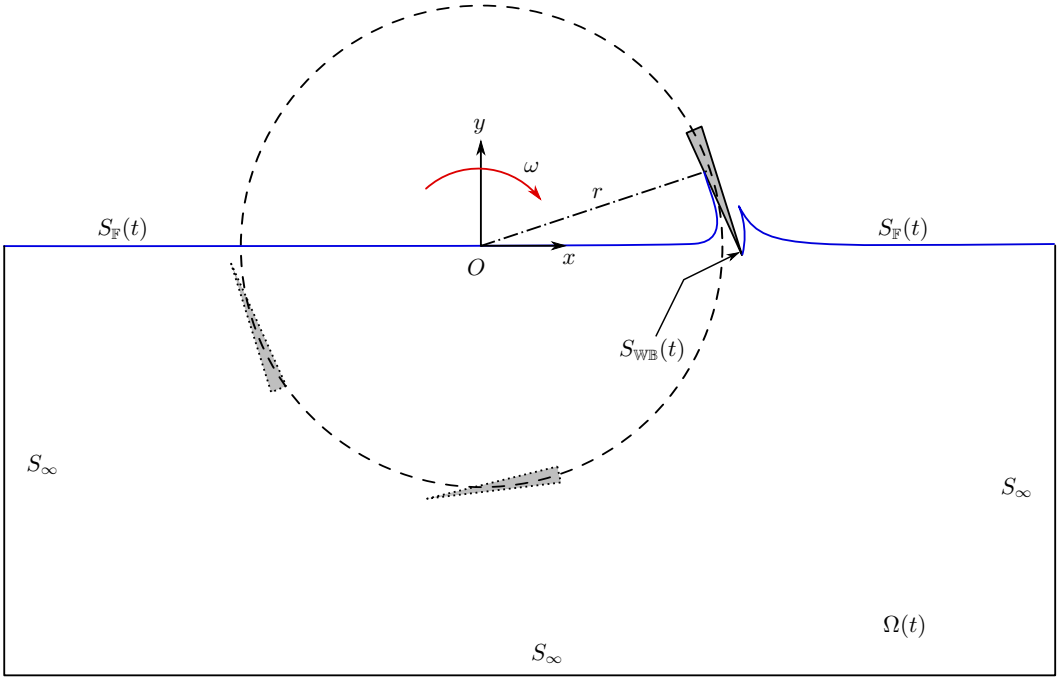

Figure 6.24: Rotating entry of a blade section : Fluid domain and corresponding boundaries

6.4.2 Results

Figures 6.26 through 6.29 show the preliminary results obtained using the rotating approach instead of the conventional vertical entry. The blade-element (wedge-shaped) has a chord of 0.04 m and rotates at a radius of r=0.1 m. These dimensions approximately correspond to a section of the 841B propeller [Olofsson 1996] at a radius of r/R=0.7. The angular velocity, ω is taken to be 100 rad/s. The simulation is started with a part of the wedge initially immersed, as shown in Figure 6.23. The initially immersed chord length of the blade-section is denoted as δ_i, which corresponds to an initial angular position of θ_i. α is the angle of attack measured with respect to the tangent along the circular path of the blade-section.

At a blade angle of 90° (see Figure 6.26), the pressure side of the hydrofoil is completely immersed. This marks the beginning of the fully submerged phase of the

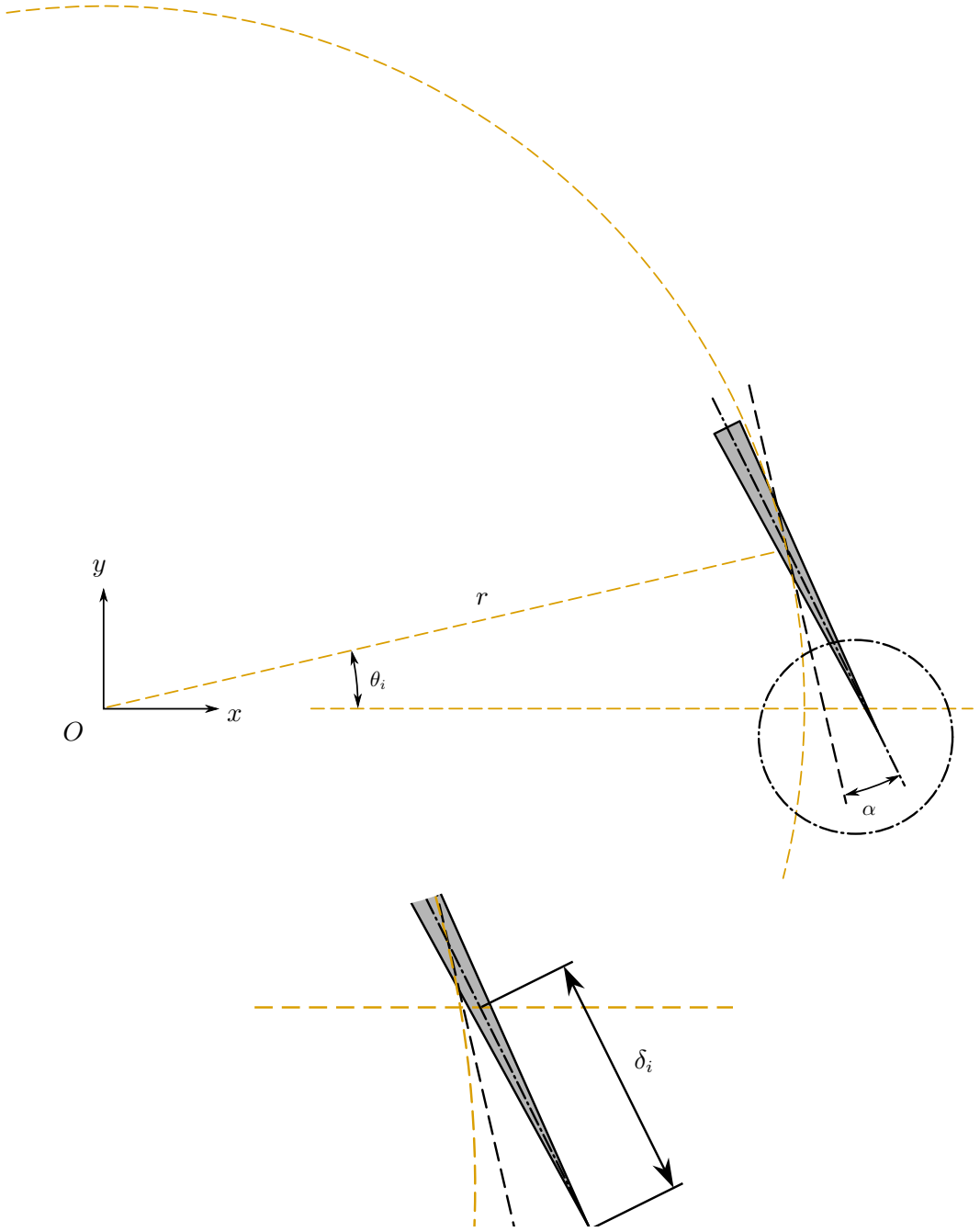

Figure 6.25: Rotating entry of a blade section : Initial configuration of the hydrofoil

hydrofoil. The free-surface is assumed to leave tangentially from the trailing edge with it being treated as a fixed separation point. Figures 6.27 and 6.29 show the position of the hydrofoil and the ventilated cavity at blade angles of 180° and 240° respectively.

The wedge has reached the exit phase at a blade angle of approximately 260° as shown in Figure 6.29. At present the simulation is stopped just before the leading edge ventilated cavity intersects the free-surface on the other side.

For the previous case, the angle of attack was such that the ventilated cavity remains open during the entire course of rotation. This is an ideal case scenario for a surface-piercing propeller. A collapsed cavity, however, is not ideal as it results in a high-drag mixture flow. Such a case is shown in Figure 6.30, which shows the ventilated cavity for an angle of attack α=-10°. The cavity is seen to collapse and hit the solid part of the suction side.

6.5 Summary

A two-dimensional BEM method has been developed to model the ventilating entry of a wedge-shaped hydrofoil or equivalently a blade-section of a surface-piercing propeller, in both vertical and rotational motion. The current scheme includes fully nonlinear free-surface boundary conditions, which is an advantage over existing methods with a negative image or a self similar flow assumption.

The vertical-entry of the wedge is modeled along the lines of the two-dimensional approach introduced by [Yim 1971] and later extended by [Wang 1977]. A systematic study of the effect of the number of panels, time-step and other numerical parameters was conducted to ascertain the accuracy of the predicted ventilated cavities. The ventilated cavity shapes for an angle of attack of 10° compared well with experimental results of [Cox 1971]. The results from the present method also compared well with a FLUENT based VOF model.

The results from the present fully nonlinear scheme were compared with SPPAN [Savineau 1996], which is based on the negative image method. The comparison between the two methods clearly indicates the shortcomings of the negative image method and gives credence to the claim that fully nonlinear free-surface boundary conditions are required in PROPCAV to improve its correlation with experiments.

The numerical scheme has also been extended to model the rotating entry of a hydrofoil. This is a novel approach in understanding the actual ventilation characteristics of a surface-piercing propeller. The scheme predicts cavity shapes that are reasonable but further studies are needed to refine the method (oscillations are seen at the opening of the ventilated cavity). Furthermore, the method needs to be extended to analyze the final exit-phase of the rotational motion.

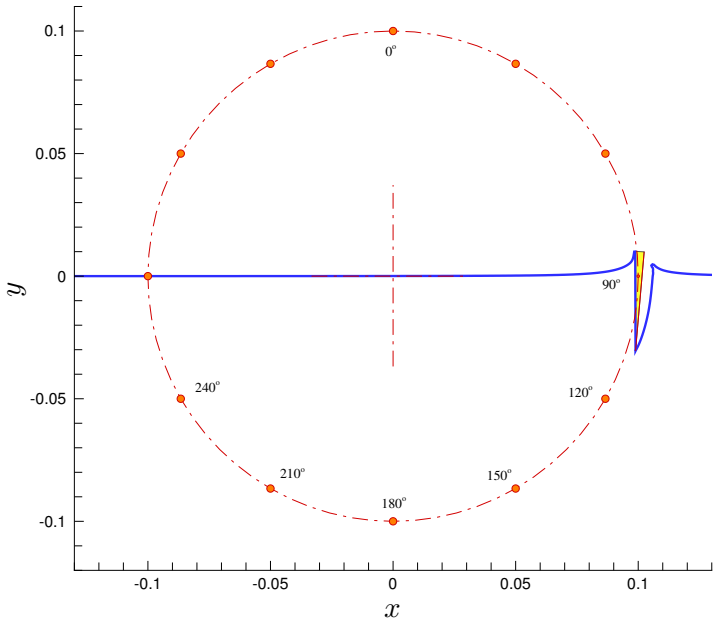

Figure 6.26: Surface-piercing propeller section in rotation : blade angle = 90°. Angle of attack α=0° (angle of attack defined in Figure 6.25)

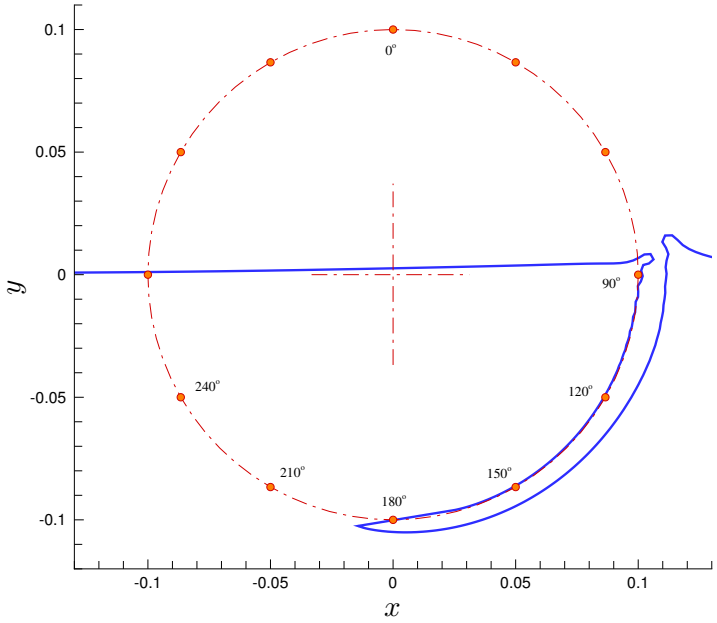

Figure 6.27: Surface-piercing propeller section in rotation : blade angle = 180°. Angle of attack α=0° (angle of attack defined in Figure 6.25)

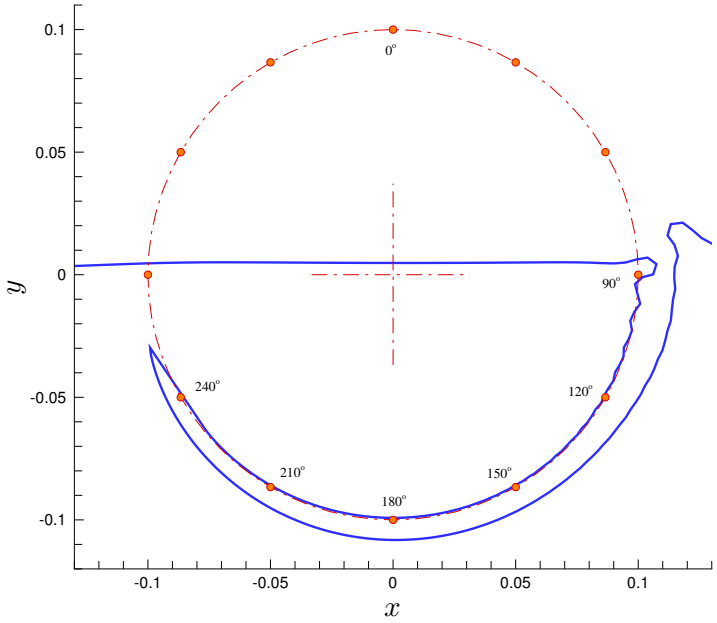

Figure 6.28: Surface-piercing propeller section in rotation : blade angle = 240°. Angle of attack α=0° (angle of attack defined in Figure 6.25)

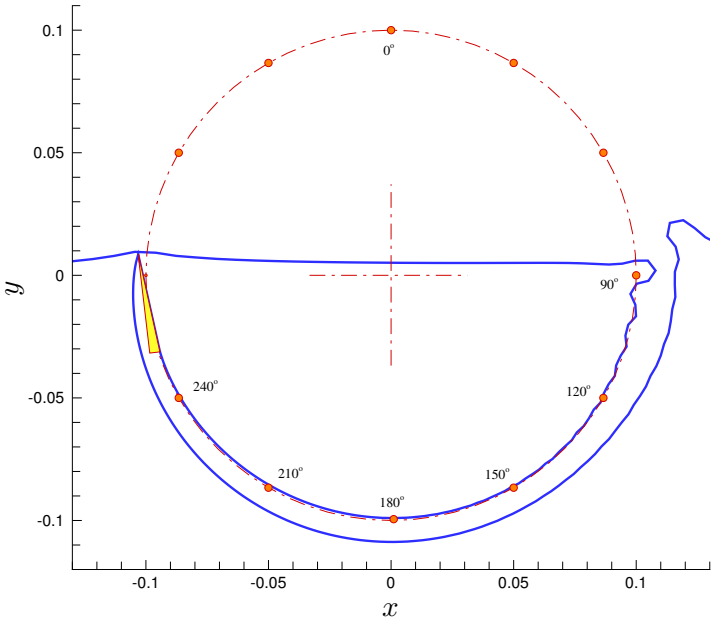

Figure 6.29: Surface-piercing propeller section in rotation : blade angle $\approx 260°$. Angle of attack α=0° (angle of attack defined in Figure 6.25)

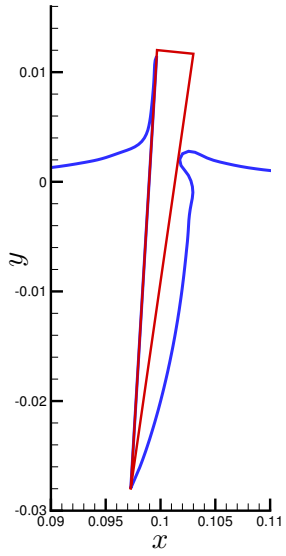

Figure 6.30: Surface-piercing propeller section in rotation, collapse of ventilated cavity. Angle of attack α=-10° (angle of attack defined in Figure 6.25)

Chapter 7

Conclusions

A two-dimensional boundary element method has been developed to model the strongly nonlinear interaction between a surface-piercing body and the free-surface. The method was applied to a class of free-surface problems with and without the presence of ventilation. The major contributions of this work include:

1. Development of a fast and reliable algorithm to predict the ventilated cavities formed as a result of the vertical entry of a surface-piercing hydrofoil or blade element of a surface-piercing propeller. The salient features of the current algorithm are the following :

   - All the nonlinearities of the free-surface body interaction are retained. Hence, the algorithm can be applied to foils operating at arbitrary Froude numbers.
   - Linearizations based on the geometry of the foil or the angle of attack at which it enters the water surface are absent. The scheme can thus be applied to foils or blade-sections of finite dimensions and arbitrary shape entering the water surface obliquely. This is an advantage over nonlinear analytical models that are applied to flat plates of semi-infinite extent under the assumptions of self-similarity (neglects the effects of gravity).

   Both these features combined make the current algorithm a unique addition to the field of performance prediction of surface-piercing propellers. The nonlinear

approach also helps assess the errors made in the 3D hydrodynamic model in PROPCAV as a result of the negative-image model for the free-surface.

The vertical-entry algorithm was developed along the lines of the two-dimensional approach of [Yim 1969; 1971; 1974] and [Wang 1977; 1979]. This approach approximates the flow-field as a horizontal layer of water sandwiched between layers of air of infinite extent. It is a clever mathematical construct but difficult to implement numerically. In this work a novel approach is proposed that looks at the entry-and-exit problem in a rotational mode instead of the traditional vertical or oblique manner. This is the first method that can predict the ventilated cavity shapes formed as a result of the rotational motion of a blade section. Once the scheme has been validated with experiments or other numerical methods, it can be used to design blade sections that ventilate over the entire submerged phase. This is as an essential requirement for maintaining the efficiency of SP propellers, as the premature collapse of the ventilated cavities on the blade can result in reduced performance.

2. Development of a potential flow solver to predict the dynamics of two-dimensional hull sections. The scheme provides a framework for validating the nonlinear free-surface dynamics relating to the large roll motion of hull-sections in a fully viscous approach.

Apart from the above mentioned applications, the algorithm developed here can be used for a whole range of problems in marine hydrodynamics :

- Asymmetric and symmetric water-entry of two-dimensional hull-sections : this has application in the field of slamming of hull sections.
- Water-entry of arbitrary cylindrical sections.

- Modeling of the wave-body interaction of marine structures. The method can also be used to simulate three-dimensional problems in an axisymmetric manner based on the formulation presented in Appendix E.

7.1 Discussions and Recommendations

The results presented in [Young 2002] show that PROPCAV predicts the mean forces with reasonable accuracy in comparison with experimental results. Based on the current work, it has been shown that the negative image method is clearly deficient in capturing the full nonlinearities of the entry phase.

PROPCAV is based on a lower-order BEM or constant-strength panel method. Extending the two-dimensional linear isoparametric scheme developed here would require at least a bi-linear distribution in the 3D model. As a first step towards improving the 3D model, a two-dimensional scheme is developed to model the non-ventilating entry of a surface-piercing hydrofoil based on a constant-strength panel method (CPM) along with fully nonlinear free-surface boundary conditions. The scheme can be considered as the 2D equivalent of a fully nonlinear 3D model in PROPCAV.

The basic difference between the linear isoparametric and constant-strength methods is the location where the variables are collocated. In the linear isoparametric scheme, the variables are calculated at the end-points of the panel while in the constant-strength scheme it is at the mid-point of the panel (see Figure 7.1). The steps in the constant-strength scheme are the following

- Solve the boundary value problem to obtain the variables (normal velocity on the Dirichlet boundary or the free-surface and velocity potential on the Neumann boundary) at the mid-points of the panels.

- On the free-surface, the velocity potential is interpolated from the mid-points

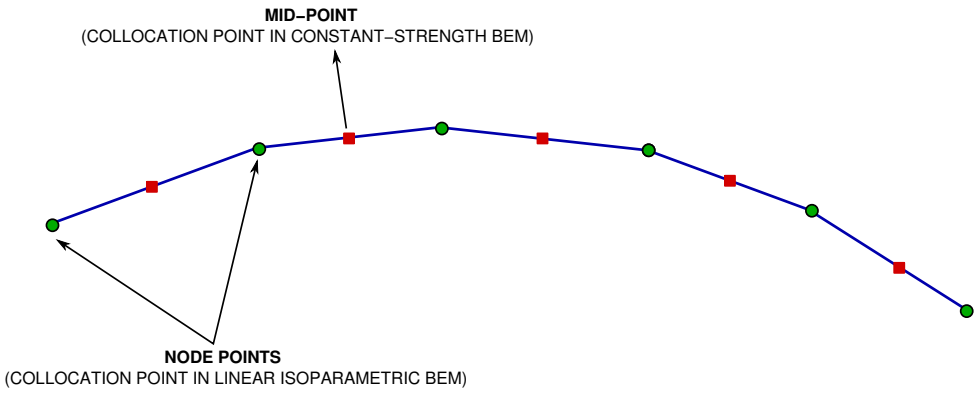

Figure 7.1: Constant-strength panel method, location of panel end-points and control points

to the end-points of the element. This interpolation is based on cubic-splines with arc-length as a parameter.

- Once the velocity potential is obtained at the end-points, further steps are similar to the ones used in the linear isoparametric scheme.

A comparison of the free-surfaces obtained from the constant and linear strength BEM schemes is shown in Figure 7.2 for a wedge with included angle α_w=18°. The overall comparison between the predicted free-surface elevations is good except for minor differences in the region of the jet (as shown in the close-up of the jet region in Figure 7.2). This difference, however, should not affect the pressure distribution as it falls within the region where the gage pressure is zero.

An important difference between the two schemes is the ratio of the sizes of adjacent panels at the free-surface body intersection. In the constant-strength method, it was found necessary to keep this ratio above four to obtain a stable free-surface. However, in the linear scheme, a much smaller ratio of one was used.

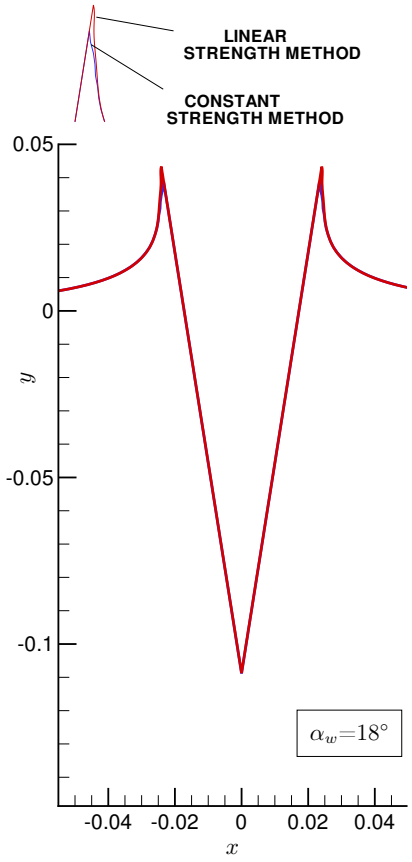

Figure 7.2: Water-entry of a wedge with an included angle, α_w=18°. Comparison of free-surface elevations predicted by the constant-strength panel and the linear-strength BEM schemes.

Computational efficiency

The computational resources required for a three-dimensional analysis of surface-piercing propellers with fully nonlinear free-surface boundary conditions are enormous. A major part of the computational time is spent on inverting a rather large dense matrix as a part of the solution of boundary value problem.

A way of increasing the efficiency is through the use of optimized or tuned BLAS and LAPACK [Anderson et al. 1999] routines provided in the ATLAS (Automati-

cally tuned linear algebra software, [Whaley and Dongarra 1997]) library. The performance of these libraries was tested in the case of the two-dimensional algorithm for the constant-strength scheme. For a comparable problem size, defined by the total number of elements or panels on the domain boundaries, the tuned routines out-performed the conventional routines by a factor of four. This can significantly improve the computational efficiency of the three-dimensional scheme.

In the context of the extension into three-dimensions, a review of the multipole expansions for the source and dipole influence coefficients for a quadrilateral panel is presented in Appendix F.

Appendices

Appendix A

2D Influence Coefficients

Details of the derivation of analytical (closed-form) expressions for the two-dimensional source and dipole influence coefficients are presented here. These influence coefficients are based on linear isoparametric panels. Consider a generic linear isoparametric panel as shown in Figure A.1. The panel is represented in a local coordinate system $O - XY$, with h being the panel length.

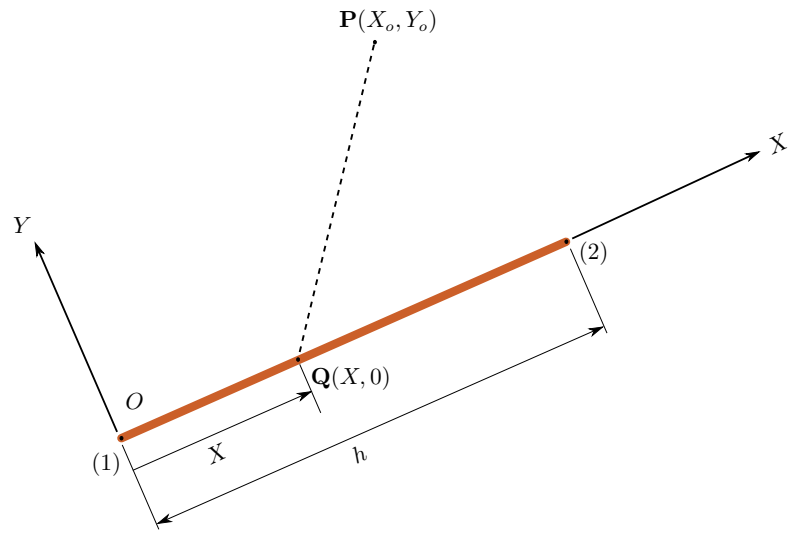

Figure A.1: Linear isoparametric element

For a collocation point $P(X_o, Y_o)$, the two-dimensional Green's function [Kellogg 1954] is given as

$$G(\mathbf{P}, \mathbf{Q}) = \frac{1}{2\pi} \ln \frac{1}{|\mathbf{P} - \mathbf{Q}|} \tag{A.1}$$

where $Q = (X, 0)$ is the integration point with $0 \leq X \leq h$ and $|\mathbf{P} - \mathbf{Q}|$ is the

Euclidean distance between $\mathbf{P}$ and $\mathbf{Q}$ given as

$$|\mathbf{P}-\mathbf{Q}| = \sqrt{(X-X_o)^2+Y_o^2} \tag{A.2}$$

Hence, the source influence function can be represented as

$$G(X) \equiv G(\mathbf{P},\mathbf{Q}) = -\frac{1}{4\pi}\ln\left[(X-X_o)^2+Y_o^2\right] \tag{A.3}$$

For the normal dipole, we have

$$G_n(X) \equiv G_n(\mathbf{P},\mathbf{Q}) = \nabla G(\mathbf{P},\mathbf{Q})\cdot\vec{n} = -\frac{1}{2\pi}\frac{Y_o}{(X-X_o)^2+Y_o^2} \tag{A.4}$$

where $\vec{n}$ is the normal vector on the panel. In summary, we have

$$\text{Source Function}: \quad G(X) = -\frac{1}{4\pi}\ln\left[(X-X_o)^2+Y_o^2\right] \tag{A.5}$$

$$\text{Dipole Function}: G_n(X) = -\frac{1}{2\pi}\frac{Y_o}{(X-X_o)^2+Y_o^2} \tag{A.6}$$

To derive the influence coefficients for a linear isoparametric panel, assume a source/dipole strength distribution of the form

$$f(X) = f_1\left(1-\frac{X}{h}\right)+f_2\frac{X}{h} \tag{A.7}$$

where f_1 and f_2 represent values of the function at the end-points of the panel, as shown in Figure A.2. Based on (A.3) and (A.7), we can write the source influence function as

$$\begin{aligned} I_s &= \int_0^h f(X)G(X)dX = \frac{f_1}{h}\left[(h-X_o)I_{sc}-I_{sl}\right]+\frac{f_2}{h}\left[X_oI_{sc}+I_{sl}\right] \\ &= f_1I_{s,1}+f_2I_{s,2} \end{aligned} \tag{A.8}$$

where,

$$\left.\begin{aligned} I_{sc} &= \int_0^h G(X)dX \\ I_{sl} &= \int_0^h (X-X_o)G(X)dX \end{aligned}\right\} \begin{aligned} I_{s,1} &= \frac{1}{h}\left[(h-X_o)I_{sc}-I_{sl}\right] \\ I_{s,2} &= \frac{1}{h}\left[X_oI_{sc}+I_{sl}\right] \end{aligned} \tag{A.9}$$

Similarly, the dipole influence function can be written as

$$\begin{aligned} I_d &= \int_0^h f(X)G(X)dX = \frac{f_1}{h}\left[(h-X_o)I_{dc} - I_{dl}\right] + \frac{f_2}{h}\left[X_o I_{dc} + I_{dl}\right] \\ &= f_1 I_{d,1} + f_2 I_{d,2} \end{aligned} \tag{A.10}$$

where,

$$\left.\begin{aligned} I_{dc} &= \int_0^h G_n(X)dX \\ I_{dl} &= \int_0^h (X-X_o)G_n(X)dX \end{aligned}\right\} \quad \left.\begin{aligned} I_{d,1} &= \frac{1}{h}\left[(h-X_o)I_{dc} - I_{dl}\right] \\ I_{d,2} &= \frac{1}{h}\left[X_o I_{dc} + I_{dl}\right] \end{aligned}\right. \tag{A.11}$$

After simplification, the final expressions for the individual components of the source and dipole influence functions are as follows

$$\begin{aligned} I_{sc} &= \frac{1}{4\pi}\left[(X_o - h)\ln A - X_o \ln B + 2h + 2Y_o W\right] \\ I_{sl} &= \frac{1}{8\pi}\left[B(\ln B - 1) - A(\ln A - 1)\right] \\ I_{dc} &= \frac{W}{2\pi} \\ I_{dl} &= \frac{Y_o}{4\pi}\left[\ln B - \ln A\right] \end{aligned} \tag{A.12}$$

where,

$$\begin{aligned} A &= (X_o - h)^2 + Y_o^2 \\ B &= X_o^2 + Y_o^2 \\ W &= \arctan\frac{Y_o}{X_o} - \arctan\frac{Y_o}{X_o - h} \end{aligned} \tag{A.13}$$

Some useful integrals and relations used in the derivation [Gradshteyn and Ryzhik 2007]:

$$\begin{aligned} \int \ln(x^2+a^2)dx &= x\ln(x^2+a^2) - 2x + 2a\arctan\frac{x}{a} \\ \int x\ln(x^2+a^2)dx &= \frac{1}{2}\left[(x^2+a^2)\ln(x^2+a^2) - x^2\right] \end{aligned} \tag{A.14}$$

$$
\begin{aligned}
\int (x^2+a^2)^{-1}dx &= \frac{1}{a}\arctan\frac{x}{a} \\
\int x(x^2+a^2)^{-1}dx &= \frac{1}{2}\ln(x^2+a^2) \\
\arctan x + \arctan x^{-1} &= +\frac{\pi}{2}[x>0] \\
\arctan x + \arctan x^{-1} &= -\frac{\pi}{2}[x<0]
\end{aligned}
\tag{A.15}
$$

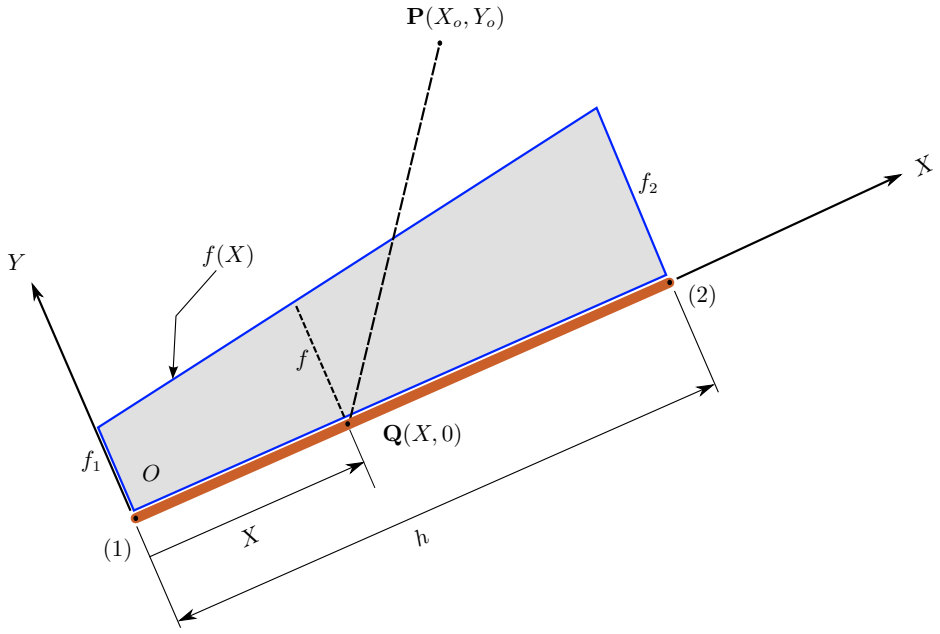

Figure A.2: Linear strength distribution

Two special cases that need to be considered separately are when the collocation point **P** coincides with end-points, (1) or (2), of the panel. These cases represent the *self-influence* part of the source and dipole influence functions.

Case 1 : **P** coincides with end-point (1). In this case $X_o = 0, Y_o = 0, A = h^2$ and $B = 0$.

$$
\left.
\begin{aligned}
I_{sc} &= \frac{1}{4\pi}\,2h(1-\ln h) \\
I_{sl} &= -\frac{1}{4\pi}\,\frac{h^2}{2}(2\ln h - 1)
\end{aligned}
\right\}
\begin{aligned}
I_{dc} &= 0 \\
I_{dl} &= 0
\end{aligned}
\tag{A.16}
$$

Case 2 : **P** coincides with end-point (2). In this case $X_o = h$,$Y_o = 0$,$A = 0$ and $B = h^2$.

$$\left.\begin{aligned} I_{sc} = & \quad \frac{1}{4\pi}\, 2h(1 - \ln h) \\ I_{sl} = & \quad \frac{1}{4\pi}\, \frac{h^2}{2}(2\ln h - 1) \end{aligned}\right\} \begin{aligned} I_{dc} &= 0 \\ I_{dl} &= 0 \end{aligned} \tag{A.17}$$

The above expressions for the source and dipole influence coefficients are presented in terms of the local coordinate system. Since the geometry of the panels are defined in the global coordinate system , a transformation has to be made from the global $o - xy$ to local $O - XY$ coordinate system. Figure A.3 shows the global representation of the generic panel shown in Figure A.1 and it is labeled as the j^{th} panel in the global numbering scheme.

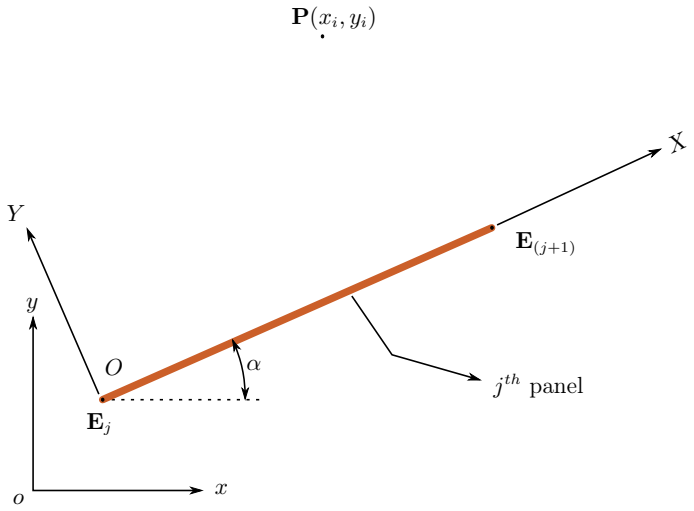

Figure A.3: Local and global systems

For the panel, $\mathrm{E}_j(x_j, y_j)$ and $\mathrm{E}_{j+1}(x_{j+1}, y_{j+1})$ are the end points, $\mathbf{P}(x_i, y_i)$ is the collocation point. Based on the geometry of the panel, the transformation from the

global to local coordinate system is given by

$$\alpha = \arctan \frac{y_{j+1} - y_j}{x_{j+1} - x_j} \tag{A.18}$$

$$X_o = (x_i - x_j)\cos\alpha + (y_i - y_j)\sin\alpha \tag{A.19}$$

$$Y_o = (x_i - x_j)\sin\alpha - (y_i - y_j)\cos\alpha \tag{A.20}$$

$$h = \sqrt{(x_{j+1} - x_j)^2 + (y_{j+1} - y_j)^2} \tag{A.21}$$

Appendix B

Free-surface remeshing

Let the free-surface consist of a set of Lagrangian markers represented as $\mathbf{P_k} = (x_k, y_k)$, $k = 1, 2, \cdots, N$ (N is the total number of particles on the free-surface). One of the commonly used parameters is the chord-length or the Euclidean distance between two consecutive particles [Rogers and Adams 1990, Ueberhuber 1997]. From Figure B.1, the chord length between points $\mathbf{P}_k$ and $\mathbf{P}_{k+1}$ can be written as

$$\begin{aligned} \tau_{k+1} - \tau_k &= |\mathbf{P}_{k+1} - \mathbf{P}_k| \\ &= \sqrt{\left[(x_{k+1} - x_k)^2 + (y_{k+1} - y_k)^2\right]} \end{aligned} \tag{B.1}$$

Based on the parameter τ_k, the equation for a single parametric cubic spline segment is given by

$$\mathbf{P}(\tau) = \sum_{i=1}^{4} B_i \tau^{i-1}, \qquad \tau_k \leq \tau \leq \tau_{k+1} \tag{B.2}$$

The above notation is based on that used in [Rogers and Adams 1990]. In Equation B.2, τ_k and τ_{k+1} are the parameter values at the beginning and end of the segment. $\mathbf{P}(\tau) = \big(x(\tau), y(\tau)\big)$ is the position vector of any point on the cubic spline segment. The constant coefficients B_i are obtained by fitting a cubic-spline through the set of Lagrangian points. The Cartesian coordinates, each have a similar formulation as Equation B.2, can be written as

$$\begin{aligned} x(\tau) &= \sum_{i=1}^{4} B_{i_x} \tau^{i-1}, \qquad \tau_k \leq \tau \leq \tau_{k+1} \\ y(\tau) &= \sum_{i=1}^{4} B_{i_y} \tau^{i-1}, \qquad \tau_k \leq \tau \leq \tau_{k+1} \end{aligned} \tag{B.3}$$

An issue with the chord-length based parametrization is that it is not very accurate in regions of high curvature. Remeshing based on chord-length as a parameter can lead to the loss of resolution in regions of high curvature. A better choice for the parametric representation is the arc-length of the cubic spline segment, given by the expression

$$s_{k+1} - s_k = \int_{\tau_k}^{\tau_{k+1}} \sqrt{(x')^2 + (y')^2} d\tau \tag{B.4}$$

where s_k and s_{k+1} represent the arc-lengths corresponding to points $\mathbf{P}_k$ and $\mathbf{P}_{k+1}$. The arc-lengths are measured from the start of the free-surface with $s_1 = 0$ corresponding to the point $\mathbf{P}_1$. The derivatives $x'(\tau)$ and $y'(\tau)$ can be found by differentiating Equation B.2 and B.3. Note that $(')$ denotes differentiation with respect to the parameter τ. We have

$$\left.\begin{aligned} \mathbf{P}'(\tau) &= \sum_{i=1}^{4} B_i (i-1)\tau^{i-2} \\ x'(\tau) &= \sum_{i=1}^{4} B_{i_x} (i-1)\tau^{i-2} \\ &= B_{2_x} + 2B_{3_x}\tau + 3B_{4_x}\tau^2 \\ y'(\tau) &= \sum_{i=1}^{4} B_{i_y} (i-1)\tau^{i-2} \\ &= B_{2_y} + 2B_{3_y}\tau + 3B_{4_y}\tau^2 \end{aligned}\right\} \tau_k \leq \tau \leq \tau_{k+1} \tag{B.5}$$

With the coefficients B_i known, the integral in Equation B.4 can be evaluated numerically to calculate the arc-length of the segment. All subsequent representations of the free-surface are based on the arc-length as a parameter.

The aim of the remeshing scheme is to transfer data from an old set of free-surface markers to a new set as accurately as possible. This is done based on the

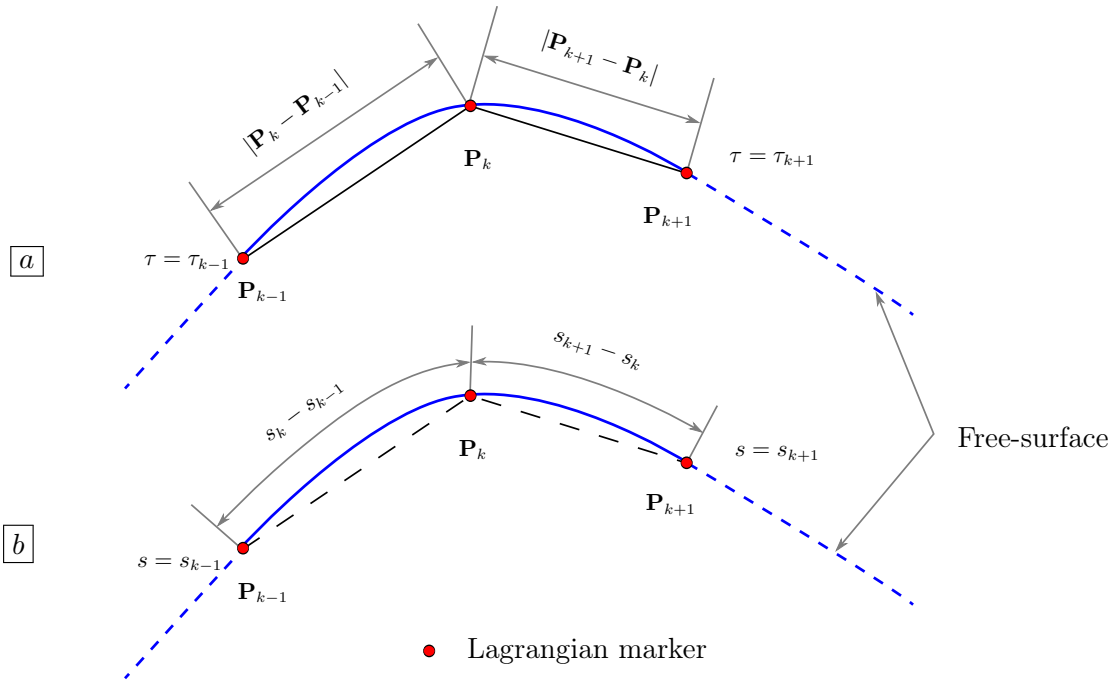

Figure B.1: Parametric representation of free-surface, $\boxed{a}$: chord-length as parameter, $\boxed{b}$: arc-length as parameter

following steps:

(i) Given a set of free-surface points represented parametrically as $(s_k, x_k^{(o)})$ and $(s_k, y_k^{(o)})$. Similarly, since the free-surface is a Dirichlet boundary, the velocity potential at these points can be represented as $(s_k, \phi_k^{(o)})$. Here s_k is the arc-length corresponding to the free-surface point $\mathbf{P}_k(x_k^{(o)}, y_k^{(o)})$ with $k = 1, 2, \cdots, N$. N is the total number of points on the free-surface. Note that the superscript $^{(o)}$ indicates a value belonging to the old set of parameters.

(ii) Obtain a cubic-spline fit for each set of data for the old free-surface. An indi-

vidual cubic-spline segment can be represented as

$$\left.\begin{aligned} x^{(o)}(s) &= \sum_{i=1}^{4} C_{i_x,k}\ s^{i-1} \\ y^{(o)}(s) &= \sum_{i=1}^{4} C_{i_y,k}\ s^{i-1} \\ \phi^{(o)}(s) &= \sum_{i=1}^{4} C_{i_\phi,k}\ s^{i-1} \end{aligned}\right\} s_k \leq s \leq s_{k+1} \tag{B.6}$$

where $C_{i_x,k}$, $C_{i_y,k}$ and $C_{i_\phi,k}$ are the coefficients obtained from the cubic-spline fit.

(iii) Calculate the new set of parameters represented as $(r_1, r_2, \cdots, r_m, \cdots, r_M)$ with $r_1 = s_1$ and $r_M = s_N$. Note that the new set consists of strictly increasing parameters. The new set of parameters can be obtained based on an equal/graded arc-length or adpative curvature based criteria.

(iv) Evaluate the new set of free-surface points $(r_m, y_k^{(n)})$ and $(r_m, y_n^{(m)})$ with velocity potential $(r_m, \phi_m^{(n)})$ based on the cubic spline representation, Equation B.6. Note that the superscript $^{(n)}$ indicates a value belonging to the new set of parameters.

Even though the above procedure is presented here with respect to the remeshing of the free-surface, it can be easily adapted to interpolate information on any boundary surface of the fluid domain.

Appendix C

Fifth-order Gravity Waves

Analytical forms of two alternate solutions for steady nonlinear waves based on the fifth-order Stokes theory of [Skjelbreia and Hendrickson 1961] and [Fenton 1985] are presented. The intent of the chapter is to provide a brief outline of the wave characteristics without presenting the underlying theory.

C.1 Nomenclature

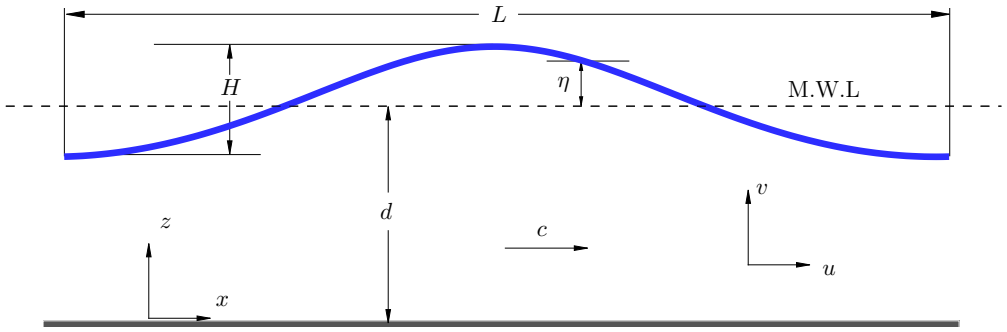

Figure C.1: Important characteristics of a nonlinear wave

H	:	wave height
L	:	wave length
T	:	wave period
c	:	wave speed
d	:	mean depth of water (distance from bottom surface to mean water line, M.W.L)
g	:	gravitational acceleration
k	:	wavenumber $= 2\pi/L$
(x, z)	:	Cartesian coordinates fixed to bottom surface through which waves move at speed c

$\eta \equiv \eta(x,t)$	:	wave elevation, elevation of free-surface above M.W.L
$\varphi \equiv \varphi(x,z,t)$	:	velociy potential with respect to (x,z) coordinate system
$u \equiv u(x,z,t)$	:	horizontal component of velocity with respect to (x,z) coordinate system
$v \equiv v(x,z,t)$	:	vertical component of velocity with respect to (x,z) coordinate system

C.2 Solution I

The analytical form of nonlinear waves based on the theory of [Skjelbreia and Hendrickson 1961].

C.2.1 Wave Elevation

The wave elevation η is expressed as a Fourier series

$$\begin{aligned} k\eta = {} & \lambda\cos(\theta) + (\lambda^2 B_{22} + \lambda^4 B_{24})\cos(2\theta) \\ & + (\lambda^3 B_{33} + \lambda^5 B_{35})\cos(3\theta) + \lambda^4 B_{44}\cos(4\theta) \\ & + \lambda^5 B_{55}\cos(5\theta) \end{aligned} \tag{C.1}$$

where $\theta = k(x - ct)$. Equation (C.1) can be written in a more simplified form as

$$k\eta = \sum_{n=1}^{5} \lambda^n b_n \cos(n\theta) \tag{C.2}$$

where,

$$b_1 = 1 \quad \left| \begin{array}{ll} b_2 = B_{22} + \lambda^2 B_{24} & b_4 = B_{44} \\ b_3 = B_{33} + \lambda^2 B_{35} & b_5 = B_{55} \end{array} \right| \tag{C.3}$$

In the above expansion, the quantity λ has no physical significance and may be interpreted as a length scale equal to the amplitude of the wave at lowest order [Fenton 1985]. The coefficients B_{ij} are dimensionless functions of d and L (given in Table C.1).

C.2.2 Wave Potential

The velocity potential can be written as

$$\begin{aligned}\frac{k}{c}\,\varphi = &(\lambda A_{11} + \lambda^3 A_{13} + \lambda^5 A_{15})\cosh(kz)\sin(\theta)\\ &+ (\lambda^2 A_{22} + \lambda^4 A_{24})\cosh(2kz)\sin(2\theta)\\ &+ (\lambda^3 A_{33} + \lambda^5 A_{35})\cosh(3kz)\sin(3\theta)\\ &+ (\lambda^4 A_{44})\cosh(4kz)\sin(4\theta)\\ &+ (\lambda^5 A_{55})\cosh(5kz)\sin(5\theta)\end{aligned} \tag{C.4}$$

Equation (C.4) can be written in a simplified form as follows

$$\frac{k}{c}\,\varphi = \sum_{n=1}^{5} \lambda^n a_n \cosh(nkz)\sin(n\theta) \tag{C.5}$$

where,

$$a_1 = A_{11} + \lambda^2 A_{13} + \lambda^4 A_{15} \quad \left|\quad \begin{array}{l} a_2 = A_{22} + \lambda^2 A_{24} \\ a_3 = A_{33} + \lambda^2 A_{35} \end{array} \quad\right| \quad \begin{array}{l} a_4 = A_{44} \\ a_5 = A_{55} \end{array} \tag{C.6}$$

The coefficients A_{ij} are dimensionless functions of d and L (given in Table C.1).

C.2.3 Velocity Components

The horizontal and vertical velocity components are derived from the expression for the velocity potential, as given in Equation (C.5).

$$\frac{k}{c}\,u = \frac{k}{c}\frac{\partial\varphi}{\partial x} = \sum_{n=1}^{5} \lambda^n a_n \cosh(nkz)\cos(n\theta)\, n\,\frac{\partial\theta}{\partial x} \tag{C.7}$$

$\because \theta = k(x - ct)$, $\dfrac{\partial\theta}{\partial x} = k$. Thus

$$\frac{u}{c} = \sum_{n=1}^{5} \lambda^n\, n\, a_n \cosh(nkz)\cos(n\theta) \tag{C.8}$$

Similarly,

$$\frac{k}{c}\,v = \frac{k}{c}\frac{\partial\varphi}{\partial z} = \sum_{n=1}^{5} \lambda^n a_n \sinh(nkz)\sin(n\theta)\, n\, k \tag{C.9}$$

or,

$$\frac{v}{c} = \sum_{n=1}^{5} \lambda^n \, n \, a_n \sinh(nkz) \sin(n\theta) \tag{C.10}$$

C.2.4 Application

For a given H, d and T, the wave length L and the parameter λ are obtained by solving a set of nonlinear equations of the form

$$\begin{aligned} \frac{\pi H}{d} &= \frac{L}{d}\left[\lambda + \lambda^3 B_{33} + \lambda^5 (B_{35} + B_{55})\right] \\ \frac{d}{L_0} &= \frac{d}{L}\tanh(kd)\left(1 + \lambda^2 C_1 + \lambda^4 C_2\right) \end{aligned} \tag{C.11}$$

where C_1 and C_2 are coefficients that are functions of d and L (given in Table C.1) and

$$L_0 = \frac{gT^2}{2\pi} \tag{C.12}$$

C.3 Solution II

The analytical form of nonlinear waves based on the theory of [Fenton 1985].

C.3.1 Wave Elevation

The wave elevation η is expressed as a Fourier series

$$\begin{aligned} k\eta = &\left[\epsilon + \epsilon^3 B_{31} - \epsilon^5 (B_{53} + B_{55})\right] \cos(\theta) \\ &+ (\epsilon^2 B_{22} + \epsilon^4 B_{42}) \cos(2\theta) \\ &+ (-\epsilon^3 B_{31} + \lambda^5 B_{53}) \cos(3\theta) \\ &+ \epsilon^4 B_{44} \cos(4\theta) \\ &+ \epsilon^5 B_{55} \cos(5\theta) \end{aligned} \tag{C.13}$$

where $\theta = k(x - ct)$. Equation (C.13) can be written in a more simplified form as

$$k\eta = \sum_{n=1}^{5} \epsilon^n b_n \cos(n\theta) \tag{C.14}$$

where,

$$b_1 = 1 + \epsilon^2 B_{31} - \epsilon^4 (B_{53} + B_{55}) \quad \left| \quad \begin{array}{l} b_2 = B_{22} + \epsilon^2 B_{42} \\ b_3 = -B_{31} + \epsilon^2 B_{53} \end{array} \right| \quad \left| \quad \begin{array}{l} b_4 = B_{44} \\ b_5 = B_{55} \end{array} \right| \tag{C.15}$$

In the above expansion, the quantity $\epsilon = kH/2$ represents the dimensionless wave height. The coefficients B_{ij} are dimensionless functions of d and L (given in Table C.2).

C.3.2 Wave Potential

The velocity potential can be written as

$$\begin{aligned} \frac{1}{C_0}\sqrt{\frac{k^3}{g}}\,\varphi = {} & (\epsilon A_{11} + \epsilon^3 A_{31} + \epsilon^5 A_{51}) \cosh(kz) \sin(\theta) \\ & + (\epsilon^2 A_{22} + \epsilon^4 A_{42}) \cosh(2kz) \sin(2\theta) \\ & + (\epsilon^3 A_{33} + \epsilon^5 A_{53}) \cosh(3kz) \sin(3\theta) \\ & + (\epsilon^4 A_{44}) \cosh(4kz) \sin(4\theta) \\ & + (\epsilon^5 A_{55}) \cosh(5kz) \sin(5\theta) \end{aligned} \tag{C.16}$$

Equation (C.16) can be written in a simplified form as follows

$$\frac{1}{C_0}\sqrt{\frac{k^3}{g}}\,\varphi = \sum_{n=1}^{5} \epsilon^n a_n \cosh(nkz) \sin(n\theta) \tag{C.17}$$

where,

$$a_1 = A_{11} + \epsilon^2 A_{31} + \epsilon^4 A_{51} \quad \left| \quad \begin{array}{l} a_2 = A_{22} + \epsilon^2 A_{42} \\ a_3 = A_{33} + \epsilon^2 A_{53} \end{array} \right| \quad \left| \quad \begin{array}{l} a_4 = A_{44} \\ a_5 = A_{55} \end{array} \right| \tag{C.18}$$

The coefficients C_0 and A_{ij} are dimensionless functions of d and L (given in Table C.2).

C.3.3 Velocity Components

The horizontal and vertical velocity components are derived from the expression for the velocity potential, as given in Equation (C.17).

$$\frac{1}{C_0}\sqrt{\frac{k^3}{g}}\,u = \frac{1}{C_0}\sqrt{\frac{k^3}{g}}\,\frac{\partial\varphi}{\partial x} = \sum_{n=1}^{5}\epsilon^n a_n \cosh(nkz)\cos(n\theta)\,n\,\frac{\partial\theta}{\partial x} \tag{C.19}$$

$\because \theta = k(x-ct)$, $\dfrac{\partial\theta}{\partial x} = k$. Thus

$$\frac{1}{C_0}\sqrt{\frac{k}{g}}\,u = \sum_{n=1}^{5}\epsilon^n\,n\,a_n \cosh(nkz)\cos(n\theta) \tag{C.20}$$

Similarly,

$$\frac{1}{C_0}\sqrt{\frac{k^3}{g}}\,v = \frac{1}{C_0}\sqrt{\frac{k^3}{g}}\,\frac{\partial\varphi}{\partial z} = \sum_{n=1}^{5}\epsilon^n a_n \sinh(nkz)\sin(n\theta)\,n\,k \tag{C.21}$$

or,

$$\frac{1}{C_0}\sqrt{\frac{k}{g}}\,v = \sum_{n=1}^{5}\epsilon^n\,n\,a_n \sinh(nkz)\sin(n\theta) \tag{C.22}$$

C.3.4 Application

For a given H, d and T, the wave length L can be obtained by solving the dispersion relation

$$C_0 + \epsilon^2 C_2 + \epsilon^4 C_4 = \frac{2\pi}{T\sqrt{gk}} \tag{C.23}$$

where C_0, C_2 and C_4 are dimensionless functions of d and L (given in Table C.2).

$$
\begin{aligned}
S &= \sinh(kd) \\
C &= \cosh(kd) \\
A_{11} &= 1/S \\
A_{13} &= -C^2(5C^2+1)/(8S^5) \\
A_{15} &= -(1184C^{10}-1440C^8-1992C^6+2641C^4-249C^2+18)/(1536S^{11}) \\
A_{22} &= 3/(8S^4) \\
A_{24} &= (192C^8-424C^6-312C^4+480C^2-17)/(768S^{10}) \\
A_{33} &= (13-4C^2)/(64S^7) \\
A_{35} &= (512C^{12}+4224C^{10}-6800C^8-12808C^6+16704C^4-3154C^2+107) \\
&\quad /[4096S^{13}(6C^2-1)] \\
A_{44} &= (80C^6-816C^4+1338C^2-197)/[1536S^{10}(6C^2-1)] \\
A_{55} &= -(2880C^{10}-72480C^8+324000C^6-432000C^4+163470C^2-16245) \\
&\quad /[61440S^{11}(6C^2-1)(8C^4-11C^2+3)] \\
B_{22} &= C(2C^2+1)/(4S^3) \\
B_{24} &= C(272C^8-504C^6-192C^4+322C^2+21)/(384S^9) \\
B_{33} &= 3(8C^6+1)/(64S^6) \\
B_{35} &= (88128C^{14}-208224C^{12}+70848C^{10}+54000C^8-21816C^6+6264C^4-54C^2-81) \\
&\quad /[12288S^{12}(6C^2-1)] \\
B_{44} &= C(768C^{10}-448C^8-48C^6+48C^4+106C^2-21)/[384S^9(6C^2-1)] \\
B_{55} &= (192000C^{16}-262720C^{14}+83680C^{12}+20160C^{10}-7280C^8+7160C^6 \\
&\quad -1800C^4-1050C^2+225) \\
&\quad /[12288S^{10}(6C^2-1)(8C^4-11C^2+3)] \\
C_1 &= (8C^4-8C^2+9)/(8S^4) \\
C_2 &= (3840C^{12}-4096C^{10}-2592C^8-1008C^6+5944C^4-1830C^2+147) \\
&\quad /[512S^{10}(6C^2-1)]
\end{aligned}
$$

Table C.1: Fifth-order gravity wave coefficients [Skjelbreia and Hendrickson 1961]

$$
\begin{aligned}
S &= \operatorname{sech}(2kd) \\
C &= 1 - S \\
A_{11} &= 1/\sinh(kd) \\
A_{22} &= 3S^2/(2C^2) \\
A_{31} &= (-4 - 20S + 10S^2 - 13S^3)/[8\sinh(kd)C^3] \\
A_{33} &= (-2S^2 + 11S^3)/[8\sinh(kd)C^3] \\
A_{42} &= (12S - 14S^2 - 264S^3 - 45S^4 - 13S^5)/(24C^5) \\
A_{44} &= (10S^3 - 174S^4 + 291S^5 + 278S^6)/[48(3 + 2S)C^5] \\
A_{51} &= (-1184 + 32S + 13232S^2 + 21712S^3 + 20940S^4 + 12554 * S^5 - 500S^6 - 3341S^7 - 670S^8) \\
&\quad /[64\sinh(kd)(3 + 2S)(4 + S)C^6] \\
A_{53} &= (4S + 105S^2 + 198S^3 - 1376S^4 - 1302S^5 - 117S^6 + 58S^7) \\
&\quad /[32\sinh(kd)(3 + 2S)C^6] \\
A_{55} &= (-6S^3 + 272S^4 - 1552S^5 + 852S^6 + 2029S^7 + 430S^8) \\
&\quad /[64\sinh(kd)(3 + 2S)(4 + S)C^6] \\
B_{22} &= \coth(kd)(1 + 2S)/(2C) \\
B_{31} &= -3(1 + 3S + 3S^2 + 2S^3)/(8C^3) \\
B_{42} &= \coth(kd)(6 - 26S - 182S^2 - 204S^3 - 25S^4 + 26S^5)/[6(3 + 2S)C^4] \\
B_{44} &= \coth(kd)(24 + 92S + 122S^2 + 66S^3 + 67S^4 + 34S^5)/[24(3 + 2S)C^4] \\
B_{53} &= 9(132 + 17S - 2216S^2 - 5897S^3 - 6292S^4 - 2687S^5 + 194S^6 + 467S^7 + 82S^8) \\
&\quad /[128(3 + 2S)(4 + S)C^6) \\
B_{55} &= 5(300 + 1579S + 3176S^2 + 2949S^3 + 1188S^4 + 675S^5 + 1326S^6 + 827S^7 + 130S^8) \\
&\quad /[384(3 + 2S)(4 + S)C^6] \\
C_0 &= \sqrt{\tanh(kd)} \\
C_2 &= C_0(2 + 7S^2)/(4C^2) \\
C_4 &= C_0(4 + 32S - 116S^2 - 400S^3 - 71S^4 + 146S^5)/(32C^5)
\end{aligned}
$$

Table C.2: Fifth-order gravity wave coefficients [Fenton 1985]

Appendix D

FLUENT® Multiphase Model

A boundary element scheme based on potential flow cannot model the effects of viscosity on the ventilating as well as non-ventilating water entry of bodies. Another feature of the flow that is overlooked is the formation of spray. An important characteristic of high-speed water-entry of bodies is the formation of jets along the wetted part. In a real fluid, these jets quickly break-up into spray under the influence of surface-tension combined with the effects of shear at the air-water interface [Greenhow and Lin 1983, Brennen 2005]. The BEM scheme, as shown in the results in the previous chapters on wetted and ventilating entry, can capture the formation of the jet and sustain its growth quite well. It cannot, however, model the break-up of the jet into spray as it keeps the free-surface body intersection point on the body at all times, neglects the effect of surface tension and ignores the dynamic effects of the surrounding air. It is important to understand the effects of spray as it tends to reduce the *effective* wetted part of the body during surface entry.

An ANSYS® FLUENT® based model is used to study these effects. The model is implemented for the water-entry of a wedge at different angles of attack and velocities of entry. This section only summarizes the two-main aspects of the FLUENT® model (a) multiphase flow to deal with the air-water interface (b) dynamic meshing to deal with the vertical translation of the wedge.

D.1 Multiphase flow

It is necessary to consider a multiphase flow since the wedge moves from an air-phase to a water-phase. FLUENT® offers three schemes to model such flows (i) the Volume of Fluid (VOF) model (ii) the mixture model, and (iii) the Eulerian model. These three schemes are classified under the Euler-Euler approach where the different phases are treated mathematically as interpenetrating continua [FLUENT Inc., Chapter 23 2006]. Each of these models is suitable for a specific class of applications.

Applications of the Eulerian multiphase model include bubble columns, risers, particle suspension, and fluidized beds. The mixture model is designed for two or more phases (fluid or particulate) and for flows with low loading or that are bubbly. An important feature of the mixture model is that it is possible to specify relative velocities for the dispersed phases. A major application of the mixture model is the prediction of cavitation. Typical application of the VOF model include the prediction of jet breakup, the motion of large bubbles in a liquid, the motion of liquid after a dam break, and the steady or transient tracking of any liquid-gas interface. Compared to the other two models, the VOF model is the most ideal for modeling the ventilating and non-ventilating water-entry problem.

D.2 Dynamic Mesh

The water-entry simulation involves the rigid-body motion of the wedge and this is specified via a user-defined-function feature (UDF) in FLUENT®. However, along with the motion of the hydrofoil, the mesh around it has to be dynamically changed to account for the motion related deformation. Initial studies were done using a spring-based-smoothing method, a scheme in which the edges between any two mesh nodes are idealized as a network of interconnected springs. This is combined with a local remeshing method to improve the mesh quality based on the maximum skewness permitted and, the minimum and maximum length scales of the mesh. Even though

the scheme is easier to implement, initial studies indicated that it was difficult to maintain a good mesh quality along the air-water interface, which is critical to the simulation.

An alternative dynamic meshing scheme is based on the concept of layering - the addition or removal of layers of cell adjacent to a moving boundary, based on the height of the layer adjacent to a moving surface. The dynamic mesh model in FLUENT® allows one to specify an ideal layer height on each moving boundary. The layer of cells adjacent to the moving boundary (layer j in Figure) is split or merged with the layer of cells next to it (layer i in Figure) based on the height (h) of the cells in layer j. If the cells in layer j are expanding, the cell heights are allowed to increase until

$$h_{min} < (1 + \alpha_s)h_{ideal} \tag{D.1}$$

where h_{min} is the minimum cell height of cell layer j, h_{ideal} is the ideal cell height, and α_s is the layer split factor. When this condition is met, the cells are split based on the specified layering option: constant height or constant ratio.

If the cells in layer j are being compressed, they can be compressed until

$$h_{min} < \alpha_c h_{ideal} \tag{D.2}$$

where α_c is the layer collapse factor. When this condition is met, the compressed layer of cells is merged into the layer of cells above the compressed layer; i.e., the cells in layer j are merged with those in layer i.

One of the limitations of the layering method is that the moving boundary has to be perpendicular to the direction of motion and this is not so in most cases of water-entry. An alternate way is to let the entire grid, except its top and bottom boundaries, translate along with the wedge. The main aspects of the layering method are as follows:

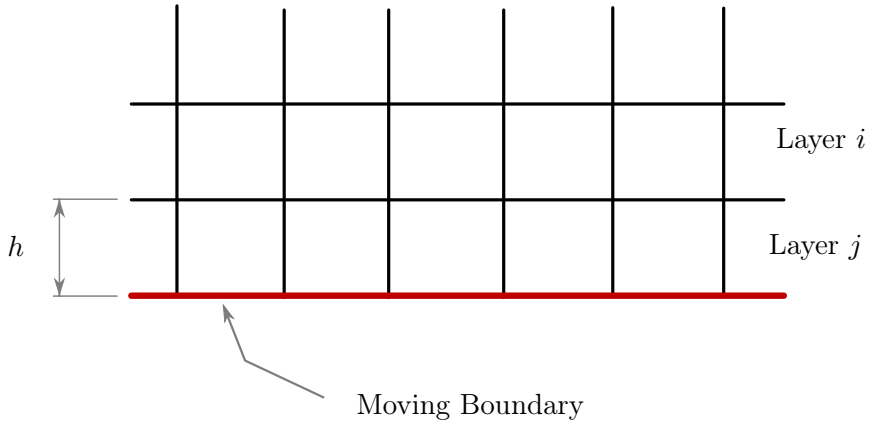

Figure D.1: Dynamic layering method (figure taken from [FLUENT Inc., Chapter 11 2006])

(i) The overall grid around the wedge is divided into three areas - top, middle and bottom (as seen in Figure D.2).

(ii) The first layer of cells in the top-area adjacent to the top boundary expands, shown in Figure D.2 as the Expansion Zone, as the grid moves vertically downward. This layer grows until the expansion criteria for the cell height, Eqn. D.1, is met. The cell layer is then split into two or more layers depending on the specified ideal height. This process is repeated during the course of the simulation adding new cell layers to the top-area.

(iii) The downward movement of the grid has the opposite effect in the bottom-area. The first layer of cells adjacent to the bottom boundary in the bottom-area, shown in Figure D.2 as the Compression Zone, shrinks until the compression criteria for the cell height, Eqn. D.2, is met. Once this criteria is reached, the cell layer gets absorbed into the adjacent cell layers and removes it from the grid. This process repeats itself during the simulation removing cell layers from the bottom-area.

(iv) The middle-area neither grows nor shrinks in size maintaining an adequate resolution required to resolve the air-water interface accurately.

The whole process of expansion and compression is shown in Figure D.2. The initial configuration is shown at time $t = t_0$. The top-area expands while the bottom-area shrinks as the grid moves downward with a velocity V_w. This aspect is seen in the configuration at times $t = t_1$ and $t = t_2$. t_0, t_1 and t_2 ($t_0 < t_1 < t_2$) have no physical significance and are used only to represent the different stages in the simulation. Note that Figure D.2 is only a schematic showing the areas and boundaries of the grid. The actual discretization of the fluid domain is not shown.

D.3 Mesh Characteristics

The characteristics of the mesh are as follows:

(i) Region C : A Cartesian grid is used in this region to facilitate the use of the layering method (layering method can only be applied to quadrilateral cell in 2D [FLUENT Inc., Chapter 11 2006]).

(ii) Region T : Triangular grid with boundary layer mesh on wedge.

(iii) Total number of cells $\approx$ 430000. Minimum face length $10^{-5}c$ and maximum face length $10^{-2}c$, where c is the chord length of the wedge.

(iv) Parameters controlling the layering scheme α_s=0.4, α_c=0.04 and h_{ideal}=$10^{-2}c$.

The details of the mesh are shown in Figure D.3.

D.4 Boundary conditions and extents of domain

The boundary conditions and the extent of the numerical domain are as shown in Figure D.4. The dimensions of the wedge are 0.5″ (12.7 mm) by 6″ (152.4 mm)

in section with a $6''$ (152.4 mm) chord. This geometry is chosen to make comparisons with the experimental measurements of [Cox 1971]. Summary of boundary conditions:

(i) W_1,W_2,W_3 : Stationary walls.

(ii) W_4 : Rigid Body Motion, No-slip wall

(iii) Pressure Outlet (volume of fraction of water = 0).

D.5 Solver characteristics

In the VOF model, the geo-reconstruct scheme is used to accurately capture the air-water interface [FLUENT Inc., Chapter 23 2006]. The time stepping is deemed first-order with the use of the dynamic mesh model. This is a limitation of the current version of FLUENT [FLUENT Inc., Chapter 11 2006]. The SST $k-\omega$ model is used to model turbulence.

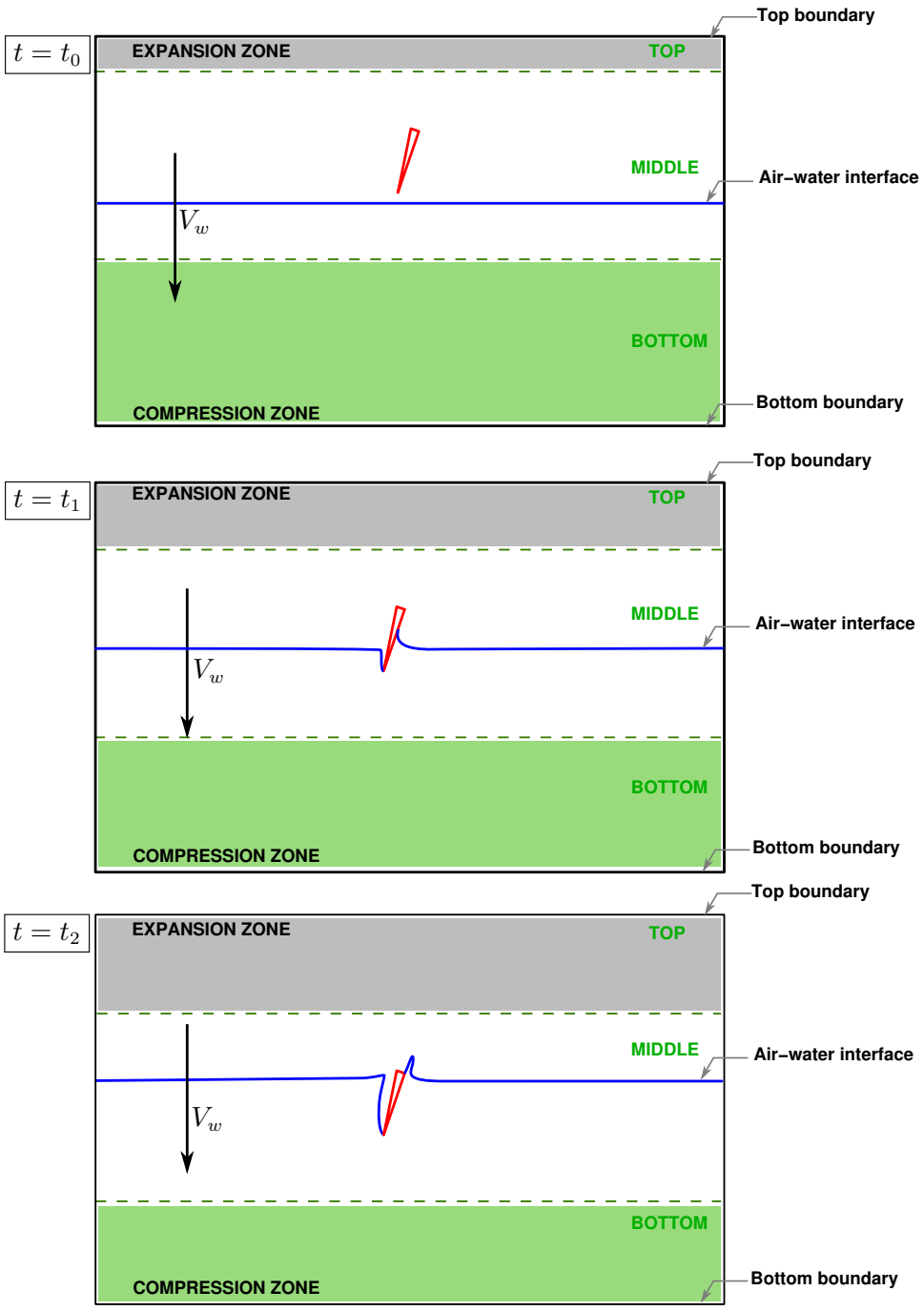

Figure D.2: Dynamic layering method for water-entry problem, at time $t = t_0, t = t_1$ and $t = t_2$, $t_0 < t_1 < t_2$

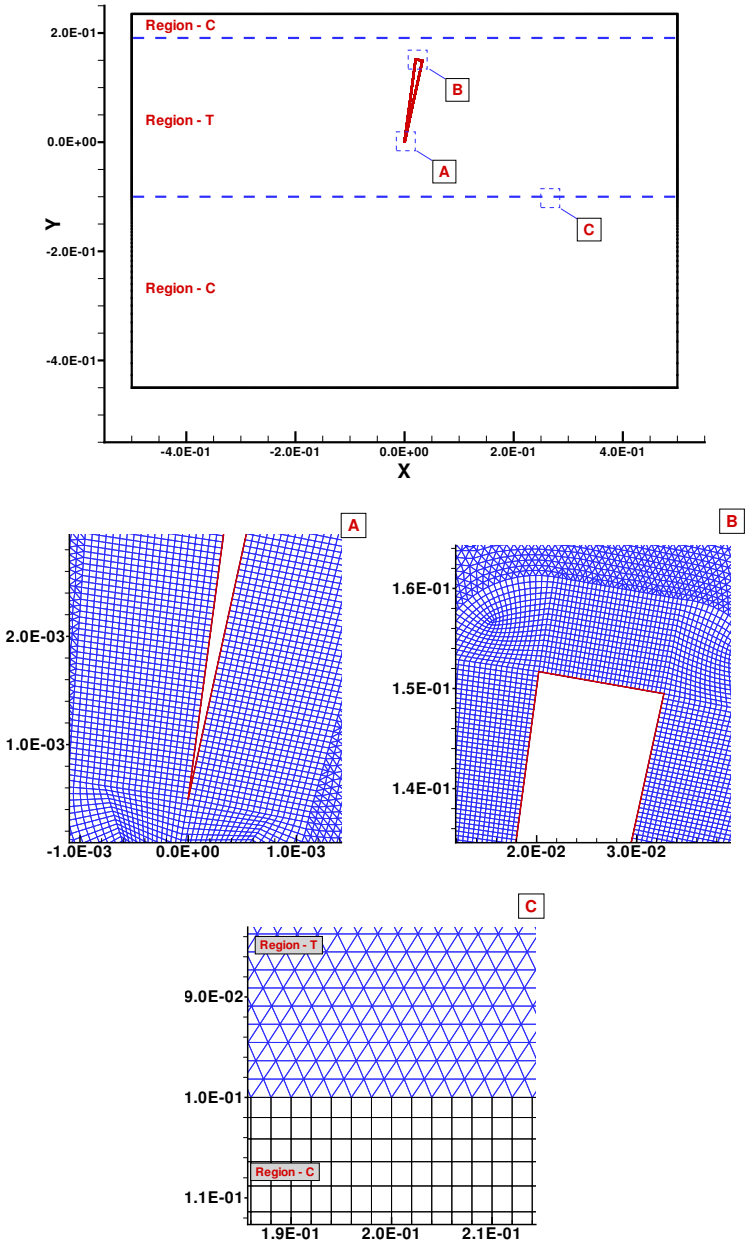

Figure D.3: Details of the mesh and magnified views of specific regions

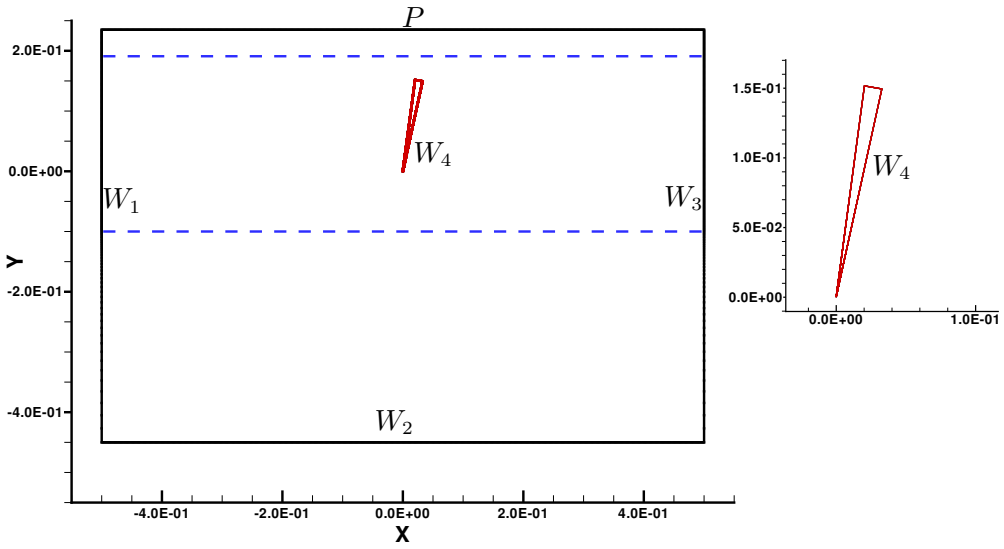

W_1, W_2, W_3 : Stationary walls

W_4 : Rigid Body Motion, No-slip wall

P : Pressure outlet

Figure D.4: Extents of domain and boundary conditions

D.6 FLUENT - Input file for case generation

```
/file/read-case Wedge_10deg.msh.gz
/grid/reorder/reorder-domain
/solve/set/gradient-scheme yes

; NOTE : Enables VOF SCHEME with "solve vof at every iteration",k-w SST
/define/models/multiphase vof 2 explicit 0.25 yes no yes
/define/models/viscous/kw-sst yes
/define/models/viscous/kw-transitional no

; NOTE  : Load Materials (Water and Air)
; AIR   : Primary Phase, WATER : Secondary Phase
/define/materials/copy fluid water-liquid
/define/phases/phase-domain phase-1 air no
/define/phases/phase-domain phase-2 water yes water-liquid

; NOTE : Set Operating Conditions
/define/operating-conditions/reference-pressure-location 0.0 0.235
/define/operating-conditions/gravity yes 0.0 -9.81
/define/operating-conditions/operating-density yes 1.225

; NOTE : Set Boundary Conditions
/define/boundary-conditions/wall side_right
mixture no yes shear-bc-spec-shear no 0 no 0 no 0 no 0
/define/boundary-conditions/wall side_left
mixture no yes shear-bc-spec-shear no 0 no 0 no 0 no 0
/define/boundary-conditions/pressure-outlet top water no 0
/define/boundary-conditions/pressure-outlet top mixture no 0 no yes no no yes 1 10

; NOTE : Enable Dynamic Mesh Option with Layering
/define/models/dynamic-mesh yes no no
/define/models/dynamic-mesh-controls/smoothing no
/define/models/dynamic-mesh-controls/layering yes
/define/models/dynamic-mesh-controls/layering-parameter/constant-height yes

; NOTE : Compile User-define-function for Rigid Body Motion
/define/user-defined/compiled-functions/compile "libudf" yes "Wedge.c" "" ""
/define/user-defined/compiled-functions/load "libudf"
/define/dynamic-zones/create fluid rigid-body wedge::libudf 0 0 0
/define/dynamic-zones/create wedge rigid-body wedge::libudf 0 0 0 fluid 0
/define/dynamic-zones/create top stationary fluid 0.002
/define/dynamic-zones/create bottom stationary fluid 0.002

; NOTE : Set Discretization Schemes, Under-relaxation Parameters
; Pressure              - 13 (BODY-FORCE WEIGHTED)
; Momenturm             - 6  (THIRD-ORDER MUSCL)
; Volume Fraction       - 16 (GEO-RECONSTRUCT)
```

```
; Turbulence (k)        - 1  (SECOND-ORDER UPWIND)
; Turbulence (omega)    - 1  (SECOND-ORDER UPWIND)
; P-V Coupling          - 22 (PISO)

/solve/set/discretization-scheme/pressure 13
/solve/set/discretization-scheme/mom 6
/solve/set/discretization-scheme/mp 16
/solve/set/discretization-scheme/k 1
/solve/set/discretization-scheme/omega 1
/solve/set/p-v-coupling 22
/solve/set/p-v-controls 1 1 no
/solve/set/under-relaxation/mom 0.5
/solve/set/under-relaxation/pressure 0.5

; NOTE : Set initialization defaults
/solve/initialize/set-defaults/water mp 0
/solve/initialize/set-defaults/mixture k 0.001
/solve/initialize/set-defaults/mixture omega 1000

; NOTE : Set residual monitors
; NOTE : Set X-Force and Y-Force Monitors
/solve/monitors/residual/convergence-criteria 1e-6 1e-6 1e-6 1e-6 1e-6
/solve/monitors/residual/n-save 10000

; NOTE : TUI option for VOF scheme
(rpsetvar 'vof/improved-wall-treatment? #t)
; NOTE : Disable "reverse flow at top:pressure-outlet boundary" warning
/solve/set/flow-warnings no

; NOTE : Set Auto-save options
/file/binary-files yes

; NOTE : Set Reference Values
/report/reference-values/density 998.2
/report/reference-values/viscosity 0.001003
/report/reference-values/velocity 2.45

; NOTE : Create Execute on demand commands
; To be created at Run : time
; Make sure Directories TECPLOT_VOF and TECPLOT_ALL exist in the RUN Directory
/solve/execute-commands/add-edit tec_export_all 100 "time-step"
"/file/export tecplot ../TECPLOT_ALL/Wedge_10deg_all_%4t
() air-vof x-velocity y-velocity velocity-magnitude
vorticity-mag pressure dynamic-pressure absolute-pressure ()"
/solve/execute-commands/add-edit write_time 1 "time-step"
"/define/user-defined execute-on-demand \"write_time::libudf\""

```

```
94  ; NOTE : SAVE Case File : Ready for Simulation
95  ; TO Run the simulation use the input file Wedge_run.inp
96  /file/write-case Wedge_10deg.cas.gz
97
98  ; NOTE : Exit FLUENT
99  /exit yes
```

D.7 FLUENT - Input file for case execution

```
1   /file/read-case Wedge_10deg.cas.gz
2
3   /file/auto-save/append-file-name-with time-step 4
4   /file/auto-save/case-frequency 100
5   /file/auto-save/data-frequency 100
6   /file/auto-save/root-name "../RUN/Wedge_10deg.gz"
7   /file/set-batch-options no yes yes no
8
9   /adapt/mark-inout-rectangle yes no -0.5 0.5 -0.45 0.0
10  /solve/initialize/initialize-flow
11  (rpsetvar 'patch/vof? #t)
12  /solve/patch water () 0 () mp 1
13
14  /solve/set/time-step 5e-7
15  /solve/set/variable-time-stepping yes no 0.25 0.06342 1e-7 1e-5 0.5 2 10
16  /solve/dual-time-iterate 6342000 120
17
18  ; Write Case and Data File of Final Time-step
19  /file/write-case-data RUN/Wedge_10deg-%4t.cas.gz
20  /file/export tecplot ../TECPLOT_ALL/Wedge_10deg_all_%4t
21  () air-vof x-velocity y-velocity
22  velocity-magnitude vorticity-mag pressure dynamic-pressure absolute-pressure ()
23  /exit yes
```

D.8 GAMBIT - Journal file for mesh generation

```
1   / Wedge Chord Length
2   $Wedge_C = 6.0*0.0254
3   / Wedge Section Thickness
4   $Wedge_t = 0.5*0.0254
5   / Angle of Attack
6   $AOA = 12
7   / Initial Position of Wedge above free-surface
8   $Init_L = 5.0e-4
9   / Dimensions of Domain
10  $D_L     = 0.500
```

```
11  $DTop_h  = 0.235
12  $DMid_h1 = 0.225
13  $DMid_h2 = 0.100
14  $DBot_h  = 0.450
15  / Mesh File Name
16  $FNAME = "Wedge_"+NTOS($AOA)+"deg.msh"
17  / Create Domain Vertices
18  / Left  (L), Right (R)
19  vertex create "L1" coordinates -0.5 0.235 0
20  vertex create "L2" coordinates -0.5 0.225 0
21  vertex create "L3" coordinates -0.5 -0.1 0
22  vertex create "L4" coordinates -0.5 -0.45 0
23  vertex create "R1" coordinates 0.5 0.235 0
24  vertex create "R2" coordinates 0.5 0.225 0
25  vertex create "R3" coordinates 0.5 -0.1 0
26  vertex create "R4" coordinates 0.5 -0.45 0
27  / Vertices of Edges
28  vertex create "P" coordinates 0 0 0
29  vertex create "A" coordinates -0.00635 0.1524 0
30  vertex create "B" coordinates 0.00635 0.1524 0
31  / Create Domain Edges
32  / Edges of Domain
33  edge create "EL1" straight "L1" "L2"
34  edge create "EL2" straight "L2" "L3"
35  edge create "EL3" straight "L3" "L4"
36  edge create "ER1" straight "R1" "R2"
37  edge create "ER2" straight "R2" "R3"
38  edge create "ER3" straight "R3" "R4"
39  edge create "EH1" straight "L1" "R1"
40  edge create "EH2" straight "L2" "R2"
41  edge create "EH3" straight "L3" "R3"
42  edge create "EH4" straight "L4" "R4"
43  / Edges of Wedge
44  edge create "PA" straight "P" "A"
45  edge create "PB" straight "P" "B"
46  edge create "AB" straight "A" "B"
47  / Rotate Wedge corresponding to Angle of Attack
48  edge move "PA" "PB" "AB" dangle -12 vector 0 0 1 origin 0 0 0
49  edge move "PA" "PB" "AB" offset 0 0.0005 0
50
51  / Create Temporary Edges for Mid-face creation
52  edge create "ET1" straight "B" "R2"
53  edge create "ET2" straight "A" "L2"
54  edge create "ET3" straight "P" "L3"
55  edge create "ET4" straight "P" "R3"
56
57  ////////////////////////////////////////////////////////////////
```

```
58  / Create Domain Faces
59  face create "FLUID_TOP" wireframe "ER1" "EH1" "EL1" "EH2" real
60  face create "FT1" wireframe "ET1" "EH2" "ET2" "AB" real
61  face create "FT2" wireframe "PA" "ET2" "EL2" "ET3" real
62  face create "FT3" wireframe "ET3" "EH3" "ET4" real
63  face create "FT4" wireframe "ET4" "ER2" "ET1" "PB" real
64  face unite faces "FT1" "FT2" "FT3" "FT4" real
65  face modify "FT1" label "FLUID_MIDDLE"
66  face create "FLUID_BOTTOM" wireframe "EH4" "ER3" "EH3" "EL3" real
67
68  ////////////////////////////////////////////////////////////////////
69  / Mesh Domain Faces
70  edge mesh "PA" "PB" firstlength ratio1 0.0001 intervals 400
71  edge mesh "AB" successive ratio1 1 intervals 15
72  blayer create first 110 growth 1.005 total 115.05 rows 10 transition 1 trows \
73    0 wedge aspectratio
74  blayer attach "b_layer.1" face "FLUID_MIDDLE" "FLUID_MIDDLE" edge "PA" "PB" \
75    add
76  blayer create first 125 growth 1.002 total 127.014 rows 9 transition 1 trows \
77    0 wedge aspectratio
78  blayer attach "b_layer.2" face "FLUID_MIDDLE" edge "AB" add
79  sfunction create sourceedges "PA" "PB" "AB" growthrate 1.03 sizelimit 0.002 \
80    attachfaces "FLUID_MIDDLE" meshed
81  sfunction bgrid attachfaces "FLUID_MIDDLE"
82  face mesh "FLUID_MIDDLE" triangle size 1
83  edge link "EH2" "EH1" directions 0 0
84  edge link "EH3" "EH4" directions 0 0
85  edge mesh "EL1" "ER1" successive ratio1 1 size 0.002
86  edge mesh "EL3" "ER3" firstlength ratio1 0.002 intervals 40
87  face mesh "FLUID_TOP" map size 1
88  face mesh "FLUID_BOTTOM" map size 1
89
90  ////////////////////////////////////////////////////////////////////
91  / Setup Boundary Conditions
92  solver select "FLUENT 5/6"
93  physics create "SIDE_LEFT" btype "WALL" edge "EL1" "EL2" "EL3"
94  physics create "SIDE_RIGHT" btype "WALL" edge "ER1" "ER2" "ER3"
95  physics create "TOP" btype "PRESSURE_OUTLET" edge "EH1"
96  physics create "BOTTOM" btype "WALL" edge "EH4"
97  physics create "FLUID" ctype "FLUID" face "FLUID_TOP" "FLUID_MIDDLE" \
98    "FLUID_BOTTOM"
99  physics create "WEDGE" btype "WALL" edge "PA" "AB" "PB"
100 export fluent5 "Wedge_12deg.msh" nozval
101 save
102 end force
```

Appendix E

Axisymmetric BEM

This chapter provides a brief mathematical and numerical formulation of an axisymmetric BEM model. The model presented here was developed as a precursor to a 3D model and to serve as tool for verifying the 3D results for axisymmetric problems. Results from the axisymmetric BEM are not included in this dissertation.

E.1 Mathematical Formulation

For a 3-D isotropic medium, the Green's function can be represented as

$$G^{3D}(p,q) = \frac{1}{4\pi\ r_{pq}} \tag{E.1}$$

where $r_{pq} = \sqrt{(x_p - x_q)^2 + (y_p - y_q)^2 + (z_p - z_q)^2}$ is the distance between the field point p and source point q. [Note: from further on, $()_p$ represents the quantities specified at the field point and $()_q$ that at the source point]

The corresponding Boundary Integral Equation can be represented as

$$\alpha_p\ \phi_p + \int_S \phi \frac{\partial \psi}{\partial n}\ dS_q = \int_S \psi \frac{\partial \phi}{\partial n}\ dS_q \tag{E.2}$$

where $\psi \equiv G^{3D}(p,q)$. Assuming that all the boundary values have axial symmetry, we can represent the $3-D$ Boundary Integral Equation in terms of cylindrical polar coordinates (R, θ, z) as

$$\alpha_p\ \phi_p + \int_\Gamma \phi \int_0^{2\pi} \frac{\partial \psi}{\partial n}\ R_q d\theta_q d\Gamma_q = \int_\Gamma \frac{\partial \phi}{\partial n} \int_0^{2\pi} \psi\ R_q d\theta_q d\Gamma_q \tag{E.3}$$

or,

$$\alpha_p \, \phi_p + \int_\Gamma \phi \frac{\partial \overline{\psi}}{\partial n} \, R_q d\Gamma_q = \int_\Gamma \overline{\psi} \frac{\partial \phi}{\partial n} \, R_q d\Gamma_q \tag{E.4}$$

where $\overline{\psi} \equiv G^{AX}(p,q)$ is the axi-symmetric Green's function and can be represented as

$$\overline{\psi} = G^{AX}(p,q) = \int_0^{2\pi} G^{3D}(p,q) d\theta_q = \frac{K(m)}{\pi\sqrt{a+b}} \tag{E.5}$$

where $K(m)$ is the complete elliptic integral of the first kind, and

$$K(m) = \int_0^{\frac{\pi}{2}} \frac{d\eta}{\sqrt{1 - m\sin^2\eta}}; \quad 0 \le m < 1 \tag{E.6}$$

with, $m = \dfrac{2b}{a+b}$, $a = R_p^2 + R_q^2 + (z_p - z_q)^2$ and $b = 2R_pR_q$.

Note that (R_p, z_p) and (R_q, z_q) are the coordinates of the field point and source point respectively in the cylindrical coordinate system. The coordinates of the field and source points can be represented using the the transformation

$$\begin{aligned} x_{(p,q)} &= R_{(p,q)} \cos\theta_{(p,q)} \\ y_{(p,q)} &= R_{(p,q)} \sin\theta_{(p,q)} \end{aligned} \tag{E.7}$$

With (E.7), we have $r_{pq} = \sqrt{R_p^2 + R_q^2 - 2R_pR_q\cos(\theta_p - \theta_q) + (z_p - z_q)^2}$.

The normal derivative of the axisymmetric Green's function can be written as:

$$\frac{\partial \overline{\psi}}{\partial n_q} = \frac{\partial \overline{\psi}}{\partial R_q}(n_R)_q + \frac{\partial \overline{\psi}}{\partial z_q}(n_z)_q \tag{E.8}$$

where,

$$\begin{aligned} \frac{\partial \overline{\psi}}{\partial R_q} &= \frac{1}{\pi\sqrt{a+b}} \, \frac{1}{2R_q} \left[\frac{R_p^2 - R_q^2 + (z_p - z_q)^2}{a-b} E(m) - K(m) \right] \\ \frac{\partial \overline{\psi}}{\partial z_q} &= \frac{1}{\pi\sqrt{a+b}} \, \frac{(z_p - z_q)}{a-b} E(m) \end{aligned} \tag{E.9}$$

and $n = n_R\hat{\mathbf{e}}_R + n_z\hat{\mathbf{e}}_z$ is the normal to the surface (positive out of the domain). $E(m)$ is the complete elliptic integral of the second kind, and

$$E(m) = \int_0^{\frac{\pi}{2}} \sqrt{1 - m\sin^2\eta}\, d\eta; \quad 0 \le m \le 1 \tag{E.10}$$

The following properties of elliptic integrals are used to simplify the evaluation of the influence coefficients [Hart et al. 1968, Hastings 1955]

E.1.1 Properties of Elliptic Integrals : Inequalities and Limiting Behavior

(a) $\dfrac{\pi}{2} = K(0) \ge K(m) + \dfrac{1}{2}\ln(1-m) \ge \ln(4)$

(b) $K(m) = \dfrac{1}{2}\ln\left(\dfrac{16}{m_1}\right) + \mathcal{O}\left[\dfrac{m_1}{2}\ln(m_1)\right]; \quad m \to 1; m_1 \to 0\,; m_1 = 1-m$

(c) $\dfrac{\pi}{2} = E(0) \ge E(m) \ge E(1) = 1$

E.1.2 Properties of Elliptic Integrals : Derivatives

(a) $2\dfrac{dK(m)}{dm} = \dfrac{E(m)}{m(1-m)} - \dfrac{K(m)}{m}$

(b) $2\dfrac{dE(m)}{dm} = \dfrac{E(m) - K(m)}{m}$

E.1.3 Properties of Elliptic Integrals : Polynomial Approximations $0 \le m < 1$

$$\left.\begin{array}{rcl} K(m) & = & A(m_1) - B(m_1)\log(m_1) \\ E(m) & = & C(m_1) - D(m_1)\log(m_1) \end{array}\right\} \tag{E.11}$$

where $m_1 = 1 - m$.

$$A(m_1) = \sum_{i=0}^{10} A_i m_1^i \quad \left\{ \begin{array}{lcl} A_0 &=& (+1)\ 0.13862\ 94361\ 11989\ 06188\ 344 \\ A_1 &=& (-1)\ 0.96573\ 59028\ 08562\ 55384\ 3 \\ A_2 &=& (-1)\ 0.30885\ 14627\ 13051\ 89866\ 31 \\ A_3 &=& (-1)\ 0.14938\ 01353\ 26871\ 65241\ 7 \\ A_4 &=& (-2)\ 0.87898\ 01874\ 55506\ 46777\ 5 \\ A_5 &=& (-2)\ 0.61796\ 27446\ 05331\ 76083\ 9 \\ A_6 &=& (-2)\ 0.68479\ 09282\ 62450\ 51197\ 3 \\ A_7 &=& (-2)\ 0.98489\ 29322\ 17689\ 37681\ 7 \\ A_8 &=& (-2)\ 0.80030\ 03980\ 64998\ 53708 \\ A_9 &=& (-2)\ 0.22966\ 34898\ 39695\ 86868\ 6 \\ A_{10} &=& (-3)\ 0.13930\ 87857\ 00664\ 67279 \end{array} \right. \tag{E.12}$$

$$B(m_1) = \sum_{i=0}^{10} B_i m_1^i \quad \left\{ \begin{array}{lcl} B_0 &=& (+0)\ 0.5 \\ B_1 &=& (+0)\ 0.12499\ 99999\ 99908\ 08051\ 006 \\ B_2 &=& (-1)\ 0.70312\ 49973\ 90383\ 52054\ 04 \\ B_3 &=& (-1)\ 0.48828\ 04190\ 68623\ 97978\ 35 \\ B_4 &=& (-1)\ 0.37377\ 73975\ 86236\ 04143\ 87 \\ B_5 &=& (-1)\ 0.30124\ 84901\ 28989\ 30266\ 25 \\ B_6 &=& (-1)\ 0.23931\ 91332\ 31107\ 90077\ 25 \\ B_7 &=& (-1)\ 0.15530\ 94163\ 19772\ 03876\ 74 \\ B_8 &=& (-2)\ 0.59739\ 04299\ 15542\ 91550\ 7 \\ B_9 &=& (-3)\ 0.92155\ 46349\ 63249\ 84638 \\ B_{10} &=& (-4)\ 0.29700\ 28096\ 65556\ 1206 \end{array} \right. \tag{E.13}$$

$$C(m_1) = \sum_{i=0}^{10} C_i m_1^i \quad \left\{ \begin{array}{lcl} C_0 &=& (+1)\ 0.1 \\ C_1 &=& (+0)\ 0.44314\ 71805\ 60889\ 52648\ 336 \\ C_2 &=& (-1)\ 0.56805\ 19456\ 75591\ 56648\ 14 \\ C_3 &=& (-1)\ 0.21831\ 81167\ 61304\ 81567\ 63 \\ C_4 &=& (-1)\ 0.11569\ 59574\ 52954\ 02174\ 53 \\ C_5 &=& (-2)\ 0.75950\ 93422\ 55943\ 22801\ 5 \\ C_6 &=& (-2)\ 0.78204\ 04060\ 95955\ 41727\ 4 \\ C_7 &=& (-1)\ 0.10770\ 63503\ 98664\ 55472\ 85 \\ C_8 &=& (-2)\ 0.86384\ 42173\ 60407\ 44302\ 4 \\ C_9 &=& (-2)\ 0.24685\ 03330\ 46072\ 27339\ 3 \\ C_{10} &=& (-3)\ 0.14946\ 62175\ 71813\ 2677 \end{array} \right. \tag{E.14}$$

$$D(m_1) = \sum_{i=0}^{10} D_i m_1^i \quad \begin{cases} D_0 &= (+0)\ 0.0 \\ D_1 &= (+0)\ 0.24999\ 99999\ 99901\ 77207\ 939 \\ D_2 &= (-1)\ 0.93749\ 99972\ 12031\ 40657\ 95 \\ D_3 &= (-1)\ 0.58593\ 66125\ 55314\ 91732\ 41 \\ D_4 &= (-1)\ 0.42717\ 89054\ 73830\ 95644\ 27 \\ D_5 &= (-1)\ 0.33478\ 94366\ 57616\ 26232\ 19 \\ D_6 &= (-1)\ 0.26145\ 01470\ 03138\ 78931\ 72 \\ D_7 &= (-1)\ 0.16804\ 02334\ 63633\ 84980\ 67 \\ D_8 &= (-2)\ 0.64321\ 46586\ 43830\ 17665\ 5 \\ D_9 &= (-3)\ 0.98983\ 32846\ 22538\ 47867 \\ D_{10} &= (-4)\ 0.31859\ 19565\ 55015\ 718 \end{cases} \tag{E.15}$$

E.2 Influence Coefficients

For linear iso-parametric elements, we have

$$\begin{array}{rcl} R_q(\xi) &=& N_1(\xi)R_1 + N_2(\xi)R_2 \\ z_q(\xi) &=& N_1(\xi)z_1 + N_2(\xi)z_2 \end{array} \tag{E.16}$$

and

$$\begin{array}{rcl} \phi(\xi) &=& N_1(\xi)\phi_1 + N_2(\xi)\phi_2 \\ \phi_n(\xi) &=& N_1(\xi)(\phi_n)_1 + N_2(\xi)(\phi_n)_2 \end{array} \tag{E.17}$$

where (R_1, z_1) and (R_2, z_2) are the coordinates of nodes (1) and (2) of the linear element. ϕ and ϕ_n are the corresponding velocity potentials and normal velocities. $N_1(\xi)$ and $N_2(\xi)$ are the shape functions of the form

$$N_1(\xi) = \frac{1}{2}(1-\xi) \quad ; \quad N_2(\xi) = \frac{1}{2}(1+\xi) \tag{E.18}$$

where ξ is the intrinsic element coordinate ($-1 \leq \xi \leq +1$). For a generic linear element, the following integral has to be evaluated

$$H^e = \int_{\Gamma^e} \phi \frac{\partial \overline{\psi}}{\partial n} R_q d\Gamma_q^e \tag{E.19}$$

and

$$G^e = \int_{\Gamma^e} \frac{\partial \phi}{\partial n}\, \overline{\psi}\, R_q d\Gamma_q^e \tag{E.20}$$

In terms of the intrinsic element coordinate ξ, we have $d\Gamma_q^e = |J|d\xi$ where $|J|$ is the Jacobian of the transformation. The Jacobian can be calculated as

$$\begin{aligned} |J| &= \sqrt{J_1^2 + J_2^2} \\ J_1 &= \frac{dR_q}{d\xi} = \frac{R_2 - R_1}{2} \\ J_2 &= \frac{dz_q}{d\xi} = \frac{z_2 - z_1}{2} \\ \Rightarrow |J| &= \frac{h}{2} \end{aligned} \tag{E.21}$$

Thus,

$$H^e = \int_{-1}^{+1} \left[N_1(\xi)\phi_1 + N_2(\xi)\phi_2\right] \frac{\partial \overline{\psi}}{\partial n} R_q(\xi) \frac{h}{2} d\xi \tag{E.22}$$

or $H^e = \phi_1 H_1 + \phi_2 H_2$, and

$$\begin{aligned} H_1 &= \frac{h}{2} \int_{-1}^{+1} N_1(\xi) \frac{\partial \overline{\psi}}{\partial n} R_q(\xi) d\xi \\ H_2 &= \frac{h}{2} \int_{-1}^{+1} N_2(\xi) \frac{\partial \overline{\psi}}{\partial n} R_q(\xi) d\xi \end{aligned} \tag{E.23}$$

Similarly,

$$G^e = \int_{-1}^{+1} \left[N_1(\xi)(\phi_n)_1 + N_2(\xi)(\phi_n)_2\right] \overline{\psi}\, R_q(\xi)\, \frac{h}{2} d\xi \tag{E.24}$$

or $G^e = (\phi_n)_1 G_1 + (\phi_n)_2 G_2$, and

$$\begin{aligned} G_1 &= \frac{h}{2} \int_{-1}^{+1} N_1(\xi) \overline{\psi}\, R_q(\xi) d\xi \\ G_2 &= \frac{h}{2} \int_{-1}^{+1} N_2(\xi) \overline{\psi}\, R_q(\xi) d\xi \end{aligned} \tag{E.25}$$

Note that $\overline{\psi}$ and $\dfrac{\partial \overline{\psi}}{\partial n}$ are implicit functions of ξ. H_1, H_2, G_1 and G_2 are evaluated using Gauss-Legendre Integration.

E.2.1 Self-Influence Coefficients

To evaluate the influence coefficient, we start with the polynomial approximations for the elliptic integrals

$$\left.\begin{aligned} K(m) &= A(m_1) - B(m_1)\log(m_1) \\ E(m) &= C(m_1) - D(m_1)\log(m_1) \end{aligned}\right\} \text{where } \; m_1 = 1 - m \tag{E.26}$$

We have $m = \dfrac{2b}{a+b} \Rightarrow m_1 = \dfrac{a-b}{a+b}$. Substituting this form in the polynomial approximation, we have

$$K(m) = A(m_1) + B(m_1)\log(a+b) - B(m_1)\log(a-b) \tag{E.27}$$

Also, by definition $a - b = (R_p - R_q)^2 + (z_p - z_q)^2$. Let $R_f = \sqrt{a-b}$ and this represents the Euclidean distance between the field and source points. Thus

$$\begin{aligned} K(m) &= A(m_1) + B(m_1)\log(a+b) - 2B(m_1)\log R_f \\ E(m) &= C(m_1) + D(m_1)\log(a+b) - 2D(m_1)\log R_f \end{aligned} \tag{E.28}$$

Case (i) : Singularity at NODE (1) : as $\xi \to -1$, $R_f \to 0$

The polynomial approximations for the elliptic integrals are modified further to account for the singularity at NODE (1) as follows:

$$\begin{aligned} K(m) &= A(m_1) + \\ &\quad B(m_1)\log(a+b) - 2B(m_1)\log\left(\frac{2R_f}{1+\xi}\right) + 2B(m_1)\log\left(\frac{2}{1+\xi}\right) \\ E(m) &= C(m_1) + \\ &\quad D(m_1)\log(a+b) - 2D(m_1)\log\left(\frac{2R_f}{1+\xi}\right) + 2D(m_1)\log\left(\frac{2}{1+\xi}\right) \end{aligned} \tag{E.29}$$

Case (ii) : Singularity at NODE (2) : as $\xi \to +1$, $R_f \to 0$

The polynomial approximations for the elliptic integrals are modified further to account for the singularity at NODE (2) as follows:

$$\begin{aligned} K(m) &= A(m_1) + B(m_1)\log(a+b) - 2B(m_1)\log\left(\frac{2R_f}{1-\xi}\right) + 2B(m_1)\log\left(\frac{2}{1-\xi}\right) \\ E(m) &= C(m_1) + D(m_1)\log(a+b) - 2D(m_1)\log\left(\frac{2R_f}{1-\xi}\right) + 2D(m_1)\log\left(\frac{2}{1-\xi}\right) \end{aligned} \tag{E.30}$$

Appendix F

Multipole Expansions

Far field expansions for the dipole and source potentials due to a quadrilateral panel can be derived from Taylor series involving the product of partial derivatives of r^{-1} with appropriate moments of the panel area [Stratton 1941]. The source potential can be expanded in the form [Hess and Smith 1967, Newman 1986]

$$\begin{aligned}\Psi &= \iint \frac{1}{r} d\xi d\eta \\ &= \sum_{m=0}^{\infty}\sum_{n=0}^{\infty} \frac{(-1)^{m+n}}{m!n!} I_{mn} \frac{\partial^{m+n}}{\partial x^m \partial y^n}\frac{1}{r}\end{aligned} \tag{F.1}$$

where, $r = \sqrt{(x^2+y^2+z^2)}$ is the distance to the field point P in the panel coordinate system and

$$I_{mn} = \iint \xi^m \eta^n d\xi d\eta \tag{F.2}$$

is the corresponding moment of the panel about the origin. The above series can be truncated at a finite order $(m+n)$, provided the distance to the field point is sufficiently large to ensure the desired degree of accuracy. To ensure sufficient accuracy, let the series be truncated such that $m+n=4$. Thus the multipole expansion given by eqn. (F.1) can be written as

$$
\begin{aligned}
\Psi = & I_{00}G \\
& - (I_{10}G_x + I_{01}G_y) \\
& + \frac{1}{2}(I_{20}G_{xx} + 2I_{11}G_{xy} + I_{02}G_{yy}) \\
& - \frac{1}{6}(I_{30}G_{xxx} + 3I_{21}G_{xxy} + 3I_{12}G_{xyy} + I_{03}G_{yyy}) \\
& + \frac{1}{24}(I_{40}G_{xxxx} + 4I_{31}G_{xxxy} + 6I_{22}G_{xxyy} + 4I_{13}G_{xyyy} + I_{04}G_{yyyy})
\end{aligned}
\tag{F.3}
$$

where $G = r^{-1}$. Note that $I_{01} = I_{10} = 0$ since the origin of the local panel coordinate system is located at the centroid of the panel.

The corresponding dipole multipole expansion can be written as (with density -4π over the panel)

$$
\begin{aligned}
\Phi = & I_{00}F \\
& - (I_{10}F_x + I_{01}F_y) \\
& + \frac{1}{2}(I_{20}F_{xx} + 2I_{11}F_{xy} + I_{02}F_{yy}) \\
& - \frac{1}{6}(I_{30}F_{xxx} + 3I_{21}F_{xxy} + 3I_{12}F_{xyy} + I_{03}F_{yyy}) \\
& + \frac{1}{24}(I_{40}F_{xxxx} + 4I_{31}F_{xxxy} + 6I_{22}F_{xxyy} + 4I_{13}F_{xyyy} + I_{04}F_{yyyy})
\end{aligned}
\tag{F.4}
$$

where $F = zr^{-3}$.

The derivatives in equations (F.3) and (F.4) are as follows:

$$G = r^{-1} \qquad F = zr^{-3}$$

$$G_x = -xr^{-3} \qquad F_x = -3zxr^{-5}$$

$$G_y = -yr^{-3} \qquad F_y = -3zyr^{-5}$$

$$G_{xx} = 3x^2r^{-5} - r^{-3} \qquad F_{xx} = 15zx^2r^{-7} - 3zr^{-5}$$

$$G_{xy} = 3xyr^{-5} \qquad F_{xy} = 15zxyr^{-7}$$

$$G_{yy} = 3y^2r^{-5} - r^{-3} \qquad F_{yy} = 15zy^2r^{-7} - 3zr^{-5}$$

$$G_{xxx} = -15x^3r^{-7} + 9xr^{-5} \qquad F_{xxx} = -105zx^3r^{-9} + 45zxr^{-7}$$

$$G_{xxy} = -15x^2yr^{-7} + 3yr^{-5} \qquad F_{xxy} = -105zx^2yr^{-9} + 15zyr^{-7}$$

$$G_{xyy} = -15xy^2r^{-7} + 3xr^{-5} \qquad F_{xyy} = -105zxy^2r^{-9} + 15zxr^{-7}$$

$$G_{yyy} = -15y^3r^{-7} + 9yr^{-5} \qquad F_{yyy} = -105zy^3r^{-9} + 45zyr^{-7}$$

$$G_{xxxx} = 105x^4r^{-9} - 90x^2r^{-7} + 9r^{-5} \qquad F_{xxxx} = 945zx^4r^{-11} - 630zx^2r^{-9} + 45zr^{-7}$$

$$G_{xxxy} = 105x^3yr^{-9} - 45xyr^{-7} \qquad F_{xxxy} = 945zx^3yr^{-11} - 315zxyr^{-9}$$

$$G_{xxyy} = 105x^2y^2r^{-9} - 15(x^2+y^2)r^{-7} + 3r^{-5} \qquad F_{xxyy} = 945zx^2y^2r^{-11} - 105z(x^2+y^2)r^{-9} + 15zr^{-7}$$

$$G_{xyyy} = 105xy^3r^{-9} - 45xyr^{-7} \qquad F_{xyyy} = 945zxy^3r^{-11} - 315zxyr^{-9}$$

$$G_{yyyy} = 105y^4r^{-9} - 90y^2r^{-7} + 9r^{-5} \qquad F_{yyyy} = 945zy^4r^{-11} - 630zy^2r^{-9} + 45zr^{-7}$$

The final form of the multipole expansions for the source and dipole potentials obtained by substituting the above derivatives can be written as

$$\Psi = T_1 + T_3 + T_5^{(1)} + T_5^{(2)} + T_7 + T_9 \tag{F.5}$$

$$\Phi = zr^{-2}[T_1 + 3T_3 + 5T_5^{(1)} + 5T_5^{(2)} + 7T_7 + 9T_9] \tag{F.6}$$

where,

$$rT_1 = I'_{00} \tag{F.7}$$

$$r^3 T_3 = -\frac{1}{3}(I'_{20} + I'_{02}) \tag{F.8}$$

$$r^5 T_5^{(1)} = (x^2 I'_{20} + xyI'_{11} + y^2 I'_{02}) \tag{F.9}$$

$$r^5 T_5^{(2)} = -x(I'_{30} + I'_{12}) - y(I'_{03} + I'_{21}) + \frac{1}{10}(I'_{40} + 2I'_{22} + I'_{04}) \tag{F.10}$$

$$r^7 T_7 = \frac{5}{3}\left[x^3 I'_{30} + 3xy\,(xI'_{21} + yI'_{12}) + y^3 I'_{03}\right] \tag{F.11}$$

$$- x^2(I'_{40} + I'_{22}) - xy(I'_{31} + I'_{13}) - y^2(I'_{22} + I'_{04}) \tag{F.12}$$

$$r^9 T_9 = \frac{7}{6}\left[x^4 I'_{40} + 2xy(x^2 I'_{31} + 3xyI'_{22} + y^2 I'_{13}) + y^4 I'_{04}\right] \tag{F.13}$$

and I'_{00} through I'_{04} are moments scaled in the following manner

$$I'_{00} = I_{00}$$

$$I'_{20} = \frac{3}{2}I_{20}; \quad I'_{11} = 3I_{11}; \quad I'_{02} = \frac{3}{2}I_{02};$$

$$I'_{30} = \frac{3}{2}I_{30}; \quad I'_{21} = \frac{3}{2}I_{21}; \quad I'_{12} = \frac{3}{2}I_{12}; \quad I'_{02} = \frac{3}{2}I_{02}$$

$$I'_{40} = \frac{15}{4}I_{40}; \quad I'_{31} = \frac{15}{2}I_{31}; \quad I'_{22} = \frac{15}{4}I_{22}; \quad I'_{13} = \frac{15}{2}I_{13}; \quad I'_{04} = \frac{15}{4}I_{04}$$

A two-term multipole expansion ($m + n = 2$) for the source and dipole potentials is equivalent to

$$\Psi = T_1 + T_3 + T_5^{(1)} \tag{F.14}$$

$$\Phi = zr^{-2}[T_1 + 3T_3 + 5T_5^{(1)}] \tag{F.15}$$

and a four-term expansion ($m + n = 4$) is equivalent to

$$\Psi = T_1 + T_3 + T_5^{(1)} + T_5^{(2)} + T_7 + T_9 \tag{F.16}$$

$$\Phi = zr^{-2}[T_1 + 3T_3 + 5T_5^{(1)} + 5T_5^{(2)} + 7T_7 + 9T_9] \tag{F.17}$$

Bibliography

Abkowitz, M. A. (1969). *Stability and motion control of ocean vehicles*. MIT Press, Cambridge, MA.

Anderson, E., Bai, Z., Bischof, C., Blackford, S., Demmel, J., Dongarra, J., Du Croz, J., Greenbaum, A., Hammarling, S., McKenney, A., et al. (1999). *LAPACK Users' guide*. Society for Industrial and Applied Mathematics.

Baird, N. (1998). *The World Fast Ferry Market*. Baird Publications, Melbourne, Australia.

Batchelor, G. K. (2000). *An introduction to fluid dynamics*. Cambridge University Press.

Battistin, D. and Iafrati, A. (2004). A numerical model for the jet flow generated by water impact. *Journal of Engineering Mathematics*, 48(3):353–374.

Birkhoff, G. and Zarantonello, E. H. (1957). *Jets, Wakes, and Cavities*. Academic Press Inc., US.

Blount, D. L. and Bartee, R. J. (1997). Design of propulsion systems for high-speed craft. *Marine technology*, 34(4):276–292.

Brebbia, C. A. and Dominguez, J. (1992). *Boundary Elements, An Introductory Course*. Computational Mechanics Publications, McGraw-Hill Book Company, Boston, 2nd edition.

Brebbia, C. A., Telles, J. C. F., and Wrobel, L. C. (1984). *Boundary Element Techniques*. Springer-Verlag, Berlin.

Brennen, C. E. (2005). *Fundamentals of multiphase flow.* Cambridge University Press.

Carlton, J. (2007). *Marine Propellers and Propulsion.* Butterworth-Heinemann, second edition.

Chekin, B. S. (1989). The entry of a wedge into an incompressible fluid. *J. Appl. Math. Mech*, 53(3):300–307.

Cox, B. D. (1971). *Hydrofoil theory for vertical water entry.* PhD thesis, Massachusetts Institute of Technology., Cambridge, Massachusetts.

Dobrovol'skaya, Z. N. (1966). The numerical solution of an integral equation of a plane self-modelling problem on the motion of a liquid with a free-surface. *Zhurnal Vychislitel'noi Matematiki i Matematicheskoi Fiziki*, 6(5):934–941.

Dobrovol'skaya, Z. N. (1969). On some problems of similarity flow of fluid with a free surface. *Journal of Fluid Mechanics*, 36(04):805–829.

Dommermuth, D. and Yue, D. (1987). Numerical simulations of nonlinear axisymmetric flows with a free surface. *Journal of Fluid Mechanics*, 178:195–219.

Dussan V, E. B. (1976). On the difference between a bounding surface and a material surface. *Journal of Fluid Mechanics*, 75(04):609–623.

Dyson, P. K. (2000). *The Modelling, Testing and Design, of a Surface Piercing Propeller Drive.* PhD thesis, Department of Mechanical Engineering, University of Plymouth.

Faltinsen, O. M. (1977). Numerical solution of transient nonlinear free-surface motion outside or inside moving bodies. In *Proceedings 2nd Int. Conf. on Num. Ship Hydrodynamics*, pages 257–266, UC Berkeley.

Faltinsen, O. M. (2005). *Hydrodynamics of High-Speed Marine Vehicles*. Cambridge University Press.

Faltinsen, O. M. and Semenov, Y. A. (2008). Nonlinear problem of flat-plate entry into an incompressible liquid. *Journal of Fluid Mechanics*, 611:151–173.

Fenton, J. (1985). A Fifth-Order Stokes Theory for Steady Waves. *Journal of Waterway, Port, Coastal and Ocean Engineering*, 111(2):216–234.

FLUENT Inc., Chapter 11 (2006). *FLUENT® , 6.3.26, Help System, User's Guide, Chapter 11 : Modeling Flows Using Sliding and Deforming Meshes*. FLUENT®, Inc.

FLUENT Inc., Chapter 23 (2006). *FLUENT® , 6.3.26, Help System, User's Guide, Chapter 23 : Modeling Multiphase Flows*. FLUENT®, Inc.

Furuya, O. (1985). A performance-prediction theory for partially submerged ventilated propellers. *Journal of Fluid Mechanics*, 151:311–335.

Gaul, L., Kögl, M., and Wagner, M. (2003). *Boundary element methods for engineers and scientists: An introductory course with advanced topics*. Springer, 1st edition.

Gilbarg, D. (1960). Jets and cavities. *Handbuch der Physik*, 9:311–445.

Gradshteyn, I. S. and Ryzhik, I. M. (2007). *Table of Integrals, Series, and Products*. Elsevier Acad. Press, Amsterdam, Netherlands, 7th edition.

Greenberg, M. D. (1998). *Advanced engineering mathematics*. Prentice Hall, Upper Saddle River, N.J., 2nd edition.

Greenhow, M. (1987). Wedge entry into initially calm water. *Applied Ocean Research*, 9(4):214–223.

Greenhow, M. and Lin, W.-M. (1983). Nonlinear free surface effects: Experiments and Theory. Technical Report No. 83-19, Department of Ocean Engineering, Massachusetts Institute of Technology, Cambridge, Massachusetts.

Grilli, S. T., Skourup, J., and Svendsen, I. A. (1989). An efficient boundary element method for nonlinear water waves. *Engineering Analysis with Boundary Elements*, 6(2):97–107.

Hadler, J. B. and Hecker, R. (1968). Performance of partially submerged propellers. In *7th ONR Symposium on Naval Hydrodynamics*, pages 1449–1496, Rome, Italy.

Hart, J. F., Cheney, E. W., Lawson, C. L., Maehly, H. J., Mesztenyi, C. K., Rice, J. R., Thacher Jr, H. G., and Witzgall, C. (1968). *Computer approximations, The SIAM series in applied mathematics.* John Wiley & Sons, New York.

Hastings, C. (1955). *Approximations for Digital Computers.* Princeton University Press, Princeton, NJ, USA.

Hess, J. L. and Smith, A. M. O. (1967). Calculation of potential flow about arbitrary bodies. *Progress in Aerospace Sciences*, 8:1–138.

Hildebrand, F. B. (1974). *Introduction to numerical analysis.* McGraw-Hill Book Company.

Hughes, O. F. (1972). Solution of the wedge entry problem by numerical conformal mapping. *Journal of Fluid Mechanics*, 56(1):173–192.

Hughes, O. F. (1973). Some characteristics of the free surface in the wedge entry problem. *Journal of Engineering Mathematics*, 7(4):367–375.

Imas, L. G. (1998). *Hydrodynamics involving a free-surface body juncture.* PhD thesis, Department of Ocean Engineering, Massachusetts Institute of Technology, Cambridge, Massachusetts.

Kacham, B. (2004). Inviscid and Viscous 2D Unsteady Flow Solvers Applied to FPSO Hull Roll Motions (also UT-OE Report 04-7). Master's thesis, Ocean Engineering Group, Department of Civil, Architectural and Environmental Engineering, University of Texas at Austin, Austin, Texas, December.

Kakar, K. (2002). Computational Modeling of FPSO Hull Roll Motions and Two-component Marine Propulsion Systems(also UT-OE Report 02-3). Master's thesis, Ocean Engineering Group, Department of Civil, Architectural and Environmental Engineering, University of Texas at Austin, Austin, Texas, August.

Kamen, P. (1990). Is there a surface-drive in your future? *Professional Boatbuilder*, pages 52–58.

Kellogg, O. D. (1954). *Foundations of potential theory.* Courier Dover Publications.

Kihara, H. (2004). Numerical modeling of flow in water entry of a wedge. In *Proc. 19th International Workshop on Water Waves and Floating Bodies, Cortona, Italy*, pages 28–31.

Kim, M. H. and Hong, S. Y. (2000). Nonlinear wave forces on a stationary vertical cylinder by HOBEM-NWT. In *Proc. 7th International Offshore and Polar Eng. Conf., ISOPE*, volume 3, pages 209–214.

Kinnas, S. A. and Fine, N. E. (1992). A nonlinear boundary element method for the analysis of unsteady propeller sheet cavitation. In *Nineteenth Symposium on Naval Hydrodynamics*, pages 717–737, Seoul, Korea.

Kinnas, S. A., Yu, Y.-H., and Vinayan, V. (2007). Numerical Methods for the Prediction of the Bilge Keel Effects on the Response of Ship-Shaped Hulls. In *Proceedings of the 26th International Conference on Offshore Mechanics and Arctic Engineering*, volume 3, pages 1023–1030, San Diego, California. ASME.

Korobkin, A. A. and Pukhnachov, V. V. (1988). Initial Stage of Water Impact. *Annual Reviews in Fluid Mechanics*, 20(1):159–185.

Korvin-Kroukovsky, B. V. and Jacobs, W. R. (1957). Pitching and heaving motions of a ship in regular waves. *Trans. Society of Naval Architects and Marine Engineers*, 65:590–632.

Kudo, T. and Kinnas, S. A. (1995). Application of unsteady vortex/source lattice method on supercavitating propellers. In *Twenty-Fourth American Towing Tank Conference*, pages 33–40, Texas A&M University.

Kudo, T. and Ukon, Y. (1994). Calculation of supercavitating propeller performance using a vortex-lattice method. In *Second International Symposium on Cavitation*, pages 403–408, Tokyo, Japan.

Kundu, P. K. and Cohen, I. M. (2004). *Fluid dynamics*. Academic Press, 3rd edition.

Lewis, E. V. et al. (1989). *Principles of Naval Architecture: Volume III - Motions in Waves and Controllability*. Society of Naval Architects and Marine Engineers.

Lin, W., Newman, J., and Yue, D. K. P. (1984). Nonlinear forced motions of floating bodies. In *Proc. 15th Intl. Symp. on Naval Hydrodynamics*, pages 1–15, Hamburg, Germany.

Lin, W. M. (1984). *Nonlinear motion of the free surface near a moving body*. PhD thesis, Massachusetts Institute of Technology. Dept. of Ocean Engineering.

Longuet-Higgins, M. and Cokelet, E. (1976). The Deformation of Steep Surface Waves on Water. I. A Numerical Method of Computation. *Proceedings of the Royal Society of London. Series A, Mathematical and Physical Sciences (1934-1990)*, 350(1660):1–26.

Longuet-Higgins, M. and Cokelet, E. (1978). The Deformation of Steep Surface Waves on Water. II. Growth of Normal-Mode Instabilities. *Proceedings of the Royal Society of London. Series A, Mathematical and Physical Sciences (1934-1990)*, 364(1716):1–28.

Mackie, A. G. (1962). A linearized theory of the water entry problem. *Q J Mechanics Appl Math*, 15(2):137–151.

Mackie, A. G. (1969). The Water Entry Problem. *Q J Mechanics Appl Math*, 22(1):1–17.

Mackie, G. C. and Hutchinson, K. W. (1997). *Turbinia* - state of the art? Then and now. In *Marine Propulsion - Turbinia and Beyond*, volume 109, pages 1–11, London. The Institute of Marine Engineers, The Institute of Marine Engineers.

Mei, C. C., Stiassnie, M., and Yue, D. K. P. (2005). *Theory and applications of ocean surface waves*. Advanced Series on Ocean Engineering. World Scientific Publishing Company.

Mei, X., Yuming, L., and Yue, D. K. P. (1999). On the water impact of general two-dimensional sections. *Applied Ocean Research*, 21(1):1 – 15.

Miller, W. and Szantyr, J. (1998). Model Experiments with Surface Piercing Propellers. *Ship Technology Research*, 45:14–21.

Milne-Thomson, L. M. (1973). *Theoretical aerodynamics*. Courier Dover Publications.

Morgan, W. (1966). The testing of hydrofoils for fully-cavitating or ventilated operations. In *Proceedings of the 11th ITTC*, Tokyo, Japan.

Newman, J. N. (1977). *Marine Hydrodynamics*. MIT press.

Newman, J. N. (1986). Distributions of sources and normal dipoles over a quadrilateral panel. *Journal of Engineering Mathematics*, 20(2):113–126.

Ogilvie, T. and Tuck, E. (1969). A Rational Strip Theory of Ship Motions: Part I. Technical Report 013, University of Michigan, Department of Naval Architecture and Marine Engineering, Ann Arbor, Michigan.

Olofsson, N. (1996). *Force and flow characteristics of a partially submerged propeller*. PhD thesis, Department of Naval Architecture and Ocean Engineering, Division of Hydromechanics, Chalmers University of Technology, Götborg, Sweden.

Pozrikidis, C. (2002). *A Practical Guide to Boundary Element Methods with the Software Library Bemlib*. Chapman & Hall/CRC Press.

Press, W. H., Teukolsky, S. A., Vetterling, W. T., and Flannery, B. P. (1992). *Numerical Recipes in C: The art of scientific computing*. Cambridge University Press, 2nd edition.

Reynolds, O. (1874). On the effect of immersion on screw propellers. *Transactions of the Institution of Naval Architects*, XV:188–191.

Roddier, D. G. H. (2000). *Hydrodynamics of Rolling Cylinders with and Without Bilge Keels*. PhD thesis, University of California, Berkeley, Spring 2000.

Rogers, D. F. and Adams, J. A. (1990). *Mathematical elements for computer graphics*. McGraw-Hill, Inc., New York, NY, USA, 2nd edition.

Rose, J. C. and Kruppa, C. (1991). Surface Piercing Propellers Methodical Series Model Test Results. In *Proceedings of FAST'91*, Norway.

Rose, J. C., Kruppa, C., and Koushan, K. (1993). Surface Piercing Propeller/Hull Interaction. In *Fast'93*, pages 867–881, Japan.

Savineau, C. M. (1996). *A Time Marching Boundary Element Method for the Prediction of the Flow Around Surface Piercing Hydrofoils.* Master's thesis, Department of Ocean Engineering, Massachusetts Institute of Technology.

Savineau, C. M. and Kinnas, S. A. (1995). A numerical formulation applicable to surface piercing hydrofoils and propellers. In *24th International Towing Tank Conference*, Texas A&M University, College Station, TX.

Scherer, J. (1977). Partially submerged and supercavitating propellers. In *Proceedings of the 18th ATTC*, Annapolis.

Shen, Y. (1975). General scaling problems on fully cavitating and ventilated flows. In *Proceedings of the 17th ATTC*, Pasadena.

Shiba, H. (1953). Air-drawing of marine propellers. Technical Report No. 9, Transportation Technical Research Institute, Mejiro, Toshimaku, Tokyo, Japan.

Skjelbreia, L. and Hendrickson, J. A. (1961). Fifth order gravity wave theory. In *Proceedings, Seventh Conference of Coastal Engineering*, pages 184–196, The Hague, The Netherlands. Council on Wave Res., The Engrg. Found.

Stratton, J. A. (1941). *Electromagnetic Theory.* McGraw-Hill New York.

Suhrbier, K. and Lecoffre, Y. (1986). Investigation of the influences of test techniques, water speed and nucliei seeding on the characteristics of a high speed model propeller in a cavitation tunnel and correlation with full scale measurements. In *International Symposium on Cavitation*, Sendai, Japan.

Sun, H. and Faltinsen, O. M. (2007). The influence of gravity on the performance of planing vessels in calm water. *Journal of Engineering Mathematics*, 58(1):91–107.

Tanizawa, K. (1995). A nonlinear simulation method of 3-d body motions in waves (1st report) : Formulation of the method with acceleration potential. *Journal of the Society of Naval Architects of Japan*, (178):179–191.

Terent'ev, A. G. (1979). Inclined entry of a thin body with ventilated cavity into an ideal imponderable liquid. *Fluid Dynamics*, 14(3):377–385.

Tsai, W. and Yue, D. K. P. (1996). Computation of nonlinear free-surface flows. *Annual Review of Fluid Mechanics*, 28(1):249–278.

Tsai, W.-T. and Yue, D. K. P. (1993). Interactions between a free surface and a vortex sheet shed in the wake of a surface-piercing plate. *Journal of Fluid Mechanics*, 257:691–721.

Ueberhuber, C. W. (1997). *Numerical computation 1: methods, software, and analysis*. Springer-Verlag, Berlin.

Vinayan, V. and Kinnas, S. A. (2007). A BEM for the Propagation of Nonlinear Planar Free-surface Waves'. *Electronic Journal of Boundary Elements*, 5(1):17–40.

Vinayan, V. and Kinnas, S. A. (2008). Numerical modeling of surface piercing hydrofoils and propellers. In *Proceedings of the 27th Symposium on Naval Hydrodynamics*, Seoul, Korea.

Vinayan, V., Kinnas, S. A., and Yu, Y.-H. (2005). Modeling of Flow Around FPSO Hull Sections Subject to Roll Motions: Effects of Nonlinear Boundary Conditions. In *Proceedings of the 24th International Conference on Offshore Mechanics and Arctic Engineering*, volume 3, pages 805–816, Halkidiki, Greece. ASME.

Vinje, T. and Brevig, P. (1981). Nonlinear ship motions. In Dearn, J.-C. and Hausssing, H. J., editors, *Proceedings of the 3rd International Conference on Numerical Ship Hydrodynamics*, pages 257–268, Palaid des Congres, Paris, France.

Von Karman, T. (1929). The impact of seaplane floats during landing. Technical report, NACA TN321.

Vugts, J. H. (1968). The hydrodynamic coefficients for swaying, heaving and rolling cylinders in a free surface. Report No. 112S, Laboratorium voor Scheepsboukunde, Technische Hageschool Delft, The Netherlands.

Wagner, H. (1932). Über stoss- und gleitvorgänge an der oberflänche von flüssigkeiten. *Z. Angew. Math. Mech.*, 12(4):pp. 192–215.

Wang, D. P. (1977). Water entry and exit of a fully ventilated foil. *Journal of Ship Research*, 21(1):44–68.

Wang, D. P. (1979). Oblique water entry and exit of a fully ventilated foil. *Journal of Ship Research*, 23(1):43–54.

Wehausen, J. V. and Laitone, E. V. (1960). Surface waves. *Handbuch der Physik*, 9(3):446–778.

Whaley, R. C. and Dongarra, J. (1997). Automatically Tuned Linear Algebra Software. Technical Report UT-CS-97-366, University of Tennessee. URL : `http://www.netlib.org/lapack/lawns/lawn131.ps`.

Wrobel, L. C. (2002). *Boundary Element Method, Volume 1: Applications in Thermo-Fluids and Acoustics*. Wiley, 1st edition.

Wu, T. Y. T. (1955). A free streamline theory for two-dimensional fully cavitated hydrofoils. Technical Report Report No. 21-17, California Institute of Technology, Pasadena, California.

Wu, T. Y. T. (1972). Cavity and Wake Flows. *Annual Review of Fluid Mechanics*, 4(1):243–284.

Yeung, R. W. (1982). Numerical methods in free-surface flows. *Annual Review of Fluid Mechanics*, 14(1):395–442.

Yim, B. (1969). An application of linearized theory to water entry and water exit problems. (Part 2) with Ventilation. Report 3171, NSRDC.

Yim, B. (1971). Investigation of gravity and ventilation effects in water entry of thin foils. In *Proceedings IUTAM Symposium on Nonsteady Flows of Water with High Velocities*, pages 471–489, Leningrad. Nauka, Moscow.

Yim, B. (1974). Linear theory on water entry and exit problems of a ventilating thin wedge. *Journal of Ship Research*, 18(1):1–11.

Young, Y. L. (2002). *Numerical Modeling of Supercavitating and Surface-piercing Propellers (also UT-OE Report No. 02-1)*. PhD thesis, Ocean Engineering Group, Department of Civil, Architectural and Environmental Engineering, University of Texas at Austin, Austin, Texas, May.

Young, Y. L. and Kinnas, S. A. (2003). Numerical modeling of supercavitating propeller flows. *Journal of Ship Research*, 47(1):48–62.

Yu, Y.-H. (2008). *Prediction of Flows around Ship-shaped Hull Sections in Roll Using an Unsteady Navier-Stokes Solver (also UT-OE Report 08-1)*. PhD thesis, Ocean Engineering Group, Department of Civil, Architectural and Environmental Engineering, University of Texas at Austin, Austin, Texas, August.

Zhao, R. and Faltinsen, O. (1993). Water entry of two-dimensional bodies. *Journal of Fluid Mechanics*, 246:593–612.

Zhao, R., Faltinsen, O. M., and Aarsnes, J. (1996). Water entry of arbitrary two-dimensional sections with and without flow separation. In *Proceedings of 21st Symposium on Naval Hydrodynamics*, pages 408–423, Trondheim, Norway. National Academy Press, Washington D.C.

Vita

Vimal Vinayan was born in Secunderabad, Andhra Pradesh, India on 17 May, 1977, the son of Rama Vinayan and R. Vinayachandran. He graduated from Kendriya Vidyalaya No. 2, Naval Base, Cochin in 1994. He attended the Department of Ship Technology, Cochin University of Science and Technology from 1994 to 1999 and received a Bachelor of Technology in Naval Architecture and Ship Building on August 12, 1999. After graduation he worked as a Naval Architect for Mazagon Dock Limited, Mumbai from 1999 through 2001. He enrolled at the Florida Atlantic University in 2001 and received the Master of Science Degree in Ocean Engineering with emphasis on Autonomous Underwater Vehicles in 2003. He started his doctoral study in the Ocean Engineering Group at the Department of Civil Engineering, University of Texas at Austin in 2003.

Permanent address: Pampa Nivas, Marottichodu Jn.
Edapally, Kerala-682024, India

This dissertation was typeset with LaTeX[†] by author.

[†]LaTeX is a document preparation system developed by Leslie Lamport as a special version of Donald Knuth's TeX Program.